Title
Synthesis and Characterization of New Metal-Organic Frameworks for Gas Adsorption Studies and as Solid Superacids

Author
Jiang, Juncong

Publication Date
2016

Synthesis and Characterization of New Metal-Organic Frameworks for Gas Adsorption Studies and as Solid Superacids

By

Juncong Jiang

A dissertation submitted in partial satisfaction of the

requirements for the degree of

Doctor of Philosophy

in

Chemistry

in the

Graduate Division

of the

University of California, Berkeley

Committee in charge:

Professor Omar M. Yaghi, Chair
Professor F. Dean Toste
Professor Jeffrey A. Reimer

Spring 2016

Abstract

Synthesis and Characterization of New Metal-Organic Frameworks for Gas Adsorption Studies and as Solid Superacids

By

Juncong Jiang

Doctor of Philosophy in Chemistry

University of California, Berkeley

Professor Omar M. Yaghi, Chair

The development of metal-organic frameworks (MOFs) has experienced three main periods: (1) discovery of new structures; (2) structure design using the principles of reticular chemistry; and (3) study of these new materials in various applications. We are now in the third period as MOFs are extensively tested in a large number of potential applications, such as gas-storage and separation, catalysis, design of energy storage devices, drug delivery, and molecule sensing and recognition. The increasing applications of MOFs is raising the demand for the materials, therefore in this dissertation, I will focus on design and synthesis of new MOFs with high storage capacity for various gases including water, ammonia, and methane; and design and synthesis of MOF-based solid acids and the study of their liquid and vapor phase catalytic properties.

The strategy of material design targets practical applications. Thus, with different gas storage purposes in mind, different materials are proposed. In the first example, the need to capture water vapor at low humidity requires MOFs to exhibit pore filling or condensation of water into the pores at $P/P_0 < 0.1$. Thus we have designed a small pore zirconium MOF, MOF-801, for this purpose. MOF-801 is shown to have high uptake of water, recyclability, and water stability. In the second example, the need to capture harmful ammonia gas requires MOFs with strong binding sites for the basic gas at low concentration. Thus we have designed and installed strongly acidic sites in a zirconium MOF, sulfated MOF-808, for this purpose. This sulfated MOF-808 is shown to take up 5.3 mmol ammonia per gram at $P < 1.5$ Torr, and 16.7 mmol ammonia at $P = 760$ Torr, one of the highest numbers for a MOF-based ammonia capture material. In the third example, high methane gas storage capacity at 80 bar was attempted using MOFs. This increase on the working capacity (between 5 and 80 bar) requires MOFs to have both high surface area and suitable pore sizes. For this purpose, we have designed zinc MOFs using organic linkers having delocalized π-electrons and with suitable pore metrics. The compound, MOF-905, shows 200 $cm^3\ cm^{-3}$ working capacity between 5 and 80 bar, the highest of all zinc MOFs and is equivalent to the benchmark HKUST-1 compound.

With regard to the design and synthesis of MOF-based solid acids, three approaches have been proposed: (1) acidic functional groups bound to the organic linker; (2) acidic ligands bound to the inorganic cluster; and (3) acidic molecules encapsulated in MOF pores. While in the first

approach, the acidity of the MOF is mostly determined by the acidity of the free acidic functional group, the latter two strategies provide for more interaction between the framework and the acidic groups, which is of great importance to understand the chemistry within the pores. A new type of MOF-based solid acid is demonstrated by the controllable sulfation of a zirconium MOF, MOF-808, on the inorganic cluster. The substitution of terminal formate groups in MOF-808 with sulfate groups has imparted strong acidity onto the sulfated MOF-808. The material has shown activity for acid catalyzed Friedel-Crafts acylation, esterification, isomerization, as well as the conversion of methylcyclopentane (MCP) into various hydrocarbons at 150-200 ^{o}C. Another MOF-based acid is synthesized by including phosphotungstic acid (PTA) into the large cages of MIL-101. Interestingly, we have found that the Brønsted acidity (originating from PTA) of the composite material is not directly proportional to the loading of PTA. Instead, the acidity is not exhibited until a threshold amount of PTA loading is reached. This is explained by the level of protonation of PTA incorporated into the material, where the material with the highest loading, Pt/60PTA/MIL-101, is shown to effectively catalyze hydroisomerization of n-hexane at 250 ^{o}C.

---

*The work includes material (text and figures) from Jiang, J.; Zhao, Y.; Yaghi, O. M. Covalent Chemistry beyond Molecules. J. Am. Chem. Soc. **2016**, 138, 3255. Jiang, J.; Yaghi, O. M. Brønsted Acidity in Metal-Organic Frameworks. Chem. Rev. **2015**, 115, 6966. Jiang, J.; Gándara, F.; Zhang, Y.-B.; Na, K.; Yaghi, O. M.; Klemperer, W. G. Superacidity in Sulfated Metal-Organic Framework-808. J. Am. Chem. Soc. **2014**, 136, 12844. Furukawa, H.; Gándara, F.; Zhang, Y.-B.; Jiang, J.; Queen, W. L.; Hudson, M. R. Yaghi, O. M. Water Adsorption in Porous Metal-Organic Frameworks and Related Materials. J. Am. Chem. Soc. **2014**, 136, 4369. and also non-published results. The use of co-authored material is permitted by all contributing authors. The material is reproduced with permission, copyright 2014, 2015, and 2016 American Chemical Society.

Table of Contents

Acknowledgements

First of all, I wish to express my gratitude to my research advisor, Professor Omar M. Yaghi, for his support and tolerance during the course of my research. He has been a true inspiration. I am fortunate to have him contribute to my intellectual, academic, and spiritual growth. I also wish to extend my appreciation to Professors F. Dean Toste and Jeffrey A. Reimer for being on my committee, and for their helpful comments and suggestions.

Secondly, I am thankful to all those who stood by my side and provided me with help, in big and small ways, towards the completion of my research and dissertation. I appreciate the efforts of Professor Walter G. Klemperer in his guidance and advice on the superacid project, and many members of the Yaghi group (both present and past): Drs. Hiroyasu Furukawa, Yuebiao Zhang, Felipe Gándara, Kyungmin Choi, Alejandro M. Fracaroli, and Alexander Schödel, and Mr. Yingbo Zhao, Christopher A. Trickett, and Christian S. Diercks for all the discussion, collaboration, and proofreading of my manuscripts. In particular, I am thankful to Dr. Yuebiao Zhang for helping me in the first a few years in the group; Drs. Hiroyasu Furukawa, Alejandro M. Fracaroli, Longyu Li, and Mr. Robinson W. Flaig for proofreading of my dissertation. I also wish to thank my collaborators outside the Yaghi group: Professors Gabor A. Somorjai, Jeffrey A. Reimer, and Stefan Wuttke, and Drs. Wendy L. Queen, Matthew R. Hudson, Kyungsu Na, Jun Xu, Kairat Sabyrov, and Waldemar Schrimpf. Many thanks to my advisors during my internship in BASF SE: Drs. Lena Arnold and Ulrich Müller. I would like to thank Professors Jeffrey R. Long, Charles Harris, and Kenneth Raymond for being on my qualifying exam committee.

Thirdly, I would like to thank my friends Mr. Rong Ye and Dr. Jun Xu. It is so much fun the time being together with you.

Finally, I thank my parents for their understanding, and unconditional love and support. It all begins with them.

Without all of you, none of this would have been possible.

Chapter I

Introduction to Metal-Organic Frameworks

Metal-organic frameworks (MOFs) are crystalline materials constructed by linking organic and inorganic secondary building units (SBUs) with strong bonds.[1] the chemistry of MOFs has been explored extensively in the areas of inorganic chemistry and materials science in the past two decades. The reasons for such intensive study stems not only from the aesthetics of creating unprecedented structures, but also from the expectation of novel properties not previously possible in the realm of molecular chemistry.[2]

The first period (1995 - 2002) of MOF materials' developments began with the first major development in MOF chemistry: the use of charged organic building units instead of neutral Lewis bases to form a stronger bond between SBUs. The bond energy between metal ions and neutral Lewis bases are reported to be in the range of 90-180 kJ mol^{-1}.[2] This leads to the thermal instability because of their frail architecture which often results in framework collapse when attempting to evacuate the space encompassed within them and thus limits the implementation of these materials in applications where open frameworks are preferred.

Conversely, the metal-charged organic linker bond, for example, the Zn(II)-carboxylate bond in MOF-5,[3] $Zn_4O(C_8H_4O_4)_3$, is estimated to have the bond energy of 300 kJ mol^{-1}, a number that is comparable to covalent bonds found in conventional molecules.[4] This has greatly enhanced the thermal stability of these MOFs as they are robust upon removal of the guest solvent molecules. Proof of permanent porosity was obtained as early as 1998 in activated MOF-2, $Zn(C_8H_4O_4)$.[5] This has allowed comparisons to be made between these frameworks and the more traditional porous material, such as zeolites and related inorganic microporous materials.

However, these strong bonds between SBUs inevitably increase the difficulty in crystallizing these extended frameworks. This difficulty is referred to in literature as the 'crystallization problem'.[2] This problem originates from the fact that strong bonds, as linkages, tend to form irreversibly under mild conditions, hampering self-correction of defects during the crystallization process. Therefore the formation of amorphous or poorly defined solids is favored. To overcome this problem in MOF chemistry, it is important to slow down the formation of strong metal-carboxylate bonds between the inorganic and organic SBUs to a time scale permitting self-correction.

The formation of the MOFs using charged organic secondary building units (SBUs) requires deprotonation of the organic acids in order to form the metal-oxygen bonds.[2] However, the rate at which this deprotonation process takes place is a critical factor in controlling the crystallization process. The key development in making MOF crystals based on metal-carboxyl bonds was the use of amide solvents such as dimethylformamide (DMF), diethylformamide, dimethylacetamide, and N-methyl-2-pyrrolidone.[5] These solvents release basic amines upon heating, which is required for crystalline MOF formation. This allows for gradual control of the deprotonation of the organic acid and thus the formation of strong bonds between inorganic and organic SBUs. MOF single crystals up to millimeters in size have been reported using these solvents.[6] This basic synthetic procedure has been employed in the synthesis of the vast majority of MOFs. Once a new MOF is discovered using this procedure, other preparation methods

involving the use of water as a solvent, microwave irradiation, and mechanochemical procedures could be deployed to make those MOFs.[7]

It was also shown that highly crystalline zirconium, aluminum and iron MOFs can be obtained by adding modulators,[8] typically monocarboxylic acids such as formic acid, acetic acid and benzoic acid. Addition of modulators with di- and multi-topic carboxylate linkers suppress the hydrolysis of the metal ions to metal oxides due to their acidity, and slows down the crystal growth process to give the control needed for obtaining MOF crystals.

In subsequent years, other organic ligands, such as catechols,[9] organosulfuric acids,[10] organophosphoric acids,[10,11] imidazoles,[12] and pyrazoles,[13] were also used to make MOF materials. Despite their differing structures and chemical properties, these ligands all have the ability to be deprotonated and form strong chemical bonds with the metal SBUs. Thus, many MOF materials are robust frameworks comparable to the metal-carboxylate based MOFs.

Sustained efforts devoted to the crystallization of these extended structures have produced highly crystalline materials and made their structural characterization possible by diffraction techniques (powder and single crystal X-ray, neutron, and electron). Over 6,000 MOF structures have been reported in the period of 1995-2002,[1] which allows for the study of rules that these structures follow and the rational design of MOF materials.

The beginning of the second period (2003 - 2009) is marked by the introduction of reticular chemistry. Reticular chemistry, or reticular synthesis, is defined as the logical approach to assemble predesigned building blocks by strong bonding into predetermined ordered structures.[4] This is achievable because the structural integrity and rigidity of the building blocks remain unaltered during the synthesis. These SBUs, can be either a duplicate from the starting materials, or be formed predictably in situ.

It is natural to make an analogy between SBUs in a MOF and atoms in a conventional molecule, as they are both the fundamental unit of a larger scale entity, not to mention there are cases in which inorganic SBUs in MOFs are single atoms by themselves. Also, they can be described using similar language: in molecules, each atom has its fixed coordination number and coordination geometry; while in MOFs, each SBU, organic or metal-containing, also has its fixed coordination number (CN) and coordination geometry. For example, in MOF-5,[3] each inorganic $Zn_4O(CO_2)_6$ SBU is bound to organic SBUs in 6 directions oriented in space as an octahedron, resembling that of the central sulfur atom in sulfur hexafluoride, thus both are described with coordination number equals 6 and octahedral coordination geometry. More often, the above is illustrated in a way that each building block is abstracted as shapes such as dots (CN = 1), lines (CN = 2), triangles (CN = 3), squares (CN = 4), tetrahedra (CN = 4), and octahedral (CN = 6). As shown in Figure 1.1, MOF-5 is represented by a cubic network consisting of octahedra connected with lines. In this way, all the organic SBUs and finite inorganic SBUs can be topologically described with MOF structures abstracted into underlying nets in their augmented versions that are special kind of periodic graphs.[14]

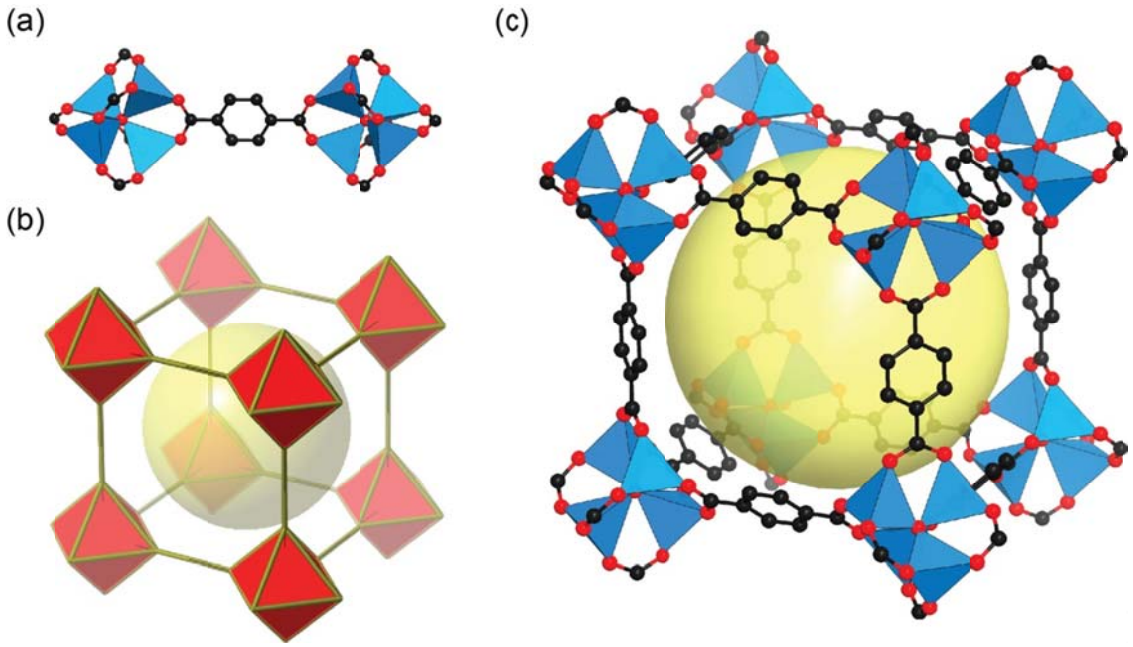

Figure 1.1. The strong bonds between $Zn_4O(\text{-}COO)_6$ clusters and terephthalate leads to MOF-5 having the **pcu** topology (b), with a crystal structure having large pores (c). The six-coordinated Zn SBUs are represented by octahedra (red) and the linear terephthalates are linking them together. Atom color scheme: C, black; O, red; Zr, blue polyhedra. H atoms are omitted for clarity. Yellow spheres indicate the space in the framework.

MOFs consisting of infinite rod-shaped metal-carboxylate SBUs, $[M_x(CO_2)_y]_\infty$ and $[M_xO_y(CO_2)_z]_\infty$, are also well known.[15] Typically, the SBUs consist of infinite $(\text{-O-C-O-M-})_\infty$ or $(\text{-O-M-})_\infty$ rods with carboxylate O atoms completing coordination around the metal atom to form a rod of discrete or edge- and corner-sharing MO_x polyhedra. Similarly, these rod-shaped SBUs can be abstracted as helices and ladders. And when they are connected with finite organic SBUs, by studying the rod-packings, it is also useful to describe them in terms of their underlying nets.

This approach has led to significant progress in the way people synthesize solid-state materials. The outcome of synthesis utilizing a mixture of SBUs could only be based on one or few number of nets that are allowed from the combination of those SBU geometries. Once a MOF is made its metrics and functionality can be altered without changing the underlying net to make what is known as isoreticular (IR) structures in reticular chemistry. Many isoreticular compounds, with systematically altered chemical composition, functionality, and molecular dimensions, have subsequently been synthesized by design.

Isoreticular MOFs were synthesized by replacing the metal atoms in the inorganic SBUs, both discrete and infinite ones. For instance, solvothermal syntheses of isoreticular HKUST-1 [$M_3(BTC)_2$, M = Cu(II), Zn(II), Fe(II), Mo(II), Cr(II), Ru(II); BTC = benzene-1,3,5-tricarboxylate],[16] MIL-101 [$M_3X(H_2O)_2O(BDC)_3$; M = Al(III), Cr(III), Fe(III); X = F, OH],[17] and MOF-74 [M_2(DOBDC); M = Zn(II), Mg(II), Mn(II), Fe(II), Co(II), Ni(II); DOT = 2,5-dihydroxybenzene-1,4-dicarboxylate][15e,18] were reported. In the same way as inorganic SBUs,

atoms in the organic SBUs were also changed to synthesize isoreticular MOFs such as the sulfur-analogue of MOF-74 [M_2(DSBDC); M = Fe(II), Mn(II)].[19]

Isoreticular functionalization of MOFs with derivatives of organic SBUs was first reported in 2002 on the basis of MOF-5 (IRMOF-1) resulted in a family of 6 cubic IRMOFs—IRMOF-2 to IRMOF-7.[20] This development heralded the adaptability of the MOF synthesis to functional groups including amino, bromo, alkoxy, aliphatic and aromatic rings. The list of functionality tolerance was subsequently expanded to other structures as well as functional groups initially thought to interfere the MOF synthesis. Hexagonal structure MOF-177 [$Zn_4O(BTB)_2$; BTB = benzene-1,3,5-tribenzoate] was recently made with a variety of 9 derivatives of BTB with varying type and position of function groups as well as an example of single BTB linker bearing 3 different kind of functional groups on its 3 branches.[21] Medium to strong Brønsted acid group functionalized BDC linkers were also reported to be 'isoreticularly' incorporated into UiO-66 [$Zr_4O_4(OH)_4(BDC)_6$] and MIL-101 type of structures.[22]

The concept of isoreticular expansion involves the use of longer organic SBUs while retaining the same underlying net.[1] In the cubic MOF-5 system, the largest member, IRMOF-16 [$Zn_4O(TPDC)_3$; TPDC = terpehyl-4,4"-dicarboxylate][20] bears a unit cell volume eight times to that of $Zn_4O(fumarate)_3$,[23] the smallest member. This record was soon broken with a series of MOF-74's with large pore apertures large enough to take in proteins. The volumetric expansion ratio between the largest MOF-74-XI and the smallest MOF-74 was measured to be 16.1.[24] And the current record holder is MOF-399, [$Cu_3(BBC)_2$; BBC = 4,4',4"-(benzene-1,3,5-triyl-tris(benzene-4,1-diyl))tribenzoate],[25] a giant 17.4 times larger than its smallest member HKUST-1. MOF-399 also holds the record for the lowest reported crystal density in all MOFs.

It is not guaranteed that isoreticular structures will always be obtained once SBUs of same shape are used. Although reticular design greatly limits the number of available structures, the final structures depend also on the details of the conditions of synthesis and parameters that go beyond geometry such as solubility of the building units. For example, reticular chemistry only allows two ways of linking $Cu_2(CO_2)_4$ squares and BTC/BTB/TATB [TATB = 4,4',4''-(1,3,5-triazine-2,4,6-triyl)tribenzoate] triangular SBUs—these are nets named after Pt_3O_4 and twisted boracite. Despite the structural similarity between BTC, BTB and TATB, MOF-14, [$Cu_3(BTB)_2$][26] is formed with Pt_3O_4 net while HKUST-1 and PCN-6, [$Cu_3(TATB)_2$],[27] adopt the twisted boracite net. Examination of the parent nets informs us that the Pt_3O_4 net requires a more flexible dihedral angle between the abstract triangle and the carboxylate groups, while that value for BTC and TATB are fixed around 0^o.

At present, reticular chemistry has entered the new stage where increasing complexity is introduced.[28] This is reflected in the larger number of building blocks incorporated in a single structure, lower symmetry and higher flexibility of the building blocks, and more selective interactions for formation strong bonds between inorganic and organic SBUs. However, as stated at the beginning of this section, the rigid building blocks and formation of strong bonds within the order of the underlying nets allow the materials to remain crystalline. That is to say, MOFs, although typically several hundreds to a few thousands times larger in each dimension, are structurally and compositionally as well-defined as conventional molecules.

The starting point of the third period (2009 - present) of MOF chemistry is not clearly marked by one incident. This period is marked by application of MOF materials in various fields. These studies have begun with the first discovery of MOF structures and have continued since.

However, the year of 2009 is especially important because the first MOF themed issue in Chem. Soc. Rev.,[29] which summarized the important rules on structure design, potential application directions, and preliminary results. More importantly MOFs were now recognized as an important and active field of study for scientists around the world.

As mentioned above, the chemistry of MOFs is designed around their pores. Thus, the applications of MOFs will inevitably be dependent upon their porosity. The permanent porosity of MOFs has allowed unparalleled precision in: expanding the pores, designing the pore shape, and the covalent attachment of functional groups to the organic linkers and/or open metal sites within the backbone of MOFs. Moreover, on a fundamental level, the ability to make MOF structures permanently porous has given access to molecules within the confines of an extended structure. Indeed, all atoms [with the exception of a central atom which might reside within an inorganic SBU, for example, the O in $Zn_4O(\text{-}COO)_6$] that make up the inorganic and organic SBUs are accessible to incoming guests such as gases and organic molecules. This advantage is only possible because the SBUs are stitched through strong bonds and thus are suspended in 3D without being solvated as discrete molecules. Additionally, they do not suffer from being inaccessible in the solid state, as would be the case in a closely packed molecular crystal.

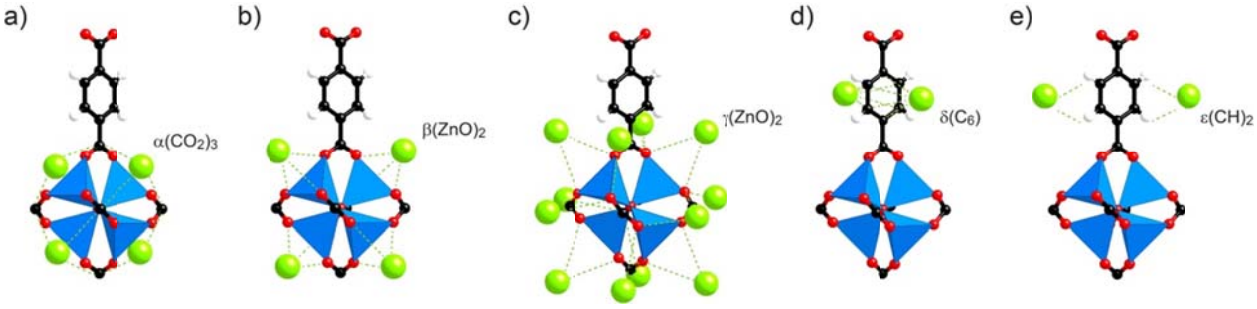

Figure 1.2. Symmetry-independent adsorption sites partially occupied by Ar atoms at 30 K. These include (a to c) three sites primarily associated with the secondary building unit and those above the (d) face and (e) edges of the linker. The absorption sites are represented as green spheres. Atom labeling scheme: Zn (blue polyhedra), C (black), O (red), and H (white).

Access to each of the atoms in MOFs was revealed by an X-ray diffraction experiment conducted on single crystals of MOF-5 at 30 K.[30] Here, small doses of Ar or N_2 introduced into the already evacuated pores revealed accessible adsorption sites: the zinc oxide SBU (Figure 1.2, a-c), the faces and the edges of the phenyl ring of the BDC linkers (Figure 1.2, d-e). This study also served as a benchmark for identifying the origin of the ultrahigh surface areas found in MOFs. Subsequently, adsorption sites for gases, such as $D_2(H_2)$, CH_4, CO_2, and H_2O, and their behavior in MOFs were identified using a variety of techniques,[31] and their interaction strength was assessed for a large variety of MOFs. Thus, suspending molecules in 3D space and having access to these molecules by covalently linking them into scaffolds is the best strategy for maximizing access to them as well as for increasing the number of adsorption sites.

All these advantages have qualified MOFs as one of the most competitive materials for applications involving gas storage and separation. Indeed, relevant studies through gas uptake

experiments with carbon dioxide,[5,32] methane,[33] and hydrogen[34] in MOFs were started as early as 1998, 2000, and 2003, respectively.

Research on MOFs for hydrogen storage has increased in the past 13 years. The US Department of Energy (DOE) set the 2017 hydrogen storage in materials target for mobile applications at a: gravimetric capacity of 5.5 wt% and volumetric capacity of 40 g L^{-1} under -40 to 85 ^{o}C.[35] According to literature reported values, MOF materials exhibit excess gravimetric hydrogen storage capacities in the range of 5 to 15 wt% at 77 K and 80 bar. Total volumetric capacities are reported in the range of 40 to 60 g L^{-1} under these conditions.[36] MOFs have also been shown to reversibly store substantial amounts of hydrogen with exhibited fast kinetics of hydrogen release. These results indicate that MOFs can potentially meet the DOE target. However, extensive studies are still needed to optimize and explore novel MOF materials, especially for room temperature hydrogen storage (MOFs now exhibit 0.5 to 1 wt% gravimetric capacity and less than 15 g L^{-1} volumetric capacity at room temperature).[36] Interest exists for exploring approaches to increase the strength of interaction between hydrogen molecules and the framework, including making noble metal@MOF composite materials to take advantage of a potential spillover effect.

Among the diverse applications of MOF as gas storage materials, their application in methane storage might be one of the most promising. BASF has commercialized some prototypic MOFs (HKUST-1 or Basolite C300) and built vehicles of both light and heavy duty equipped with natural gas fuel systems containing MOF materials. In 2012, the US DOE updated the target of methane storage in materials for adsorbed natural gas (ANG) mobile application. This new target details an escalated system gravimetric capacity of 50 wt% and a volumetric capacity of 250 g L^{-1}.[37] Accordingly, new porous adsorbents are required to meet these challenging storage targets in order for the ANG technology to become practical. Currently, MOF materials exhibit gravimetric and volumetric methane storage capacity in the range of 15 to 37 wt% and 140 to 192 g L^{-1} at 298 K and 65 bar, respectively.[38] These results clearly show that MOFs are promising adsorption materials for this application, but more scientific studies will still be necessary to target some new porous MOFs for higher methane storage capacity. Several potential research directions include: (a) synthesis of new MOFs with 10 Å (diameter) pores, as these small cages have proven to be extremely important for high volumetric methane storage; (b) clarification of the pertinent organic functional groups on MOFs' methane storage capacities and identify the powerful organic functional groups; (c) modification of the pore interiors of extended MOFs to augment the interactions between methane molecules and the MOF backbone. This includes introduction of metal ions, nanoparticles, and complexes; and (d) formation of an intimate collaboration with industry to facilitate the measurement at higher pressure (up to 250 bar), increasing the scale of synthesis, and optimizing the fabrication of materials.

Another use of MOFs is in the important gas storage/separation process involving the removal of carbon dioxide from flue gas streams. The plethora of choices of metal centers and organic linkers make it possible to synthesize MOFs with desired pore structures and environments for carbon dioxide capture and separation. The state-of-the-art strategies for carbon dioxide capture in MOFs employ carefully designed open metal sites and/or basic functional groups on the framework.[39] MOFs with open metal sites show moderate to high carbon dioxide uptake at low pressure, particularly at 0.15 bar and 298 K. The major factors that affect capacity and selectivity of CO_2/N_2 are the nature and density of open metal sites. Materials belonging to this category include M-MOF-74 (CPO-27) and $M_2(dobpdc)_2$, M = Mg, Co, Ni, Zn, with Mg-

MOF-74 holding the record for gravimetric capacity, 26.0 wt% CO_2 at 0.15 bar and 298 K. However, since the flue gas consists of ~6 % water vapor, which is known to bind strongly to MOF open metal sites, it is challenging to use open metal sites to capture carbon dioxide under humid conditions. To overcome this challenge, several strategies have been applied in MOF design and synthesis: (a) development of water-stable MOFs using high valent metal clusters, such as Al(III), Fe(III), and Zr(IV), and/or nitrogen-based linkers, such as imidazolate, triazolate, and pyrazolate; (b) design of hydrophobic MOF pores, including attaching alkyl and perfluoroalkyl groups on the linker to shield the metal SBU, or designing frameworks in which the hydrophobic moieties on the linkers are positioned toward the pores (as illustrated in some zeolitic imidazolate frameworks); and (c) exploration of carbon dioxide capture mechanisms that either react synergistically or be unreactive towards water vapor. MOFs with basic sites such as covalently bound amino groups are of the latter category.

Compared to the relatively large body of work done on the storage of hydrogen, methane and carbon dioxide in MOFs, water adsorption in MOFs is in its infancy. This is mainly due to the combination of two factors. The first being that water stable MOFs [e.g. with Zr(IV), Al(III), and Fe(III)] compose only a small fraction of all MOFs discovered and their discovery is relatively recent. The second being that the strong intermolecular interaction between water molecules and between water molecule and the MOF framework leads to a very distinct behavior of water compared to other gases. To date, studies on water adsorption in MOFs focus on three promising applications: (a) MOFs as adsorption materials for dehumidifiers; (b) MOFs as adsorbents for heat pump or adsorption chiller applications; and (c) MOFs as adsorbents for harvesting water from air.[40] Targeting these three applications, general requirements are proposed for the materials: good water stability, the presence of steep, well-defined pore condensation at a low relative pressure, high uptake to allow maximum working capacity, and facile recyclability of the material during water adsorption. According to these criteria, materials such as M-MIL-100 (M = Al, Fe), Cr-MIL-101, UiO-66, M-MOF-74 (M = Mg, Co, Ni), MOF-801, and MOF-841, are identified as promising candidates.

It is also be interesting to compare the different water-adsorption behavior between MOFs and other porous materials. For example, Zeolites have the ability to capture water at very low relative pressures because of their great affinity for water.[41] However, as consequence of the strong interaction with the framework, heating to a high temperature is required to desorb the water and regenerate the adsorbent. Large pore materials, such as mesoporous silicas and carbons can achieve high water uptake capacity,[42] but due to their hydrophobic nature, the water capture is restricted to the condensation at high relative pressure values with these materials being difficult to chemically manipulate to significantly modify their sorption profile. Among various MOFs, there are scenarios where stronger sorption sites can be incorporated in the form of open metal sites, as in MOF-74. As one would expect, similar to the case of zeolites, these are found to be very strong sorption sites for water and require higher temperatures to desorb the water molecules. There are also cases where the large pore MOFs, MOF-100 and MIL-101, exhibit a large total uptake with a step position at high P/P_0 (0.3-0.5). This behavior indicates that the hydrophobic nature of the organic linker dominates the water sorption profile of the MOF, similar to that observed in mesoporous silicas and carbons. However, there are MOFs that fall in the middle where moderate interaction between water molecules and frameworks can be achieved by altering the pore size of MOFs or introducing polar or hydrophilic organic functional groups into the frameworks. These MOFs typically exhibit uptake steps at medium

P/P_0 (0.05-0.3) and can be easily regenerated by evacuation or moderate heating to ~80 ^oC. Nevertheless, extensive study is still required in this field. Firstly more water stable MOFs must be identified as potential candidates. Also systems must be developed that can adsorb water at low P/P_0 (< 0.05), while being regenerated easily (room temperature under vacuum or heating to 80 ^oC). These materials must also be producible on a large-scale and prototypic devices using these materials with the attempts to lower costs must be designed.

To some extent, ammonia and water are alike, despite the fact that ammonia has stronger basicity. Thus, few MOFs are reported to be stable to multiple adsorption/desorption cycles of ammonia. Two potential ammonia adsorption applications for MOFs are irreversible ammonia capture and ammonia storage.[43] Each application requires specific material properties. The first application targets the toxic gas removal for instance for gas masks. The performance of materials is evaluated by both static adsorption measurements using volumetric or gravimetric systems, and dynamic breakthrough measurements where the gas mixture containing ammonia is passed through the material and the different gas compositions are recorded before and after adsorbent materials. Two properties of the material are important for this particular application. First, the capturing agent should be able to remove ammonia from environments in which the gas is present at low concentrations, and store it irreversibly to keep its concentration levels below those recommended values (CAL-OSHA permissible ammonia exposure limit: 25 ppm).[44] The second criterion is the competitive ammonia removal under moist conditions due to the presence of significant amount of moisture in potential fields of application (for example, exhaled gas from human). The latter aims at reversible capture of ammonia in applications such as ammonia transportation and recycling. It is beneficial to use solid adsorbents to replace the toxic, corrosive, and difficult-to-handle compressed liquid ammonia. For this purpose, criteria such as high ammonia uptake capacity at 1 bar or even higher pressure, high cycling performance, and ammonia stability of the material are important. Compared to the irreversible ammonia capture, studies related to this application are limited and preliminary, mainly due to the lack of stable MOFs toward multi-cycle ammonia adsorption/desorption. To guarantee a high ammonia uptake at low pressure, strong interactions between adsorbents and adsorbates are preferred. MOFs with open metal sites (MOF-74) show strong interaction towards ammonia. The reported ammonia capture capacities are in the range of 2.6 to 7.6 mmol g^{-1} at 1440 ppm for these MOFs. However, up to 75 % of capacity loss were observed when attempting to capture ammonia under humid conditions (80 % RH), indicating a favorable water competition with ammonia molecules for the open metal sites.[45] To mitigate the competitive effect of water, Brønsted acidic sites are introduced into the framework with the expectation that it shows higher selectivity of ammonia over water. Functional groups including phenolic hydroxyl groups, ammonium groups, sulfonic acid groups, carboxylic acid groups are reported. The reported ammonia capture capacities are in the range of 2.6 to 3.5 mmol g^{-1} at ~ 500 ppm for MOFs with these functional groups. However, to date, no reports have appeared for evaluating the ammonia capture capacity for these Brønsted acidic MOFs under humid conditions.

Another important application for MOF materials is their use as versatile heterogeneous catalysts for efficient catalytic organic transformations.[46] As shown in Figure 1.3, the number of publications detailing catalysis by MOFs since 2005 is increasing, and there are approximately 500 papers published annually now. The versatility of MOF-based catalysts stems from the ability to introduce multiple catalytic active sites within the framework. Based on their positions, these active sites can be grouped into four main categories: (a) active species encapsulated within

the pores; (b) active sties on the metal/metal clusters of the framework; (c) active sites covalently bound to the organic linkers of the framework; and (d) active species forming mesoscopic composites with MOF materials. The last one includes core-shell type or support type of catalysts, which is different to the first type as no active species are confined in the MOF pores.

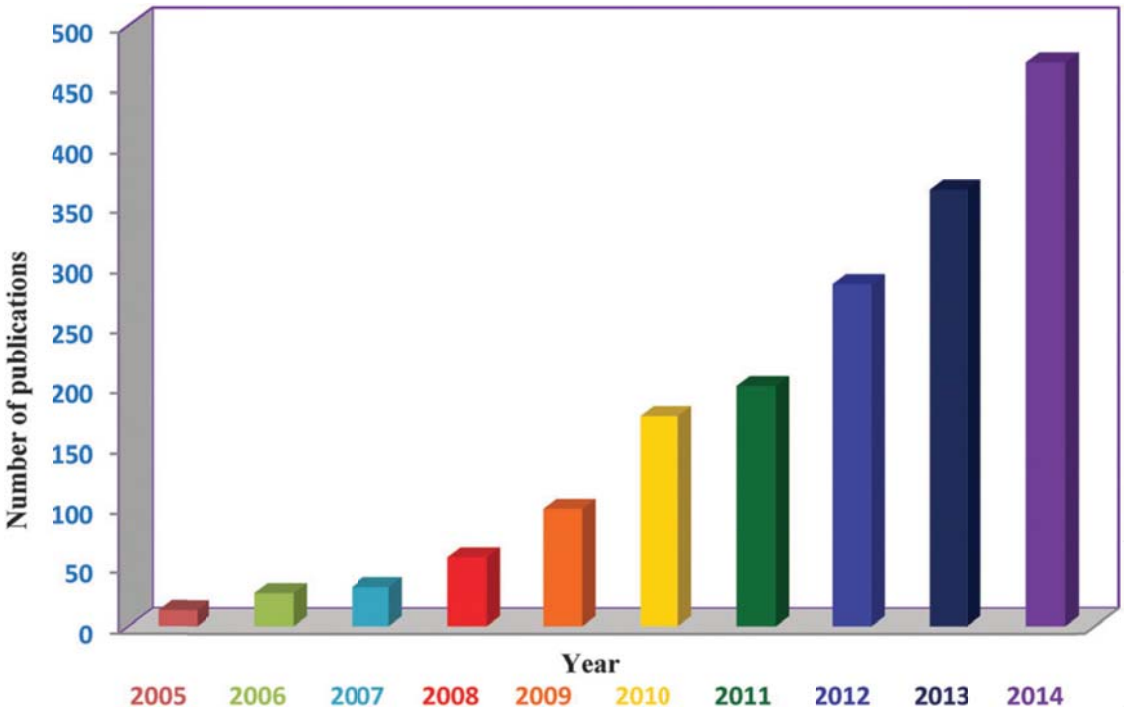

Figure 1.3. Publications related to catalysis by MOFs since 2005 (Source: Sci Finder, key word: catalysis by MOFs). Reproduced with permission for ref 46(d). Copyright Royal Society of Chemistry 2015.

Table 1.1. List of known catalytic Brønsted acidic MOFs and summary of reactions catalyzed[43b]

MOF materials[a]	Substrate(s)	Reaction(s) catalyzed
$H_3PW_{12}O_{40}@[Cr_3F(H_2O)_2O(BDC)_3]$	Styrene oxide and methanol	Alcoholysis
	Resorcinol and ethyl acetate; acetic acid and n-butanol	Pechmann reaction; esterification
	Acetaldehyde; acetaldehyde and phenol; acetaldehyde and methanol	Aldol condensation; Baeyer condensation; acetalization
	Glucose; Fructose	Carbohydrate dehydration
$H_3PW_{12}O_{40}@[Cu_3(BTC)_2]$	Acetic acid and n-propanol	Esterification
$H_4SiW_{12}O_{40}@[Cu_3(BTC)_2]$	Methanol; acetic acid and ethylene	Etherification; esterification
$H_3PW_{12}O_{40}@[Al_3F(H_2O)_2O(BDC\text{-}NH_2)_3]$	Acetaldehyde	Aldol condensation

$Pt/H_3PW_{12}O_{40}@[Cr_3F(H_2O)_2O(BDC\text{-}NH_2)_3]$	Hydrogen and toluene; carbon monoxide and oxygen	Hydrogenation; oxidation
$Ru/H_3PW_{12}O_{40}@[Cr_3F(H_2O)_2O(BTC)_2]$	Cellulose and hydrogen	Cellulose conversion
$Ru/H_3PW_{12}O_{40}@[Cu_3(BTC)_2]$	Cellulose and hydrogen	Cellulose conversion
$[SO_3H\text{-}(CH_2)_4\text{-}IM][HSO_4]$ and $[SO_3H\text{-}(CH_2)_4\text{-}TEDA][HSO_4]@[Cr_3F(H_2O)_2O(BDC)_3]$	Benzaldehyde and glycol	Acetalization
$[SO_3H\text{-}(CH_2)_3\text{-}HIM]_3PW_{12}O_{40}@Fe_3F(H_2O)_2O(BDC)_3]$	Oleic acid and ethanol	Esterification
$Zn_3(OH)_2(BDC)_2(DEF)_2$, $Zn_4O(BDC)_3$ and $Zn_4O(NDC)_3$	Toluene, biphenyl and tert-butyl chloride	Friedel-Craft alkylation
$Cu_3(BTC)_2$	Furfuryl alcohol; benzaldehyde and malononitrile	Knoevenagel reaction; oligomerization
$V(OH)(BDC\text{-}NH_2)$	Styrene oxide and carbon dioxide	Carbonation reaction
$Fe_3F(H_2O)_2O(BTC)_2$	1,3-Cyclohexadiene and dimethyl fumarate; α-pinene oxide; citronellal	Diels-Alder reaction; isomerization
$Cr_3F(H_2O)_2O(BDC)_3$, $Cr_3F(H_2O)_2O(BDC\text{-}NO_2)_3$, and $Cr_3F(H_2O)_2O(BDC\text{-}NH_2)_3$	Benzaldehyde and methanol	Acetalization
$Al_3F(H_2O)_2O(BDC\text{-}NH_2)_3$	Benzaldehyde dimethylacetal and malononitrile	Deacetalization-Knoevenagel condensation
$Zr_6O_5(OH)_3(BTC)_2(SO_4)_{2.5}(H_2O)_{2.5}$	Anisole and benzoic acid; oleic acid and methanol; methylcyclopentane; α-pinene	Friedel-Craft acylation; esterification; isomerization
$Cr_3F(H_2O)_2O(BDC)_x(BDC\text{-}OSO_3H)_{3-x}$	Acetic acid and n-butanol	Esterification
$Cr_3F(H_2O)_2O(BDC\text{-}SO_3H)_3$	Acetic acid and n-hexanol	Esterification
	2-Butanol	Dehydration
	Fructose	Carbohydrate dehydration
	Cellulose	Hydrolysis
Al(OH)(BDC-AMMal), and Al(OH)(BDC-AMSuc)	cis-2,3-epoxybutane and methanol	Alcoholysis
$Zr_6O_4(OH)_4(BPDC)_x(BPDC\text{-}Squar)_{6-x}$	Indole and β-nitrostyrene	Friedel-Craft alkylation
$Zr_6O_4(OH)_4[BDC\text{-}(COOH)_2]_6$	Methyl benzylidenecarbamate and nitromethane	Mannich reaction
$Zr_6O_4(OH)_4(BDC\text{-}NH_2)_x(BDC\text{-}NHCH_2CH_2CH_2SO_3H)_{6-x}$	Benzaldehyde and methanol; benzaldehyde and o-phenylenediamine	Acetalization; condensation

Al(III)@$Cr_3F(H_2O)_2O$(BDC-$SO_3H)_3$	Mesitylene and benzyl alcohol	Friedel-Craft alkylation
[Ln(H_2DBBP)(H_3DBBP)($H_2O)_4$]($H_2O)_x$ Ln = La, Ce, Pr, Nd, Sm, Gd	Benzaldehyde and cyanotrimethylsilane	Cyanosilylation of aldehydes
Cu(L-ASP)$(BPE)_{0.5}$(HCl)(H_2O), and Cu(D-ASP)$(BPE)_{0.5}$(HCl)(H_2O)	cis-2,3-epoxybutane and methanol	Alcoholysis
[(R)-TBBP-1]$Cu_2(H_2O)_2$, and [(R)-TBBP-2]$Cu_2(H_2O)_2$	Indole and N-sulfonyl aldimines	Friedel-Craft alkylation

[a] IM = Imidazole; TEDA = Triethylenediamine; H_2NDC = Naphthalene-2,6-dicarboxylic acid; H_2BDC-AMMal = 4-((2,5-Bis(carboxylate)phenyl)-amino)-4-oxobut-2-enoic acid; H_2BDC-AMSuc = 4-((2,5-Bis(carboxylate)phenyl)amino)-4-oxobutanoic acid; H_2BPDC = Biphenyl-4,4′-dicarboxylate; H_2BPDC-Squar = 3-((3,5-Bis(trifluoromethyl)phenyl)amino)-4-(2-(4′-carboxylphenyl)-5-carboxylphenyl)-cyclobut-3-ene-12-dione; H_4DBBP = 2,2′-Diethoxy-1,1′-binaphthalene-6-6′-bisphophonic acid; H_4(R)-TBBP-1 = (R)-3,3′,6,6′-Tetrakis(4-benzoic acid)-1,1′-binaphthyl phosphate; H_4(R)-TBBP-2 = (R)-4,4′,6,6′-Tetrakis(4-benzoic acid)-1,1′-binaphthyl phosphate.

Although, catalysis is a developing application of MOFs, a number of MOFs have been employed as solid catalysts or catalyst supports for a variety of organic transformations.[46] These include Knoevenagel condensation, aldol condensation oxidation reactions, epoxide formation, hydrogenation, Suzuki coupling, ketalization reactions, ring-opening, alkylation of amines, cyclopropanation reactions, Henry reactions, Friedel–Crafts reactions, cyanosilylation, cyclization reactions, Friedlander reaction, acetalization, hydroformylation, Biginelli reaction, Claisen–Schmidt condensation, Beckmann rearrangement, Sonogashira reaction, and polymerization.

Among various catalysis reactions, acid catalysis is mainly used for organic chemical reactions. Many possible chemical compounds can act as sources for the protons to be transferred in an acid catalysis system. Solid acids, as heterogeneous catalysts, do not dissolve in the reaction medium. Well-known examples include zeolites, alumina, and various other metal oxides and promoted metal oxides. Such acids are often used in cracking in industrial scale chemistry. A particularly large-scale application is alkylation, e.g. the combination of benzene and ethylene to give ethylbenzene. Another important application is isomerization, e.g. the isomerization of n-alkanes to their branched isomers to increase the octane number.

Compared to the relatively large body of work done on inorganic solid acids, MOF-based solid acids are emerging as a new type of material. Catalogued in Table 1.1 are the majority of the known catalytically active MOF-based solid acids.[43b] The possibility of encapsulating large Brønsted acidic molecules into MOF pores welcomed the first group of catalytically active MOF-based solid acids. Brønsted acidic Keggin-type POM, phosphotungstic acid (PTA) and its analogues, when encapsulated in MOF pores, were shown to exhibit activity comparable to the free acids.[47] More importantly, acid-base and acid-metal binary systems were reported for these PTA loaded in various MOFs including MIL-101, MIL-100, and HKUST-1.[48] In the acid-metal binary system, the highly dispersed PTA molecules in the MOF pores were reported to function as molecular anchors for the Pt precursors.[48b] Another advantage of these multifunctional systems is their ability to catalyze tandem reactions as exhibited by Ru supported on Keggin-type polyacids@MIL-100 system toward conversion of cellulose. Apart from Keggin-type polyacids, Brønsted acidic ionic liquids (BAILs) have also been encapsulated in MOF pores for catalysis. A

tandem procedure was adopted to incorporate BAILs into MIL-100 and MIL-101's mesopores.[49]

The active sites in the second major group of MOF-based solid acid catalysts are more ambiguousas they often coexist with Lewis acidic sites. Typically, this type of MOF-based solid acids will have Brønsted acidic sites located on or near their SBUs, which are difficult to characterize. MOFs in this category could be non-acidic or exhibit only Lewis acidity when they are "perfect" structures. The former case includes MOF-5 and IRMOF-8. Although no acidic sites are expected from the coordinatively saturated $Zn_4O(\text{-}COO)_6$ SBUs, catalytic activity towards Friedel-Craft alkylation reactions was observed in both MOFs.[50] It is widely accepted now that the presence of defects in these MOFs should be considered in evaluating their acidity, and Brønsted acidity is believed to be generated from uncoordinated carboxylic acid groups of the linker, especially considering the formation of hydrogen chloride as a byproduct in these reactions. In the latter case, previously considered "pure Lewis acidic" HKUST-1 was also examined for the existence of Brønsted acidic components from protonated carboxylates when used as acid catalyst.[51] MOF-based solid acids can also be generated from the interaction between a metal ion and a protic solvent ligand, often water molecules. Thus MIL-100 and MIL-101 are capable of catalyzing reactions including Diel-Alder reactions, acetalizations, and isomerization of pinene oxide and citronellal.[52]

As the third major group of MOF-base solid acids, MOFs with strong Brønsted acid groups covalently bound to the organic linkers have been shown to effectively catalyze esterification reactions and hydrolysis of cellobiose. Recently, synergistic effects between post-synthetically introduced catalytic active Lewis acidic Al(III) moieties and framework-bearing Brønsted acidic $\text{-}SO_3H$ groups was also reported in MOF-base solid acids.[53] Enantio- and stereo-selective catalysis is another focus for MOF catalysis to impart unique catalytic performances that are not possible in other materials. This also applies to MOF based solid acid catalysis.[54]

Overall, the field of MOF-based solid acid catalysis is still only focused on a limited number of MOFs, raising the demand for further development of acid stable MOFs. Regarding the term 'stability', two aspects are involved. First, stability towards acidic protons: Brønsted acid catalyzed reactions involve the transfer of protons from the catalyst acidic sites to substrates for the activation of the reactant, which, however, could lead to the slow destruction of the framework if those protons migrate to the carboxylates in the framework instead of returning to their origin. Second, stability towards reactivation: the MOFs have to be stable towards conditions to regenerate the acidic sites or to access the channels, which is typically accomplished through high temperature calcination or use of harsh chemicals. The need exists for developing MOFs in which the metal-link binding units are not carboxylates but other more acid resistant linkages.

The objectives of this dissertation are: (a) to propose and implement strategies for designing MOFs for gas storage applications, including water and methane storage, and ammonia capture; (b) to outline and test different strategies in designing MOF-based solid acids for catalytic reactions in both liquid and gas phases.

The work described in Chapter II demonstrates the designability of zirconium-based MOFs through exquisite control of the coordination mode of inorganic SBUs. It is well-known that zirconium MOFs share the same $Zr_6O_8^{8+}$ core, nevertheless, using terminal ligands to block different coordination sites on the core can potentially lead to nine highly symmetric SBUs from 3-coordinated triangle to 12-coordinated cuboctahedron, five of which are realized and reported

in this work. Details are provided for the formation of single crystals of these zirconium MOFs. Due to their water stability, zirconium MOFs are promising candidates for water-adsorption related applications. All zirconium MOFs presented in this Chapter are subject to consecutive cycles of water adsorption/desorption measurements, through which two compounds, MOF-801-P and MOF-841, are identified. It is proposed that the pore size of these materials is the key factor leading to desired water adsorption properties.

Continuing the system of zirconium-based MOFs, in Chapter III, a novel strategy is demonstrated to introduce Brønsted acidity into MOFs. With the inspiration obtained from sulfated zirconia, a controllable sulfation on MOF-808, one of the zirconium MOFs reported in the previous Chapter, is carried out through sulfate group/formate group substitution. The resulted MOF-808-xSO_4, where x = number of sulfate groups per zirconium SBU, is shown to completely retain the crystallinity and porosity of MOF-808. Through a combination of Hammett indicator test, solid-state NMR experiments and adsorption experiments of basic molecules as probes, the acidity of these sulfated MOF-808's is systematically characterized.

Having these novel MOF-based solid acid materials at hand, in Chapter IV, a series of studies is performed to test their catalytic activity towards different acid-catalyzed reactions. It is shown that as the number of sulfate groups per zirconium SBU increases in MOF-808-xSO_4, the materials exhibit increased Lewis acidic reactivity and newly generated strong Brønsted acid reactivity. The fully sulfated material, MOF-808-2.5SO_4, shows catalytically activity in Friedel-Crafts acylation, esterification, and isomerization of terpenes, as well as in the conversion of methylcyclopentane (MCP) into various hydrocarbons at 150-200 ^{o}C; the latter being a test reaction for catalytic reforming. MOF-808-2.5SO_4 is also found to be a powerful ammonia capture material that shows high uptake capacity at both low pressure (P < 1.5 Torr) and ambient pressure (P = 760 Torr).

In Chapter V, zinc-based MOFs are studied for the effect of pore size and different organic functional groups on MOFs' methane adsorption properties in MOFs. The zinc-based system is chosen to rule out the uptake activity from open metal sites. Using a novel double bond-containing tritopic linker, five new MOFs and three known MOFs are prepared and characterized. Methane uptakes are measured up to 80 bar at 298 K. The results show that the new MOFs all exhibit high methane uptake with working capacities (between 5 and 80 bar) approaching the benchmark compound HKUST-1. Pore size is shown to be the most important factor for methane storage properties of MOFs.

Chapter VI describes the construction of a bifunctional MOF-based solid acid system. The system, composed of MOF material encapsulated with phosphotungstic acid (PTA) and supported Pt nanoparticles shows catalytic activity towards gas phase n-hexane isomerization. The results indicate a close relationship between PTA added during the synthesis and the catalytic activity. Through a series of study and characterization, it is shown that the presence and quantity of strong Brønsted acidic sites (presumably on encapsulated PTA molecules) are key factors for understanding the catalytic activity of this type of solid acid.

References and Notes

(1) Furukawa, H.; Cordova, K. E.; O'Keeffe, M.; Yaghi, O. M. Science **2013**, 341, 1230444.

(2) Jiang, J.; Zhao, Y.; Yaghi, O. M. J. Am. Chem. Soc. **2016**, 138, 3255.

(3) Li, H.; Eddaoudi, M.; O'Keeffe, M.; Yaghi, O. M. Nature, **1999**, 402, 276.

(4) Yaghi, O. M.; O'Keeffe, M.; Ockwig, N. W.; Chae, H. K.; Eddaoudi, M.; Kim, J. Nature **2003**, 423, 705.

(5) Li, H.; Eddaoudi, M.; Groy, T. L.; Yaghi, O. M. J. Am. Chem. Soc. **1998**, 120, 8571.

(6) (a) Deng, H.; Doonan, C. J.; Furukawa, H.; Ferreira, R. B.; Towne, J.; Knobler, C. B.; Wang, B.; Yaghi, O. M. Science **2010**, 327, 846. (b) Li, L.; Sun, F.; Jia, J.; Borjigin, T.; Zhu, G. CrystEngComm **2013**, 15, 4094.

(7) (a) Stock, N.; Biswas, S. Chem. Rev. **2012**, 112, 933. (b) Pichon, A.; Lazuen-Garay, A.; James, S. L. CrystEngComm. **2006**, 8, 211.

(8) (a) Schaate, A.; Roy, P.; Godt, A.; Lippke, J.; Waltz, F.; Wiebcke, M.; Behrens, P. Chem. Eur. J. **2011**, 17, 6643. (b) Cavka, J. H.; Jakobsen, S.; Olsbye, U.; Guillou, N.; Lamberti, C.; Bordiga, S.; Lillerud, K. P. J. Am. Chem. Soc. **2008**, 130, 13850. (c) Ren, J.; Musyoka, N. M.; Langmi, H. W.; Segakweng, T.; North, B. C.; Mathe, M.; Kang, X. Int. J. Hydrogen Energy **2014**, 39, 12018. (d) Guo, H.; Zhu, Y.; Wang, S.; Su, S.; Zhou, L.; Zhang, H. Chem. Mater. **2012**, 24, 444.

(9) (a) Hmadeh, M.; Lu, Z.; Liu, Z.; Gándara, F.; Furukawa, H.; Wan, S.; Augustyn, V.; Chang, R.; Liao, L.; Zhou, F.; Perre, E.; Ozolins, V.; Suenaga, K.; Duan, X.; Dunn, B.; Yamamto, Y.; Terasaki, O.; Yaghi, O. M.; Chem. Mater. **2012**, 24, 3511. (b) Nguyen, N. T. T.; Furukawa, H.; Gándara, F.; Trickett, C. A.; Jeong, H. M.; Cordova, K. E.; Yaghi, O. M. J. Am. Chem. Soc. **2015**, 137, 15394.

(10) Shimizu, G. K. H.; Vaidbyanathan, R.; Taylor, J. M. Chem. Soc. Rev. **2009**, 38, 1430.

(11) Gagnon, K. J.; Perry, H. P.; Clearfield A. Chem. Rev. **2012**, 112, 1034.

(12) Phan, A.; Doonan, C. J.; Uribe-Romo, F. J.; Knobler, C. B.; O'Keeffe, M.; Yaghi, O. M. Acc. Chem. Res. **2010**, 43, 58.

(13) (a) Choi, H. J.; Dincă, M.; Long, J. R. J. Am. Chem. Soc. **2008**, 130, 7848. (b) Colombo, V.; Galli, S.; Choi, H. J.; Han, G. D.; Maspero, A.; Palmisano, G.; Masciocchi, N.; Long, J. R. Chem. Sci. **2011**, 2, 1311. (c) Tabacaru, A.; Galli, S.; Pettinari, C.; Masciocchi, N.; McDonald, T. M.; Long, J. R. Cryst. Eng. Comm. **2015**, 17, 4992.

(14) (a) Li, M.; Li, D.; O'Keeffe, M.; Yaghi, O. M. Chem. Rev. **2014**, 114, 1343. (b) O'Keeffe, M.; Yaghi, O. M. Chem. Rev. **2012**, 112, 675.

(15) (a) Barthelet, K.; Marrot, J.; Riou, D.; Férey, G. Angew. Chem. Int. Ed. **2002**, 41, 281. (b) Serre, C.; Millange, F.; Thouvenot, C.; Noguès, M.; Marsolier, G.; Louër, D.; Férey, G. J. Am. Chem. Soc. **2002**, 124, 13519. (c) Barthelet, K.; Riou, D.; Noguès, M.; Férey, G. Inorg. Chem. **2003**, 42, 1739. (d) Sanselme, M.; Grenèche, J. M.; Riou-Caveliec, M.; Férey, G. Chem. Commun. **2002**, 2172. (e) Rosi, N. L.; Kim, J.; Eddaoudi, M.; Chen, B.; O'Keeffe, M.; Yaghi, O. M. J. Am. Chem. Soc. **2005**, 127, 1504.

(16) (a) Chui, S. S. Y.; Lo, S. M. F.; Charmant, J. P. H.; Orpen, A. G.; Williams, I. D. Science **1999**, 283, 1148. (b) Kramer, M.; Schwarz, U.; Kaskel, S. J. Mater. Chem. **2006**, 16, 2245. (c) Wade, C. R.; Dincă, M. Dalton Trans. **2012**, 41, 7931. (d) Murray, L. J.; Dincă, M.; Yano, J.; Chavan, S.; Bordiga, S.; Brown, C. M.; Long, J. R. J. Am. Chem. Soc. **2010**, 132, 7856. (e) Xie, L.; Liu, S.; Gao, C.; Cao, R.; Cao, J.; Sun, C.; Su, Z. Inorg. Chem. **2007**, 46, 7782. (f) Maniam, P.; Stock, N. Inorg. Chem. **2011**, 50, 5085. (g) Kozachuk, O.; Luz, I.; Llabrés i Xamena, F. X.; Noei, H.; Kauer, M.; Albada, H. B.; Bloch, E. D.; Marler, B.; Wang, Y.; Muhler, M.; Fischer, R. A. Angew. Chem. Int. Ed. **2014**, 53, 7058 (h) Kozachuk, O.; Yusenko, K.; Noei, H.; Wang, Y.; Walleck, S.; Glaser, T.; Fischer, R. A. Chem. Commun. **2011**, 47, 8509. (i) Feldblyum, J. I.; Liu, M.; Gidley, D. W.; Matzger, A. J. J. Am. Chem. Soc. **2011**, 133, 18257.

(17) (a) Férey, G.; Mellot-Draznieks, C.; Serre, C.; Millange, F.; Dutour, J.; Surblé, S.; Margiolaki, I. Science **2005**, 309, 2040. (b) Bauer, S.; Serre, C.; Devic, T.; Horcajada, P.; Marrot, J.; Férey, G.; Stock, N. Inorg. Chem. **2008**, 47, 7568. (c) Serra-Crespo, P.; Ramos-Fernandez, E. V.; Gascon, J.; Kapteijn, F. Chem. Mater. **2011**, 23, 2565.

(18) (a) Dietzel, P. D. C.; Blom, R.; Fjellvag, H. Eur. J. Inorg. Chem. **2008**, 3624. (b) Dietzel, P. D. C.; Panella, B.; Hirscher, M.; Blom, R.; Fjellvag, H. Chem. Commun. **2006**, 959. (c) Dietzel, P. D. C.; Morita, Y.; Blom, R.; Fjellvag, H. Angew. Chem. Int. Ed. **2005**, 44, 6354. (d) Bhattacharjee, S.; Choi, J.-S.; Yang, S.-T.; Choi, S. B.; Kim, J.; Ahn, W.-S. J. Nanosci. Nanotechnol. **2010**, 10, 135. (e) Zhou, W.; Wu, H.; Yildirim, T. J. Am. Chem. Soc. **2008**, 130, 15268. (f) Sanz, R.; Martínez, F.; Orcajo, G.; Wojtas, L.; Briones, D. Dalton Trans. **2013**, 42, 2392.

(19) Sun, L.; Hendon, C. H.; Minier, M. A.; Walsh, A.; Dincă, M. J. Am. Chem. Soc. **2015**, 137, 6164.

(20) Eddaoudi, M.; Kim, J.; Rosi, N. L.; Vodak, D. T.; Wachter, J.; O'Keeffe, M.; Yaghi, O. M. Science **2002**, 295, 469.

(21) Zhang, Y.-B.; Furukawa, H.; Ko, N.; Nie, W.; Park, H. J.; Okajima, S.; Cordova, K. E.; Deng, H.; Kim, J.; Yaghi, O. M. J. Am. Chem. Soc., **2015**, 137, 2641.

(22) (a) Biswas, S.; Zhang, J.; Li, Z.; Liu, Y.-Y.; Grzywa, M.; Sun, L.; Volkmer, D.; Van Der Voort, P. Dalton Trans. **2013**, 42, 4730. (b) Foo, M. L.; Horike, S.; Fukushima, T.; Hijikata, Y.; Kubota, Y.; Takata, M.; Kitagawa, S. Dalton Trans. **2012**, 41, 13791.(c) Akiyama, G.; Matsuda, R.; Sato, H.; Takata, M.; Kitagawa, S. Adv. Mater. **2011**, 23, 3294.

(23) Xue, M.; Liu, Y.; Schaffino, R. M.; Xiang, S.; Zhao, X.; Zhu, G. S.; Chen, B. Inorg. Chem. **2009**, 48, 4649.

(24) Deng, H.; Grunder, S.; Cordova, K. E.; Valente, C.; Furukawa, H.; Hmadeh, M.; Gándara, F.; Whalley, A. C.; Liu, Z.; Asahina, S.; Kazumori, H.; O'Keeffe, M.; Terasaki, O.; Stoddart, J. F.; Yaghi, O. M. Science **2012**, 336,1018.

(25) Furukawa, H.; Go, Y. B.; Ko, N.; Park, Y. K.; Uribe-Romo, F. J.; Kim, J.; O'Keeffe, M.; Yaghi, O. M. Inorg. Chem. **2011**, 50, 9147.

(26) Chen, B.; Eddaoudi, M.; Hyde, S.; O'Keeffe M.; Yaghi, O. M. Science **2001**, 291, 1021.

(27) Ma, S.; Sun, D.; Ambrogio, M.; Fillinger, J.; Parkin, S.; Zhou, H. J. Am. Chem. Soc. **2007**, 129, 1858.

(28) Furukawa, H.; Müller, U.; Yaghi, O. M. Angew. Chem. Int. Ed., **2015**, 54, 3417.

(29) Themed issue: Metal-organic frameworks, Chem. Soc. Rev. **2009**, 38, 1201-1508.

(30) Rowsell, J. L. C.; Spenser, E. C.; Eckert, J.; Howard, J. A. K.; Yaghi, O. M. Science **2005**, 309, 1350.

(31) (a) Carrington, E. J.; Vitórica-Yrezábal, I. J.; Brammer, L. Acta Cryst. **2014**, B70, 404. (b) Furukawa, H.; Gándara, F.; Zhang, Y.-B.; Jiang, J.; Queen, W. L.; Hudson, M. R.; Yaghi, O. M. J. Am. Chem. Soc. **2014**, 136, 4369. (c) Stallmach, F.; Gröger, S.; Künzel, V.; Kärger, J.; Yaghi, O. M.; Hesse, M.; Müller, U. Angew. Chem. Int. Ed. **2006**, 45, 2123. (d) Kong, X.; Scott, E.; Ding, W.; Mason, J. A.; Long, J. R.; Reimer, J. A. J. Am. Chem. Soc. **2012**, 134, 14341. (e) Lin, L.-C.; Kim, J.; Kong, X.; Scott, E.; McDonald, T. M.; Long, J. R.; Reimer, J. A.; Smit, B. Angew. Chem. Int. Ed. **2013**, 52, 4410. (f) McDonald, T. M.; Mason, J. A.; Kong, X.; Bloch, E. D.; Gygi, D.; Dani, A.; Crocellà, V.; Giordanino, F.; Odoh, S. O.; Drisdell, W. S.; Vlaisavljevich, B.; Dzubak, A.; Poloni, R.; Schnell, S. K.; Planas, N.; Lee, K.; Pascal, T.; Wan, L. F.; Prendergast, D.; Neaton, J. B.; Smit, B.; Kortright, J. B.; Gagliardi, L.; Bordiga, S.; Reimer, J. A.; Long, J. R. Nature **2015**, 519, 303. (g) Cho, H. S.; Deng, H.; Miyasaka, K.; Dong, Z.; Cho, M.; Nelmark, A. V.; Kang, J. K.; Yaghi, O. M.; Terasaki, O. Nature **2015**, 527, 503.

(32) Millward, A. R.; Yaghi, O. M. J. Am. Chem. Soc. **2005**, 127, 17998.

(33) Noro, S.; Kitagawa, S.; Kondo, M.; Seki, K. Angew. Chem. Int. Ed. **2000**, 39, 2082.

(34) Rosi, N. L.; Eddaoudi, M.; Vodak, D. T.; Eckert, J.; O'Keeffe, M.; Yaghi, O. M. Science **2003**, 300, 1127.

(35) US Department of Energy: Targets for onboard hydrogen storage systems for light duty vehicles, http://www1.eere.energy.gov/hydrogenandfuelcells/storage/pdfs/targets onboard hydro storageexplanation.pdf, **2013**, 22.

(36) (a) Murray, L. J.; Dincă, M.; Long, J. R. Chem. Soc. Rev. **2009**, 38, 1294. (b) Suh, M. P.; Park, H. J.; Prasad, T. K.; Lim, D.-W. Chem. Rev. **2012**, 112, 782. (c) Langmi, H. W.; Ren, J.; North, B.; Mathe, M.; Bessarabov, D. Electrochimica Acta, **2014**, 128, 368

(37) DOE MOVE program at https://arpa-e-foa.energy.gov/.

(38) (a) He, Y.; Zhou, W.; Qian, G.; Chen, B. Chem. Soc. Rev. **2014**, 43, 5657. (b) Mason, J. A.; Veenstra, M.; Long, J. R. Chem. Sci. **2014**, 5, 32.

(39) (a) Yazaydın, A. O.; Snurr, R. Q.; Park, T. H.; Koh, K.; Liu, J.; LeVan, M. D.; Low, J. J. J. Am. Chem. Soc. **2009**, 131, 18198. (b) Sumida, K.; Rogow, D. L.; Mason, J. A.; McDonald, T. M.; Bloch, E. D.; Herm, Z. R.; Bae, T.-H.; Long, J. R. Chem. Rev. **2012**, 112, 724. (c) Zhang, Z.; Yao, Z.-Z.; Xiang, S.; Chen, B. Energy Environ. Sci. **2014**, 7, 2868.

(40) Burtch, N. C.; Jasuja, H.; Walton, K. S. Chem. Rev. **2014**, 114, 10575.

(41) (a) Gopal, R.; Hollebone, B. R.; Langford, C. H.; Shigeishi, R. A. Solar Energy **1982**, 28, 421. (b) Dzhigit, O.; Kiselev, A.; Mikos, K.; Muttik, G.; Rahmanav, T. A. Trans. Faraday Soc. **1971**, 67, 458.

(42) (a) Llewellyn, P. L.; Schueth, F.; Grillet, Y.; Rouquerol, F.; Rouquerol, J.; Unger, K. K. Langmuir **1995**, 11, 574. (b) Inagakia, S; Fukushima, Y.; Kuroda, K.; Kuroda, K. J. Colloid Interface Sci. **1996**, 180, 623. (c) Branton, P. J.; Hall, P. G.; Sing, K. S. W. Adsorption **1995**, 1, 77.

(43) (a) DeCoste, J. B.; Peterson, G. W. Chem. Rev. **2014**, 114, 5695. (b) Jiang, J.; Yaghi, O. M. Chem. Rev. **2015**, 115, 6966.

(44) Permissible Exposure Limits for Chemical Contaminants; Cal/OSHA: Oakland, CA; http://www.dir.ca.gov/title8/5155table_ac1.html (accessed on March 12, 2016).

(45) (a) Britt, D.; Tranchemontagne, D.; Yaghi, O. M. Proc. Natl. Acad. Sci. **2008**, 105, 11623. (b) Glover, T. G.; Peterson, G. W.; Schindler, B. J.; Britt, D.; Yaghi, O. M. Chem. Eng. Sci. **2011**, 66, 163.

(46) (a) Gascon, J.; Corma, A.; Kapteijn, F.; Llabrés i Xamena, F. X. ACS Catal. **2014**, 4, 361. (b) Liu, J.; Chen, L.; Cui, H.; Zhang, J.; Zhang, L.; Su, C.-Y. Chem. Soc. Rev. **2014**, 43, 6011. (c) Zhang, T.; Lin, W. Chem. Soc. Rev. **2014**, 43, 5982. (d) Chughtai, A. H.; Ahmad, N.; Younus, H. A.; Laypkov, A.; Verpoort, F. Chem. Soc. Rev. **2015**, 44, 6804. (e) Yoon, M.; Srirambalaji, R.; Kim, K. Chem. Rev. **2012**, 112, 1196. (f) Lee, J. Y.; Farha, O. K.; Roberts, J.; Scheidt, K. A.; Nguyen, S. T.; Hupp, J. T. Chem. Soc. Rev. **2009**, 38, 1450.

(47) (a) Wee, L. H.; Bonino, F.; Lamberti, C.; Bordiga, S.; Martens, J. A. Green Chem. **2014**, 16, 1351. (b) Khder, A. E. R. S.; Hassan, H. M. A.; El-Shall, M. S. Appl. Catal. A **2014**, 487, 110. (c) Bromberg, L.; Hatton, T. A. ACS Appl. Mater. Interfaces **2011**, 3, 4756. (d) Zhang, Y.; Degirmenci, V.; Li, C.; Hensen, E. J. M. ChemSusChem **2011**, 4, 59. (e) Janssens, N.; Wee, L. H.; Bajpe, S.; Breynaert, E.; Kirschhock, C. E. A.; Martens, J. A. Chem. Sci. **2012**, 3, 1847. (f) Liang, D.-D.; Liu, S.-X.; Ma, F.-J; Wei, F.; Chen, Y.-G. Adv. Synth. Catal. **2011**, 353, 733.

(48) (a) Bromberg, L.; Su, X.; Hatton, T. A. ACS Appl. Mater. Interfaces **2013**, 5, 5468. (b) Ramos-Fernandez, E. V.; Pieters, C.; van der Linden, B.; Juan-Alcañiz, J.; Serra-Crespo, P.; Verhoeven, M. W. G. M.; Niemantsverdriet, H.; Gascon, J.; Kapteijn, F. J. Catal. **2012**, 289, 42. (c) Chen, J.; Wang, S.; Huang, J.; Chen, L.; Ma, L.; Huang, X. ChemSusChem **2013**, 6, 1545. (d) Wang, S.; Chen, J.; Chen, L. Catal. Lett. **2014**, 144, 1728.

(49) Luo, Q.-X.; Ji, M.; Lu, M.-H.; Hao, C.; Qiu, J.-S.; Li, Y.-Q. J. Mater. Chem. A **2013**, 1, 6530.

(50) (a) Ravon, U.; Domine, M. E.; Gaudillere, C.; Desmartin-Chomel, A.; Farrusseng, D. New J. Chem. **2008**, 32, 937. (b) Nguyen, L. T. L.; Nguyen, C. V.; Dang, G. H.; Le, K. K. A.; Phan, N. T. S. J. Mol. Catal. A **2011**, 349, 28.

(51) (a) Ameloot, R.; Vermoortele, F.; Hofkens, J.; Schryver, F. C. D.; De Vos, D. E.; Roeffraers, M. B. J. Angew. Chem. Int. Ed. **2013**, 52, 401. (b) Položij, M.; Rubeš, M.; Čejka, J.; Nachtigall, P. ChemCatChem **2014**, 6, 2821.

(52) (a) Vermoortele, F.; Ameloot, R.; Alaerts, L.; Matthessen, R.; Carlier, B.; Ramos Fernandez, E. V.; Gascon, J.; Kapteijn, F.; De Vos, D. E. J. Mater. Chem. **2012**, 22, 10313. (b) Herbst, A.; Khutia, A.; Janiak, C. Inorg. Chem. **2014**, 53, 7319.

(53) Li, B.; Leng, K.; Zhang, Y.; Dynes, J. J.; Wang, J.; Hu, Y.; Ma, D.; Shi, Z.; Zhu, L.; Zhang, D.; Sun, Y.; Chrzanowski, M.; Ma, S. J. Am. Chem. Soc. **2015**, 137, 4243.

(54) (a) Evans, O. R.; Ngo, H. L.; Lin, W. J. Am. Chem. Soc. **2001**, 123, 10395. (b) Ingleson, M. J.; Barrio, J. P.; Bacsa, J.; Dickinson, C.; Park, H.; Rosseinsky, M. J. Chem. Commun. **2008**, 1287. (c) Zheng, M.; Liu, Y.; Wang, C.; Liu, S.; Lin, W. Chem. Sci. **2012**, 3, 2623.

Chapter II

Design, Synthesis and Characterization of Zirconium Metal-Organic Frameworks and Their Water-Adsorption Properties

Introduction

The design, synthesis, and characterization of metal-organic frameworks (MOFs) have received much attention in the last two decades and significant achievements have been realized in this field.[1] The introduction of reticular chemistry provides many possibilities leading to a diversity of MOFs materials with different pore metrics and properties.[2] This logical approach to assembly of predesigned building blocks by strong bonds into predetermined ordered structures has led to thousands of MOFs discovered each year.[1]

Among the library of MOFs, zirconium-based MOFs (Zr-MOFs) are of special interest because of their mechanical, thermal and chemical stability compared to MOFs composed of other metals.[3,4] This gives Zr-MOFs invaluable advantages in applications where contact of the frameworks with moisture and acids are inevitable. The adsorption of water by porous solids is important for many applications requiring capture and release of water. Temperature-triggered capture and release of atmospheric water is expected to be useful in climates where there is a large temperature difference between day and night. Here, water is adsorbed at night and released during the day, making it possible to deliver fresh water without electric power.[5] More recently, water capture by porous solids is being investigated in the design of adsorption driven heat exchangers[6] for their use as air-conditioning units in vehicles: heating and cooling are achieved upon adsorption and desorption of water into/from a porous solid, respectively.

In such water capture applications, three criteria are important in the design of a suitable porous material.[7] First, the pore filling or condensation of water into the pores of the solid must occur at low relative pressure (relative humidity) and exhibit a steep uptake behavior. The former criterion is important because water is being captured from media where it is present at low concentrations, and the latter criterion is related to the working capacity of the material. Thus the water adsorption isotherm should exhibit a steep uptake at a specific relative pressure (P/P_0, where P_0 is the saturation pressure of water). For on-board vehicle implementation of heat exchangers (so-called thermal batteries),[8] water capture is desirable at low relative pressures ($P/P_0 < 0.1$) as it reduces the need to incorporate compressors or to raise the evaporation temperature for the adsorption/desorption cycles. The second criterion is the high water uptake capacity for maximum delivery of water, and facile adsorption/desorption processes for energy efficiency. Third, high cycling performance and water stability of the material are required. Hence, porous materials with very large pore size and pore volume might exhibit large uptake capacity, but it is typically reached only at high relative pressure values (close to saturation) and after a gradual uptake.[9] Conversely, microporous zeolites can capture water at very low P/P_0 values with steep uptake behavior, however their recyclability is energetically demanding because of the strong interactions between water and the zeolite framework. Therefore, there is a need for the design and study of porous materials whose water adsorption behavior meets these three requirements. Metal-organic frameworks (MOFs) have been examined for their water capture properties and they were found to be promising materials.[10] In this work, we expect to

show that Zr-MOFs can be designed to meet these three criteria and exhibit excellent performances as water capture materials.

Despite the dramatically growing popularity and population of Zr-MOFs since the first discovery of UiO-66,[4] completely tunable design and synthesis of desired new Zr-MOF structures is still far from satisfactory. The difficulty comes from two aspects: first, the limited variety of Zr-based SBUs from which frameworks can be derived, and second, the difficulty in growing single crystals of Zr-MOFs.

Recently, topologically novel structures of Zr-MOFs are reported based on the $Zr_6O_8^{8+}$ SBUs but with a different number of connectivity of the SBU. The number of connectivity of the SBU refers to the number of the closest SBUs that are connected to the target SBU by an organic linker. The commonly found number of connectivity in Zr-MOFs are 12 in UiO-66, $Zr_6O_4(OH)_4(BDC)_6$, BDC = benzene-1,4-dicarboxylate, and its isoreticular structures. However, it is shown that by using other organic linkers, the number of connectivity in Zr-MOFs can be reduced to 10 and 8. For instance, 10-connected Zr-SBUs are found in DUT-69,[11] and 8-connected Zr-SBUs are reported in MOF-545,[12] DUT-51,[13] DUT-67[11] et al. These findings greatly increase the diversity of Zr-MOF structures, which enables us to discover Zr-MOFs with different pore metrics and thus adsorption properties.

It is also shown that the size of Zr-MOF crystallites can be controlled by using additional modulators, usually monocarboxylic acids. The commonly accepted mechanism of modulation is based on the competition of modulators with the linkers in binding to the growing crystal thus slowing down the crystal growth process and resulting in large single crystals.[14] This led to the production of the first single crystals of a Zr-MOF followed by single-crystal structural analysis in 2011.[15] The role of the modulator has also been further extended as structure directing agent, leading to the unsaturated (less than 12-connected) structures mentioned above where the remaining coordination sites are usually capped either by solvent molecules or the modulator molecules as shown by single crystal X-ray diffraction analysis.

This work reports the synthesis and crystal structures of three new zirconium MOFs, $Zr_6O_4(OH)_4(PZDC)_5(HCOO)_2(H_2O)_2$, MOF-802; $Zr_6O_4(OH)_4(BTC)_2(HCOO)_6$, MOF-808; and $Zr_6O_4(OH)_4(MTB)_2(HCOO)_4(H_2O)_4$, MOF-841. This work also summarizes the synthesis and the X-ray single-crystal structure of an additional Zr-MOF, $Zr_6O_4(OH)_4(fumarate)_6$, hereafter MOF-801, which was reported earlier as a microcrystalline powder. Utilizing these MOFs, the diversity of Zr-SBUs and modulated synthesis of single crystals of Zr-MOFs are discussed. We also tested the water adsorption properties of these materials, among which, MOF-801 and MOF-841, swiftly capture water at well-defined, low relative pressure values and exhibit high uptake, recyclability, and water stability.

Experimental Section

Chemicals used in this work. N,N-Dimethylformamide (DMF), formic acid (purity > 98 %) and anhydrous methanol were obtained from EMD Millipore Chemicals; anhydrous acetone was obtained from Acros Organics; zirconium oxychloride octahydrate ($ZrOCl_2 \cdot 8H_2O$, purity ≥ 99.5%) and Sigmacote® siliconizing reagent were obtained from Sigma-Aldrich Co. Fumaric acid, thiophene-2,5-dicarboxylic acid (H_2TDC), 1H-pyrazole-3,5-dicarboxylic acid (H_2PZDC), and 1,3,5-benzenetricarboxylic acid (H_3BTC) were obtained from Aldrich. 4,4',4'',4'''-

Methanetetrayltetrabenzoic acid (H_4MTB) was prepared according to the published procedure.[16] All starting materials and solvents, unless otherwise specified, were used without further purification.

Analytical techniques. Single-crystal X-ray diffraction (SXRD) data were collected on a Bruker D8-Venture diffractometer equipped with Mo- (λ = 0.71073 Å) and Cu-target (λ = 1.54184 Å) micro-focus X-ray tubes and a PHOTON 100 CMOS detector. Additional data was collected using synchrotron radiation in the beamline 11.3.1 of the Advanced Light Source, LBNL. Powder X-ray diffraction patterns (PXRD) were recorder using a Bruker D8 Advance diffractometer (Göbel-mirror monochromated Cu Kα radiation λ = 1.54056 Å). Solution ^{1}H NMR spectra were acquired on a Bruker AVB-400 NMR spectrometer. Elemental microanalyses (EA) were performed in the Microanalytical Laboratory of the College of Chemistry at UC Berkeley, using a Perkin Elmer 2400 Series II CHNS elemental analyzer. Attenuated total reflectance (ATR) FTIR spectra of neat samples were performed in-house on a Bruker ALPHA Platinum ATR-FTIR Spectrometer equipped with a single reflection diamond ATR module. Thermal gravimetric analysis (TGA) curves were recorded in-house on a TA Q500 thermal analysis system under air flow. Low-pressure gas (N_2 and Ar) adsorption isotherms were recorded in-house on a Quantachrome Autosorb-1 volumetric gas adsorption analyzer. Liquid nitrogen and argon baths were used for the measurements at 77 and 87 K, respectively. Water isotherms were measured in-house on a BEL Japan BELSORP-aqua3, and the water uptake in weight percent (wt%) unit is calculated as [(adsorbed amount of water)/(amount of adsorbent)×100], consistent with the established procedures. Prior to the water adsorption measurements, water (analyte) was flash frozen under liquid nitrogen and then evacuated under dynamic vacuum at least five times to remove any gases in the water reservoir. The measurement temperature was controlled with a water circulator. Helium was used for the estimation of dead space for gas and water adsorption measurements. Ultra-high-purity grade N_2, Ar, and He gases (Praxair, 99.999% purity) were used throughout the experiments.

Synthesis and Characterization of MOFs:

General procedure for sample preparation. To reduce nucleation in the growth of MOF single-crystals, the inner surface of glass containers were rinsed with Sigmacote® siliconizing reagent, washed three times with acetone, and dried in oven before use. Solvent exchange of the MOFs is performed by immersing the sample in anhydrous methanol or acetone for three days, during which time the solvent was decanted and freshly replenished three times per day. For supercritical CO_2 activation, the solvent-exchanged MOFs were fully exchanged with liquid CO_2, kept under supercritical CO_2 atmosphere, and then bled using a Tousimis Samdri PVT-3D critical point dryer.

Single crystal sample of $Zr_6O_4(OH)_4$(fumarate)$_6$, MOF-801-SC. A solvent mixture of fumaric acid (0.081 g, 0.70 mmol) and $ZrOCl_2 \cdot 8H_2O$ (0.23 g, 0.70 mmol) in a solvent mixture of DMF/formic acid (35 mL/5.3 mL) were placed in a 60-mL screw-capped glass jar, which was heated at 120 °C for one day. Octahedral colorless crystals were collected and quickly washed three times with 5 mL of fresh DMF (Yield: 0.10 g; 63% based on fumaric acid). ^{1}H digested solution NMR of as-synthesized sample (400 MHz, DMSO-d_6, ppm): 8.103 (s, 0.5H, 0.5 × HCOOH), 7.917 (s, 1H, 1 × DMF), 6.621 (s, 2H, 1 × Fumarate), 2.871 (s, 3H, 1 × DMF), 2.714 (s, 3H, 1 × DMF). EA of as-synthesized sample: Calcd. for

$[Zr_6O_4(OH)_4(C_4H_2O_4)_6](C_3H_7NO)_6(HCOOH)_3(H_2O)_{10}$: C, 25.49; H, 3.99; N, 3.96%. Found: C, 25.22; H, 3.19; N, 3.95%. ATR-FTIR (4000–400 cm^{-1}): 3151 (br), 1651 (m), 1566 (s), 1384 (s), 1200 (w), 1098 (w), 1062 (w), 984 (m), 793 (m), 739 (w), 640 (s), 483 (s).

As-synthesized MOF-801-SC was rinsed three times per day with 10 mL of DMF for three days and immersed in 10 mL of anhydrous methanol for three days, during which time the solvent was replaced three times per day.. The solid was then evacuated at 150 ºC for 24 hours to yield activated sample. EA of activated sample: Calcd. for $Zr_6C_{24}H_{28}O_{38}$ = $[Zr_6O_4(OH)_4(C_4H_2O_4)_6](H_2O)_6$: C, 19.59; H, 1.92%. Found: C, 19.40; H, 1.77%. ATR-FTIR (4000–400 cm^{-1}): 3217 (br), 1574 (m), 1397 (s), 1212 (w), 983 (w), 795 (w), 653 (s), 490 (m).

Microcrystalline powder sample of $Zr_6O_4(OH)_4$(fumarate)$_6$, MOF-801-P. MOF-801-P was prepared according to published procedures with slight modification.[14] Fumaric acid (5.8 g, 50 mmol) and $ZrOCl_2 \cdot 8H_2O$ (16 g, 50 mmol) were dissolved in a solvent mixture of DMF/formic acid (200 mL/70 mL) in a 500-mL screw-capped jar, which was heated at 130 °C for 6 h. White precipitate was filtrated using Nylon membrane filters (pore size 0.2-μm), and washed three times with 20 mL of fresh DMF and three times with 50 mL of methanol (Yield: 10 g; 90% based on fumaric acid). As-synthesized MOF-801-P was rinsed three times per day with 50 mL of DMF for three days, and immersed in 100 mL methanol for three days, during which time the methanol was replaced three times per day. The solid was then evacuated at 150 °C for 24 hours to yield activated sample. EA of activated sample: Calcd. for $Zr_6C_{24}H_{28}O_{38}$ = $[Zr_6O_4(OH)_4(C_4H_2O_4)_6](H_2O)_6$: C, 19.59; H, 1.92%; Found: C, 19.25; H, 1.05%.

$Zr_6O_4(OH)_4(PZDC)_5(HCOO)_2(H_2O)_2$, MOF-802. H_2PZDC (0.27 g, 1.5 mmol) and $ZrOCl_2 \cdot 8H_2O$ (0.40 g, 1.3 mmol) in a solvent mixture of DMF/formic acid (50 mL/35 mL) were placed in a 125-mL screw-capped glass jar, which was heated at 130 °C for three days. Block colorless crystals were collected and washed three times with 5 mL of fresh DMF (Yield: 0.12 g; 39% based on H_2PZDC). ^1H digested solution NMR of as-synthesized sample (400 MHz, DMSO-d_6, ppm): 8.108 (s, 1H, 1 × HCOOH), 7.924 (s, 0.8H, 0.8 × DMF), 7.086 (s, 1H, 1 × PZDC), 2.871 (s, 2.4H, 0.8 × DMF), 2.714 (s, 2.4H, 0.8 × DMF). EA of as-synthesized sample: Calcd. for $Zr_6C_{42}H_{66}O_{50}N_{14}$ = $[Zr_6O_4(OH)_4(C_5H_2N_2O_4)_5(HCOO)_2(H_2O)_2](C_3H_7NO)_4(HCOOH)_3(H_2O)_6$: C, 23.86; H, 3.15; N, 9.27%. Found: C, 23.52; H, 3.34; N, 9.18%. ATR-FTIR (4000–400 cm^{-1}): 3082 (br), 1653 (m), 1566 (s), 1503 (m), 1463 (m), 1432 (m), 1363 (s), 1196 (m), 1097 (m), 1059 (w), 996 (m), 865 (w), 823 (w), 780 (m), 739 (w), 649 (s), 598 (m), 537 (m), 475 (s).

As-synthesized MOF-802 was rinsed three times per day with 10 mL of DMF for three days, and immersed in 10 mL of anhydrous acetone for three days, during which time the solvent was replaced three times per day. Acetone-exchanged material was activated with the supercritical CO_2 activation protocol and evacuated at 120 ºC for 24 hours to yield activated sample. EA of activated sample: Calcd. for $Zr_6C_{27}H_{20}O_{34}N_{10}$ = $[Zr_6O_4(OH)_4(C_5H_2N_2O_4)_5(HCOO)_2(H_2O)_2]$: C, 20.58; H, 1.28; N, 8.89%. Found: C, 18.39; H, 0.72; N, 7.56%. ATR-FTIR (4000–400 cm^{-1}): 2870 (vw), 1656 (w), 1557 (m), 1462 (w), 1434 (w), 1360 (s), 1187 (w), 1095 (w), 1015 (w), 989 (w), 817 (w), 798 (w), 778 (w), 758(w), 737 (w), 645 (s), 543 (w), 470 (s).

$Zr_6O_4(OH)_4(BTC)_2(HCOO)_6$, MOF-808. H_3BTC (0.11 g, 0.50 mmol) and $ZrOCl_2 \cdot 8H_2O$ (0.16 g, 0.50 mmol) in a solvent mixture of DMF/formic acid (20 mL/20 mL) were placed in a 60-mL screw-capped glass jar, which was heated at 100 °C for seven days. Octahedral colorless crystals were collected and washed three times with 10 mL of fresh DMF (Yield: 0.098g, 70 %

based on Zr). ^{1}H digested solution NMR of as-synthesized sample (400 MHz, DMSO-d_6, ppm): 8.630 (s, 3H, 1 × BTC), 8.114 (s, 2H, 2 × HCOOH), 7.928 (s, 5H, 5 × DMF), 2.874 (s, 15H, 5 × DMF), 2.716 (s, 15H, 5 × DMF). EA of as-synthesized sample: Calcd. for $Zr_6C_{52}H_{94}O_{43}N_{10}$ = $[Zr_6O_4(OH)_4(C_9H_3O_6)_2(HCOO)_4](C_3H_7NO)_{10}(H_2O)_5$: C, 29.82; H, 4.52; N, 6.69%; Found: C, 29.74; H, 5.13; N, 6.69%. ATR-FTIR (4000–400 cm^{-1}): 3381 (br), 2930 (vw), 2861 (vw), 1651 (m), 1614 (m), 1573 (m), 1497 (w), 1437 (m), 1372 (s), 1252 (m), 1099 (m), 1061 (w), 940 (w), 864 (w), 802 (w), 783 (w), 756 (m), 717 (w), 702 (w), 646 (s), 569 (w), 501 (w), 477 (m), 445 (s).

As-synthesized MOF-808 was rinsed three times per day with DMF for three days, and immersed in 10 mL of anhydrous acetone for three days, during which time the acetone was replaced three times per day. Acetone exchanged material was then applied with supercritical CO_2 activation protocol and evacuated at 150 °C for 24 hours to yield activated sample. EA of activated sample: Calcd. for $Zr_6C_{25.5}H_{21.5}O_{33.5}N_{0.5}$ = $[Zr_6O_4(OH)_4(C_9H_3O_6)_2(HCOO)_6](C_3H_7NO)_{0.5}(H_2O)$: C, 21.59; H, 1.53, N, 0.49%. Found: C, 21.46; H, 1.46; N, 0.77%. ATR-FTIR (4000–400 cm^{-1}): 2867 (br), 1603 (m), 1583 (m), 1447 (m), 1379 (s), 1110 (w), 944 (w), 758 (w), 740 (w), 703 (m), 657 (s), 572 (w), 500 (m), 451 (s).

$Zr_6O_4(OH)_4(MTB)_2(HCOO)_4(H_2O)_4$, MOF-841. H_4MTB (0.12 g, 0.25 mmol) and $ZrOCl_2 \cdot 8H_2O$ (0.32 g, 1.0 mmol) in a solvent mixture of DMF/formic acid (40 mL/25 mL) were placed in a 125-mL screw-capped glass jar, which was heated at 130 °C for two days. Mother liquor of the reaction mixture was separated and further heated at 130 ºC for another two days. Colorless block crystals were collected and washed three times with 5 mL of fresh DMF (Yield: 0.13g, 55 % based on H_4MTB). ^{1}H digested solution NMR of as-synthesized sample (400 MHz, DMSO-d_6, ppm): 8.111 (s, 2H, 2 × HCOOH), 7.929 (s, 5H, 5 × DMF) , 7.883 (d, J = 4.4 Hz, 8H, 1 × MTB), 7.335 (d, J = 4.4 Hz, 8H, 1 × MTB), 2.875 (5s, 15H, 5 × DMF), 2.717 (s, 15H, 5 × DMF). EA of as-synthesized sample: Calcd. for $Zr_6C_{92}H_{134}O_{54}N_{10}$ = $[Zr_6O_4(OH)_4(C_{29}H_{16}O_8)_2(HCOO)_4(H_2O)_4](C_3H_7NO)_{10}(H_2O)_8$: C, 39.58; H, 4.84; N, 5.02%; Found: C, 39.11; H, 4.91; N, 5.09%. ATR-FTIR (4000–400 cm^{-1}): 3382 (br), 2930 (vw), 2860 (vw), 1652 (m), 1602 (m), 1583 (m), 1564 (m), 1541 (m), 1407 (s), 1253 (m), 1191 (m), 1151 (w), 1096 (w), 1061 (w), 1017 (w), 860 (w), 837 (w), 772 (m), 743 (w), 719 (w), 695 (w), 646 (s), 523 (m), 454 (s).

As-synthesized MOF-841 was rinsed three times per day with 10 mL of DMF for three days and immersed in 10 mL of anhydrous acetone for three days, during which time the acetone was replaced three times per day. Acetone exchanged material was then applied with supercritical CO_2 activation protocol and evacuated at 120 °C for 24 hours to yield activated sample. EA of activated sample: Calcd. for $Zr_6C_{62}H_{48}O_{36}$ = $[Zr_6O_4(OH)_4(C_{29}H_{16}O_8)_2(HCOO)_4(H_2O)_4]$: C, 38.86; H, 2.52%; Found: C, 39.15; H, 2.16%. ATR-FTIR (4000–400 cm^{-1}): 2858 (vw), 1596 (m), 1559 (m), 1407 (s), 1380 (m), 1366 (m), 1336 (m), 1194 (w), 1152 (w), 1019 (w), 839 (w), 771 (m), 751 (m), 719 (m), 664 (m), 570 (w), 525 (m), 457 (s).

$Zr_6O_4(OH)_4(TDC)_4(HCOO)_4$, DUT-67. DUT-67 was prepared according to published procedures with slight modification.[11] H_2TDC (0.069 g, 0.40 mmol) and $ZrOCl_2 \cdot 8H_2O$ (0.19 g, 0.60 mmol) in a solvent mixture of DMF/formic acid (20 mL/11 mL) were placed in a 60-mL screw-capped glass jar, which was heated at 130 °C for three days. Cubic colorless crystals were collected and washed three times with 10 mL of fresh DMF (Yield: 0.11 g, 73% based on H_2TDC). ^{1}H digested solution NMR of activated sample (400 MHz, DMSO-d_6, ppm): 8.110 (s, 1H, 1 × HCOOH), 7.927 (s, 2H, 2 × DMF), 7.697 (s, 2H, 1 × TDC), 2.873 (s, 6H, 2 × DMF),

2.716 (s, 6H, 2 × DMF). EA of as-synthesized sample: Calcd. for $Zr_6C_{52}H_{88}O_{48}N_8S_4$ = $[Zr_6O_4(OH)_4(C_6H_2O_4S)_4(HCOO)_4](C_3H_7NO)_8$ $(H_2O)_8$: C, 27.53; H, 3.91; N, 4.94; S, 5.65%. Found: C, 27.72; H, 4.01; N, 4.52; S, 5.34%. ATR-FTIR (4000–400 cm^{-1}): 3270 (br), 2928 (vw), 2859 (vw), 1650 (m), 1591 (m), 1562 (m), 1527 (m), 1436 (w), 1374 (s), 1252 (m), 1097 (m), 1061 (w), 1026 (w), 848 (w), 801 (w), 767 (s), 740 (m), 685 (m), 642 (s), 475 (s).

As-synthesized DUT-67 was rinsed three times per day with 10 mL of DMF for three days, and immersed in anhydrous acetone for three days, during which time the acetone was replaced three times per day. The acetone exchanged material was then applied with supercritical CO_2 activation protocol and evacuated at 120 °C for 24 hours to yield activated sample. EA of activated sample: Calcd. for $Zr_6C_{28}H_{26}O_{37}S_4$ = $[Zr_6O_4(OH)_4$ $(C_6H_2O_4S)_4(HCOO)_4](H_2O)_5$: C, 20.63; H, 1.61, S, 7.87%. Found: C, 20.51; H, 1.27; S, 7.12%. ATR-FTIR (4000–400 cm^{-1}): 3233 (br), 1558 (m), 1527 (m), 1373 (s), 1323 (s), 1212 (w), 1125 (w), 1028 (w), 839 (w), 765 (s), 685 (m), 646 (s), 511 (m), 456 (s).

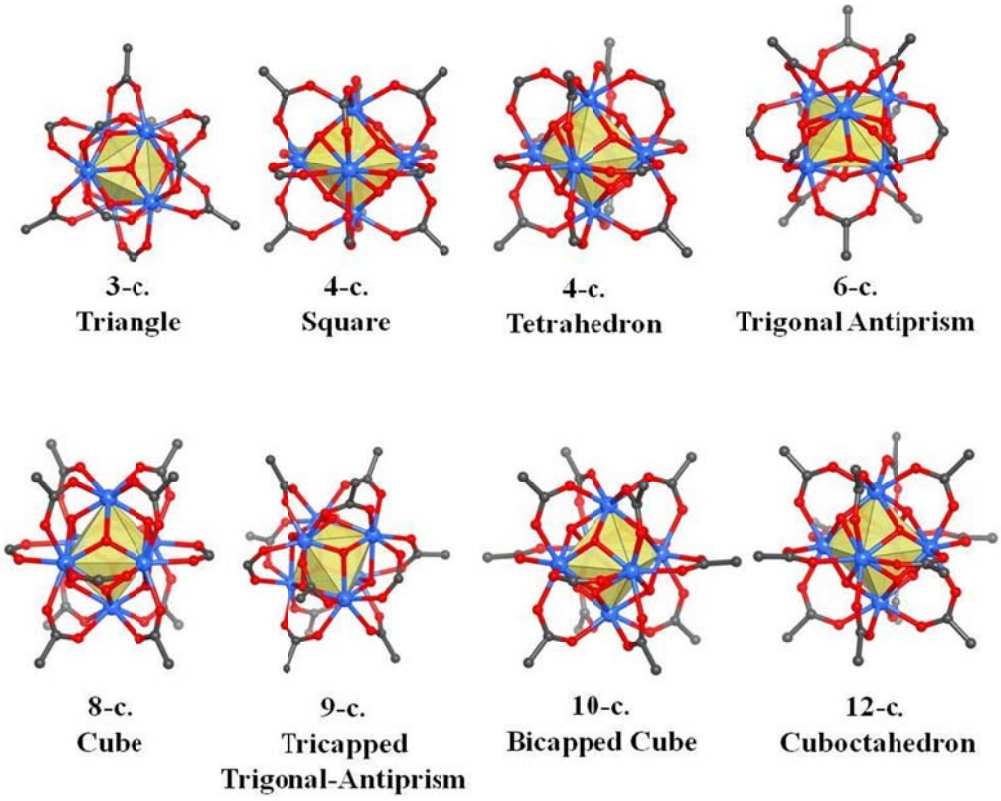

Figure 2.1. Possible coordinating polyhedra based on the Zr-SBU of different number of connection.

Results and Discussion

Tracking down the diversity of Zr-SBUs. In essence, MOF chemistry has taken coordination chemistry beyond molecules to build up crystals of extended structures linked by strong bonds, and to carry out reactions on such crystals as if they are discrete molecules. The

ability to stitch various molecular building units together by strong bonds (e.g. metal-carboxylate bonds) has generated a large number of extended structures. Very often, this number is further propagated by the fact that multiple type of molecular building units can be formed using the same metal under different conditions. For example, zinc-based MOFs is reported to have trigonal prism, octahedron, distorted rectangular prism, and infinite SBUs when bound to carboxylates.[17] However, unlike other transitional metals, zirconium's behavior when encountering carboxylates is much more monotonous. Ever since the discovery of UiO-66, the octahedral zirconium oxide cluster $Zr_6O_8^{8+}$ core that every 12-connected Zr SBU grows from, has reappeared in all the Zr-MOFs reported, except for two.[18,19]

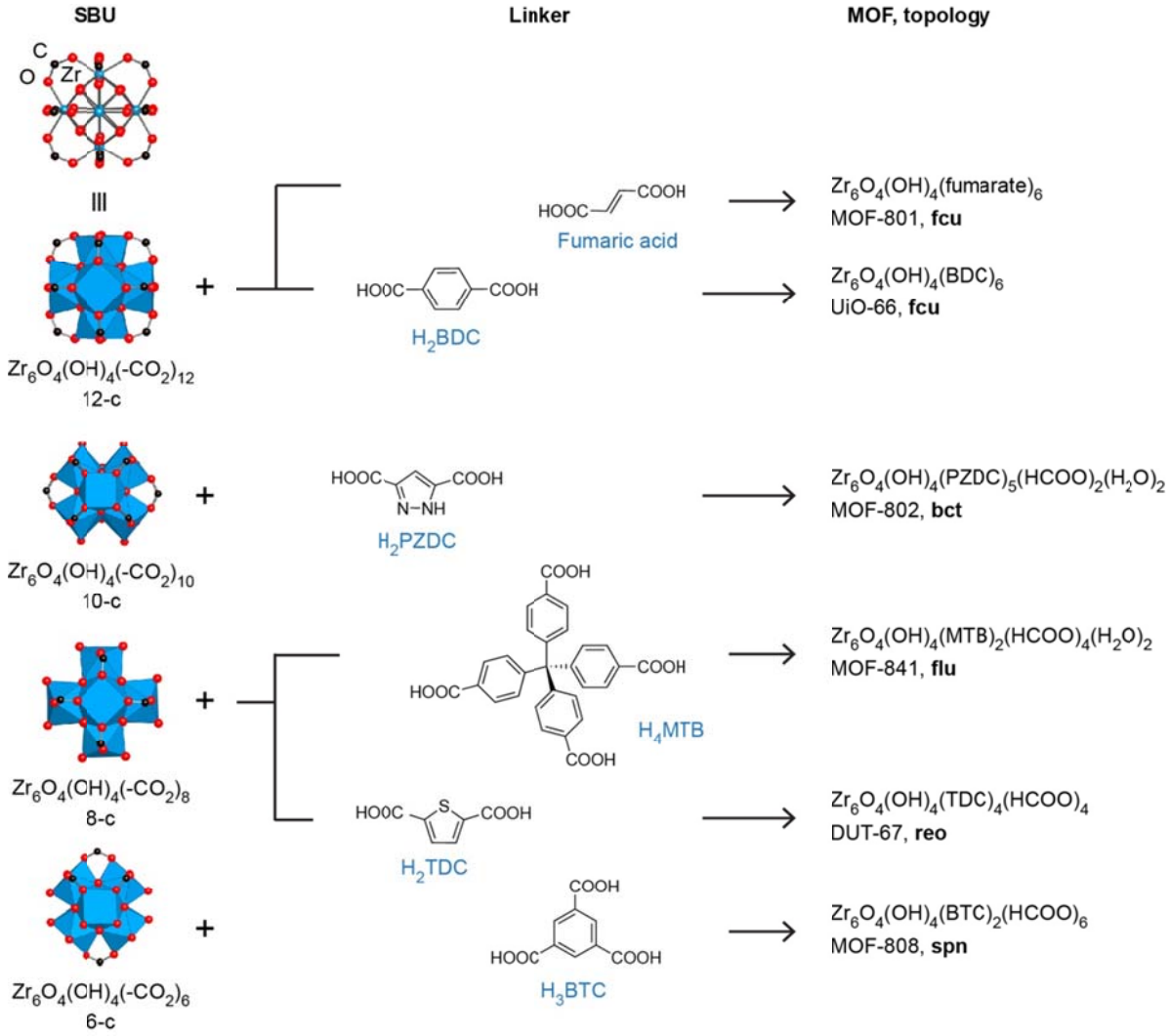

Figure 2.2. $Zr_6O_4(OH)_4(-CO_2)_n$ secondary building units (SBUs) with different coordination numbers listed under each of the SBUs as n-c (left column) are connected with organic linkers (middle) to form MOFs (right column) of various topologies (three letter codes in right column).

However, as shown in Figure 2.1, based on a theoretical analysis, it is quite interesting and possible that a family of Zr-SBUs with different number of connections and thus different coordination polyhedra can be formed on the basis of this very simple $Zr_6O_8^{8+}$ core. These different coordination polyhedra range from the most common 12-connected cuboctahedron to a 3-connected triangle, all with high symmetry, thus may be incorporated into MOFs structures. The fact that Zr-MOFs are usually prepared solvothermally from a reaction mixture where there are N and/or O-containing organic solvents, water, and monocarboxylic acids makes it even more realistic to synthesize the above SBUs, as these solvent and modulator molecules can serve as terminal ligands for those vacant coordinated sites on the $Zr_6O_8^{8+}$ core when the number of coordination is less than 12.

To reduce the connectivity of the $Zr_6O_8^{8+}$ core, the simplest way is through increasing the steric hindrance of the organic linker so that there is less room to accommodate 12 linkers around a single Zr-SBU. This strategy can be achieved in two ways: 1) introducing bulky groups, for instance Br, i-Pr, t-Bu et al., onto the organic linker; 2) using a bent linker in which the angle between two carboxylate groups is less than 180 degrees. The former route has failed as use of 2-bromoterephthalic acid led to an UiO-66 analogue while all efforts in obtaining a MOF out of 2,6-dibromoterephthalic acid resulted in no crystallization. Synthetically, the latter strategy was carried out using a series of bent linkers as shown in Figure 2.2, with angles between the adjacent carboxylates decreasing from 180° in fumaric acid to 109° in H_4MTB.

Modulated synthesis of single crystals of Zr-MOFs. Study of various factors and their effects on single crystal growth of Zr-MOFs is discussed using MOF-801 as an example.

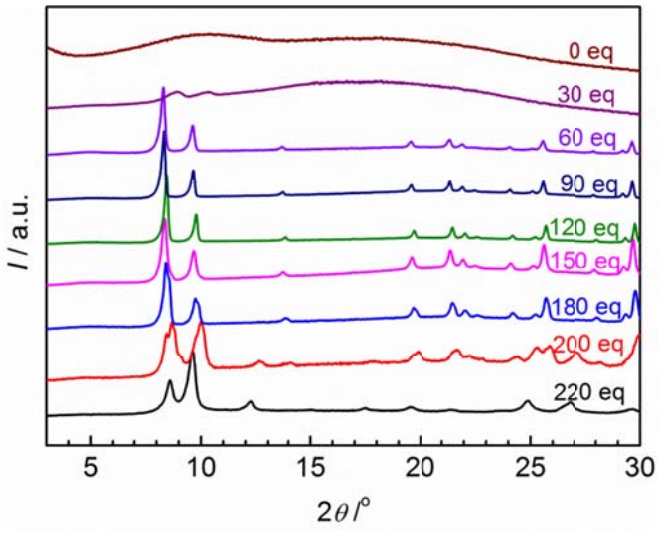

Fig. 2.3. Comparison of PXRD patterns of the products synthesized from the mixture of fumaric acid and zirconium oxychloride in the presence of different equivalents (with respect to Zr) of formic acid as modulator.

First of all, the effect of the modulating agent formic acid was investigated. The amount of modulator added to a synthesis batch consisting of fumaric acid (0.4 mmol), $ZrOCl_2 \cdot 8H_2O$ (0.4 mmol) and DMF (10 ml) is stated in relation to the amount of Zr as equivalents (eq). In Figure

2.3, the PXRD patterns of the products of these syntheses are shown. Without addition of formic acid, a gel-like amorphous phase is obtained in 3 hours. With the addition of 30 eq of the modulator, two very broad reflections can be discerned from the back ground. The product prepared in presence of 60 to 150 eq of formic acid shows the full set of reflections of a crystalline phase. However, when more than 180 eq of formic acid was added to the reaction mixture, a suspicious phase came out with a distinguishable shoulder peak appearing right next to the lowest angle (2θ) peak of MOF-801. The impure phase was later determined to be an extended structure of zirconium formate, in which the same $Zr_6O_8^{8+}$ core is connected with bridging formate anions.

The samples were further examined by SEM in order to obtain information of particle size and morphology. Figure 2.4 shows two characteristic images from both of the corresponding solids that gave sharp reflections under powder X-ray diffraction analysis. Both images reveal the nature of MOF-801 and its propensity for the formation of octahedral crystals while the microcrystals obtained at smaller formic acid amount (60 eq) show strongly inter-grown habits (~1 μm size) while increasing the modulator concentration not only leads to larger crystal size (~5μm) but also resolves the aggregation phenomenon.

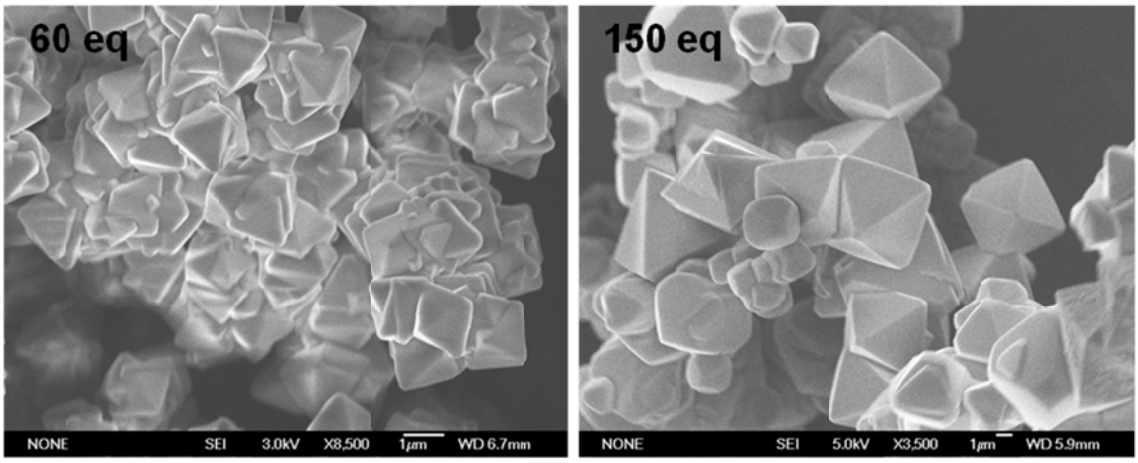

Fig. 2.4. SEM images of the products of MOF-801 in the presence of different amount of formic acid (as given in the images).

The observed trend of formic acid as modulator matches well with precedent in aprevious publication.[14] However, the amount of formic acid needed to get sharp edged crystals is much greater than previously reported. This is due to the difference in zirconium salts used as the metal source. Compared to $ZrCl_4$, $ZrOCl_2 \cdot 8H_2O$ has bridging OH groups connecting the two Zr centers in its structure, resulting in a greater tendency to form gel-like zirconium hydroxides. Thus more formic acid is required to slow down and prevent the formation of the amorphous hydroxide precipitation.

Unlike crystallization of small molecules, the formation of Zr-MOF crystals is a combination of controllable hydrolysis which determines the formation rate of $Zr_6O_8^{8+}$ core and slow ligand exchange process through which the $Zr_6O_8^{8+}$ core can extend into a framework. Based on this notion, it is quite straightforward to understand the role that modulators play in

MOF crystal growth. In the case of controllable hydrolysis, the acidity of the modulator stops the formation of zirconium hydroxides; the stronger the acid, the more time it takes to form precipitates. This has been proven by a simple control experiment where 120 equivalents of hydrochloric acid, sulfuric acid, formic acid, acetic acid and benzoic acid each with respect to Zr were added to the reaction mixture. A turbid solution was observed after 2 hours for syntheses using acetic acid and benzoic acid, and after 12 hours for batches with formic acid and hydrochloric acid. The solution remained clear even after 2 weeks heating at 130°C for experiments containing sulfuric acid as the modulator. The volatility of hydrochloric acid may be a factor in the explanation of why synthesis of Zr-MOF with HCl as a modulator was unsuccessful. Because DMF decomposes during the heating process and formic acid evaporates, the pH of the reaction mixture gradually goes up, allowing $Zr_6O_8^{8+}$ cores to be slowly formed in the solution.

At this stage, formic acid still dominates the coordination sites of the $Zr_6O_8^{8+}$ cores since it is usually a stronger acid than normal carboxylic acid linkers used and it is present in a large excess. Then the ligand exchange processes take place when the capping formates are reversibly substituted by carboxylates from the linker and a single $Zr_6O_8^{8+}$ core will gradually extend into a crystal of Zr MOF under continuous self-correction to rule out defects and disorders. If more formic acid is present in the system than is necessary, bridging formates will dominate the extension instead of linker anions. This causes the formation of an undesired Zr formate phase. This explains why the appearance of impurities instead of further growth of MOF-801 microcrystal is observed when more than 180 eq of formic acid is added to the reaction system.

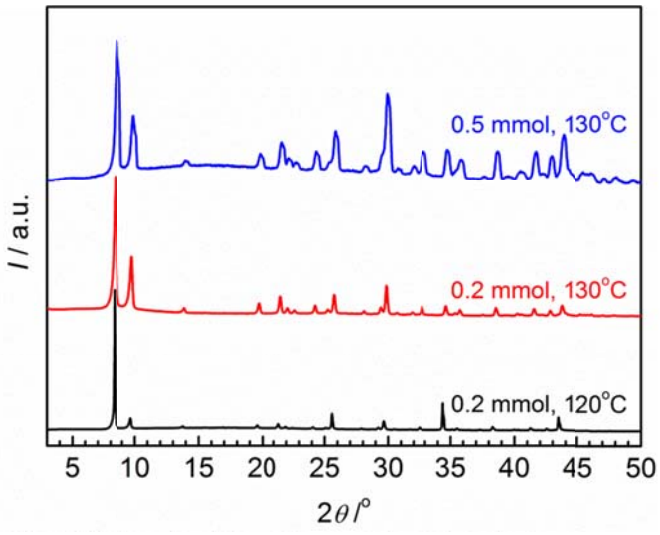

Fig. 2.5. PXRD patterns of the products of syntheses of MOF-801 performed in the presence of different concentration of fumaric acid and zirconyl chloride at different temperature.

To grow the MOF-801 into larger crystals, measures other than increasing the amount of modulators must be taken. As mentioned above, the growth of MOF crystals is different with small molecules. The two factors that crystallography experts commonly alter are temperature and concentration, and these factors still apply to the MOF system. Fig. 2.5 demonstrates how moderately cooling down the synthesis temperature and reducing the reagent concentration can

help to obtain microcrystals exhibiting the much sharper PXRD patterns which is indicative of better crystallinity. Again, this can be explained as lower temperature slows down the decomposition of DMF and evaporation of formic acid, together with diluting the reaction mixture, makes the hydrolysis and the framework growth more reversible, in turn allowing larger crystal to grow. One thing which should be noted is that dilution of the reaction mixture allows for the presence of more DMF and thus a more basic system. Therefore, the amount of added formic acid should be slightly increased.

For the first time, single crystals of MOF-801 were successfully obtained by finely tuning the above conditions. Optical images of MOF-801 crystals were shown in Figure 2.3. Similarly, single crystals of MOF-802, MOF-808, and MOF-841 were obtained. This enables the study of their crystal structures by single crystal X-ray diffraction experiments.

Crystal structures of the Zr-MOFs:

MOF-801: MOF-801 was prepared with the ditopic fumarate linker (Figure 2.2). This material was originally reported by Wißmann et al.,[14] who elucidated its crystal structure based on analysis of the PXRD pattern. The microcrystalline powder form of MOF-801 was obtained under optimized synthetic conditions. Under different synthetic conditions, we have been able to grow crystals suitable for SXRD studies. As explained below, the two forms of MOF-801 [large single crystals, MOF-801-SC and microcrystalline powder, MOF-801-P] consistently show different sorption properties, and are described here as separate materials. The analysis of the single crystal diffraction data reveals that MOF-801 crystallizes in the cubic $Pn\bar{3}$ space group, with unit cell parameters a = 17.504(3) Å. In MOF-801 each inorganic SBU is connected to twelve organic linkers. The resulting three-dimensional framework has a **fcu** topology. In this structure, there are two crystallographically independent tetrahedral cavities, with slightly different diameters of 5.6 Å and 4.8 Å. The diameter of the octahedral cavity is 7.4 Å (Figure 2.7).

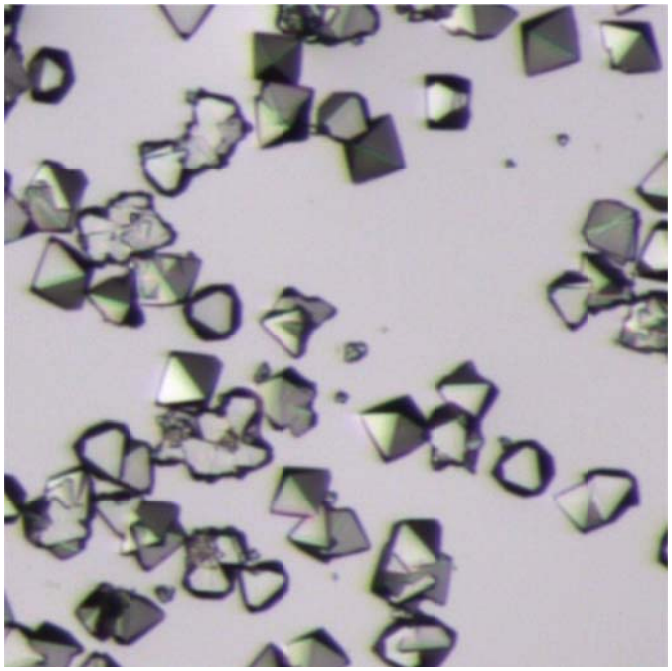

Fig. 2.6. Optical image of single crystals of MOF-801.

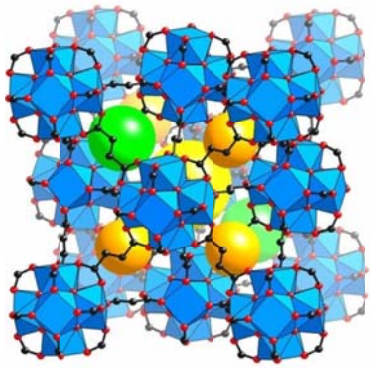

Figure 2.7. MOF-801 is the smallest Zr-MOF with fcu topology. Atom color scheme: C, black; O, red; Zr, blue polyhedra. Yellow, orange and green balls indicate the space in the framework.

MOF-802: MOF-802 is prepared with the bent ditopic PZDC linker (Figure 2.2). The analysis of the single crystal diffraction data reveals that MOF-802 crystallizes in the Fdd2 space group, with unit cell parameters a = 39.222(3) Å, b = 26.018(2) Å and c = 27.887(2) Å. In MOF-802 each inorganic SBU is connected to ten organic linkers, with formate and DMF ligands occupying the remaining two coordination sites. The resulting three-dimensional framework has a **bct** topology (Figure 2.8a). In this topology there is only one kind of cavity, which in the case of MOF-802 has a maximum diameter of 5.6 Å (Figure 2.8b and c).

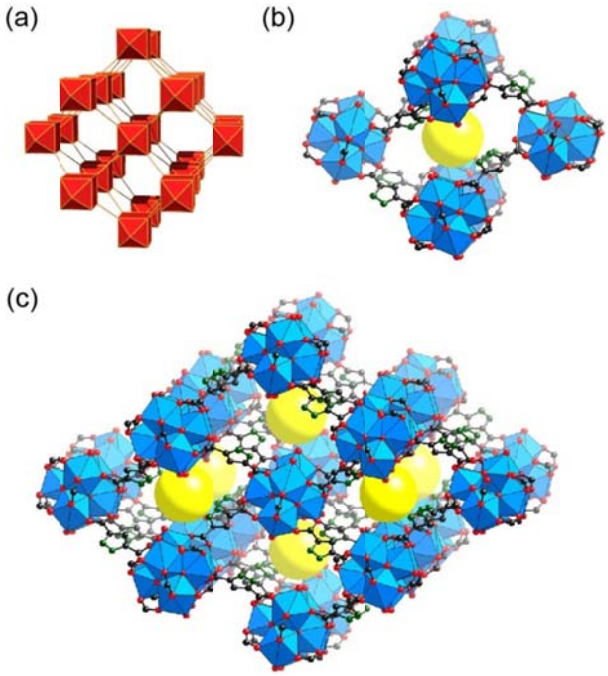

Figure 2.8. Representation of the **bct** topology (a). One cavity in MOF-802 is shown in (b), and the packing of several unit cells is shown in (c). Atom color scheme: C, black; N, green; O, red;

Zr, blue polyhedra. H atoms are omitted for clarity. Yellow balls indicate the space in the framework.

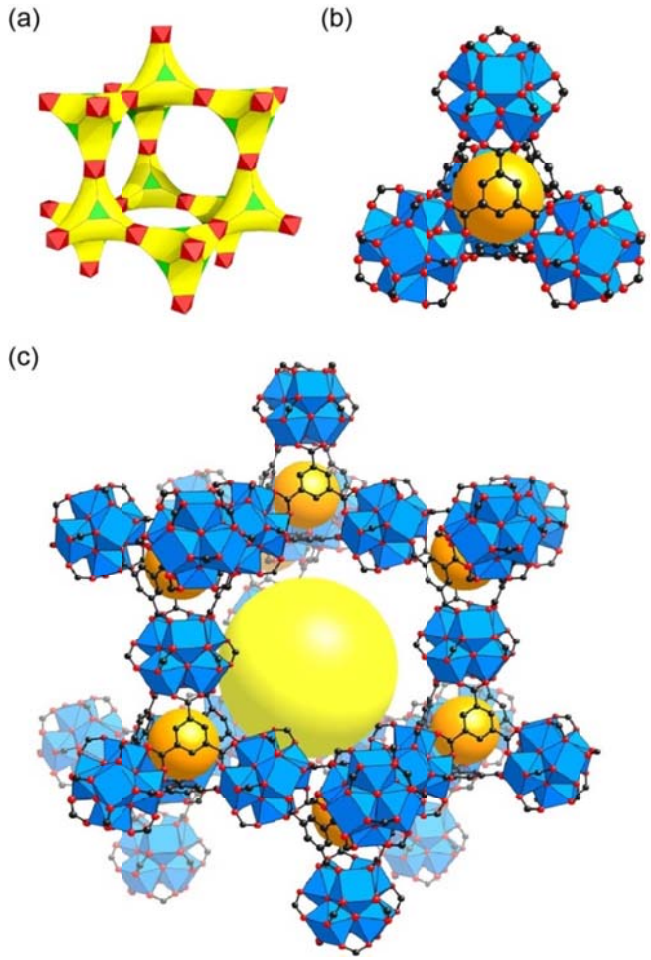

Figure 2.9. Representation of the **spn** topology (a) exhibited by MOF-808, which is built with octahedral (red) and triangular (green) units, resulting in the formation of tetrahedral cage (b) and large adamantane pores (c). Atom color scheme: C, black; O, red; Zr, blue polyhedra. H atoms are omitted for clarity. Yellow and orange balls indicate the space in the framework.

MOF-808: Octahedral crystals of MOF-808 are prepared with the tritopic BTC as a linker (Scheme 1). Single crystal diffraction data analysis shows that MOF-808 crystallizes in the cubic space group $Fd\bar{3}m$ with lattice parameter a = 35.076(1) Å. The crystal structure solution reveals that the inorganic SBUs are connected to six BTC linkers and each of the linkers is coordinated to three SBUs. In addition, the coordination of the SBU is completed with six formate ligands, which account for the charge balance. These formate anions are found coordinated to the Zr atoms and disordered as both mono- and bidentate ligands. MOF-808 has a 6,3-connencted three-dimensional framework with an overall **spn** topology (Figure 2.9a). Tetrahedral cages with internal pore diameter of 4.8 Å are formed, with the inorganic SBUs at the vertices and the BTC linkers at the faces of the tetrahedron (Figure 2.9b). The tetrahedral cages are sharing vertices in such a way that the overall connectivity of MOF-808 can be simplified to an augmented diamond net. A large adamantane cage is formed with an internal pore diameter of 18.4 Å (Figure 2.9c).

MOF-841: Crystals of MOF-841 were prepared with MTB as a linker (Figure 2.2). Structural analysis carried out with single crystal X-ray diffraction data reveals that MOF-841 belongs to the tetragonal space group I4/m, with lattice parameter a = 14.6766(6) Å and c = 28.033(1) Å. Each SBU in MOF-841 is connected to eight linkers. Water and formate ligands complete the coordination of the SBU. The combination of 8-connected SBUs with tetrahedral linkers results in a three-dimensional framework with **flu** topology (Figure 2.10a). This is the default, high symmetry, edge transitive network, obtained with the combination of cubic and tetrahedral building units. Only one type of cages is formed in this structural type. For MOF-841 the diameter of the cage (without terminating formic acid) is 11.6 Å (Figure 2.10b).

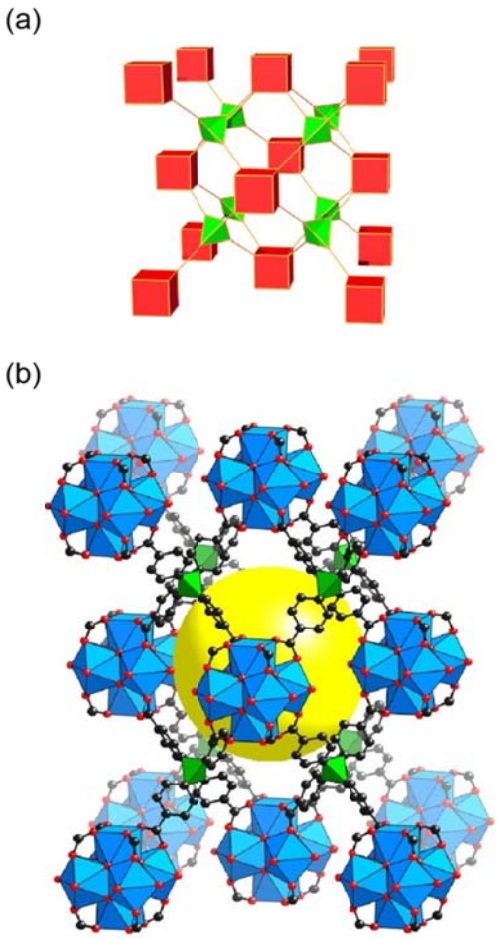

Figure 2.10. The combination of tetrahedral units with icosahedral or cubic units produces the **flu** network (a) when tetrahedral units are combined with cubic ones, as in the case of MOF-841 (b). Atom color scheme: C, black; O, red; Zr, blue polyhedra. Green polyhedra represent central tetrahedral carbon. H atoms are omitted for clarity. Yellow balls indicate the space in the framework.

Structural aspects of other zirconium MOFs examined in this study. The well-known UiO-66 is formed with BDC as the linker, and the tetrahedral and octahedral cavities are 7.4 Å

and 8.4 Å of diameter, respectively.[4] DUT-67 is prepared with the bent ditopic TDC linker (Figure 2.2) and has a **reo** topology, with two types of cavities with 8.8 Å and 16.6 Å in diameter.

Permanent porosity of new and reported zirconium-MOFs. Prior to the water sorption measurements, we recorded N_2 and/or Ar adsorption isotherms for the Zr-MOFs to confirm their permanent porosity and to calculate their surface area. The N_2 and/or Ar isotherms can be found in the Appendices (Figures A2.11-A2.17). For easy reading, the BET and Langmuir surface areas, pore volume, crystal density, pore diameter, and water uptake capacity for each Zr-MOF sample are summarized in Table 2.1.

Water adsorption properties of zirconium MOFs

Condensation pressure and uptake capacity. The water isotherms are shown in Figure A2.18-A2.24. For comparison, we first studied the water uptake properties of the prototypical Zr-MOF, UiO-66 (Figure A2.23), and compared it to data reported by other researchers. The water isotherm of UiO-66 has a sigmoidal shape with a moderate hysteresis loop at P/P_0 = 0.3-0.4. Maximum water uptake at 25 °C reaches 535 $cm^3\ g^{-1}$ (43 wt%) at P/P_0 = 0.9 (Table 2.1). These results, recorded on a volumetric instrument (uptake vs. P/P_0), show the same trend as those previously reported and measured on a gravimetric system (uptake vs. relative humidity, RH%).[21]

Table 2.1. Summary of the sorption, physical and pore-structure properties of the studied zirconium MOFs.

Material	Surface area, $m^2\ g^{-1}$		V_p, $cm^3\ g^{-1}$	$d_{crystal}$, g cm^{-3} [a]	Pore diameter, Å [b]	Water uptake, $cm^3\ g^{-1}$		
	BET	Langmuir				P/P_0 = 0.1	P/P_0 = 0.3	P/P_0 = 0.9
MOF-801-P	990	1070	0.45	N/A	7.4, 5.6, 4.8	280	380	450
MOF-801-SC	690	770	0.27	1.68	7.4, 5.6, 4.8	170	270	350
MOF-802	< 20	< 20	< 0.01	1.47	5.6	35	70	110
UiO-66	1290	1390	0.49	1.23	8.4, 7.4	20	125	535
MOF-808	2060	2390	0.84	0.86	18.4	55	160	735
MOF-841	1390	1540	0.53	1.05	9.2	10	550	640
DUT-67	1560	1720	0.60	1.04	16.6, 8.8	100	390	625

[a]From single crystal X-ray diffraction data; [b]Calculated with Platon.[20]

The water isotherm of MOF-801-SC measured at 25 °C is shown in Figure A2.19 (blue squares). The adsorbed amount of water gradually increases with increasing pressure up to P/P_0 = 0.05, followed by abrupt water uptake in the pressure range from P/P_0 = 0.05 to 0.1, and the maximum uptake is 350 cm^3 g^{-1} (28 wt%) at P/P_0 = 0.9. The step pressure is much lower than that of UiO-66, indicating a higher water affinity for this material. A similar trend is observed in MOF-801-P (A2.18), while the maximum water uptake is now 1.3 times greater than MOF-801-SC [450 cm^3 g^{-1} (36 wt%) at P/P_0 = 0.9]. This difference in maximum uptake between the two forms of MOF-801 was also observed in the N_2 sorption measurements, and we attribute this to the possibility of a large amount of missing linker defects in MOF-801-P.[25] MOF-802 shows a Type I isotherm (Figure A2.20, green squares). Although this compound does not show significant N_2 and Ar uptake, the total water uptake is 100 cm^3 g^{-1} (8.0 wt%) at P/P_0 = 0.9, indicating that the pore is large enough to allow inclusion water molecules due to its smaller kinetic diameter (2.6 Å).

The water isotherms for MOF-808, MOF-841, and DUT-67 display significant steps with a hysteresis loop (Figure A2.21, A2.22, and A2.24). The limited water uptake at lower pressure from these steps indicates low affinity of water to the MOF surface. This is related to the hydrophobicity of the organic linker; therefore, higher pressure of water vapor is required to induce the pore filling. The maximum uptake of DUT-67 and MOF-808 is 625 cm^3 g^{-1} (50 wt%) and 735 cm^3 g^{-1} (59 wt%), respectively. DUT-67 shows several steps in its isotherm, which can be correlated to the filling of the variously sized cavities that are present in this structure. MOF-841 shows an isotherm with a steep adsorption commencing at P/P_0 = 0.2 and reaching 550 cm^3 g^{-1} at P/P_0 = 0.3 (640 cm^3 g^{-1} at P/P_0 = 0.9).

Thus, to fill the micropores with water in the desirable pressure range (especially below P/P_0 = 0.1) and realize the steep water uptake (i.e. the first criterion mentioned above), the pore size of the MOF structure plays a primary role.

Ease of regeneration and cycle performance in water uptake. The third criterion for the applicability of MOFs as water adsorbents is the ease of regeneration and material stability to maximize water delivery. To evaluate these factors, the samples were evacuated at 25 °C for 2 hours after the isotherm measurements. Typical pressure in the sample cell after the regeneration process was 5 Pa. We then collected the water isotherms for five cycles in the Zr-MOFs. The isotherms are shown in the Appendices (Figure A2.18-A2.24). The cycle performance results show that for MOF-808, the uptake constantly drops in every cycle (Figure A2.21). The surface area of these MOFs was remeasured after the water cycle tests, showing a significant decrease. This observation suggests that the loss of water uptake capacity is related to the loss of porosity.

For DUT-67, we find a significant decrease from the first to the second cycle and a nearly constant uptake thereafter (Figure A2.24). This behavior can be explained if some of the water molecules are strongly bound to the framework, not being desorbed under the aforementioned regeneration conditions. If this is the case, the water release requires further energy input (higher temperature and/or better vacuum). In practical terms, the working capacity of these materials is strongly limited due to the high energetic regeneration cost.

Finally, we find that MOF-801-P, MOF-802, MOF-841, and UiO-66 exhibit the best and closest to the ideal cycling performance. These materials show robust cycling performance as indicated by the similarity of water uptake in all five cycles (Figure A2.18, A2.20, A2.22, and A2.23). Since these materials are stable under humid conditions, and have no strong binding sites

(e.g. open metal sites) for water to bind, it is expected that their working capacity (deliverable amount of water) will not be strongly influenced by the regeneration conditions.

Best performing porous materials for water adsorption. As mentioned above, different applications require different operation pressures. Whereas, for on-board heat exchange systems, it is preferable to have materials capable of taking up large amounts of water in low pressure regions ($P/P_0 \leq 0.1$), temperature-triggered water capture and release systems are expected to operate at P/P_0 values close to 0.3.

At $P/P_0 = 0.1$, the water uptake of MOF-801-P is higher than 20 wt%, which outperforms any of the other MOFs. The water uptake capacity increases for all materials at $P/P_0 = 0.3$. However, the order is slightly different from the one observed at relative pressure of 0.1: Here, MOF-841 outperforms the other materials. The isotherm profile of this material (Figure A2.22), which shows a significant step in the pressure range from $P/P_0 = 0.2$ to 0.3, indicates that water rapidly condenses in the pore of this MOF in this pressure range. In addition, the uptake is nearly constant throughout the five cycles. After the fifth cycle, the uptake is still greater than 40 wt%. To the best of our knowledge, this is the highest value of water uptake at $P/P_0 = 0.3$ for any porous solid.

Temperature dependence of water uptake. Since water adsorption is an exothermic process, a large amount of heat can be utilized if the adsorption enthalpy is large. With that in mind, released heat can increase the temperature in adsorbent beds so that the uptake capacity can be drastically influenced by this temperature change. Therefore, we measured the water sorption isotherms for the best performers, MOF-801-P and MOF-841, at various temperatures between 15 to 55 °C (Figure A2.25, A2.27). These isotherms show that the maximum uptake capacity is not significantly influenced by temperature, indicating that water molecules are easily condensed within the MOF pores.[22] We estimated the isosteric heat of adsorption (Q_{st}) of water from the isotherms measured at various temperatures (Figures A2.26, A2.28). The Q_{st} value in the low water coverage range for MOF-841 is around 50 kJ mol^{-1}, which remains nearly constant throughout the entire adsorption process, and represent 25% greater energy than the latent energy of water (40.7 kJ mol^{-1}). The Q_{st} value for MOF-801-P is even greater than MOF-841, approximately 60 kJ mol^{-1}.

Applications to thermal battery and water delivery in remote desert regions. With these values, we can estimate how much heat can be stored in 15 kg of MOF-801-P. Assuming that the storage capacity and Q_{st} of MOF-801-P are 20 wt% (at $P/P_0 = 0.1$) and 60 kJ mol^{-1}, respectively, the total heat expected to be released is 10 MJ. If such a system is operated for 1 hour with 65% efficiency, the power capability is equivalent to 1.8 kW — a value approaching the 2.5 kW power target for typical thermal batteries as set by the DOE.[23]

The temperature effect on water uptake is also important to realize another application of water adsorption in MOFs: temperature-triggered water capture and release systems, where atmospheric water would be captured and delivered at different temperatures in areas with high temperature contrasts between day and night. For example, in the city of Tabuk in Saudi Arabia, the typical summer temperature and relative humidity during day time are respectively 40 °C and 5%, drastically changing at night to 25 °C and 35%. Assuming $P/P_0 \times 100 = RH\%$, the working capacity of MOF-841 between $P/P_0 = 0.05$-0.35 is more than 40 wt%, which is the largest obtained among all Zr-MOFs. If 15 kg of MOF-841 is deployed in Tabuk under these optimal conditions, it should be able to deliver 6.3 L of pure water per day.

Conclusion

This chapter describes the design and synthesis of three new zirconium MOFs, MOF-802, MOF-808, and MOF-841. These MOFs were prepared based on the assumption towards different connection polyhedra of Zr-SBUs. By using organic linkers that have different angles between the carboxylate groups, the number of connection of the Zr-SBU is successfully reduced from 12 to 10, 8, and 6, greatly increasing the diversity of Zr-MOFs. Besides, using MOF-801 as an example, we have also studied how different synthetic conditions affect the crystallinity and crystal growth of Zr-MOFs. Special attention is paid to the function of formic acid as modulator to obtain single crystals of Zr-MOFs. Finally, we have evaluated the water sorption properties of MOF-801, MOF-802, MOF-808, and MOF-841, along with other reported zirconium MOFs, UiO-66, and DUT-67, with the aim of finding new water capture materials with optimal response in the most important criteria to be considered for this important application: position at which the adsorption occurs and steepness of the process, uptake, and reuse and stability. Two materials, MOF-801-P and MOF-841 show excellent performance when considering all these three criteria: MOF-801-P takes up 22.5 wt% of water at $P/P_0 = 0.1$, and MOF-841 takes up 44% at $P/P_0 = 0.3$. These uptakes are steep and nearly constant after five consecutive cycles where the materials are easily regenerated with a low energetic cost. Due to these characteristics, MOF-801 is a good candidate to be used in advanced thermal batteries while MOF-841 has potential to be used in capture and release of atmospheric water in remote desert areas.

Appendices

Table A2.1. Crystal data and structure refinement for MOF-801-SC (CCDC #: 1002676).

Identification code	MOF-801-SC
Empirical formula	$C_{24}H_{12}O_{32}Zr_6$
Formula weight	1359.66
Temperature/K	363.15
Crystal system	cubic
Space group	Pn-3
a/Å	17.504(3)
b/Å	17.504(3)
c/Å	17.504(3)
α/°	90
β/°	90
γ/°	90
Volume/Å^3	5363.1(6)
Z	4
ρ_{calc}/mg mm^{-3}	1.592
m/mm^{-1}	1.450
F(000)	2608.0
Crystal size/mm^3	0.02 × 0.02 × 0.015
Radiation	Synchrotron (λ = 0.7749Å)
2Θ range for data collection	6.1 to 57.68°
Index ranges	$-19 \leq h \leq 20$, $-20 \leq k \leq 22$, $-8 \leq l \leq 22$
Reflections collected	14847
Independent reflections	1918 [R_{int} = 0.1340, R_{sigma} = 0.0797]
Data/restraints/parameters	1918/0/98
Goodness-of-fit on F^2	1.095
Final R indexes [I>=2σ (I)]	R_1 = 0.0619, wR_2 = 0.1553
Final R indexes [all data]	R_1 = 0.1002, wR_2 = 0.1733
Largest diff. peak/hole / e Å^{-3}	1.45/-0.77

Table A2.2. Crystal data and structure refinement for MOF-802 (CCDC #: 1002674).

Identification code	MOF-802
Empirical formula	$C_{39}H_{16}N_{14.5}O_{39}Zr_6$
Formula weight	1859.65
Temperature/K	100.0
Crystal system	orthorhombic
Space group	Fdd2
a/Å	39.222(3)
b/Å	26.018(2)
c/Å	27.887(2)
α/°	90
β/°	90
γ/°	90
Volume/Å^3	28459(4)
Z	16
ρ_{calc}/mg mm^{-3}	1.736
m/mm^{-1}	7.853
F(000)	14461.0
Crystal size/mm^3	0.25 × 0.21 × 0.18
Radiation	CuKα (λ = 1.54178 Å)
2Θ range for data collection	4.506 to 137.604°
Index ranges	$-41 \leq h \leq 47$, $-31 \leq k \leq 30$, $-29 \leq l \leq 33$
Reflections collected	27657
Independent reflections	10910 [R_{int} = 0.0142, R_{sigma} = 0.0197]
Data/restraints/parameters	10910/145/797
Goodness-of-fit on F^2	1.074
Final R indexes [I>=2σ (I)]	R_1 = 0.0382, wR_2 = 0.1135
Final R indexes [all data]	R_1 = 0.0388, wR_2 = 0.1157
Largest diff. peak/hole / e Å^{-3}	1.55/-0.83
Flack parameter	-0.021(4)

Table A2.3. Crystal data and structure refinement for MOF-808 (CCDC #: 1002672).

Identification code	MOF-808
Empirical formula	$C_{24}H_6O_{44.35}Zr_6$
Formula weight	1551.21
Temperature/K	100.15
Crystal system	cubic
Space group	Fd-3m
a/Å	35.0764(10)
b/Å	35.0764(10)
c/Å	35.0764(10)
α/°	90
β/°	90
γ/°	90
Volume/Å^3	43156(4)
Z	16
$\rho_{calc/}$ mg mm^{-3}	0.955
m/mm^{-1}	0.781
F(000)	11917.0
Crystal size/mm^3	0.01 × 0.01 × 0.01
Radiation	Synchrotron (λ = 0.7749 Å)
2Θ range for data collection	3.58 to 67.398°
Index ranges	$-49 \leq h \leq 50$, $-50 \leq k \leq 50$, $-50 \leq l \leq 50$
Reflections collected	180989
Independent reflections	3133 [R_{int} = 0.0851, R_{sigma} = 0.0213]
Data/restraints/parameters	3133/0/126
Goodness-of-fit on F^2	1.126
Final R indexes [I>=2σ (I)]	R_1 = 0.0396, wR_2 = 0.1334
Final R indexes [all data]	R_1 = 0.0475, wR_2 = 0.1431
Largest diff. peak/hole / e Å^{-3}	0.85/-0.78

Table A2.4. Crystal data and structure refinement for MOF-841 (CCDC #: 1002670)**.**

Identification code	MOF-841
Empirical formula	$C_{62}H_{36}O_{36}Zr_6$
Formula weight	1904.23
Temperature/K	150(2)
Crystal system	tetragonal
Space group	I4/m
a/Å	14.6766(6)
b/Å	14.6766(6)
c/Å	28.0033(10)
α/°	90.00
β/°	90.00
γ/°	90.00
Volume/Å^3	6032.0(4)
Z	2
$\rho_{calc/}$ mg mm^{-3}	1.048
m/mm^{-1}	0.5485
F(000)	3504.0
Radiation	MoKα (λ = 0.71073 Å)
2Θ range for data collection	4.88 to 51.98°
Index ranges	$-18 \leq h \leq 18$, $-18 \leq k \leq 18$, $-34 \leq l \leq 34$
Reflections collected	41321
Independent reflections	3043 [R_{int} = 0.0415, R_{sigma} = 0.0165]
Data/restraints/parameters	3043/72/135
Goodness-of-fit on F^2	1.233
Final R indexes [I>=2σ (I)]	R_1 = 0.0519, wR_2 = 0.1763
Final R indexes [all data]	R_1 = 0.0597, wR_2 = 0.1897
Largest diff. peak/hole / e Å^{-3}	1.48/-0.60

Figure A2.1. Comparison of the experimental PXRD patterns of MOF-801-SC: as-prepared (red) and simulated pattern (black) from single-crystal X-ray data.

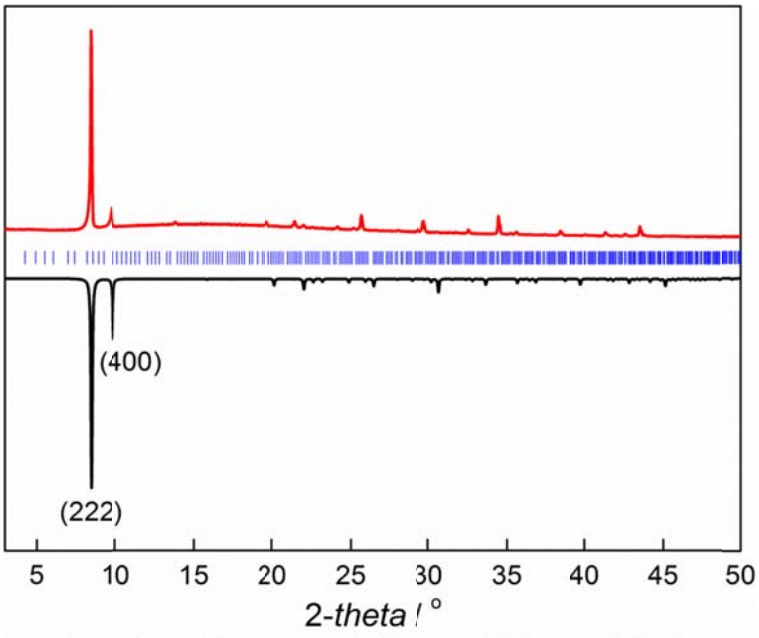

Figure A2.2. Comparison of the experimental PXRD patterns of MOF-801-P: as-prepared (red) and simulated pattern (black) from single-crystal X-ray data.

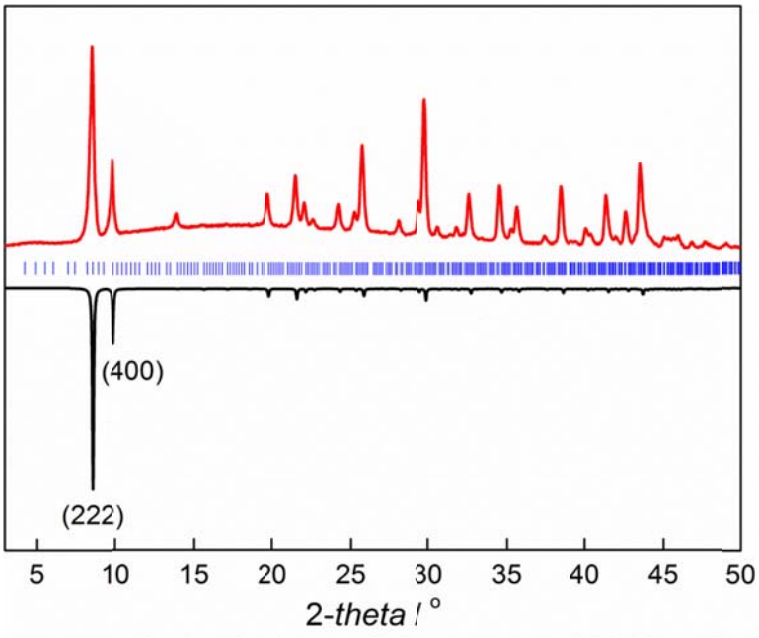

Figure A2.3. Comparison of the experimental PXRD patterns of MOF-802: as-prepared (red) and simulated pattern (black) from single-crystal X-ray data.

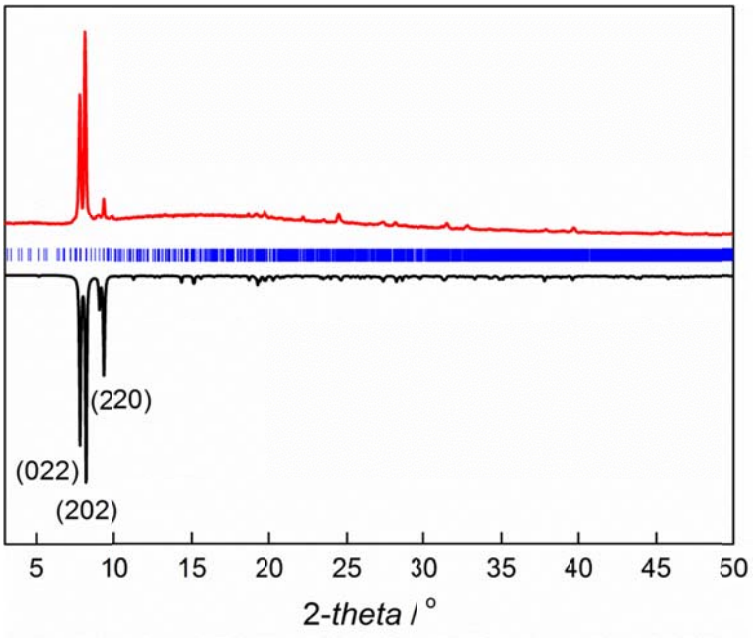

Figure A2.4. Comparison of the experimental PXRD patterns of MOF-808: as-prepared (red) and simulated pattern (black) from single-crystal X-ray data.

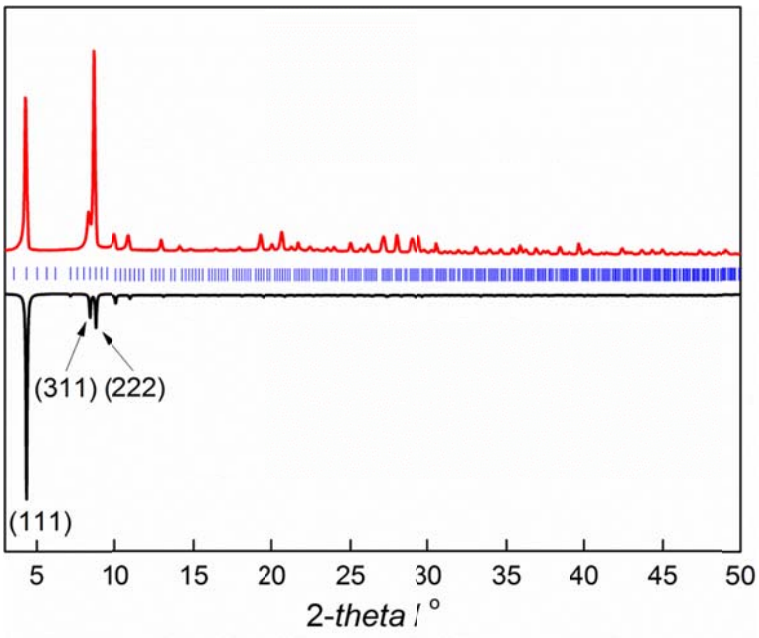

Figure A2.5. Comparison of the experimental PXRD patterns of MOF-841: as-prepared (red) and simulated pattern (black) from single-crystal X-ray data.

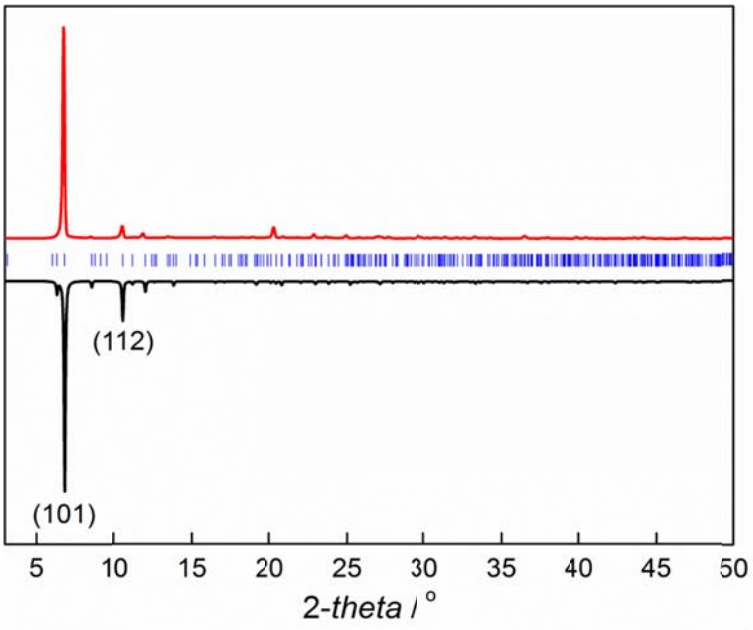

Figure A2.6. TGA trace for as-prepared MOF-801-P, heating rate: 5 °C min^{-1} in air.

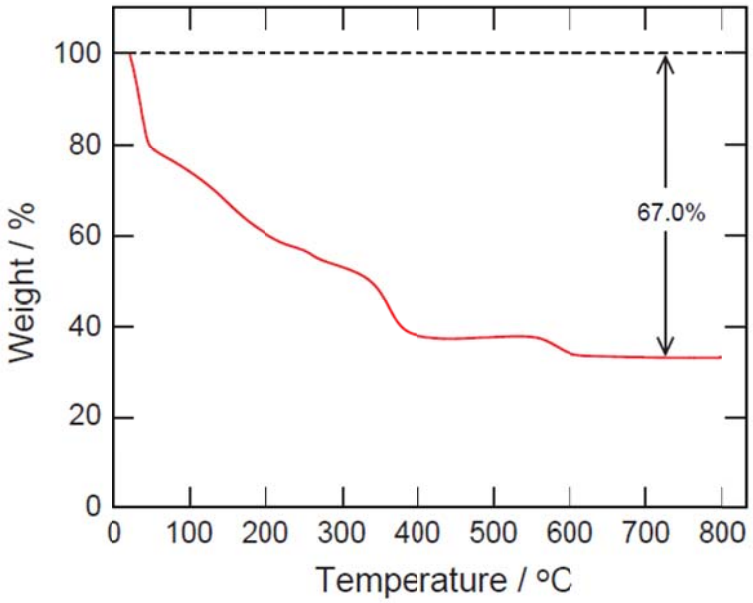

Figure A2.7. TGA trace for as-prepared MOF-801-SC, heating rate: 5 °C min^{-1} in air.

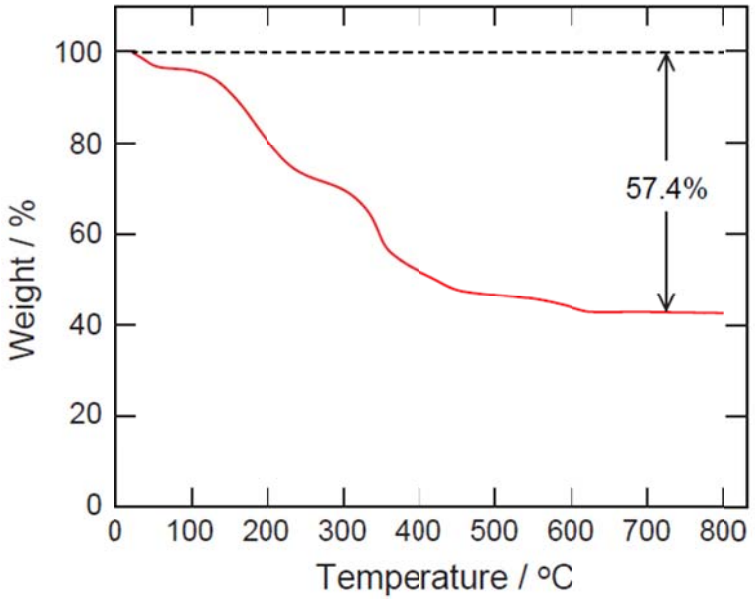

Figure A2.8. TGA trace for as-prepared MOF-802, heating rate: 5 °C min^{-1} in air.

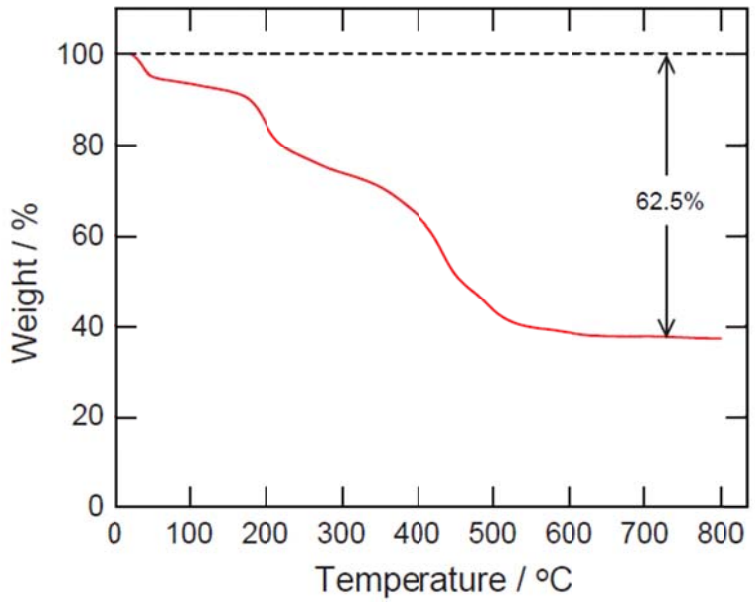

Figure A2.9. TGA trace for as-prepared MOF-808, heating rate: 5 °C min^{-1} in air.

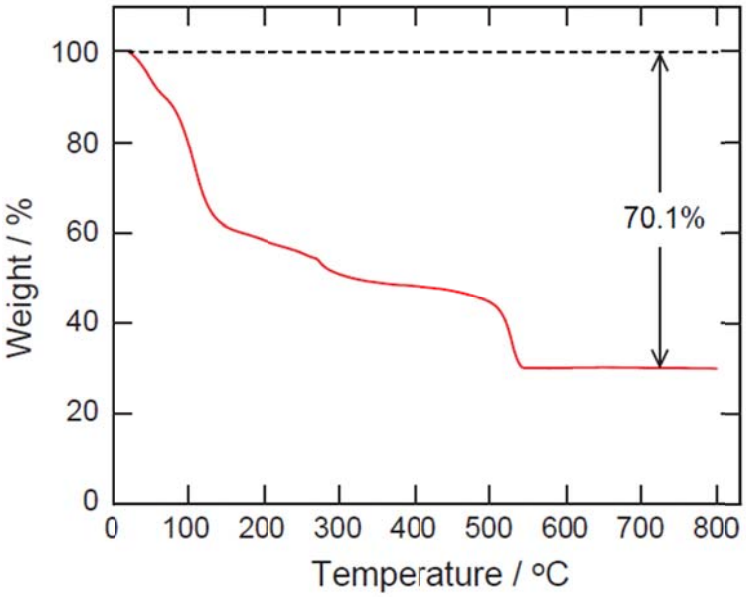

Figure A2.10. TGA trace for as-prepared MOF-841, heating rate: 5 °C min^{-1} in air.

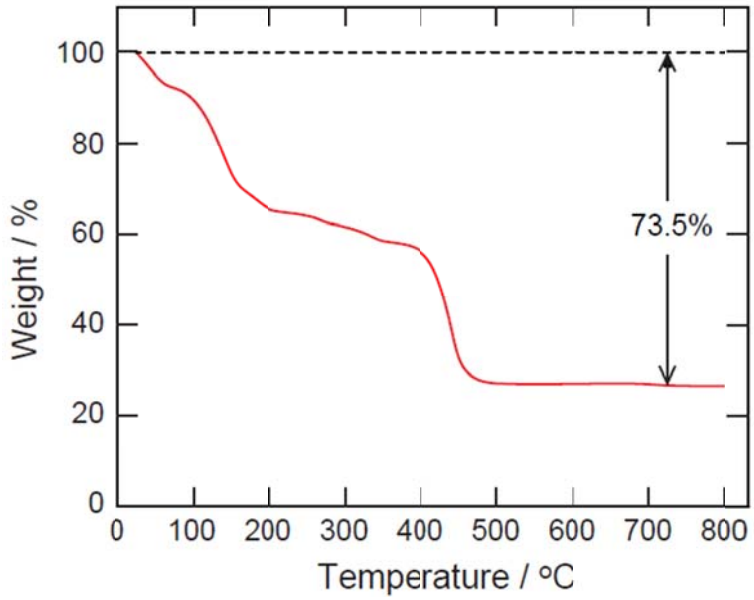

Figure A2.11. N_2 (red) and Ar (blue) isotherm of MOF-801-P at 77 K and 87 K, respectively.

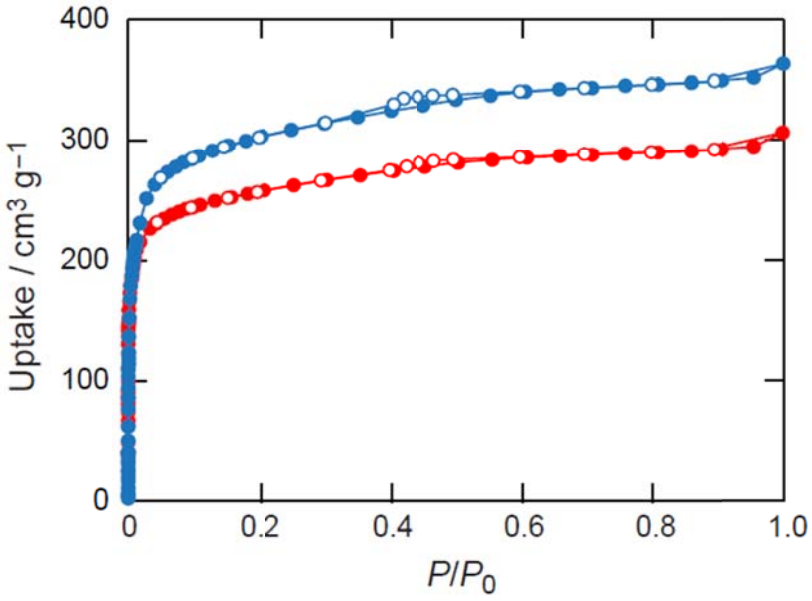

Figure A2.12. N_2 isotherm of MOF-801-SC at 77 K.

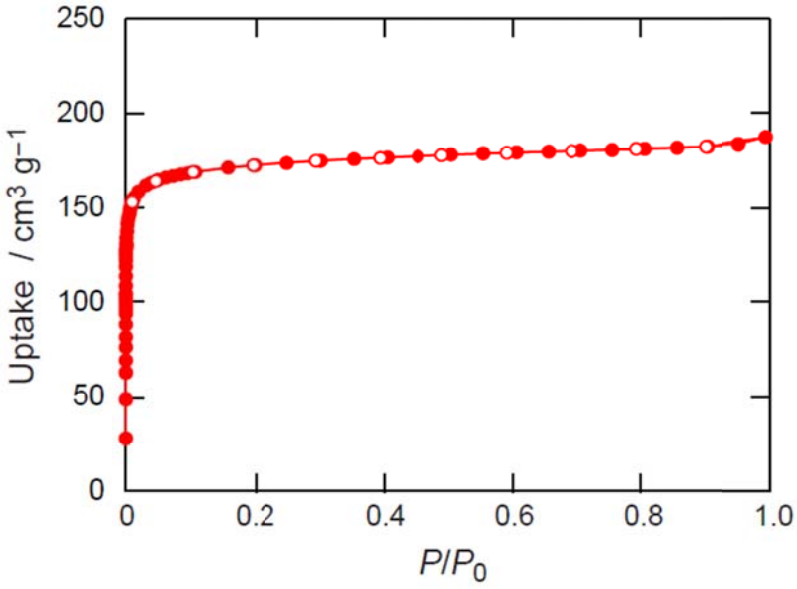

Figure A2.13. N_2 (red) and Ar (blue) isotherm of MOF-802 at 77 K and 87 K, respectively.

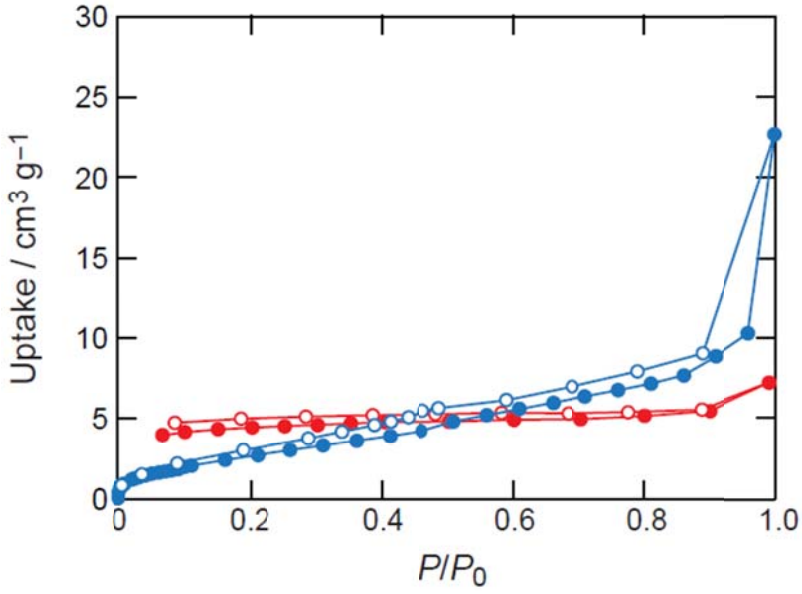

Figure A2.14. N_2 isotherm of DUT-67 at 77 K.

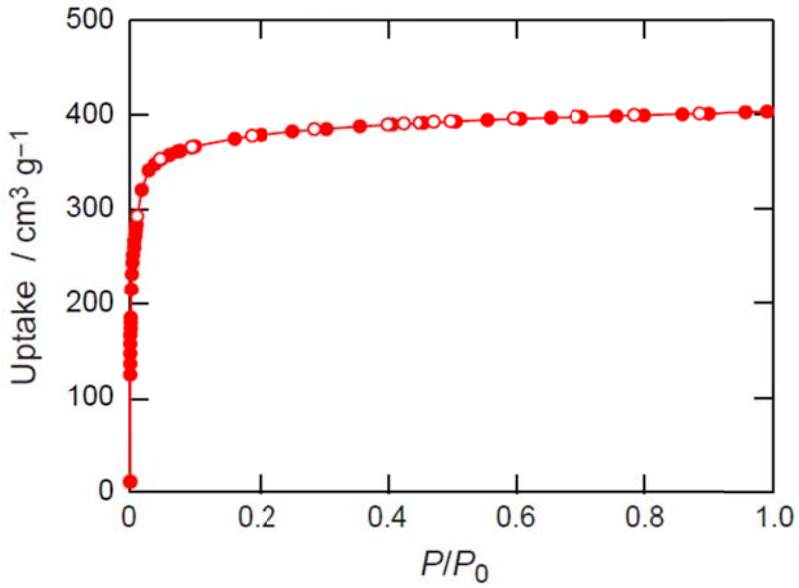

Figure A2.15. N_2 (red) and Ar (blue) isotherm of MOF-808 at 77 K and 87 K, respectively.

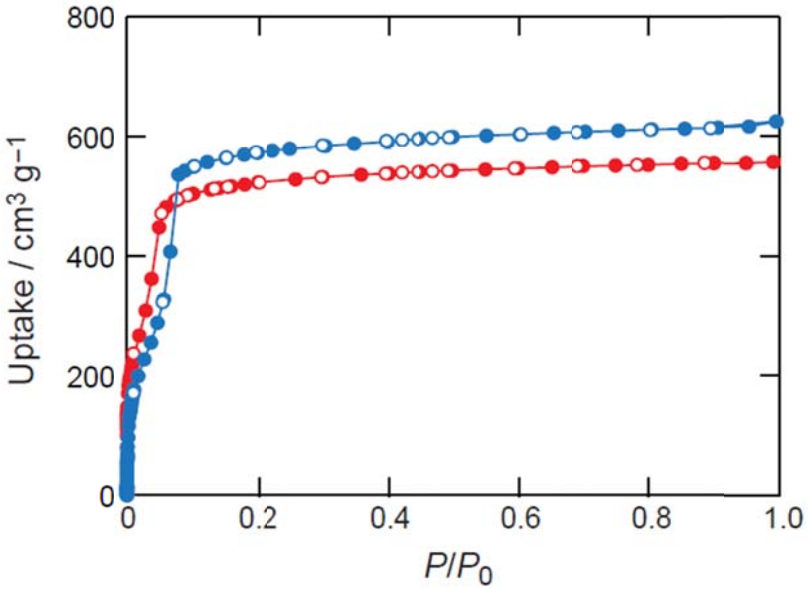

Figure A2.16. N_2 isotherm of MOF-841 at 77 K.

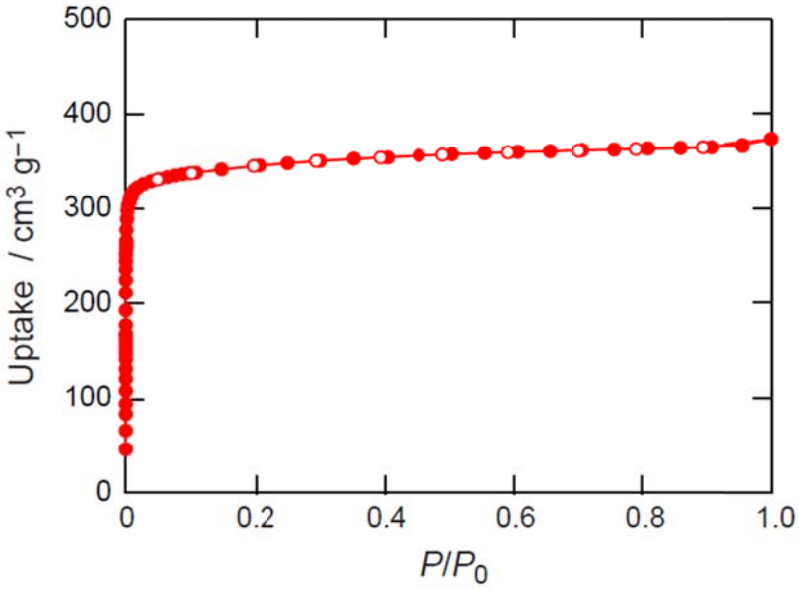

Figure A2.17. N_2 isotherm of UiO-66 at 77 K.

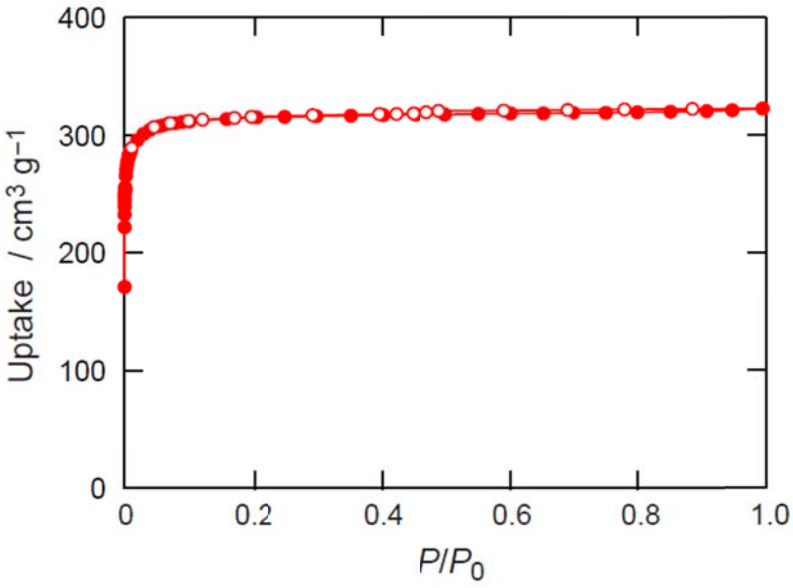

Figure A2.18. Cycle performance of water uptake in MOF-801-P at 25 °C. The sample was evacuated for 2 hours at 25 °C between the cycles.

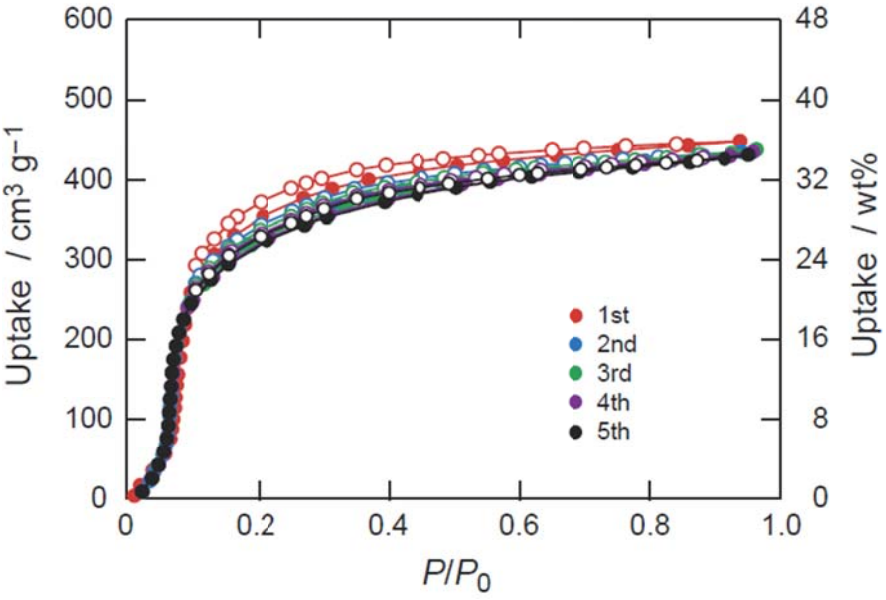

Figure A2.19. Cycle performance of water uptake in MOF-801-SC at 25 °C. The sample was evacuated for 2 hours at 25 °C between the cycles.

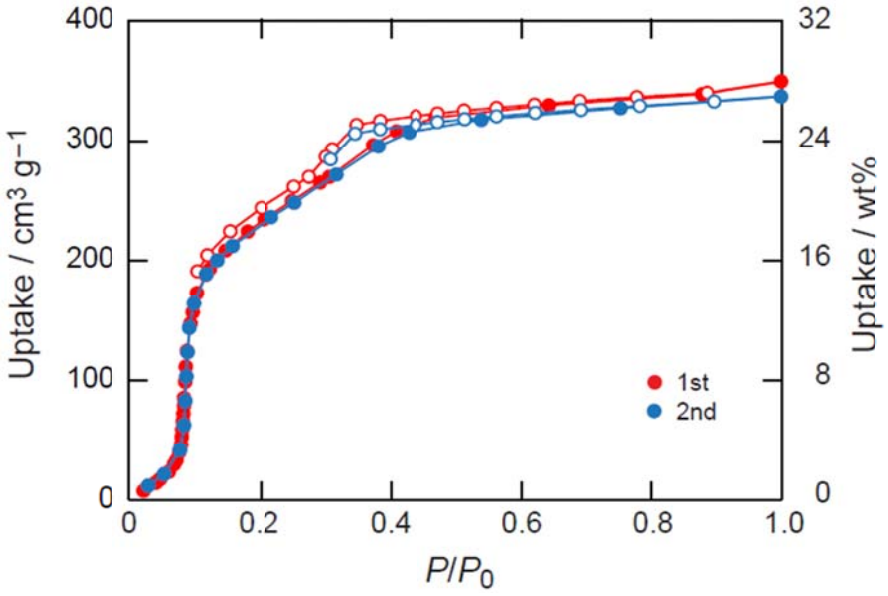

Figure A2.20. Cycle performance of water uptake in MOF-802 at 25 °C. The sample was evacuated for 2 hours at 25 °C between the cycles.

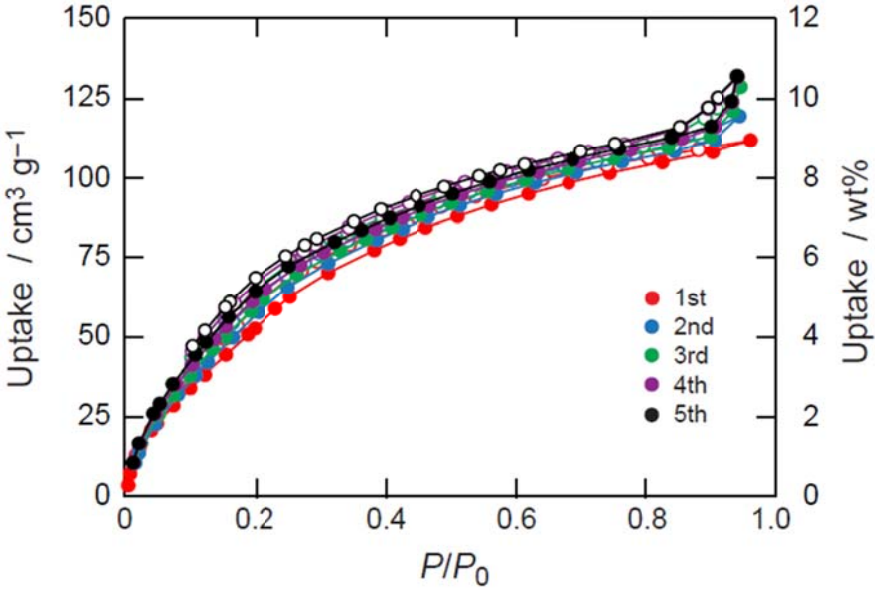

Figure A2.21. Cycle performance of water uptake in MOF-808 at 25 °C. The sample was evacuated for 2 hours at 25 °C between the cycles.

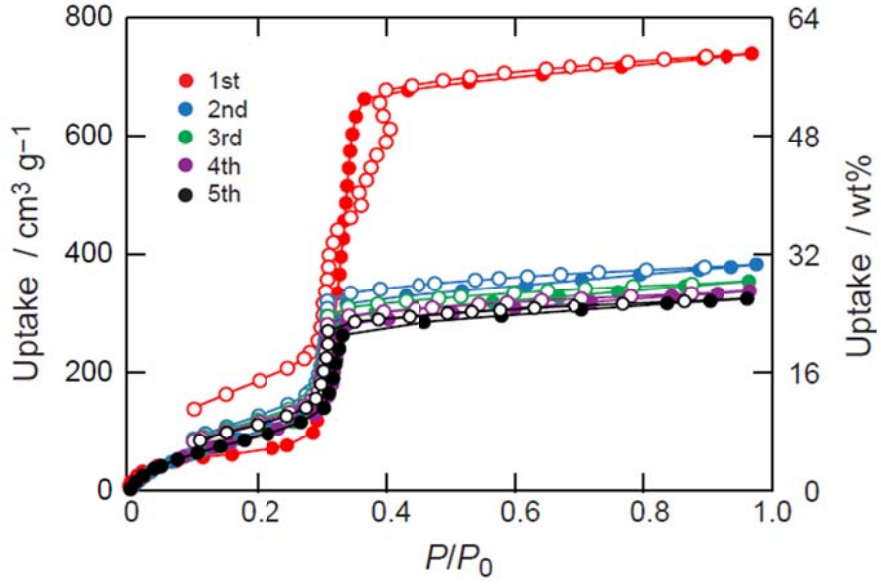

Figure A2.22. Cycle performance of water uptake in MOF-841 at 25 °C. The sample was evacuated for 2 hours at 25 °C between the cycles.

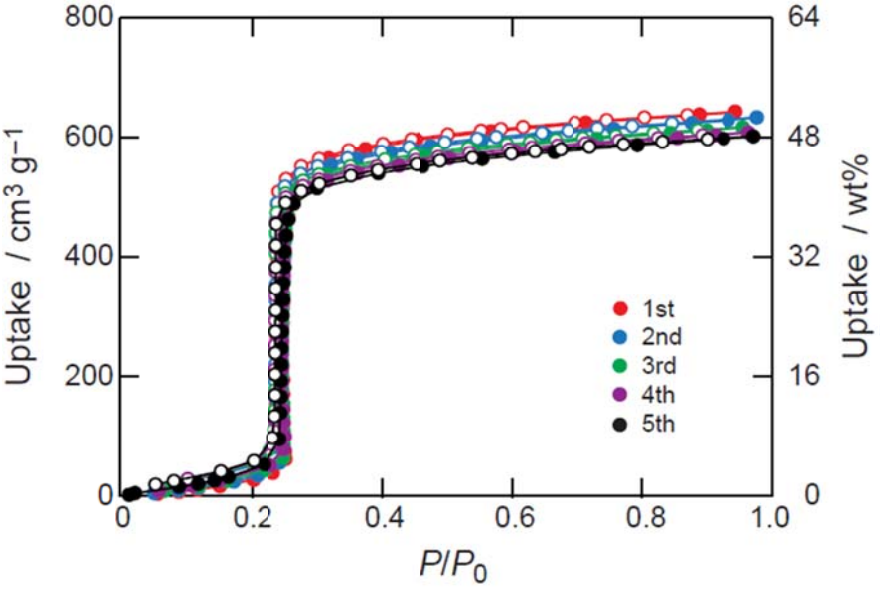

Figure A2.23. Cycle performance of water uptake in UiO-66 at 25 °C. The sample was evacuated for 2 hours at 25 °C between the cycles.

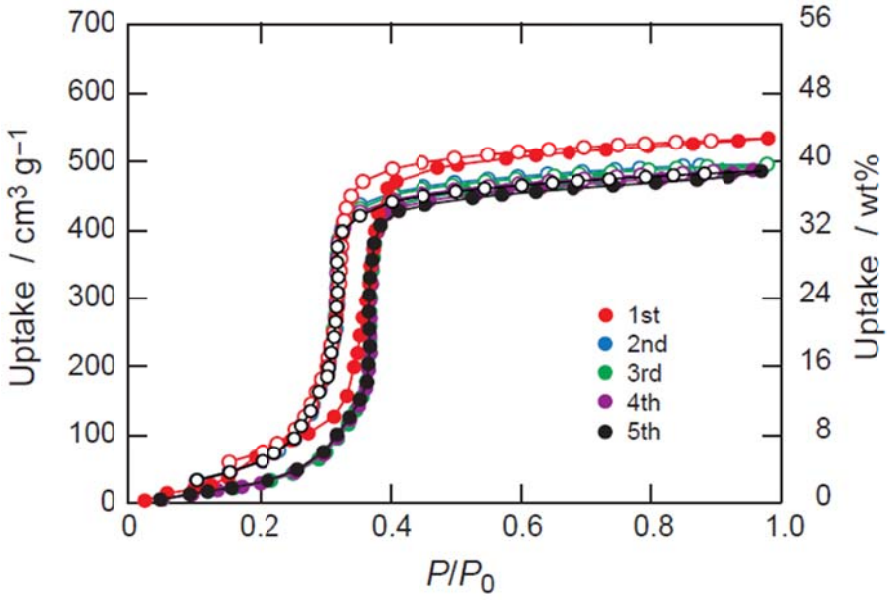

Figure A2.24. Cycle performance of water uptake in DUT-67 at 25 °C. The sample was evacuated for 2 hours at 25 °C between the cycles.

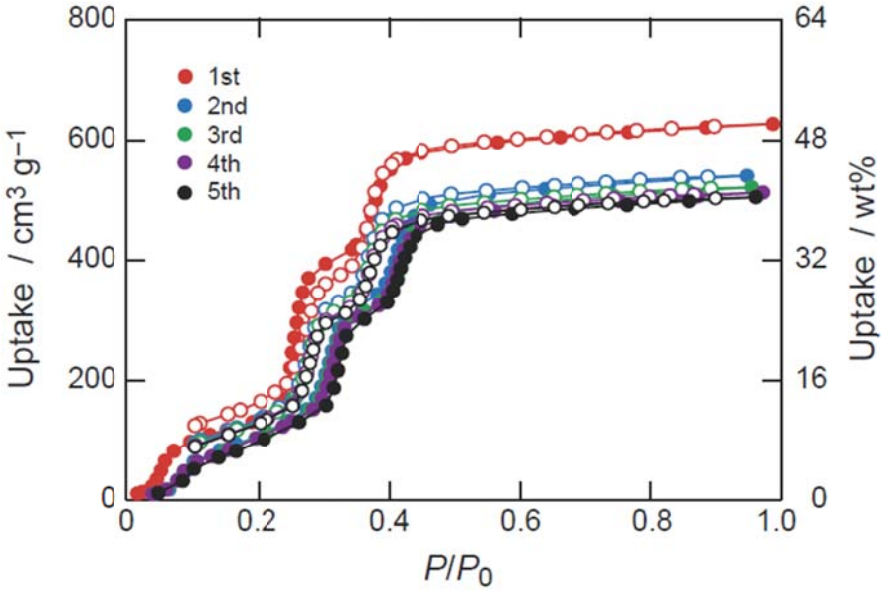

Figure A2.25. Water isotherms of MOF-801-P measured at 25, 35, 45, and 55 °C.

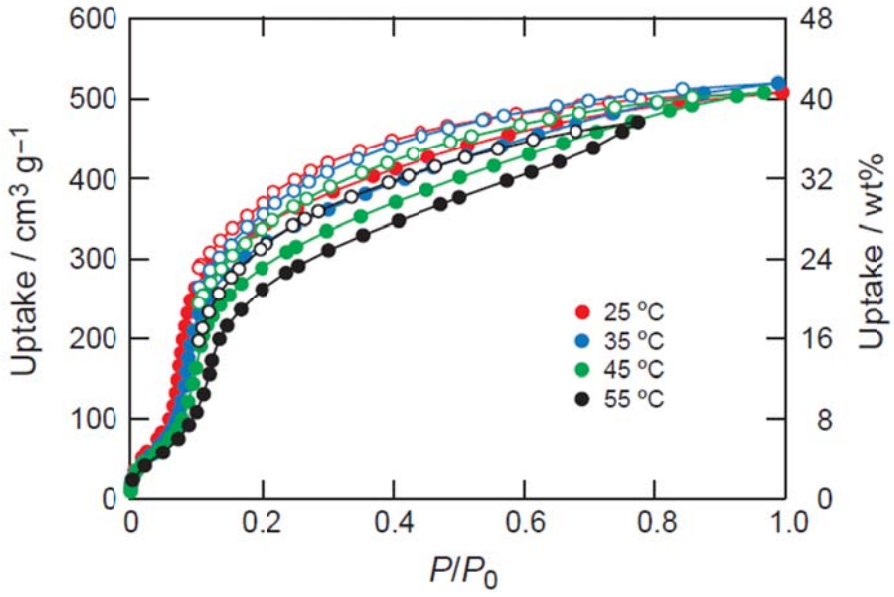

Figure A2.26. Isosteric heat of water adsorption for MOF-801-P.

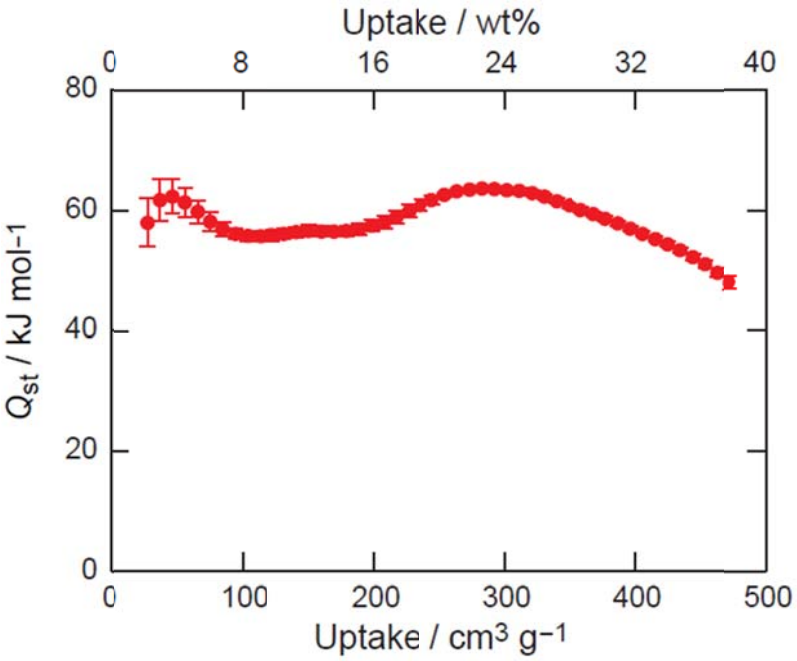

Figure A2.27. Water isotherms of MOF-841 measured at 15, 25, 35, and 45 °C.

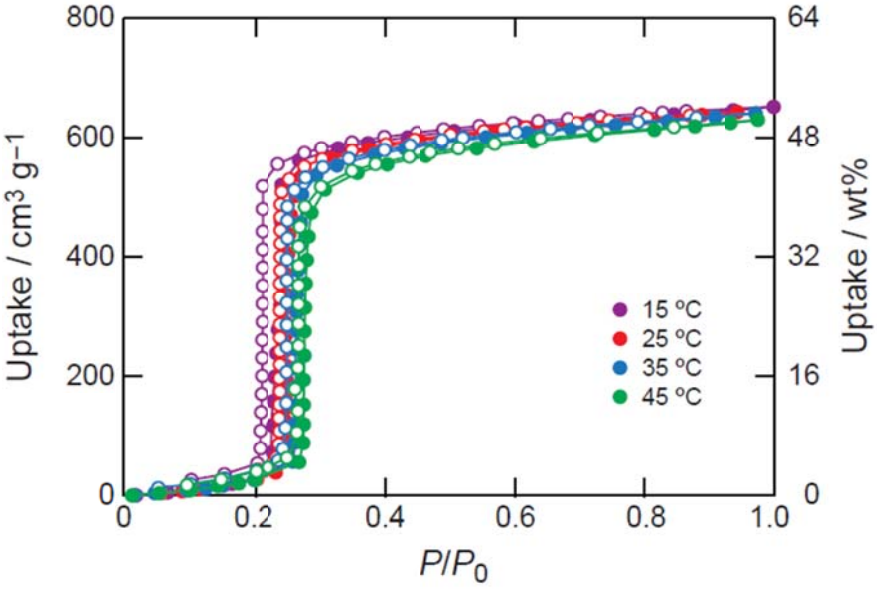

Figure A2.28. Isosteric heat of water adsorption for MOF-841.

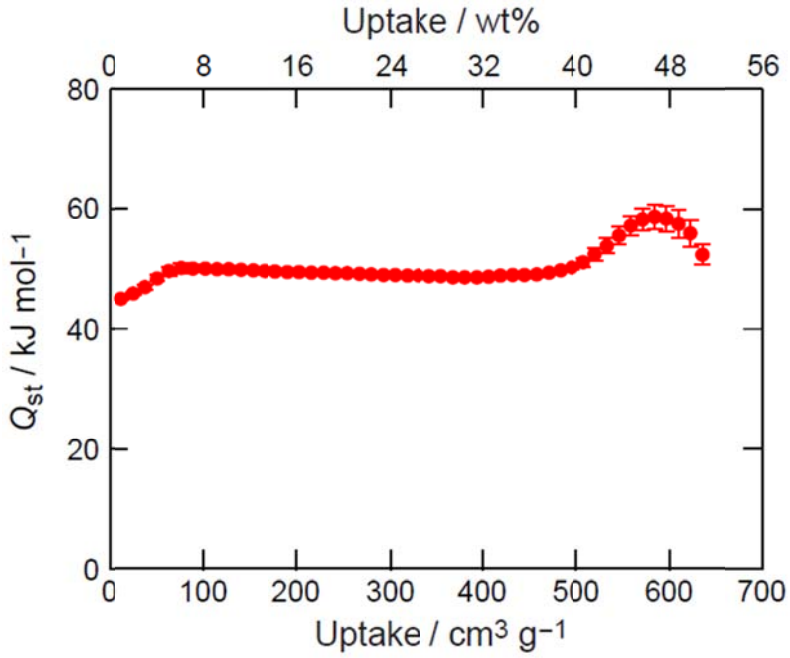

References and Notes

(1) Furukawa, H.; Cordova, K. E.; O'Keeffe, M.; Yaghi, O. M. Science **2013**, 341, 1230444.

(2) Yaghi, O. M.; O'Keeffe, M.; Ockwig, N. W.; Chae, H. K.; Eddaoudi, M.; Kim, J. Nature **2003**, 423, 705.

(3) Wu, H.; Yildirim, T.; Zhou, W. J. Phys. Chem. Lett. **2013**, 4, 925

(4) Cavka, J. H.; Jakobsen, S.; Olsbye, U.; Cuillou, N.; Lamberti, C.; Bordiga, S.; Lillerud, K. P. J. Am. Chem. Soc. **2008**, 130, 13850.

(5) Yang, H.; Zhu, H.; Hendrix, M. M. R. M.; Lousberg, N. J. H. G. M.; de With, G.; Esteves, A. C. C.; Xin, J. H. Adv. Mater. **2013**, 25, 1150.

(6) (a) Gur, I.; Sawyer, K.; Prasher, R. Science **2012**, 335, 1454. (b) Demir, H.; Mobedi, M.; Ülkü, S. Renew. Sust. Energ. Rev. **2008**, 12, 2381. (c) Hepbasli, A.; Kalinci, Y. Renew. Sust. Energ. Rev. **2009**, 13, 1211. (d) Henninger, S. K.; Schmidt, F. P.; Henning, H. M. Appl. Therm. Eng. **2010**, 30, 1692. (e) Henninger, S. K.; Jeremias, F.; Kummer, H.; Janiak, C. Eur. J. Inorg. Chem. **2012**, 2625.

(7) Furukawa, H.; Gándara, F.; Zhang, Y.-B.; Jiang, J.; Queen, W. L.; Hudson, M. R. Yaghi, O. M. J. Am. Chem. Soc. **2014**, 136, 4369.

(8) Narayanan, S.; Li, X.; Yang, S.; McKay, I.; Kim, H.; Wang E. N. Proceedings of the ASME 2013 Heat Transfer Summer Conference **2013**, HT2013-17472.

(9) Thommes, M.; Morell, J.; Cychosz, K. A.; Fröba, M. Langmuir **2013**, 29, 14893.

(10) (a) Wang, Q. M.; Shen, D.; Buelow, M.; Lau, M. L.; Deng, S.; Fitch, F. R.; Lemcoff, N. O.; Semanscin, J. Microporous Mesoporous Mater. **2002**, 55, 217. (b) Dietzel, P. D. C.; Johnsen, R. E.; Blom, R.; Fjellvåg, H. Chem. Eur. J. **2008**, 14, 2389. (c) Yazaydın, A. Ö.; Benin, A. I.; Faheem, S. A.; Jakubczak, P.; Low, J. J.; Willis, R. R.; Snurr, R. Q. Chem. Mater. **2009**, 21, 1425. (d) Kusgens, P.; Rose, M.; Senkovska, I.; Froede, H.; Henschel, A.; Siegle, S.; Kaskel, S. Microporous Mesoporous Mater. **2009**, 120, 325. (e) Paranthaman, S.; Coudert, F.-X.; Fuchs, A. H. Phys. Chem. Chem. Phys. **2010**, 12, 8123. (f) Akiyama, G.; Matsuda, R.; Kitagawa, S. Chem. Lett. **2010**, 39, 360. (g) Hauptvogel, I. M.; Biedermann, R.; Klein, N.; Senkovska, I.; Cadiau, A.; Wallacher, D.; Feyerherm, R.; Kaskel, S. Inorg. Chem. **2011**, 50, 8367. (h) Ehrenmann, J.; Henninger, S. K.; Janiak, C. Eur. J. Inorg. Chem. **2011**, 471. (i) Goesten, M. G.; Juan-Alcañiz, J.; Ramos-Fernandez, E. V.; Gupta, K. B. S. S.; Stavitski, E.; van Bekkum, H.; Gascon, J.; Kapteijn, F. J. Catal. **2011**, 281, 177. (j) Čelič, T. B.; Mazaj, M.; Guillou, N.; Elkaïm, E.; El Roz, M.; Thibault-Starzyk, F.; Mali, G.; Rangus, M.; Čendak, T.; Kaučič, V.; Logar, N. Z. J. Phys. Chem. C **2013**, 117, 14608. (k) Wade, C. R.; Corrales-Sanchez, T.; Narayan, T. C.; Dincă, M. Energy Environ. Sci. **2013**, 6, 2172. (l) Jeremias, F.; Lozan, V.; Henninger, S. K.; Janiak, C. Dalton Trans. **2013**, 42, 15967. (m) Wickenheisser, M.; Jeremias, F.; Henninger, S. K.; Janiak, C. Inorg. Chim. Acta **2013**, 407, 145. (n) Seo, Y.-K.; Yoon, J. W.; Lee, J. S.; Hwang, Y. K.; Jun, C.-H.; Chang, J.-S.; Wuttke, S.; Bazin, P.; Vimont, A.; Daturi, M.; Bourrelly, S.; Llewellyn, P. L.; Horcajada, P.; Serre, C.; Férey, G. Adv. Mater. **2012**, 24, 806. (o) Khutia, A.; Rammelberg, H.; Schmidt, T.; Henninger, S.; Janiak, C. Chem. Mater. **2013**, 25, 790. (p) Akiyama, G.; Matsuda, R.; Sato, H.; Hori, A.; Takata, M.; Kitagawa, S. Microporous Mesoporous Mater. **2012**, 157, 89. (q) Cmarik, G.; Kim, M.; Cohen, S.; Walton, K. Langmuir **2012**, 28, 15606. (r) Yang, Q; Vaesen, S.; Ragon, F.; Wiersum, A. D.; Wu, D.; Lago, A.; Devic, T.; Martineau, C,; Taulelle, F.;

Llewellyn, P. L.; Jobic, H.; Zhong, C.; Serre, C.; De Weireld, G.; Maurin, G. Angew. Chem. Int. Ed. **2013**, 52, 10316. (s) Liu, J.; Wang, Y.; Benin, A. I.; Jakubczak, P.; Willis, R. R.; LeVan, M. D. Langmuir **2010**, 26, 14301. (t) Schoenecker, P. M.; Carson, C. G.; Jasuja, H.; Flemming, C. J. J.; Walton, K. S. Ind. Eng. Chem. Res. **2012**, 51, 6513. (u) Zhang, J.-P.; Zhu, A.-X.; Lin, R.-B.; Qi, X.-L.; Chen, X.-M. Adv. Mater. **2011**, 23, 1268.

(11) Bon, V.; Senkovska, I.; Baburin, I. A.; Kaskel, S. Cryst. Growth Des. **2013**, 13, 1231.

(12) Morris, W.; Volosskiy, B.; Demir, S.; Gandara, F.; McGrier, P. L.; Furukawa, H.; Cascio, D.; Stoddart, J. F.; Yaghi, O. M. Inorg. Chem. **2012**, 51, 6443.

(13) Bon, V.; Senkovskyy, V.; Senkovska, I.; Kaskel, S. Chem. Commun. **2012**, 48, 8407.

(14) Wiβmann, G.; Schaate, A.; Lilienthal, S.; Bremer, I.; Schneider, A. M.; Behrens, P. Micropor. Mesopor. Mater. **2012**, 152, 64.

(15) Schaate, A.; Roy, P.; Godt, A.; Lippke, J.; Waltz, F.; Wiebcke, M.; Behrens, P. Chem. Eur. J. **2011**, 17, 6643.

(16) (a) Grimm, M.; Kirste, B.; Kurreck, H. Angew. Chem., Int. Ed. Engl. **1986**, 25, 1097. (b) Hoskins, B. F.; Robson, R. J. Am. Chem. Soc. **1990**, 112, 1546.

(17) Tranchemontagne, D. J.; Mendoza-Cortés, J. L.; O'Keeffe, M.; Yaghi, O. M. Chem. Soc. Rev. **2009**, 38, 1257.

(18) Feng, D.; Jiang, H.-L.; Chen, Y.-P.; Gu, Z.-Y.; Wei, Z.; Zhou, H.-C. Inorg. Chem. **2013**, 52, 12661.

(19) Guillerm, V.; Ragon, F.; Dan-Hardi, M.; Devic, T.; Vishnuvarthan, M.; Campo, B.; Vimont, A.; Clet, G.; Yang, Q.; Maurin, G.; Férey, G.; Vittadini, A.; Gross, S.; Serre, C. Angew. Chem. Int. Ed. **2012**, 51, 9267.

(20) Spek, A. L. Acta Cryst. **2009**, D65, 148.

(21) It has been recently reported that UiO-66 might contain different amounts of missing linker defects depending on the amount of acid modulator employed during the synthesis. Indeed, MOF-801-P was prepared with a higher concentration of formic acid than MOF-801-SC, which would result in a large amount of such defects: Wu, H.; Chua, Y.; Krungleviciute, V.; Tyagi, M.; Chen, P.; Yildirim, T.; Zhou, W., J. Am. Chem. Soc. **2013**, 135, 10525.

(22) Thommes, M.; Morell, J.; Cychosz, K. A.; Froba, M. Langmuir **2013**, 29, 14893.

(23) https://arpa-e-foa.energy.gov/Default.aspx?Search=DE-FOA-0000471

Chapter III

Controllable Sulfation of Zirconium Metal-Organic Framework-808 and Generation of MOF-Based Superacid

Introduction

Structural modification of MOFs, where the secondary building units (SBUs) are modified with incoming molecules or functional groups, plays an important role in tuning the properties of and applying MOFs to gas storage, separation, and catalysis.[1] The strong bonds between SBUs of MOFs have allowed covalent chemistry to be employed to modify MOF crystals as if they were discrete molecules, because the MOF building units retain the same underlying structure and essential chemical reactivity as their molecular counterparts.

Of the several approaches devised to modify the structure of MOFs, post synthetic modification (PSM), is the most frequently applied and frequently reviewed approach.[1] PSM involves either carrying out organic reactions to modify the organic linkers of the MOF and/or covalently bonding incoming ligands to open metal sites.[2] These modifications are performed orthogonally to the MOF backbone structure. Such chemical reactions are carried out at precise locations within the crystal and the product remains atomically well defined (i.e. crystalline). The ability to carry out reactions on extended solids in this manner is possible because of the robustness of the MOF structure due to the strong covalent bonds composing the framework. Furthermore, this chemistry allows functional groups that are not compatible with the MOF synthesis to be incorporated, and for the design of a series of MOFs of different functionality using a single set of synthetic conditions. Thus, PSM is a powerful tool to design complexity within MOFs.

PSM performed on extended solids requires reagents to diffuse throughout the crystal. Reactions involving insoluble heterogeneous reagents and catalysts or those producing insoluble byproducts present a challenge to PSM of MOFs. The candidate reactions for PSM should also be chemically compatible with the MOF backbone. Therefore, another challenge for PSM in MOFs is encountered when incorporation of strong acidic functionalities is desired. Increasingly, MOFs with unusual stability in aqueous and non-aqueous conditions are being developed and employed. Recently, several stable MOFs in acidic and basic media have been reported.[3] These materials provide with a large number of opportunities for performing efficient PSMs to develop completely novel chemistry in MOFs.

Superacids, refers to any acid systems stronger than 100% sulfuric acid,[4] that is, Hammett acidity function $H_0 \leq -12$ (Figure 3.1).[5] On the basis of various measurements, $HF–SbF_5$, HSO_3F and CF_3SO_3H are typically considered liquid Brønsted superacid catalysts widely used for activation of the hydrocarbons at low temperature.[6] The development and utilization of solid superacids is another important direction of study which has yielded several solid superacid systems including sulfate ion-promoted metal oxides (e.g. SO_4^{2-}/ZrO_2), Nafion-H, and zeolite (e.g. ZSM-5).[7] However, challenges still remain in this chemistry concerning the precise determination of the level of acidity, knowledge of the nature of the acid sites, and the discovery of new designable superacid systems.

Metal-organic frameworks (MOFs) have a great potential for the development of new solid superacids due to their structural diversity, crystalline structure, and tunable porosity. Robust, acid-stable MOFs displaying Brønsted acidity have been prepared by utilizing sulfonated organic linkers or hydroxyl and water ligands coordinated to metal sites within the framework.[8] The acidity of these MOFs is either undetermined or has been measured from the shift of the -OH group vibration induced by CO adsorption and found to have H_0 = -3 to -8. Up to date, no MOF has displayed superacidity (i.e. $H_0 \leq$ -12).

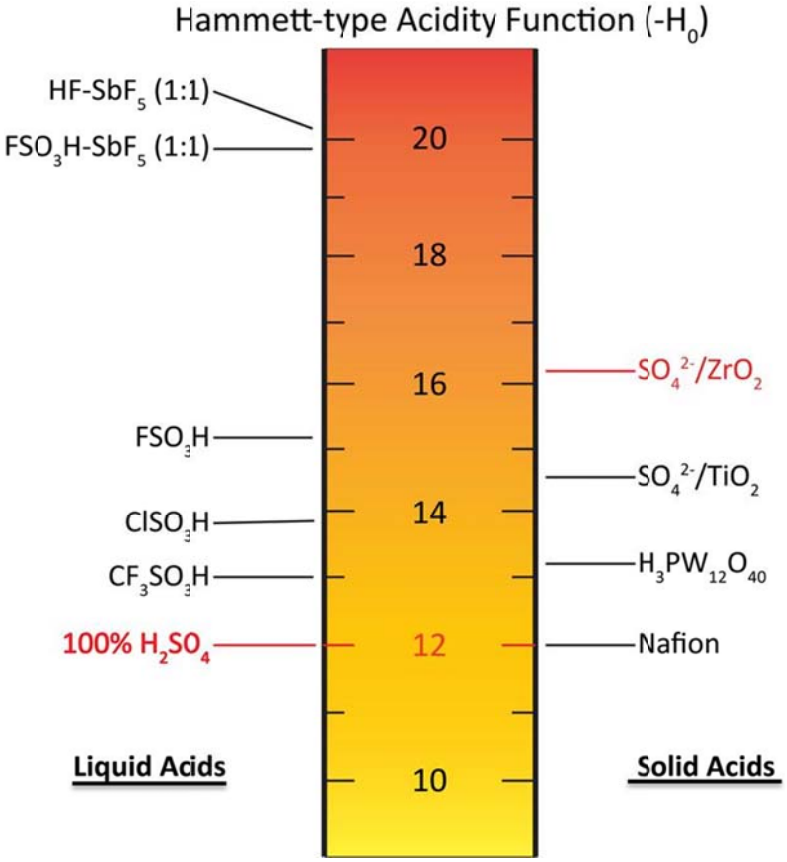

Figure 3.1. Acid strength of typical liquid and solid superacids.

One elaborate way of generating superacidity in inorganic solids is through sulfuric acid treatment, as in sulfate-ion promoted metal oxides. Here, we show that superacidity can be achieved by treating a microcrystalline powder of the zirconium(IV) MOF-808[9] [MOF-808-P: $Zr_6O_5(OH)_3(BTC)_2(HCOO)_5(H_2O)_2$, BTC = 1,3,5-benzenetricarboxylate] with aqueous sulfuric acid. The resulting sulfated MOF-808 [MOF-808-2.5SO_4: $Zr_6O_5(OH)_3(BTC)_2(SO_4)_{2.5}$] has $H_0 \leq$ -14.5 by the Hammett indicator method — a value corresponding to a higher acidity than 100% sulfuric acid (H_0 = -12). This provides, for the first time, evidence of superacidity in MOFs. The presence of sulfate units bound to the zirconium centers of the MOF framework was established by single crystal X-ray diffraction and infrared spectroscopy. We believe these studies serve as a benchmark for producing and measuring superacidity in MOFs.[10]

Experimental Section

Chemicals and supplies. N,N-Dimethylformamide (DMF), anhydrous methanol and formic acid (purity > 98%) were obtained from EMD Millipore Chemicals; anhydrous acetone and anhydrous toluene were obtained from Acros Organics; zirconium oxychloride octahydrate ($ZrOCl_2 \cdot 8H_2O$, purity ≥ 99.5%), sulfuric acid (H_2SO_4, purity ≥ 95%), hydrofluoric acid (HF, 48 wt% in water), anhydrous benzene, and anhydrous chloroform with amylenes as stabilizer were obtained from Sigma-Aldrich. 1,3,5-Benzenetricarboxylic acid (H_3BTC) was obtained from Aldrich. Trimethylphosphine oxide (TMPO) was obtained from Alfa Aesar. Acetonitrile-d_3 (99.8 atom% D) was obtained from TCI America.

Hammett Indicators: 4-Phenylazoaniline (analytical standard) and 2,4-dinitroaniline (analytical standard, 99.9%) were obtained from Fluka. 2-Nitroaniline (purity ≥ 98%), 4-nitrodiphenylamine (purity ≥ 99%), anthraquinone (purity ≥ 97%), and 4-nitrofluorobenzene (purity ≥ 99%) were obtained from Aldrich, 2,4-Dichloro-6-nitroaniline (purity > 98%) and 2-benzoylnaphthalene (purity ≥ 98%) were obtained from Alfa Aesar. 2-Bromo-4,6-dinitroaniline (purity ≥ 98.0%), 4-nitrotoluene (purity ≥ 99.0%), and 2,4-dinitrotoluene (purity ≥ 99.0%) were obtained from TCI. 2,4-Dinitrofluorobenzene (purity ≥ 99%) were obtained from Sigma.

All starting materials, reagents and solvents were used without further purification.

All glassware used to handle activated MOFs was dried at 120 ^{o}C for 12h and used immediately.

Analytical techniques. Single-crystal X-ray diffraction (SXRD) data were collected using synchrotron radiation in beamline 11.3.1 of the Advanced Light Source, Lawrence Berkeley National Laboratory (LBNL). Powder X-ray diffraction (PXRD) patterns were recorded using a Rigaku Miniflex 600 diffractometer (Bragg-Brentano geometry, Cu Kα radiation λ = 1.54056 Å). Solution ^{1}H NMR spectra were acquired on a Bruker Avance-400 MHz NMR spectrometer. Carbon, hydrogen, nitrogen and sulfur elemental microanalyses (EA) were performed in the Microanalytical Laboratory of the College of Chemistry at UC Berkeley, using a Perkin Elmer 2400 Series II CHNS elemental analyzer. Inductively coupled plasma-optical emission spectroscopy (ICP-OES) was performed on a PerkinElmer Optical Emission Spectrometer Optima 7000DV instrument. Scanning electron microscope (SEM) images were obtained using a Zeiss Gemini Ultra-55 analytical scanning electron microscope with a working distance of 8.4 mm and a low acceleration voltages (5 keV) to avoid damage to the samples during observation. All MOF SEM samples were prepared by direct deposition of MOF/acetone dispersion (1 mg mL^{-1}) on the silicon substrate heated on a hot plate (60 °C). Low-pressure gas (N_2 and Ar) adsorption isotherms were recorded on a Quantachrome Autosorb-1 volumetric gas adsorption analyzer. Liquid nitrogen and argon baths were used for the measurements at 77 and 87 K, respectively. Helium was used for the estimation of dead space for gas adsorption measurements. Ultra-high-purity grade N_2, Ar, and He gases (Praxair, 99.999% purity) were used throughout the adsorption experiments. Attenuated total reflectance (ATR) FTIR spectra of neat samples were performed on a Bruker ALPHA Platinum ATR-FTIR Spectrometer equipped with a single reflection diamond ATR module. Solid-state nuclear magnetic resonance (SSNMR) spectra were acquired on a Bruker Avance-500 MHz NMR spectrometer using a standard Bruker double resonance magic angle-spinning (MAS) probe.

Synthesis and Characterization of MOFs:

General procedure for MOF formulation. Activated MOFs were analyzed using microanalyses (C, H, N, and S), ICP-OES analyses (Zr) and integrated solution ^{1}H NMR spectra of digested samples to determine their formula. A mixture containing 580 μL of DMSO-d_6 and 20 μL of hydrofluoric acid (48 wt% in water) was used to digest 10 mg of each MOF for NMR measurements. The formulation procedure used the formula $[Zr_6O_{10-x-2y}(OH)_{x+2y-2}(C_9H_3O_6)_2(HCOO)_x(SO_4)_y](H_2O)_z$ as a starting point. The value of x was determined using the ratio of integrated formate and trimesate resonances in the solution ^{1}H NMR spectrum of each digested sample. The value of y was determined from the results of C and S microanalyses. Finally, the value of z was determined by matching the calculated elemental microanalyses results with the found values.

Microcrystalline powder sample of MOF-808-P. Microcrystalline powder samples of MOF-808-P were prepared using slightly modified published procedures.[9] H_3BTC (2.1 g, 10 mmol) and $ZrOCl_2 \cdot 8H_2O$ (9.7 g, 30 mmol) were dissolved in DMF/formic acid (450 mL/450 mL) and placed in a 1-L screw-capped glass jar, which was heated to 130 °C for two days. A white precipitate was collected by filtration and washed three times with 200 mL of fresh DMF. As-synthesized MOF-808-P was then immersed in 100 mL of anhydrous DMF for three days, during which time the DMF was replaced three times per day. The DMF-exchanged compound was filtrated off and immersed in 100 mL of water for three days, during which time the water was replaced three times per day. Water exchanged material was then immersed in 100 mL of anhydrous acetone for three days, during which time the acetone was replaced three times per day. The acetone-exchanged sample was then evacuated at room temperature for 24 h and at 150 °C for 24 h to yield activated sample (Yield: 5.1 g, 76 % based on Zr). ^{1}H solution NMR spectra of digested, activated sample (400 MHz, DMSO-d_6, ppm): 8.64 (s, BTC), 8.12 (s, HCOOH), peak area ratio (BTC:HCOOH) = 6.0:5.0. Anal. Calcd for $Zr_6C_{23}H_{18}O_{32}$ = $[Zr_6O_5(OH)_3(C_9H_3O_6)_2(HCOO)_5](H_2O)_2$: Zr, 40.43; C, 20.41; H, 1.34%. Found: Zr, 40.3; C, 21.02; H, 1.37%.

MOF-808-2.3SO_4 single crystal. Single crystals of MOF-808 were prepared following the reported procedure (S1). As-synthesized MOF-808 single crystals were immersed in anhydrous DMF for three days followed by water for three days, during which time the solvent was exchanged three times per day. Roughly 50 mg of water-exchanged MOF-808 crystals were immersed in 5 mL of 0.1 M sulfuric acid for 24 h during which time the mixture was stirred about once every two hours. The single crystals were then solvent exchanged with water for three days (water exchanged three times per day), quickly exchanged with anhydrous acetone for several times and immersed in anhydrous chloroform for three days during which time chloroform was exchanged three times per day. The chloroform in the solvent-exchanged crystals was removed under dynamic vacuum (30 mTorr) for 24 h at room temperature and 6 h at 80 °C. ^{1}H solution NMR spectra of digested, activated samples (400 MHz, DMSO-d_6, ppm): 8.64 (s, BTC), 8.12 (s, HCOOH), peak area ratio (BTC:HCOOH) = 6.0:0.04. Anal. Calcd for $Zr_6C_{18}H_{42.4}O_{16.2}S_{2.3}$ = $[Zr_6O_{5.6}(OH)_{2.4}(C_9H_3O_6)_2(SO_4)_{2.3}](H_2O)_{17}$: C, 13.35; H, 2.64; S, 4.55%. Found: C, 13.28; H, 2.61; S, 4.45%.

MOF-808-0.65SO_4 microcrystalline powder. Activated MOF-808-P microcrystalline powder (0.50 g, 0.37 mmol) was immersed in 50 mL of 0.005 M sulfuric acid (0.25 mmol) for 24 h during which time the mixture was stirred about once every two hours. The solution was then decanted and the remaining solid material was then solvent exchanged with 50 mL water for

three days (water exchanged three times per day), quickly exchanged with 5 × 50 mL anhydrous acetone and immersed in 50 mL anhydrous chloroform for three days during which time chloroform was exchanged three times per day. The chloroform-exchanged material was activated under dynamic vacuum (30 mTorr) for 24 h at room temperature and 24 h at 150 °C to afford MOF-808-0.65SO_4 as white powder which was stored under Ar to avoid hydration (Yield: 0.49 g). ^{1}H solution NMR spectra of digested, activated sample (400 MHz, DMSO-d_6, ppm): 8.63 (s, BTC), 8.12 (s, HCOOH), peak area ratio (BTC:HCOOH) = 6.0:3.0. Anal. Calcd for $Zr_6C_{21}H_{13.3}O_{29.6}S_{0.65}$ = $[Zr_6O_{5.7}(OH)_{2.3}(C_9H_3O_6)_2(HCOO)_3(SO_4)_{0.65}](H_2O)$: Zr, 41.87; C, 19.29; H, 1.03; S, 1.59%. Found: Zr, 41.9; C, 19.91; H, 1.11; S, 1.40%.

MOF-808-1.3SO_4 microcrystalline powder. Activated MOF-808-P microcrystalline powder (0.50 g, 0.37 mmol) was immersed in 50 mL of 0.01 M sulfuric acid (0.5 mmol) for 24 h during which time the mixture was stirred about once every two hours. The solution was then decanted and the remaining solid material was then solvent exchanged with 50 mL water for three days (water exchanged three times per day), quickly exchanged with 5 × 50 mL anhydrous acetone and immersed in 50 mL anhydrous chloroform for three days during which time chloroform was exchanged three times per day. The chloroform-exchanged material was activated under dynamic vacuum (30 mTorr) for 24 h at room temperature and 24 h at 150 °C to afford MOF-808-1.3SO_4 as white powder which was stored under Ar to avoid hydration (Yield: 0.47 g). ^{1}H solution NMR spectra of digested, activated sample (400 MHz, DMSO-d_6, ppm): 8.63 (s, BTC), 8.12 (s, HCOOH), peak area ratio (BTC:HCOOH) = 6.0:1.8. Anal. Calcd for $Zr_6C_{19.8}H_{10.2}O_{28.8}S_{1.3}$ = $[Zr_6O_{5.6}(OH)_{2.4}(C_9H_3O_6)_2(HCOO)_{1.8}(SO_4)_{1.3}]$: Zr, 42.18; C, 18.33; H, 0.79; S, 3.20%. Found: Zr, 41.8; C, 19.01; H, 0.96; S, 3.04%.

MOF-808-2.3SO_4 microcrystalline powder. Activated MOF-808-P microcrystalline powder (0.50 g, 0.37 mmol) was immersed in 50 mL of 0.05 M sulfuric acid (2.5 mmol) for 24 h during which time the mixture was stirred about once every two hours. The solution was then decanted and the remaining solid material was then solvent exchanged with 50 mL water for three days (water exchanged three times per day), quickly exchanged with 5 × 50 mL anhydrous acetone and immersed in 50 mL anhydrous chloroform for three days during which time chloroform was exchanged three times per day. The chloroform-exchanged material was activated under dynamic vacuum (30 mTorr) for 24 h at room temperature and 24 h at 150 °C to afford MOF-808-2.3SO_4 as white powder which was stored under Ar to avoid hydration (Yield: 0.48 g). ^{1}H solution NMR spectra of digested, activated sample (400 MHz, DMSO-d_6, ppm): 8.63 (s, BTC), 8.11 (s, HCOOH), peak area ratio (BTC:HCOOH) = 6.0:0.2. Anal. Calcd for $Zr_6C_{18.2}H_{13}O_{31.6}S_{2.3}$ = $[Zr_6O_{5.2}(OH)_{2.8}(C_9H_3O_6)_2(HCOO)_{0.2}(SO_4)_{2.3}](H_2O)_2$: Zr, 40.29; C, 16.09; H, 0.96; S, 5.43%. Found: Zr, 39.9; C, 16.69; H, 0.79; S, 5.47%.

MOF-808-2.5SO_4 microcrystalline powder. Activated MOF-808-P microcrystalline powder (0.50 g, 0.37 mmol) was immersed in 50 mL of 0.1 M sulfuric acid (5 mmol) for 24 h during which time the mixture was stirred about once every two hours. The solution was then decanted and the remaining solid material was then solvent exchanged with 50 mL water for three days (water exchanged three times per day), quickly exchanged with 5 × 50 mL anhydrous acetone and immersed in 50 mL anhydrous chloroform for three days during which time chloroform was exchanged three times per day. The chloroform-exchanged material was activated under dynamic vacuum (30 mTorr) for 24 h at room temperature and 24 h at 150 °C to afford MOF-808-2.5SO_4 as white powder which was stored under Ar to avoid hydration (Yield: 0.48 g). ^{1}H solution NMR spectra of digested, activated sample (400 MHz, DMSO-d_6, ppm):

8.63 (s, BTC), 8.12 (s, HCOOH), peak area ratio (BTC:HCOOH) = 6.0:0.05. Anal. Calcd for $Zr_6C_{18}H_{14}O_{32.5}S_{2.5}$ = $[Zr_6O_5(OH)_3(C_9H_3O_6)_2(SO_4)_{2.5}](H_2O)_{2.5}$: Zr, 39.73; C, 15.69; H, 1.02; S, 5.82%. Found: Zr, 39.9; C, 15.85; H, 1.18; S, 5.62%.

Characterization of Acidity in MOFs:

Hammett indicator tests. A set of stock Hammett indicator solutions (0.5 wt%) was prepared in an inert atmosphere glovebox by dissolving Hammett indicators (Table 3.1) in anhydrous benzene. Hammett indicator stock solution (5 mL) was added to 20 mg of each activated MOF-808-xSO_4 sample in a 20-mL glass vial in the glovebox. The suspension was swirled every 30 mins, and after 4 h the color of the solid was then recorded (Table 3.1).

^{31}P MAS NMR Characterizations. About 200 mg of each MOF sample was placed in a Pyrex cell equipped with a stopcock. The sample was then outgassed under vacuum at 150 °C for 24 h, and 3.0 mL of 0.2 M trimethylphosphine oxide (TMPO) in dichloromethane was then added to the sample cell inside an inert atmosphere glovebox. After thoroughly mixing the TMPO solution and the MOF sample, the dichloromethane was removed under vacuum, first at room temperature for 24 h and then at 50 °C for 8 h. The sample was then transferred, inside the glovebox, into a 4 mm (o.d.) Bruker ZrO_2 NMR sample rotor with a gastight cap.[11]

Solid-state nuclear magnetic resonance (SSNMR) spectra were acquired on a Bruker Avance-500MHz NMR spectrometer using a standard Bruker double resonance magic angle-spinning (MAS) probe. The magic angle was adjusted by maximizing the number and amplitudes of the signals of the rotational echoes observed in the ^{79}Br MAS FID signal from KBr. The transmitter frequency was 202.46 MHz. High-power two-pulse phase modulation (TPPM) ^{1}H heteronuclear decoupling was applied for ^{31}P NMR data acquisition.[12] A 90^o ^{31}P pulse (6.75 □s) was used and the ^{1}H decoupling field corresponded to 30 kHz. The recycling delay between scans was 60s, and the sample spinning rate was 10 kHz. The ^{31}P chemical shifts were externally referenced to an 85% H_3PO_4 aqueous solution (as zero ppm).

To afford quantitative determination of acid sites, each TMPO-loaded sample was also subject to elemental analysis by ICP-OES. The assignments of ^{31}P NMR resonances, namely their chemical shifts and relative distributions (i.e., their corresponding integrated areas) in each spectrum were achieved by simulation using the Gaussian Deconvolution method using a Win-NMR software program (Bruker Topspin) allowed for curve fitting through appropriate choices of ^{31}P NMR peaks based on observed resonance lineshape. The chemical shifts, distributions and concentrations of acid sites derived in conjunction with elemental analyses by ICP-OES are depicted in Table A3.2.

^{1}H MAS NMR Characterizations. All ^{1}H MAS solid-state NMR experiments were carried out on a Bruker AV-500 spectrometer operating at a Larmor frequency of 500.2 MHz using a single-pulse sequence with a pulse width of 4 μs, a recycle delay of 60s, and a sample spinning rate of 12kHz. Tetramethylsilane was taken as an external reference for the ^{1}H NMR chemical shift. Prior to the NMR experiment, each sample was subjected to activation treatment under dynamic vacuum at 150 ^{o}C for 24 hours and was then transferred to 4 mm ZrO_2 rotor in glovebox. The assignments of ^{1}H NMR resonances, namely their chemical shifts and relative distributions (i.e., their corresponding integrated areas) in each spectrum were achieved by simulation using the Gaussian Deconvolution method using a Win-NMR software program (Bruker Topspin) allowed for curve fitting through appropriate choices of ^{1}H NMR peaks based on observed resonance lineshape.

Acetonitrile adsorption measurements. Acetonitrile vapor adsorption isotherms were measured in-house on a BEL Japan BELSORP-aqua3. Prior to the vapor adsorption measurements, acetonitrile-d_3 (analyte) was flash frozen under liquid nitrogen and then evacuated under dynamic vacuum at least five times to remove any gases in the liquid reservoir. The measurement temperature was controlled with a water circulator. Helium was used for the estimation of dead space for gas and water adsorption measurements. Ultra-high-purity grade He gas (Praxair, 99.999% purity) was used throughout the experiments.

Each sample is measured for three consecutive cycles, and the sample was evacuated for 2 h at 25 °C between the cycles. After the measurement, sample of MOF-808-P and MOF-808-2.5SO_4 were further evacuated for 2 h at 25 °C, before being transferred to 4 mm ZrO_2 rotor in glovebox and subjected to ^{1}H MAS NMR measurements.

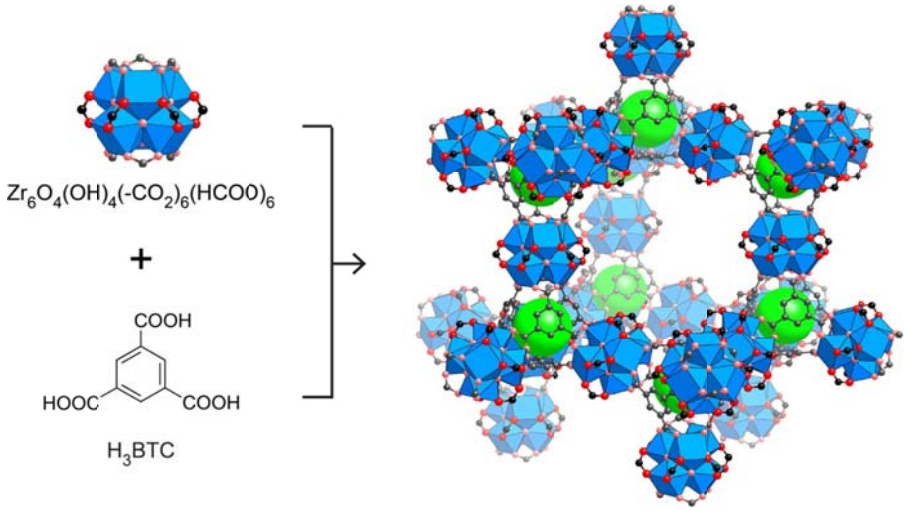

Figure 3.2. $Zr_6O_4(OH)_4(-CO_2)_6(HCOO)_6$ secondary building units (SBUs) are combined with BTC linkers to form MOF-808, which has a porous, three-dimensional framework containing large adamantane-shaped cages (open) and small tetrahedral cages (filled with green spheres). Atom labeling scheme: formate carbon and oxygen atoms, black and red spheres, respectively; other carbon and oxygen atoms, grey and pink spheres, respectively; Zr coordination polyhedra, blue. Hydrogen atoms are omitted for clarity.

Results and Discussion

Controllable sulfation of MOF-808. Zirconium MOFs have been shown to have exceptional chemical stability in acidic media,[3c,8] and therefore serve as ideal materials for use in the production of sulfate-promoted superacids in MOFs. A close examination of the crystal structure of MOF-808[9] has revealed that each Zr-SBU, $Zr_6O_4(OH)_4(-CO_2)_6(HCOO)_6$, is linked to six BTC units to form a three-dimensional porous framework containing two different types of pores (Figure 3.2). The smaller, tetrahedral pore is inaccessible to guests because of its small, 1.2-Å aperture diameter, while the larger, adamantane-shaped pore has much larger internal pore and aperture diameters of 18 and 14 Å, respectively. Since all the formate ligands are accessible through the large pore, we believed they could be replaced by sulfate ligands. Furthermore, the

formate ligands would be far more reactive than the BTC linkers since they are connected to only one as opposed to three zirconium SBUs.

Our studies were carried out on a new microcrystalline form of MOF-808 designated MOF-808-P, which was prepared on a 5-gram scale using a modified version of the single-crystal MOF-808 synthesis.[9] MOF-808-P formed more rapidly than MOF-808 and was obtained as powders of 200-800 nm-sized, octahedral microcrystals (Figure 3.3a). Phase purity and porosity were established using powder X-ray diffraction (PXRD) and nitrogen sorption measurements (Figures 3.3b and 3.3c), respectively, and its chemical composition was found to include five instead of six formate ligands per Zr SBU using elemental analysis and integrated ^{1}H NMR spectra of samples digested in a mixture of HF and DMSO-d_6. It is likely that the missing formate group was replaced by the solvent used in the synthesis (DMF) or water, which were removed later in the activation process.

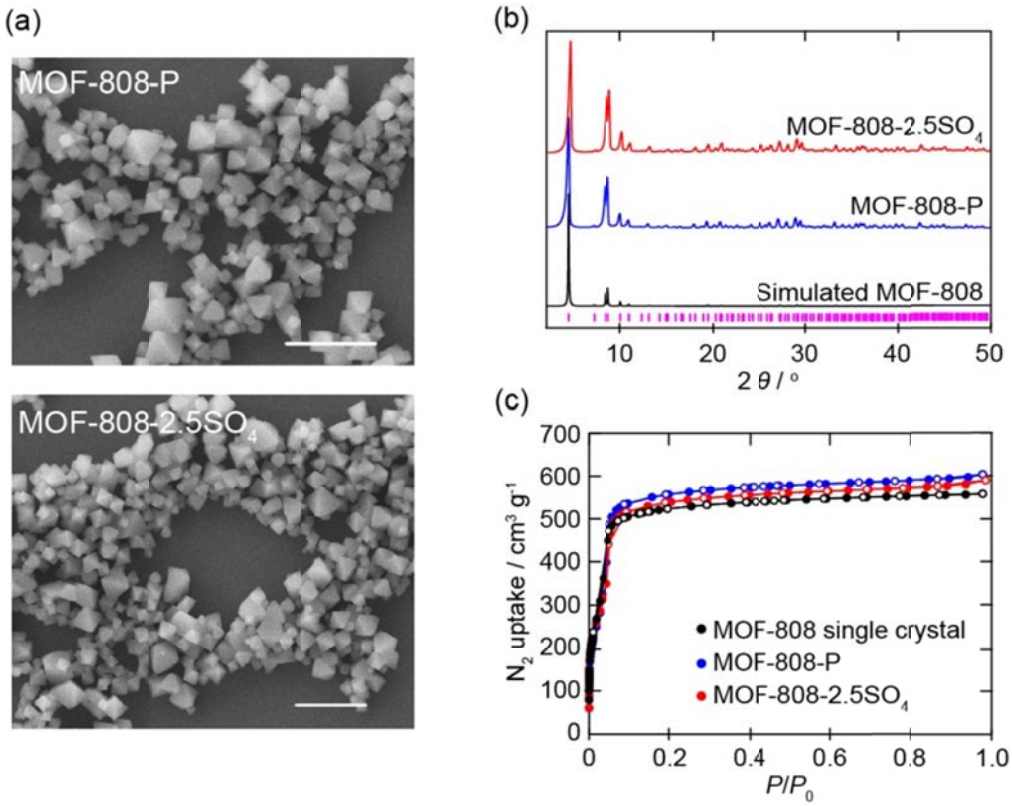

Figure 3.3. (a) Scanning electron microscopy (SEM) images for MOF-808-P and MOF-808-2.5SO_4 (scale bar: 2 μm). (b) Comparison of experimental powder X-ray diffraction patterns of MOF-808-P (blue) and MOF-808-2.5SO_4 (red) with simulated pattern (black) calculated from the single-crystal structure of MOF-808.[9] (c) Nitrogen adsorption isotherms for MOF-808 single crystal (black), MOF-808-P (blue) and MOF-808-2.5SO_4 powder (red) at 77K with adsorption and desorption branches represented by closed and open circles, respectively. P/P_0, relative pressure.

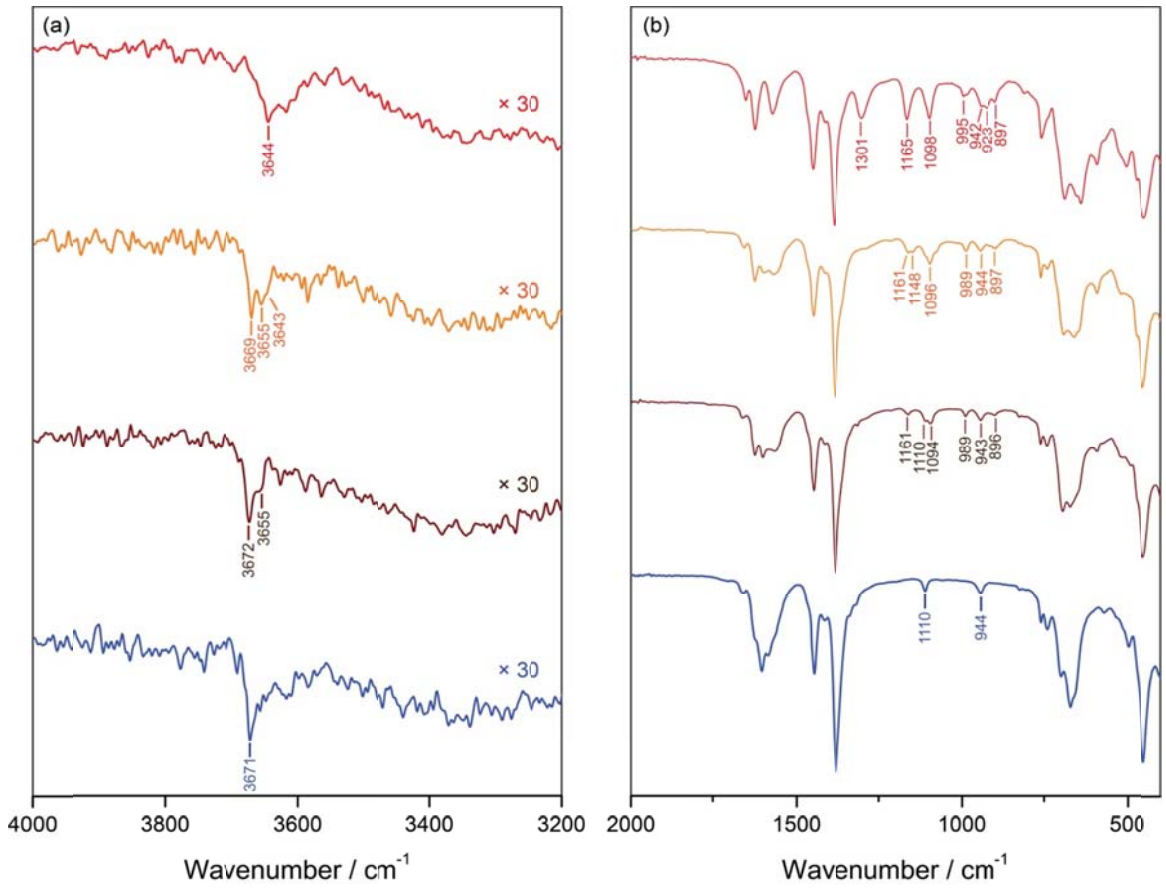

Figure 3.4. Infrared spectra of activated MOF-808-P (blue), MOF-808-0.65SO_4 (wine), MOF-808-1.3SO_4 (orange) and MOF-808-2.5SO_4 (red) recorded at room temperature, showing the absorption bands at 3700–3600 cm^{-1} (a) and 1300–900 cm^{-1} (b).

Sulfation of MOF-808-P was achieved by submersion in different concentrations of aqueous sulfuric acid for one day. In each case, 500 mg of MOF-808-P was added to 50 mL of 0.005-0.1 M aqueous sulfuric acid and the resulting suspension was stirred for one minute about once every two hours. The crystal shape and color of these crude products were the same as those of MOF-808-P according to scanning electron microscopy (SEM) (Figure A3.2) and optical microscopy. These crude reaction products were washed with acetone and chloroform and then dried at ambient and elevated temperature under vacuum to obtain final products, which were stored in an inert atmosphere to avoid hydration. The final products displayed PXRD patterns coincident with those of the original unsulfated MOF-808-P material and, remarkably, nearly identical porosities (Figures 3.3b and 3.3c, Figures A3.9-A3.12). Their formula were determined using elemental analysis and integrated solution ^{1}H NMR spectra of digested samples. Replacement of formate by sulfate was also monitored in this fashion, and the different materials were designated MOF-808-xSO_4, x = 0.65, 1.3, 2.3, and 2.5, where x = number of sulfate groups per SBU. It is found that when less than 0.5 equiv. of sulfuric acid respect to formate ligands was added, i.e. in the cases of MOF-808-0.65SO_4 and MOF-808-1.3SO_4, an almost quantitative incorporation of sulfates with roughly twice that amount of formate content decrease was observed. Furthermore, when the amount of sulfuric acid went beyond that number, as in the cases of MOF-808-2.3SO_4 and MOF-808-2.5SO_4, approximately 2.5 sulfur atoms per zirconium

SBU are incorporated, and only a trace amount of formate ligands were seen in the ^{1}H NMR spectra of digested samples. The crystallinity, porosity, and superacidity of the sulfated frameworks could not be obtained if the aqueous solvent was removed directly from the pores of the initial reaction product by application of heat and vacuum. Instead, they required removal of the water molecules in the MOF pores by solvent exchange with acetone and chloroform followed by evacuation, first at room temperature and then at elevated temperature.

Initial evidence for metal-bound sulfate groups was obtained from infrared spectra of sulfated MOFs MOF-808-xSO_4. As shown in Figure 3.4, characteristic bands were observed in spectra of MOF-808-xSO_4 samples between 800 and 1500 cm^{-1} that were not observed in those of unsulfated MOF-808-P and could be assigned to sulfate ligands. New bands appear in MOF-808-0.65SO_4 and MOF-808-1.3SO_4 at 1216, 1161, 1095, 989 and 896 cm^{-1}, with the first four bands assigned to ν_3 and ν_1 modes of bidentate SO_4^{2-} ion in C_{2v} symmetry, and the fifth band also observed in sulfate ion-promoted zirconia material.[13] In MOF-808-2.5SO_4, extra bands at 1301 and 923 cm^{-1} appeared, which could be explained as multiple sulfur species present. Besides, at the ν(OH) region (4000–3000 cm^{-1}), the minor but sharper band at 3672 cm^{-1} corresponding to the isolated μ_3-OH groups on the zirconium secondary building unit,[14] was identified, but shifted to 3640 cm^{-1} in MOF-808-2.5SO_4, indicating change of the protonic acidity.

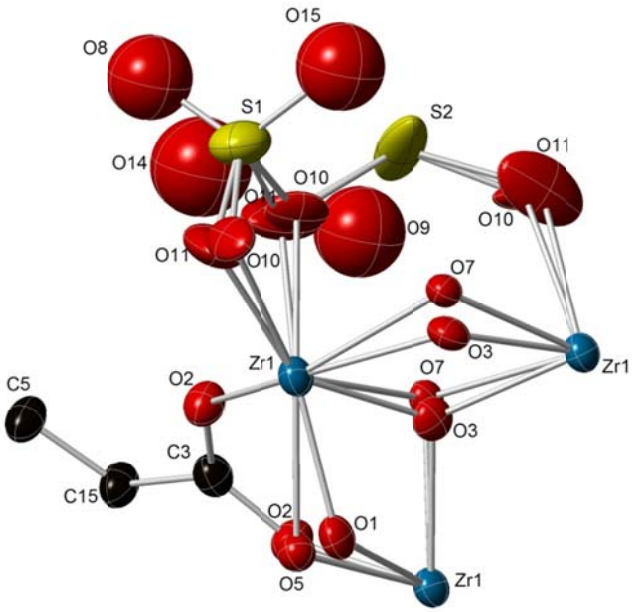

Figure 3.5. ORTEP representation (50% probability) showing more than the asymmetric unit of MOF-808-2.3SO_4.

MOF-808-2.3SO_4 single crystal. An X-ray diffraction study of a MOF-808-2.3SO_4 single crystal provided unequivocal evidence for metal-bound sulfate groups incorporated into a crystalline, porous MOF.

A single crystal of partially activated MOF-808-2.3SO_4 was selected and mounted in a cryoloop. Diffraction data covering a sphere of the reciprocal space was collected on Bruker

ApexII CCD detector using synchrotron radiation with $\lambda = 0.7749$ Å. Unit cell parameters were determined with a set of 300 reflections with $(I)/\sigma(I) > 10$. After data reduction and absorption correction, the structure was solved with direct methods as implemented in ShelXS. Full-matrix least-squares on F^2 were carried out using ShelXL and OLEX2.[15]

All framework atoms were located and refined anisotropically. As shown in Figure 3.5, two independent positions were assigned to the μ_3 oxygen atoms, which correspond to either μ_3-O (O7 and O5) or μ_3-OH (O1 and O3) groups, consistent with our previous findings.[9] The chemical occupancy of these oxygen atoms was therefore fixed to 0.5.

Two symmetrically independent positions, S1 and S2, were assigned to the sulfur atoms of the sulfate groups, and their chemical occupancy was first refined and then fixed to a value of 0.2.

An oxygen atom coordinated to the zirconium atoms in the SBU was disordered over two positions (O10 and O11) with partial occupancy of 0.5 for each position. This atom belongs to either one of the two sulfate groups or to a terminal ligand when the sulfate group is not present.

Two additional oxygen atoms, O8 and O15, were located, completing the sulfate group of S1. The occupancy values of these two atoms were fixed to be the same as the one of the corresponding sulfur atom. These oxygen atoms were refined isotropically. Anisotropic refinement resulted in large anisotropic displacement parameters (ADP), suggesting disorder. The bond distances and angles of the sulfur and oxygen atoms of this sulfate group are in the expected ranges.

In the case of the sulfate group corresponding to sulfur atom S2, only the position of the oxygen atoms coordinating to the zirconium atoms could be located. However, an area of residual electron density was observed in the vicinity of the sulfur atom and at a position expected for the missing oxygen atoms. Attempts to assign and refine the positions of these two oxygen atoms were unsuccessful, suggesting that this sulfate group exhibits disorder over several positions which could not be resolved due to low occupancies at these positions.

Finally, several areas of residual electron density were found inside the framework pores. Since the sample was not fully activated at 150 °C prior to the single crystal measurement, we attribute this electron density to organic solvent and/or water molecules left in the pores upon activation or those were adsorbed during the sample mounting in ambient conditions.

Overall, the found electron density in MOF-808 indicates approximately 2.4 bound sulfates per Zr SBU, in a good agreement with the obtained results from elemental analysis for the same sample.

Characterization of acidity in sulfated MOF-808. The successful sulfation of Zr-MOF, MOF-808, with different sulfate loadings in a controllable manner revealed the necessity to further evaluate the acidity of them.

Typically, the characterization of acidity in solid acid materials requires to address the following questions: (i) What type of acid sites are present (Brønsted, Lewis, or both)? (ii) What is the acid strength? and (iii) What is the acid concentration? In order to answer these questions, a number of techniques have been used to characterize the surface acidity, and several of which were used in this work to study the acidity in sulfated MOF-808 materials.

Hammett indicator tests. The acidity of a material is defined relative to a base used in acid-base interaction. Therefore, the solid Brønsted acid is defined as a solid which protonates or at

least partially transfers protons to a base. By use of an appropriate series of bases, in other words, indicators, the acidity scale is given by the Hammett acidity function H_0.[5] The H_0 scale can be understood as an extrapolation of the pH scale from diluted aqueous media to all media, with a similar written form definition:

$H_0 = pK_a + \log [B]/[HB^+]$

where [B] and $[HB^+]$ are the concentrations of the indicator in its base and acid form, respectively.

The acid strength of a solid acid can be qualitatively estimated using a series of indicators, known as Hammett indicators,[16] which will have a bright color in their conjugated acid form that is intense enough to mask the color of their base form.[17] If immersion of a solid in a specific indicator solution changes the color of the solid to that of the acid form of the indicator, the H_0 value of the solid is the same as or is lower than the pK_a value of the conjugate acid of the indicator.[7e,8]

As shown in Table 3.1, while the pristine MOF-808-P and MOF-808-0.65SO_4 display relatively low acidity ($H_0 \leq -2.8$) and moderate acidity ($-4.4 \leq H_0 \leq -5.9$), respectively, MOF-808-1.3SO_4 and MOF-808-2.5SO_4 displayed color change even in a solution of 2,4-dinitrofluorobenzene in benzene, yielding a H_0 value of ≤ -14.5. This places these MOFs in the superacid regime ($H_0 \leq -12$). Additionally, all samples showed low acidity ($H_0 \leq -2.8$) after exposing to ambient air, which could be explained as neutralization of the superacidity by moisture.

^{31}P MAS NMR Characterizations. ^{31}P MAS NMR technique developed using trialkylphosphine oxides as probe molecules has been shown to be sensitive, reliable and versatile to provide the types (Brønsted or Lewis acidity), distribution and strength of acid sites in various solid acids.[18] Trimethylphosphine oxide (TMPO; kinetic diameter ca. 5.5 Å) was chosen as a probe because of its suitable size for diffusion into MOF pores. TMPO is known to complex to both Brønsted and Lewis acid sites. The ^{31}P chemical shift of adsorbed TMPO on Brønsted acid site moves down-field with the increase of acid strength.[18] ^{31}P MAS NMR spectrum of TMPO adsorbed on MOF-808-P and MOF-808-xSO_4 samples are shown in Figure 3.6. For MOF-808-P, the two resonances assigned to adsorbed TMPO appeared at 62 ppm and 56 ppm, while a third resonance assigned to free TMPO trapped in the MOF pores appeared at 43 ppm.[18] The same three resonances were observed in spectra of MOF-808-0.65SO_4, albeit with different relative intensities. In addition, a new resonance appeared at 69 ppm in spectra of MOF-808-1.3SO_4 and MOF-808-2.5SO_4. Since the appearance of this new peak correlates with the observation of alpha-pinene conversion, the 69 ppm resonance was assigned to TMPO adsorbed on a strongly acidic site. In good agreement with this conclusion, exposure of MOF-808-2.5SO_4 to atmospheric moisture caused the 69 ppm resonance to lose almost all of its intensity in the same way that MOF-808-2.5SO_4 loses of its ability to display Hammett superacidity after exposure to atmospheric moisture.

Table 3.1. Hammett Indicators and Acidity of MOF-808-xSO_4 Measured by Hammett Indicator Tests.

Indicators	Color[a]		pK_a[a]	Hammett Indicator Tests[b]			
	Acid Form	Base Form		MOF-808-P	MOF-808-0.65SO_4	MOF-808-1.3SO_4	MOF-808-2.5SO_4
4-Phenylazoaniline	Red	Orange	+2.8	–	+	+	+
2-Nitroaniline	Red	Yellow	-0.2	–	+	+	+
4-Nitrodiphenylamine	Red	Yellow	-2.4	–	+	+	+
2,4-Dichloro-6-nitroaniline	Red	Yellow	-3.2	–	+	+	+
2,4-Dinitroaniline	Red	Yellow	-4.4	–	+	+	+
2-Benzoylnaphthalene	Yellow	Colorless	-5.9	–	–	+	+
2-Bromo-4,6-dinitroaniline	Red	Yellow	-6.6	–	–	+	+
Anthraquinone	Yellow	Colorless	-8.1	–	–	+	+
4-Nitrotoluene	Yellow	Colorless	-11.4	–	–	+	+
4-Nitrofluorobenzene	Yellow	Colorless	-12.4	–	–	+	+
2,4-Dinitrotoluene	Yellow	Colorless	-13.8	–	–	+	+
2,4-Dinitrofluorobenzene	Yellow	Colorless	-14.5	–	–	+	+

[a] See ref 5,7e,8.
[b] Results of Hammett indicator tests are denoted as color change observed (+) and color change not observed (-).

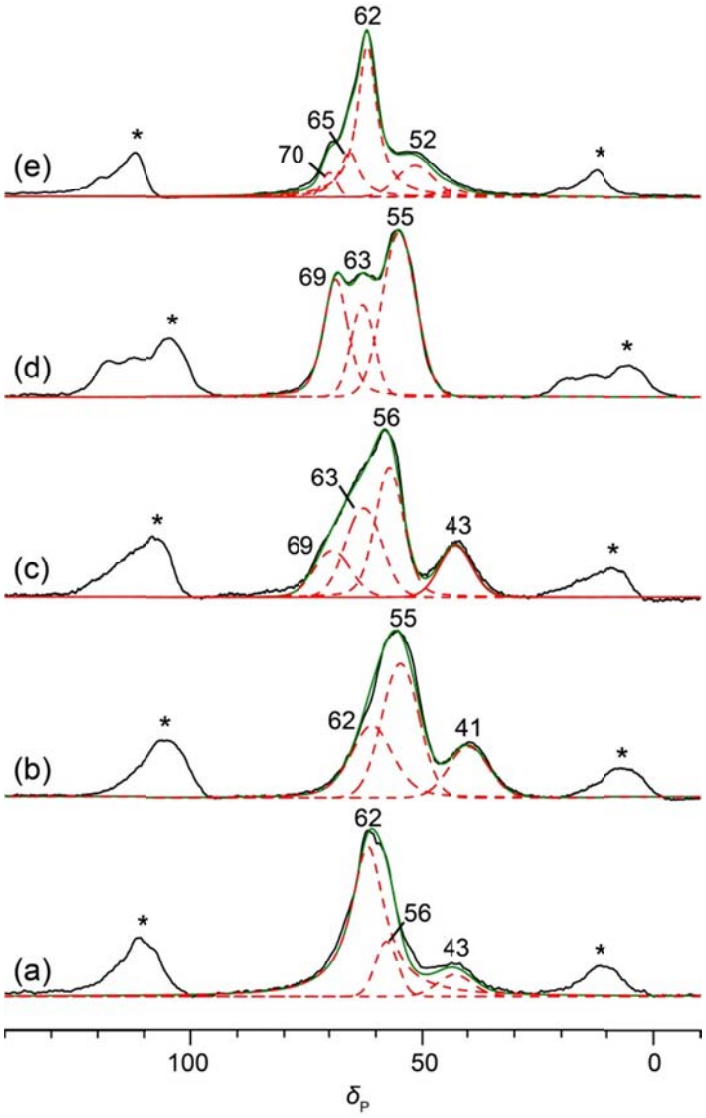

Figure 3.6. ^{31}P MAS NMR spectra of TMPO loaded on MOF-808-P (a), MOF-808-0.65SO_4 (b), MOF-808-1.3SO_4 (c), MOF-808-2.5SO_4 (d) and MOF-808-2.5SO_4 exposed to atmosphere moisture (e). Experimental spectra are shown in black, deconvoluted peaks in red dash, and the sum of the deconvoluted peaks in green. The asterisks denote spinning sidebands.

^{1}H MAS NMR Characterizations. Direct characterization of Brønsted acidic protons is commonly achieved using ^{1}H MAS NMR of solid samples. Despite the highly sensitive nature of ^{1}H chemical shift to proton's chemical environment, the movement of ^{1}H chemical shift towards down-field indicates a more acidic proton. ^{1}H MAS NMR spectrum of activated MOF-808-P and MOF-808-2.5SO_4 are shown in Figure 3.7.The ^{1}H MAS NMR spectrum of MOF-808-P contains four main resonances. Two resonances assigned to H atoms on BTC linker and formates appeared at 9.0 ppm and 8.0 ppm and the other two resonances are assigned to H atoms on μ_3-OH of the Zr SBU. A rough peak area ratio after Gaussian deconvolution indicates the

6.0:4.8:3.3 for H atoms on BTC linker, formate ligands, and μ_3-OH's (two resonances combined). This ratio is a good match of measured formula of MOF-808-P.

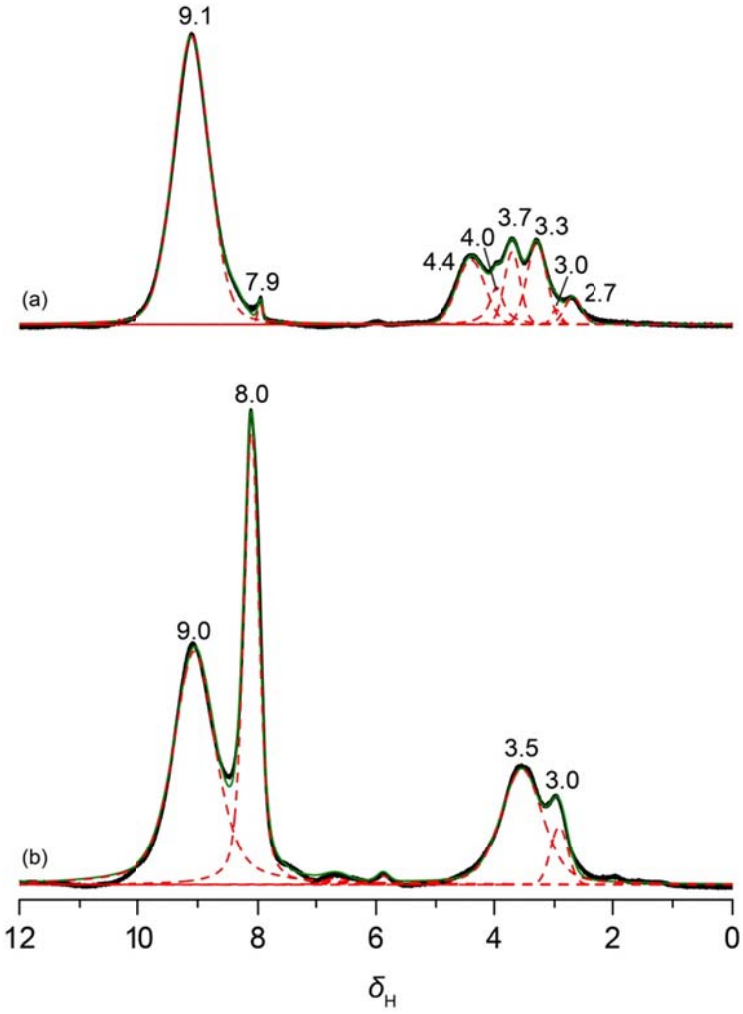

Figure 3.7. ^{1}H MAS NMR spectra of activated MOF-808-P (a) and MOF-808-2.5SO_4 (b). Experimental spectra are shown in black, deconvoluted peaks in red, and the sum of the deconvoluted peaks in green.

The sulfuric acid treatment significantly changed the spectrum of MOF as shown in Figure 3.7b. First, only trace amount of formate ligands were found left in MOF-808-2.5SO_4, which explains the small resonance at 7.9 ppm, in good agreement with the quantitative substitution of the formate ligands by sulfate groups. Also, six major resonances were observed at high-field region, at 4.4, 4.0, 3.7, 3.3, 3.0 and 2.7 ppm. However, despite extensive efforts, we were not able to assign these peaks confidently. It would be very interesting if these protons could be assigned, as we believe, the strong acidic proton that is introduced by sulfation of the Zr SBU is among them.

Acetonitrile adsorption measurements. Adsorption of volatile bases such as NH_3, pyridine, n-butylamine, to mention a few, can be used to determine the number of acid sites on solid acid materials. Typically, this is done by exposing solid acid materials to an excess amount of basic molecules followed by removal of those physisorbed ones by evacuation over a long time period. Whatever is left on the surface is considered to be chemisorbed, with the amount equal to that of the acid sites in the solids and acid strength related to the heat of adsorption or the temperature required for desorption, measured by calorimetry[19] and temperature programmed desorption (TPD)[20] using commercially available calorimeter and chemisorption analyzer, respectively.

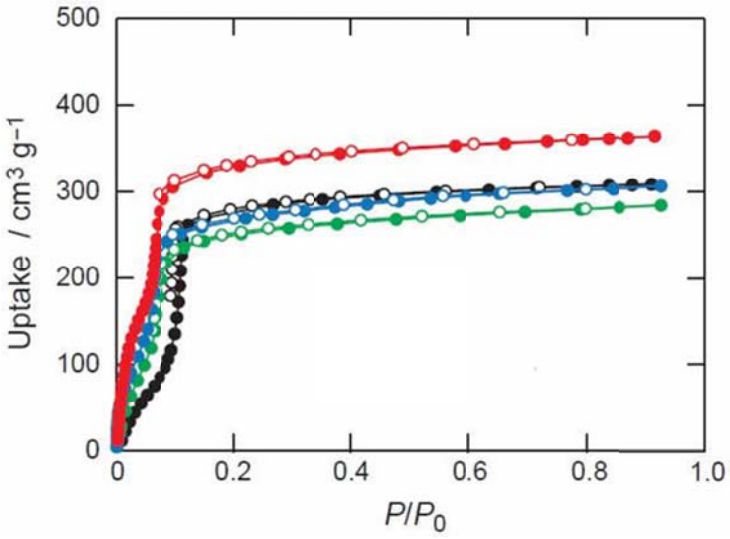

Figure 3.8. Acetonitrile-d_3 isotherms of MOF-808-P (black), MOF-808-0.65SO_4 (green), MOF-808-1.3SO_4 (blue), and MOF-808-2.5SO_4 (red) measured at 25 °C with adsorption and desorption branches represented by closed and open circles, respectively. P/P_0, relative pressure.

These methods, although frequently adopted for the characterization of inorganic solid acids, is to date not applicable to Brønsted acidic MOFs since the desorption temperature for protonated NH_3 or pyridine are generally above 400 °C, a temperature that is shown to decompose the MOFs. Thus we are now focusing on less basic molecules (e.g. acetonitrile) for probing the acidity in MOFs by gas sorption techniques.

Acetonitrile is a small molecule with low basicity (pK_b = 24) that appears an attractive probe for acidity in solids. The acetonitrile-d_3 isotherm of MOF-808-P measured at 25 °C is shown in Figure 3.8, black circles. The adsorbed amount of acetonitrile gradually increases with increasing pressure up to P/P_0 = 0.10, followed by abrupt acetonitrile uptake in the pressure range from P/P_0 = 0.10 to 0.13, with maximum uptake of 300 cm^3 g^{-1} at P/P_0 = 0.9. A different trend is observed by MOF-808-0.65SO_4 (Figure 3.8, green circles), characterized by the significant adsorption below P/P_0 = 0.05, indicating a higher acetonitrile affinity for this material compared to MOF-808-P. This is a sign of acidic sites within this material. The abrupt acetonitrile uptake also reveals itself at a lower P/P_0, now ranging from P/P_0 = 0.05 – 0.1. This uptake step is attributed to the micropore-filling by acetonitrile molecules, a lower relative pressure would indicate smaller pores, which is also consistent with our observation of a strong adsorbed first layer in

MOF-808-0.65SO_4. A similar trend is observed by MOF-808-1.3SO_4 and MOF-808-2.5SO_4 (Figure 3.8), except that the larger uptake is observed at a lower pressure range (P/P_0 = 0 – 0.05), and this strongly adsorbed first layer consists of more and more acetonitrile molecules as more and more sulfate groups are incorporated into the MOF.

The strength of acidic sites is characterized by the ease of dissociation of acetonitrile. To evaluate this factor, the samples were evacuated at 25 °C for 2 hours after the isotherm measurements. Typical pressure in the sample cell after the regeneration process was 5 Pa. We then collected the acetonitrile isotherms up to three cycles for the Zr-MOFs studied here. The isotherms are shown in Figures A3.13-A3.17. The cycling performance results show that for MOF-808-P and MOF-808-0.65SO_4, the uptake for all three cycles are the same. Since we know that MOF-808-P bears only low acidity, it is expected that the mainly physisorbed acetonitrile molecules could be easily removed by evacuation at room temperature. As discussed above, MOF-808-0.65SO_4 is shown to have stronger acidity than that of MOF-808-P, however, the strength of these acidic sites are not strong enough to hold acetonitrile molecules upon low-pressure evacuation.

In both MOF-808-1.3SO_4 and MOF-808-2.5SO_4, we found a significant decrease from the first to the second cycle and a constant uptake thereafter, mainly due to the decreased uptake at lower pressure range (P/P_0 = 0 – 0.05). This behavior can be explained by some acetonitrile molecules being strongly bound to the framework, not being desorbed under the aforementioned regeneration conditions. If this is the case, the acetonitrile release requires further energy input (higher temperature and/or stronger vacuum). Apparently, MOF-808-1.3SO_4 and MOF-808-2.5SO_4 contains acidic sites that are stronger than those of MOF-808-0.65SO_4 as acetonitrile molecules adsorbed in the latter can be removed under this condition, but not all the adsorbed molecules in the former two materials can be removed under the same conditions. This supports the results from above. From the difference of uptake at low pressure between the first two runs, we estimated the concentration of strong acidic sites in MOF-808-1.3SO_4 and MOF-808-2.5SO_4 to be 1.2 and 2.4 mmol g^{-1}, respectively.

Conclusion

In this chapter, we report superacidity in a sulfated metal-organic framework (MOF) obtained by treating the microcrystalline form of MOF-808 [MOF-808-P: $Zr_6O_5(OH)_3(BTC)_2(HCOO)_5$, BTC = 1,3,5-benzenetricarboxylate] with aqueous sulfuric acid to generate its sulfated analogue, MOF-808-2.5SO_4 [$Zr_6O_5(OH)_3(BTC)_2(SO_4)_{2.5}$]. The sulfation process is shown to be controllable with respect to the incorporation of different amount of sulfate groups. The resultant materials are characterized using a indicator, MAS NMR, and vapor sorption techniques for their acidity. We show that the acidity these materials is highly dependent upon the amount of sulfate groups incorporated. The fully sulfated material, MOF-808-2.5SO_4 has a Hammett acidity function $H_0 \leq -14.5$ and is thus identified as a superacid, providing the first evidence for superacidity in MOFs. The superacidity is attributed to the presence of zirconium-bound sulfate groups structurally characterized using single-crystal X-ray diffraction analysis.

Appendices

Table A3.1. Crystal data and structure refinement for MOF-808-2.3SO_4 single crystal (CCDC #: 1027470).

Identification code	MOF-808-2.3SO_4
Empirical formula	$C_{18}H_6O_{41.85}S_{2.40}Zr_6$
Formula weight	1516.09
Temperature/K	100.15
Crystal system	cubic
Space group	Fd-3m
a/Å	35.32 (2)
b/Å	35.32 (2)
c/Å	35.32 (2)
alpha/°	90
beta/°	90
gamma/°	90
Volume/$Å^3$	44078(63)
Z	16
$\rho_{calc/}$ mg mm^{-3}	0.914
Mu/mm^{-1}	0.817
F(000)	11635.0
Crystal size/mm^3	0.01 × 0.01 × 0.02
Radiation	Synchrotron (λ = 0.7749 Å)
2theta range for data collection	5.48 to 60.332°
Index ranges	$-45 \leq h \leq 44$, $-45 \leq k \leq 45$, $-45 \leq l \leq 44$
Reflections collected	97539
Independent reflections	2397 [R_{int} = 0.1869, R_{sigma} = 0.0393]
Data/restraints/parameters	2397/0/104
Goodness-of-fit on F^2	1.092
Final R indexes [I>=2σ (I)]	R_1 = 0.0512, wR_2 = 0.1501
Final R indexes [all data]	R_1 = 0.0763, wR_2 = 0.1662
Largest diff. peak/hole / e $Å^{-3}$	0.86/-0.67

Figure A3.1. Experimental PXRD patterns of microcrystalline powder MOF-808-P (blue), MOF-808-0.65SO_4 (wine), MOF-808-1.3SO_4 (orange), MOF-808-2.3SO_4 (green), MOF-808-2.5SO_4 (red) and simulated pattern (black) from single-crystal X-ray data of MOF-808.[9]

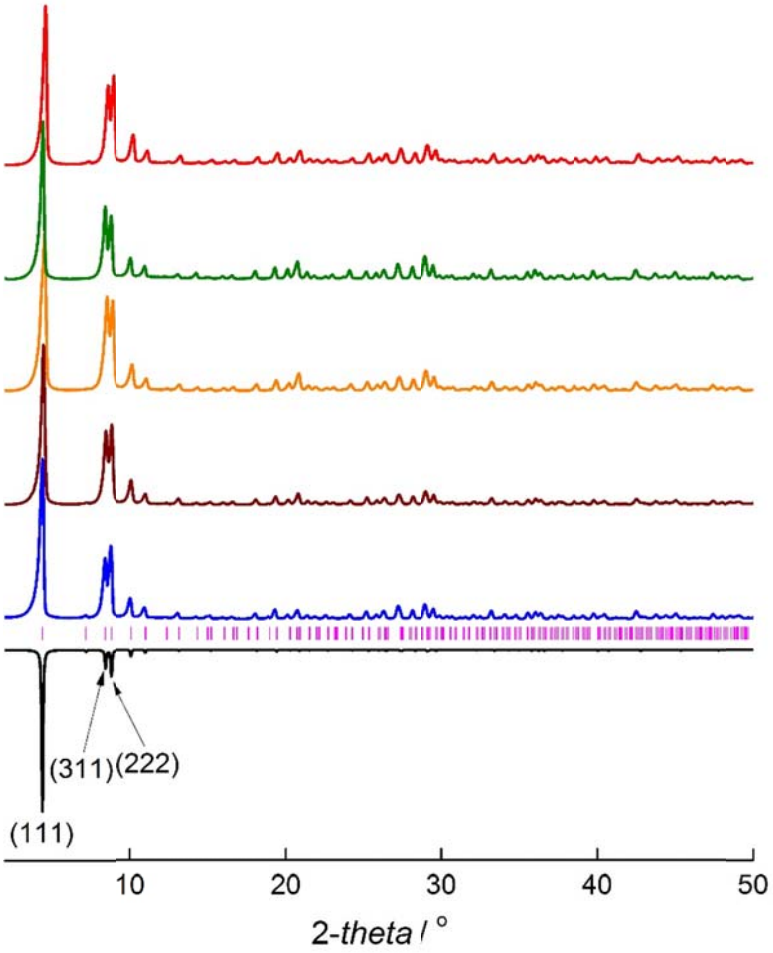

Figure A3.2. Scanning electron microscopy (SEM) images of MOF-808-0.65SO_4 (a), MOF-808-1.3SO_4 (b) and MOF-808-2.3SO_4 (c) (scale bar: 2 μm).

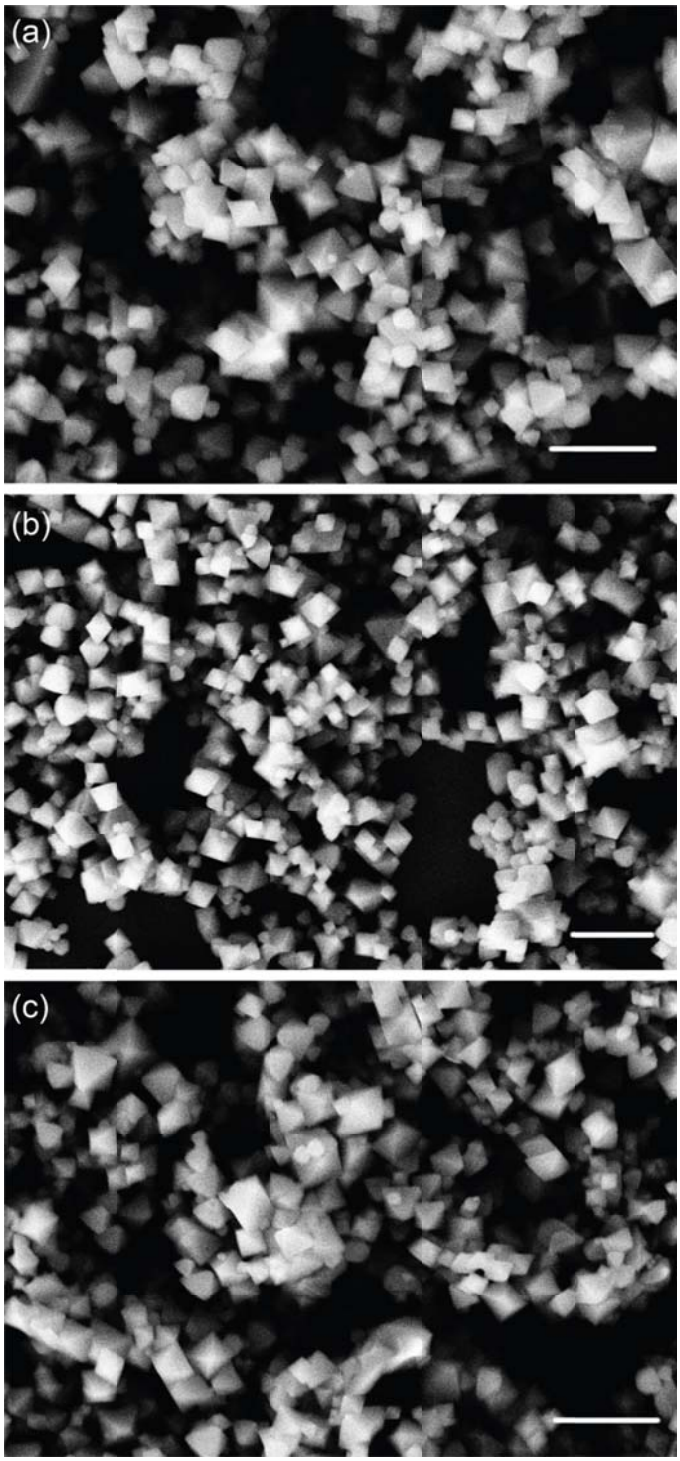

Figure A3.3. TGA trace for activated microcrystalline powder MOF-808-P, heating rate: 5 °C min^{-1} in nitrogen.

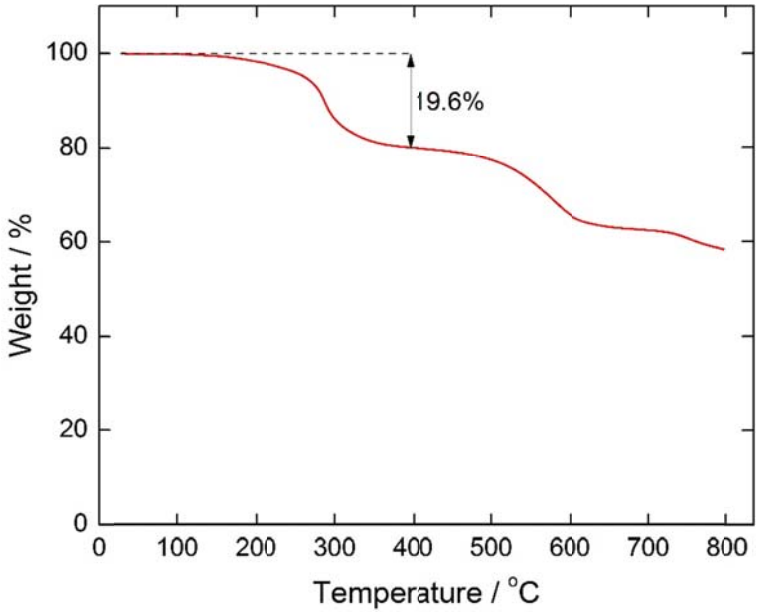

Figure A3.4. TGA trace for activated microcrystalline powder MOF-808-0.65SO_4, heating rate: 5 °C min^{-1} in nitrogen.

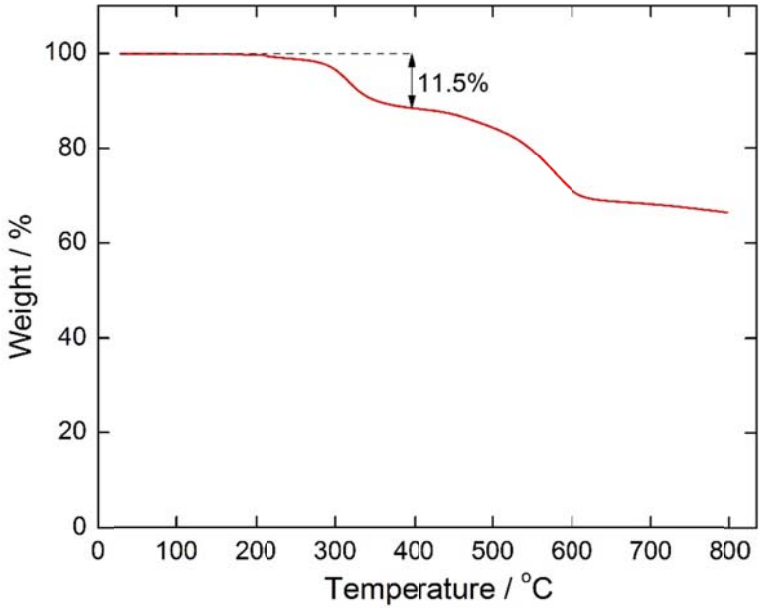

Figure A3.5. TGA trace for activated microcrystalline powder MOF-808-1.3SO_4, heating rate: 5 °C min^{-1} in nitrogen.

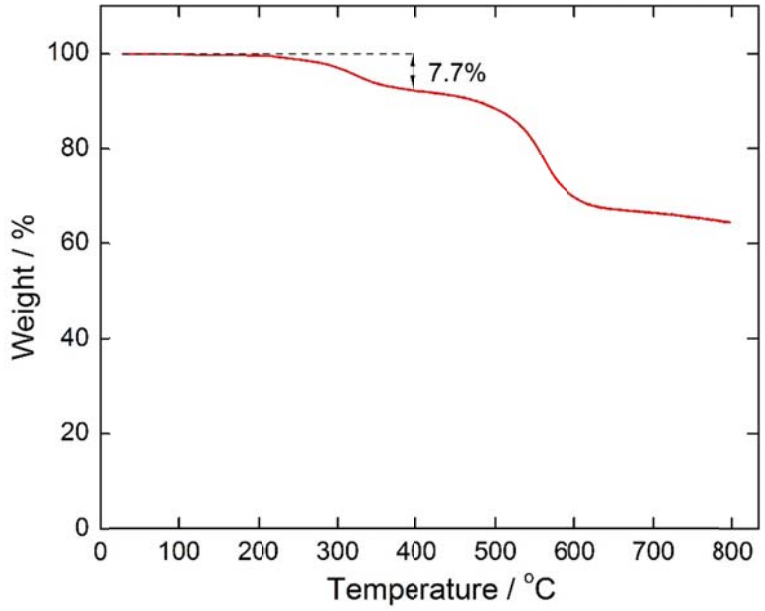

Figure A3.6. TGA trace for activated microcrystalline powder MOF-808-2.3SO_4, heating rate: 5 °C min^{-1} in nitrogen.

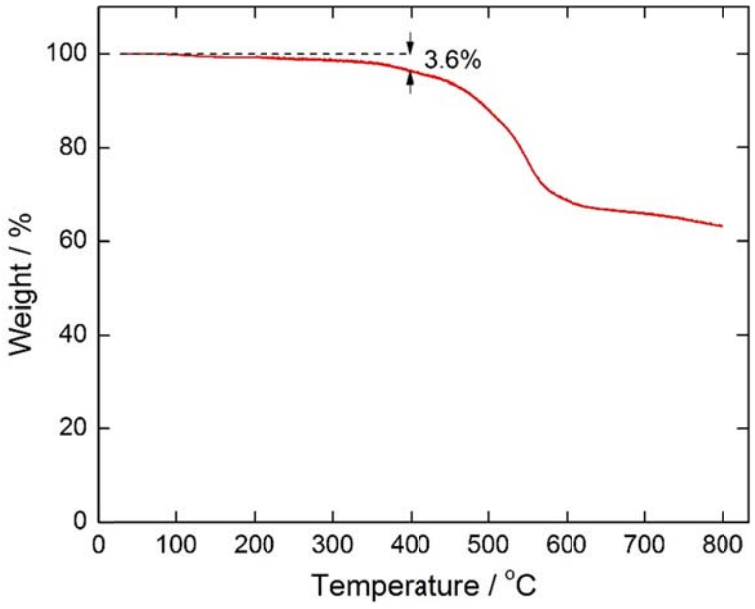

Figure A3.7. TGA trace for activated microcrystalline powder MOF-808-2.5SO_4, heating rate: 5 °C min^{-1} in nitrogen.

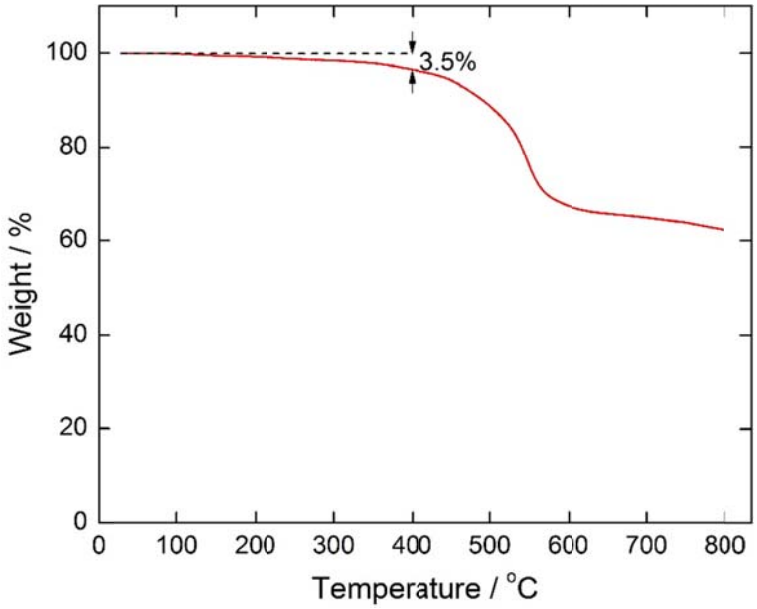

Figure A3.8. N_2 (red) and Ar (blue) isotherms of microcrystalline powder MOF-808-P at 77 K and 87 K, respectively.

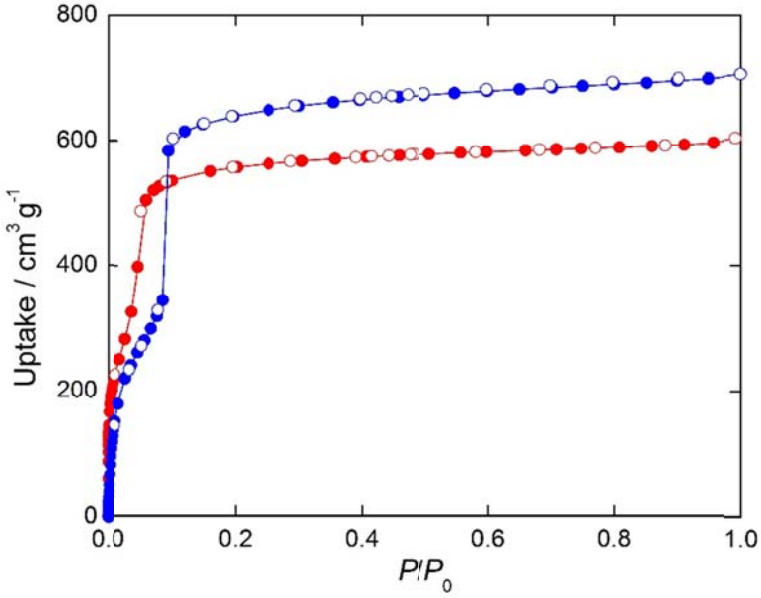

Figure A3.9. N_2 isotherm of microcrystalline powder MOF-808-0.65SO_4 at 77 K.

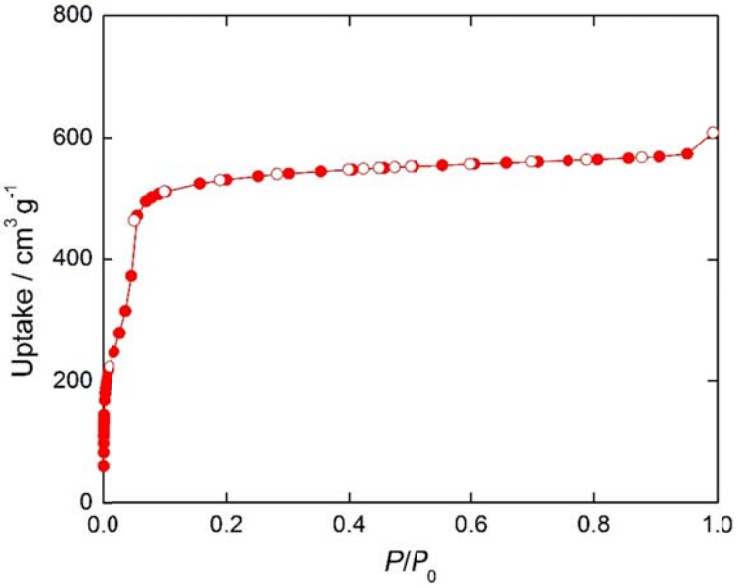

Figure A3.10. N_2 isotherm of microcrystalline powder MOF-808-1.3SO_4 at 77 K.

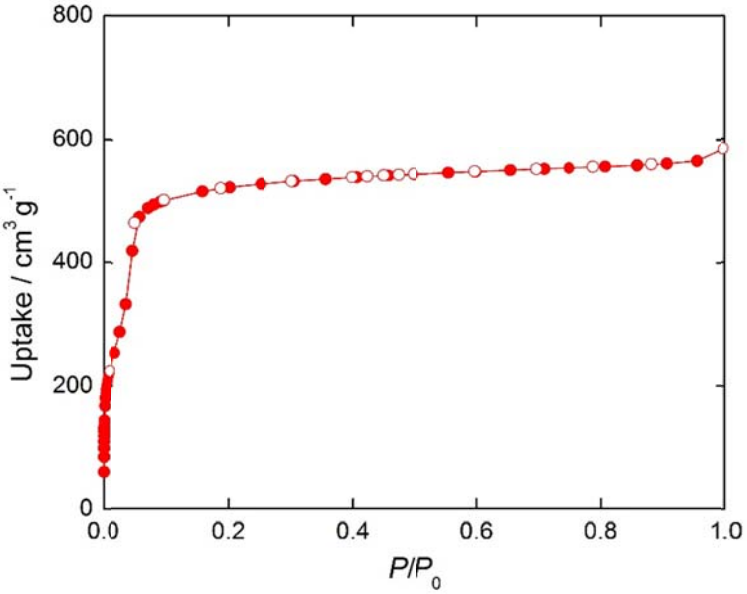

Figure A3.11. N_2 isotherm of microcrystalline powder MOF-808-2.3SO_4 at 77 K.

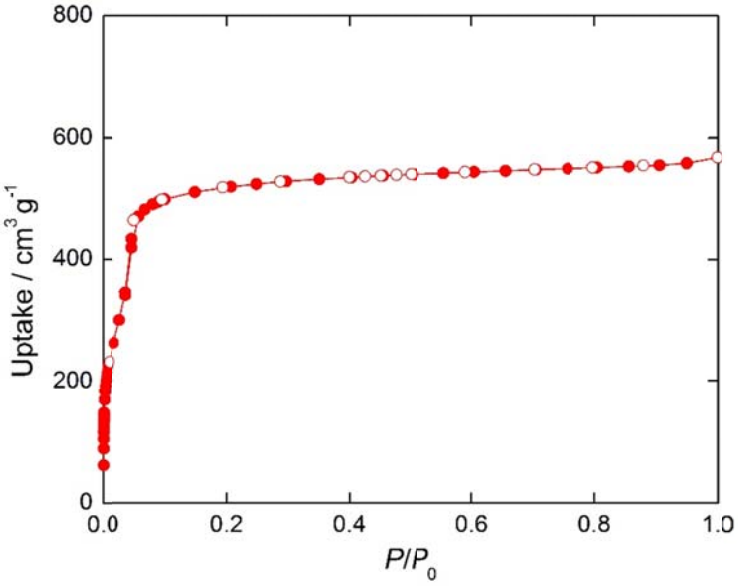

Figure A3.12. N_2 (red) and Ar (blue) isotherms of microcrystalline powder MOF-808-2.5SO_4 at 77 K and 87 K, respectively.

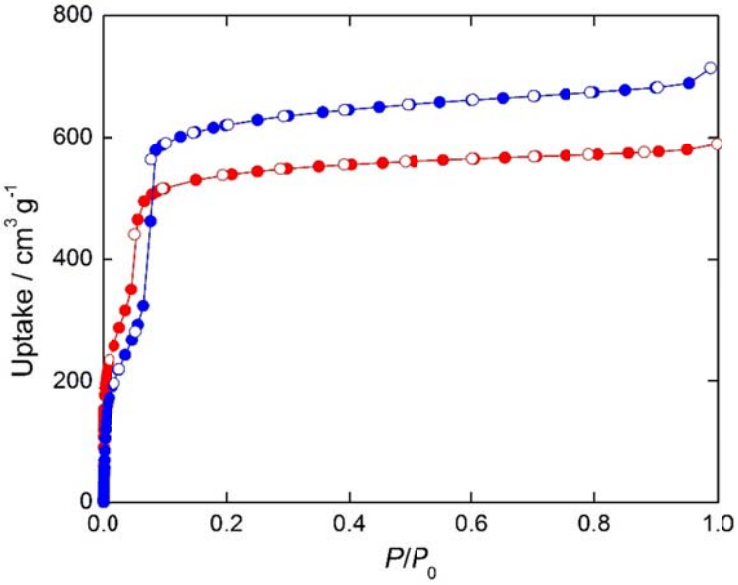

Figure A3.13. Infrared spectra of activated MOF-808-P (blue), MOF-808-0.65SO_4 (brown), MOF-808-1.3SO_4 (orange) and MOF-808-2.5SO_4 (red) recorded at room temperature, showing the range of 4000–400 cm^{-1}.

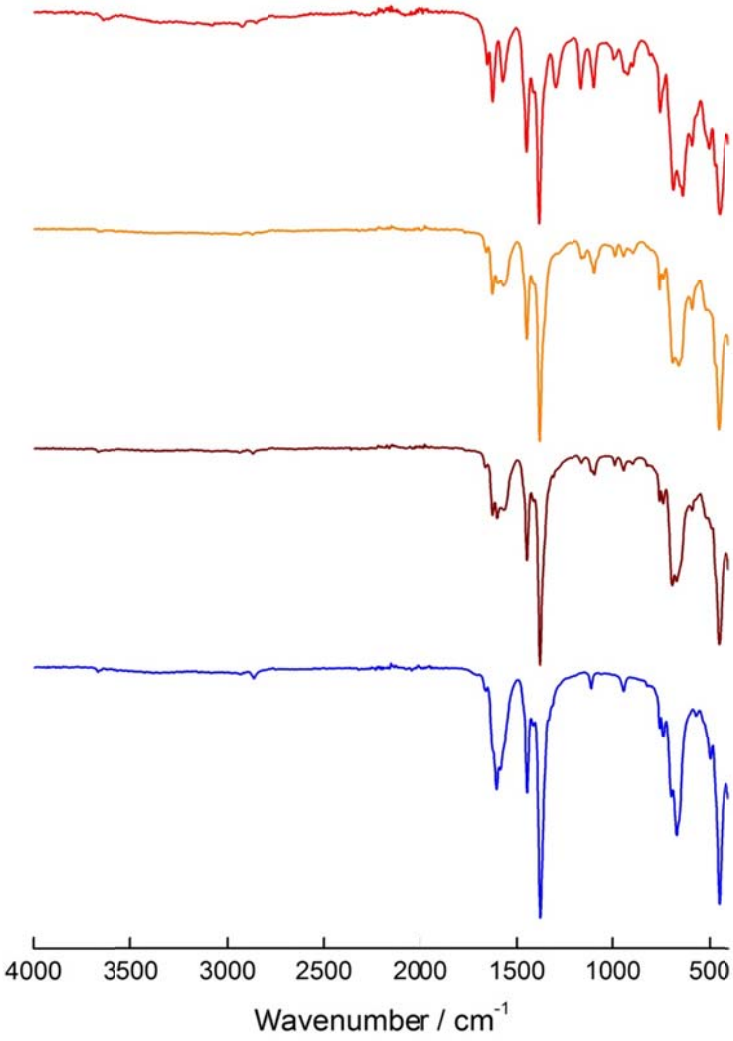

Table A3.2. ^{31}P MAS NMR chemical shift assignments and distribution of acid sites for MOF-808-xSO$_4$ loaded with TMPO.

Sample	Chemical shift (ppm)[a]						Acid amount (mmol/g)[d]			
	[69][b]	65	62	{55}[c]	51	P[d]	[Brønsted][b]	{Lewis}[c]	Total	B/L
MOF-808-P	–	–	83.5% (1.71)	16.5% (0.34)	–	Y	0	0.34	0.34	0
MOF-808-0.65SO$_4$	–	–	39.7 % (0.95)	60.3% (1.44)	–	Y	0	1.44	1.44	0
MOF-808-1.3SO$_4$	19.4% (0.50)	–	36.8% (0.95)	43.8% (1.13)	–	Y	0.50	1.13	1.63	0.4
MOF-808-2.5SO$_4$	28.8% (0.81)	–	19.9% (0.56)	51.2% (1.44)	–	N	0.81	1.44	2.25	0.6
MOF-808-2.5SO$_4$ exposed to air	5.8% (0.13)	17.5% (0.36)	58.2% (1.21)	–	18.5% (0.39)	Y	0.13	0	0.13	∞

[a] Data denote relative concentration of acid sites (%); whereas data in parentheses represent acid concentration (mmol g^{-1}) of the corresponding acid site, as derived from elemental analyses by ICP-OES.
[b] Chemical shift in square bracket assigned to presumably Brønsted superacidic sites.
[c] Chemical shift in curly bracket assigned to Lewis acid sites.
[d] Resonance peaks with chemical shift lower than 50 ppm, which arise from physisorbed TMPO, are excluded during derivations of acid amount.

Figure A3.14. Cycle performance of acetonitrile-d_3 uptake in MOF-808-P at 25 °C. The sample was evacuated for 2 hours at 25 °C between the cycles.

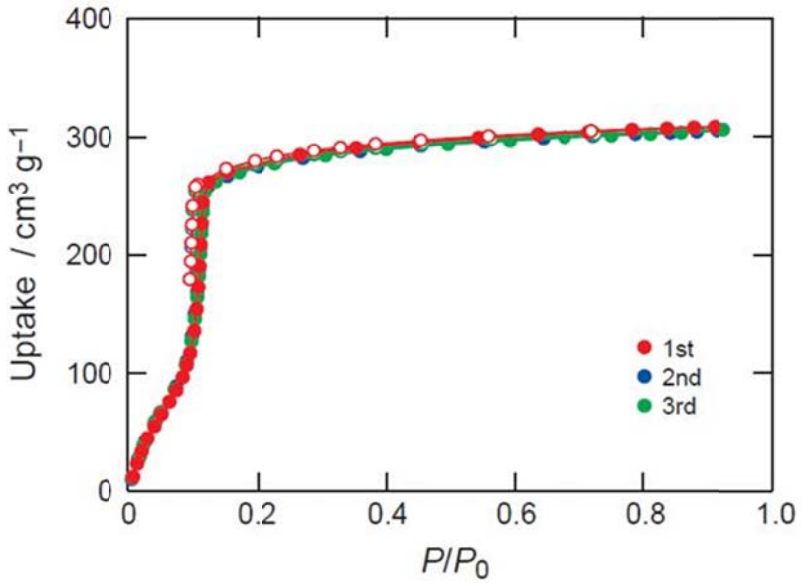

Figure A3.15. Cycle performance of acetonitrile-d_3 uptake in MOF-808-0.65SO_4 at 25 °C. The sample was evacuated for 2 hours at 25 °C between the cycles.

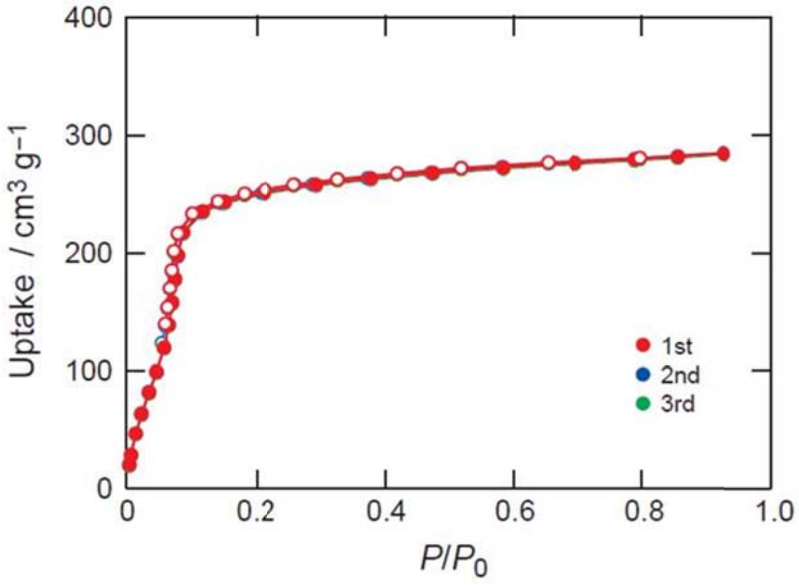

Figure A3.16. Cycle performance of acetonitrile-d_3 uptake in MOF-808-1.3SO_4 at 25 °C. The sample was evacuated for 2 hours at 25 °C between the cycles.

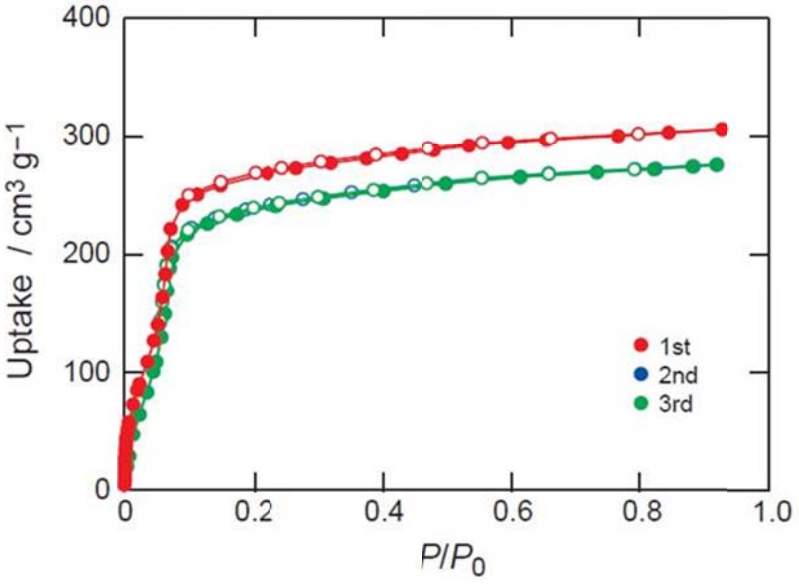

Figure A3.17. Cycle performance of acetonitrile-d_3 uptake in MOF-808-2.5SO_4 at 25 °C. The sample was evacuated for 2 hours at 25 °C between the cycles.

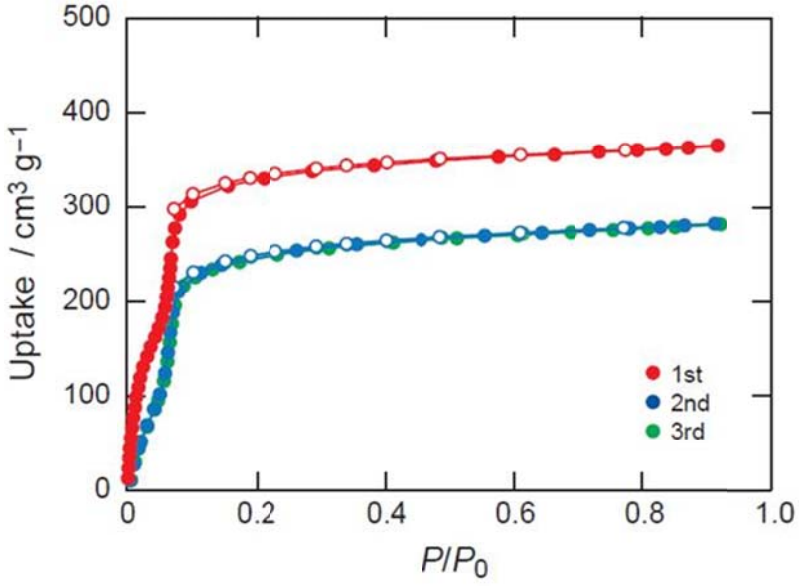

References and Notes

(1) (a) Cohen, S. M. Chem. Rev. **2012**, 112, 970. (b) Evans, J. D.; Sumby, C. J.; Doonan, C. J. Chem. Soc. Rev. **2014**, 43, 5933. (c) Deria, P.; Mondloch, J. E.; Karagiaridi, O.; Bury, W.; Hupp, J. T.; Farha, O. K. Chem. Soc. Rev. **2014**, 43, 5896.

(2) (a) Burrows, A. D.; Frost, C. G.; Mahon, M. F.; Richardson, C. Chem. Commun. **2009**, 4218. (b) Morris, W.; Doonan, C. J.; Furukawa, H.; Banerjee, R.; Yaghi, O. M. J. Am. Chem. Soc. **2008**, 130, 12626. (c) Fracaroli, A. M.; Furukawa, H.; Suzuki, M.; Dodd, M.; Okajima, S.; Gándara, F.; Reimer, J. A.; Yaghi, O. M. J. Am. Chem. Soc. **2014**, 136, 8863. (d) Mir, M. H.; Koh, L. L.; Tan, G. K.; Vittal, J. J. Angew. Chem. Int. Ed. **2010**, 49, 390. (e) Kim, M.; Garibay, S. J.; Cohen, S. M. Inorg. Chem. **2011**, 50, 729. (f) Bloch, E. D.; Britt, D.; Lee, C.; Doonan, C. J.; Uribe-Romo, F. J.; Furukawa, H.; Long, J. R.; Yaghi, O. M. J. Am. Chem. Soc. **2010**, 132, 14382. (g) Chen, C.; Allen, C. A.; Cohen, S. M. Inorg. Chem. **2011**, 50, 10534. (h) Goto, Y.; Sato, H.; Shinkai, S.; Sada, K. J. Am. Chem. Soc. **2008**, 130, 14354. (i) Dugan, E.; Wang, Z.; Okamura, M.; Medina, A.; Cohen, S. M. Chem. Commun. **2008**, 3366. (j) Nguyen, J. G.; Cohen, S. M. J. Am. Chem. Soc. **2010**, 132, 4560.

(3) (a) Park, K. S.; Ni, Z.; Côté, A. P.; Choi, J. Y.; Huang, R.; Uribe-Romo, F. J.; Chae, H. K.; O'Keeffe, M.; Yaghi, O. M. Proc. Natl. Acad. Sci. **2006**, 103, 10186. (b) Férey, G.; Draznieks, C. M.; Serre, C.; Millange, F.; Dutour, J.; Surblé, S.; Margiolaki, I. Science **2005**, 309, 2040. (c) Cavka, J. H.; Jakobsen, S.; Olsbye, U.; Guillou, N.; Lamberti, C.; Bordiga, S.; Lillerud, K. P. J. Am. Chem. Soc. **2008**, 130, 13850.

(4) (a) Gillespie, R. J.; Peel, T. E. Adv. Phys. Org. Chem. **1971**, 9, 1. (b) Gillespie, R. J.; Peel, T. E. J. Am. Chem. Soc. **1973**, 95, 5173.

(5) Hammett, L. P.; Deyrup, A. J. J. Am. Chem. Soc. **1932**, 54, 2721.

(6) (a) Gold, V.; Laali, K.; Morris, K. P., Zdunek, L. Z. J. Chem. Soc., Chem. Commun. **1981**, 769. (b) Howells, R. D.; McCown, J. D. Chem. Rev. **1977**, 77, 69. (c) Stang, P. J.; White, M. R. Aldrichimica Acta **1983**, 16, 15. (d) Yamaguchi, T. Appl. Catal. **1990**, 61, 1. (e) Olah, G. A.; Prakash, G. K. S.; Molnár, Á.; Sommer, J. Superacid Chemistry, 2nd ed.; John Wiley & Sons, Inc.: New Jersey, **2009**; Chapter 2 & 5. (f) Song, X.; Sayari, A. Catal. Rev.-Sci. Eng. **1996**, 38, 329. (g) Arata, K. Green Chem. **2009**, 11, 1719. (h) Yadav, G. D.; Nair, J. J. Microporous Mesoporous Mater. **1999**, 33, 1. (i) Schmidt, F. Appl. Catal. A **2001**, 221, 15.

(7) (a) Olah, G. A.; Kaspi, J.; Bukala, J. J. Org. Chem. **1977**, 42, 4187. (b) Mirodatos, C.; Barthomeuf, D. J. Chem. Soc. Chem. Commun. **1981**, 39. (c) Garralón, G.; Corma, A.; Fornés, V. Zeolites, **1989**, 9, 84. (d) Arata, K. Adv. Catal. **1990**, 37, 165. (e) Corma, A. Chem. Rev. **1995**, 95, 559. (f) Okuhara, T. Chem. Rev. **2002**, 102, 3641. (g) Arata, K.; Matsuhashi, H.; Hino, M.; Nakamura, H. Catal. Today **2003**, 81, 17.

(8) Jiang, J.; Yaghi, O. M. Chem. Rev. **2015**, 115, 6966.

(9) Furukawa, H.; Gándara, F.; Zhang, Y.-B.; Jiang, J.; Queen, W. L.; Hudson, M. R.; Yaghi, O. M. J. Am. Chem. Soc. **2014**, 136, 4369.

(10) Jiang, J.; Gándara, F.; Zhang, Y.-B.; Na, K.; Yaghi, O. M.; Klemperer, W. G. J. Am. Chem. Soc. **2014**, 136, 12844.

(11) (a) Haw, J. F.; Zhang, J.; Shimizu, K.; Venkatraman, T. N.; Luigi, D.-P.; Song, W.; Barich, D. H.; Nicholas, J. B. J. Am. Chem. Soc. **2000**, 122, 12561. (b) Chen, W.-H.; Ko, H.-H.;

Sakthivel, A.; Huang, S.-J.; Liu, S.-H.; Lo, A.-Y.; Tsai, T.-C.; Liu, S.-B. Catal. Today **2006**, 116, 111.

(12) Bennett, A. E.; Rienstra, C. M.; Auger, M.; Lakshmi, K. V.; Griffin, R. G. J. Chem. Phys. **1995**, 103, 6951.

(13) (a) Babou, F.; Goudurier, G.; Vedrine, J. C. J. Catal. **1995**, 152, 341. (b) Sohn, J. R.; Km, H. J. J. Mol. Catal. **1989**, 52, 379. (c) Adeeva, V.; de Haan, J. W.; Jänchen, J.; Lei, G. D.; Schüneann, V.; van de Ven, L. J. M.; Sachtler, W. M. H.; van Santen, R. A. J. Catal. **1995**, 151, 364. (d) Jin, T.; Yamaguchi, T.; Tanabe, K. J. Phys. Chem. **1986**, 90, 4794.

(14) Valenzano, L.; Civalleri, B.; Chavan, S.; Bordiga, S.; Nilsen, M. H.; Jakobsen, S.; Lillerud, K. P.; Lamberti, C. Chem. Mater. **2011**, 23, 1700.

(15) Sheldrick, G. M. Acta Cryst. **2008**, 64, 112.

(16) Walling, C. J. Am. Chem. Soc. **1950**, 72, 1164.

(17) Benesi, H. A. J. Am. Chem. Soc. **1956**, 78, 5490.

(18) (a) Baltusis, L.; Frye, J. S.; Maciel, G. E. J. Am. Chem. Soc. **1986**, 108, 7119. (b) Haw, J. F.; Zhang, J.; Shimizu, K.; Venkatraman, T. N.; Luigi, D.-P.; Song, W.; Barich, D. H.; Nicholas, J. B. J. Am. Chem. Soc. **2000**, 122, 12561. (c) Zheng, A.; Huang, S.-J.; Liu, S.-B.; Deng, F. Phys. Chem. Chem. Phys. **2011**, 13, 14889.

(19) (a) Auroux, A. Mol. Sieves **2008**, 6, 45. (b) Mekki-Rarrada, A.; Aurroux, A. Thermal Methods, in Characterization of Solid Materials and Heterogeneous Catalysis, From Structure to Surface Reactivity, Che, M.; Védrine, J. C. Eds., Wiley-VCH, Weinheim, **2012**, p 747.

(20) (a) Rodríguez-González, L.; Hermes, F.; Bertmer, M.; Rodríguez-Castellón, E.; Jiménez-López, A.; Simon, U. Appl. Catal. A **2007**, 328, 174. (b) Niwa, M.; Katada, N. Chem. Rec. **2013**, 13, 432.

Chapter IV

Catalytic Properties of Sulfated Zirconium MOF-808 as Solid Acid and Its Ammonia Adsorption Properties

Introduction

Development of MOF-base acid catalysts began at the very onset of MOF chemistry as the first example of Lewis acidic MOF was reported for catalyzing the cyanosilylation of aldehydes.[1] In successive years, coordinative unsaturation or open metal sites[2] on metal SBUs were synthesized and found to be suitable as Lewis acid sites. In this case, several coordination positions of the metal center are occupied by solvent molecules, which can be removed by heating and/or evacuation during the activation process without collapse of the framework. In this group of MOFs, the metal center simultaneously acts as a structural building unit and a Lewis acid site for use in catalysis. Examples involving HKUST-1 [$Cu_3(BTC)_2$; BTC = benzene-1,3,5-tricarboxylate][3], M-MIL-101 [$M_3X(H_2O)_2O(BDC)_3$; M = Al, Cr, Fe; X = F, OH; BDC = benzene-1,4-dicarboxylate] or functionalized MIL-101[4], and NU-1000 [$Zr_6O_4(OH)_4(H_2O)_4(OH)_4(TBAPy)_2$; TBAPy = 1,3,6,8-(p-benzoate)pyrene][5] were found to be catalytically active in various reactions: aldehyde cyanosilylation, α-pinene oxide isomerization, citronellal cyclization, Knoevenagel condensation, selective oxidation of organic compounds, and decomposition of chemical warfare agents.[5,6] We note that MOFs without open-metal sites per se can act as Lewis acids because of accessibility to metal centers within the SBUs. Several reviews on this property of MOFs are available in the literature.[7]

Compared to the relatively large body of work done on the Lewis acidic MOFs, Brønsted acid chemistry in MOFs is beginning to emerge as an alternative catalytic scheme.[8] The methods for the preparation of Brønsted acidic MOFs can be classified into three categories: (i) Brønsted acidic molecules such as polyoxometalates (POMs) can be encapsulated within the MOF pores; (ii) Brønsted acid moieties can be ligated onto metal sites of SBUs; or (iii) Brønsted acid functional groups can be covalently bound to organic linking units. Due to their different composition, catalysts based on Brønsted acidic MOFs derived from each category also bear their own characteristics: (i) Brønsted acidic Keggin-type POM, phosphotungstic acid (PTA) and its analogues, when encapsulated in MOF pores, were shown to exhibit activity comparable to those free acids.[9] They are often reported to form acid-base and acid-metal binary systems in various MOFs including MIL-101, MIL-100, and HKUST-1;[10] (ii) when Brønsted acid sites are located on or near the metal SBUs, they are often coexisting with Lewis acidic sites, making it more difficult to clarify the activity and characterize the active sites; (iii) MOFs with strong Brønsted acid groups covalently bound to the organic linkers have often been shown to retain activity despite being covalently linked to the framework. This has attracted attention to the field of enantio- and stereo-selective catalysis by MOFs imparting unique catalytic properties that are not possible in other materials.[11]

As shown in Chapter III, sulfation of zirconium MOF-808 has generated novel acidity in the framework and we also showed that using the Hammett indicator test, the fully sulfated version, MOF-808-2.5SO_4 exhibits evidences of superacidity. Thus, it is natural to look at its catalytic properties. Here, we confirm the coexistence of both Lewis and Brønsted acidity in sulfated

MOF-808 materials and, through a series of test reactions, we study the amount and strength of these acid sites as a function of sulfate groups incorporated. This is followed by a survey of reactions to confirm MOF-808-2.5SO_4, the most active compound, to as a useful material for various acid-catalyzed reactions including Friedel-Crafts acylation, esterification, and isomerization, as well as in the conversion of methylcyclopentane (MCP) into various hydrocarbons at 150-200 ^oC; the last being a test reaction for catalytic reforming.

Ammonia is one of the unpleasant chemicals related to life, contributing to a number of environmental problems including pollution in the form of atmospheric particulate matter, acidification of soil, and alteration of the global greenhouse gas balance.[12] Atmospheric ammonia levels, from contributors including agricultural sector (fertilizer and livestock operations), losses from ammonia refrigeration systems, and oxidative degradation of amine-based solvents in CO_2 capture plants, is predicted to continue rising, worsening the aforementioned issues. Therefore, safe removal of ammonia is necessary for a pleasant environment and better human health.

There are two main categories for ammonia capture applications, each requiring materials to bear specific merits.[8] One is the irreversible ammonia removal. This direction targets at toxic gas removal applications like gas masks. Two criteria are prominent here. First, the absorption or adsorption of ammonia occurs at low ammonia concentration. This is important because the capturing agent should still be able to remove ammonia from the environment where it is present at low concentration to make sure the concentration afterwards is below the harmful level, for example, 25 ppm the recommended CAL-OSHA permissible ammonia exposure limit.[13] The second criterion is the competitive ammonia removal under moist conditions due to the presence of significant amount of moisture in real world applications (for example, exhaled gas from human). The other direction aims at reversible capture of ammonia in applications such as ammonia transportation and recycling. It is beneficial to use solid adsorbents to replace the toxic, corrosive, and difficult-to-handle compressed liquid ammonia. For this purpose, criteria such as high ammonia uptake capacity at 1 bar or even higher pressure, high cycling performance, and ammonia stability of the material are important.

MOFs have attracted tremendous attention in the fields of gas storage and gas separation over the past 20 years. Preliminary investigations have proved MOFs and also related MOF/graphite oxide composite materials as potentially promising materials for ammonia capture.[14] A series of MOFs have been surveyed including MOFs with Lewis acidic open metal sites (MOF-74, HKUST-1), MOFs without acidic sites per se (MOF-177, IRMOF-3 and IRMOF-62), and MOFs with Brønsted acidic sites (MIL-101-SO_3H and UiO-66-NH_3Cl) for capture of ammonia.[15] The good performance of these materials indicates acidic MOFs are promising capturing materials for ammonia.

Here, we also explore our MOF-808-2.5SO_4 material for its ammonia adsorption properties to evaluate its performance according to aforementioned criteria and potentiality to become a promising ammonia capture material.

Experimental Section

Chemicals and supplies. Anhydrous methanol was obtained from EMD Millipore Chemicals. Anhydrous toluene was obtained from Acros Organics. Benzoic acid (purity ≥

99.5%), benzophenone (purity ≥ 99 %), oleic acid (analytical standard), methyl heptadecanoate (analytical standard), methylcyclopentane (purity ≥ 98%), anhydrous ethyl acetate, anhydrous anisole, anhydrous dichloromethane, and anhydrous chloroform with amylenes as stabilizer were obtained from Sigma-Aldrich. (±)-Citronellal (GC, purity ≥ 95%), (+)-isopulegol (purity ≥ 99%), (-)-isopulegol (purity ≥ 99%), alpha-pinene (purity ≥ 98%), camphene (purity ≥ 95%), 4-methoxybenzophenone (purity ≥ 97%) and benzoic anhydride (purity ≥ 95%) were obtained from Aldrich. (R)-(+)-Limonene (analytical standard) and 2-chlorobenzoyl chloride (purity ≥ 97.0%) were obtained from Fluka.

MOF-808 and sulfated MOF-808 materials are synthesized according to reported procedure.[16]

All starting materials, reagents and solvents were used without further purification.

All glassware used to handle activated MOFs was dried at 120 ^{o}C for 12h and used immediately.

Analytical techniques. Powder X-ray diffraction (PXRD) patterns were recorded using a Rigaku Miniflex 600 diffractometer (Bragg-Brentano geometry, Cu Kα radiation λ = 1.54056 Å). Scanning electron microscope (SEM) images were obtained using a Zeiss Gemini Ultra-55 analytical scanning electron microscope with a working distance of 8.4 mm and a low acceleration voltage (5 keV) to avoid damage to the samples during observation. All MOF SEM samples were prepared by direct deposition of MOF/acetone dispersion (1 mg mL^{-1}) on the silicon substrate heated on a hot plate (60 °C). Low-pressure gas (N_2) adsorption isotherms were recorded on a Quantachrome Autosorb-1 volumetric gas adsorption analyzer. Liquid nitrogen bath was used for the measurements at 77 K. Helium was used for the estimation of dead space for gas adsorption measurements. Ultra-high-purity grade N_2, and He gases (Praxair, 99.999% purity) were used throughout the adsorption experiments. Low-pressure ammonia adsorption isotherms were recorded on a Micromeritcs ASAP 2020 accelerated surface area and porosimetry system. The measurement temperature was controlled with a water circulator. Anhydrous ammonia gas (Praxair, 99% purity) was used throughout the adsorption experiments.

Catalysis tests of MOFs:

Citronellal cyclization: The citronellal cyclization reactions were carried out in 15-mL Ace pressure tube (Sigma-Aldrich) loaded with 50 mg of activated catalysts. Each catalyst was first activated under dynamic vacuum at 150 °C for 24 h and stored in an inert atmosphere glovebox. After adding a solution of 1.5 mL (±)-citronellal in 5 mL toluene to the reactor (c.a. citronellal:Zr^{4+} mole ratio = 35) in the glovebox, the vessels were placed in an aluminum heating block at 60 ^{o}C with stirring. Reaction samples were removed in the dry box at different reaction times (0.5, 1, 1.5, 2, 3, 4, 5, 6, and 8 h), filtered through a 0.2 μm PTFE membrane filter, diluted 250 times with ethyl acetate and analyzed with a Shimadzu GCMS-QP2010 SE GC-MS, equipped with a SHRXI-5MS capillary column. Column temperature was initially 75 °C for 3 minutes, then gradually increased to 200 °C at 3 °C/min. Cyclohexanone was added as internal standard, and calibration curves for (±)-citronellal and (±)-isopulegol were obtained using commercially available (±)-citronellal and (±)-isopulegol for quantification. Conversions of (±)-citronellal at a given reaction time were calculated by dividing the amount of (±)-citronellal left in the reaction mixture at that given reaction time (calculated using the calibration curve) over

the initial amount of (±)-citronellal added. Selectivity towards (±)-isopulegol was calculated by dividing the amount of (±)-isopulegol produced in the reaction mixture over the amount of the (±)-citronellal had been converted to that time.

Recyclability tests were performed on MOF-808-2.5SO_4 to test for catalyst stability. Here, the catalyst after the reaction was thoroughly washed by submerging it in anhydrous chloroform for one day, exchanging the solvent six times during the day, and dried under vacuum at 150 °C between consecutive runs. For filtration experiments to test for catalyst leaching, the reaction slurry was split in two parts after 0.5 h. While one part was left undisturbed, from the other part the catalyst was removed by filtration. The supernatant was allowed to react further in a separate reactor.

alpha-Pinene isomerization: The alpha-pinene isomerization reactions were carried out in 4-mL Ace pressure tube (Sigma-Aldrich) loaded with 100 mg of activated catalysts. Each catalyst was first activated under dynamic vacuum at 150 °C for 24 h and stored in an inert atmosphere glovebox. After adding 3 mL of alpha-pinene to the reactor (c.a. pinene:Zr^{4+} mole ratio = 40) in glovebox, the vessels were placed in an aluminum heating block at 120 °C with stirring. Reaction samples were removed in the dry box at different reaction times (12, 24, 36, and 48 h), diluted 1000 times with ethyl acetate, filtered through a 0.2 μm PTFE membrane filter, and analyzed with a Shimadzu GCMS-QP2010 SE GC-MS, equipped with a SHRXI-5MS capillary column. Column temperature was initially 50 °C for 5 minutes, then gradually increased to 100 °C at 2 °C/min, and finally increased to 200 °C at 5 °C/min. Calibration curves for alpha-pinene, camphene and limonene were obtained using commercially available alpha-pinene, camphene and (R)-(+)-Limonene for quantification. Conversions of alpha-pinene at a given reaction time were calculated by dividing the amount of alpha-pinene left in the reaction mixture at that given reaction time (calculated using the calibration curve) over the initial amount of alpha-pinene added. Selectivity towards camphene and limonene was calculated by dividing the amount of camphene and limonene produced in the reaction mixture over the amount of the alpha-pinene had been converted to that time.

Recyclability tests were performed on MOF-808-2.5SO_4 to test for catalyst stability. Here, the catalyst after the reaction was thoroughly washed by submerging it in anhydrous chloroform for one day, exchanging the solvent six times during the day, and dried under vacuum at 150 °C between consecutive runs. For filtration experiments to test for catalyst leaching, the reaction slurry was split in two parts after 12 h. While one part was left undisturbed, from the other part the catalyst was removed by filtration. The supernatant was allowed to react further in a separate reactor.

Friedel-Crafts acylation of anisole: The Friedel-Crafts acylation of anisole was carried out in 15-mL Ace pressure tube (Sigma-Aldrich) loaded with 50 mg of activated catalysts (250 mg when using benzoic acid as the acylation reagent). Each catalyst was first activated under dynamic vacuum at 150 °C for 24 h and stored in an inert atmosphere glovebox. After adding a solution of acylation reagents in 5 mL anisole to the reactor in the glovebox (c.a. carboxylic acid:Zr^{4+} mole ratio = 0.4; carboxylic anhydride:Zr^{4+} mole ratio = 2; acyl chloride:Zr^{4+} mole ratio = 9), the vessels were placed in an aluminum heating block at 110 ^{o}C with stirring (180 ^{o}C when using benzoic acid as the acylation reagent). Reaction samples were removed after 12 h, filtered through a 0.2 μm PTFE membrane filter, diluted 20 times with ethyl acetate and analyzed with a Shimadzu GCMS-QP2010 SE GC-MS, equipped with a SHRXI-5MS capillary column. Column temperature was initially 40 °C for 1 minutes, then gradually increased to 300 °C at

10 °C/min. Benzophenone was added as internal standard. Conversions of acylation reactions were calculated by dividing the amount of acylation reagents left in the reaction mixture over the initial amount added.

Esterification of oleic acid with methanol: The esterification of oleic acid with methanol was carried out in 15-mL Ace pressure tube (Sigma-Aldrich) loaded with 200 mg of activated catalysts. Each catalyst was first activated under dynamic vacuum at 150 °C for 24 h and stored in an inert atmosphere glovebox. After adding a solution of 1.0 g oleic acid in 10 mL anisole to the reactor in the glovebox (c.a. oleic acid:Zr^{4+} mole ratio = 4), the vessels were placed in an aluminum heating block at 65 ^{o}C with stirring. Reaction samples were removed in the dry box at different reaction times (1, 2, 3, 4, 5, and 6 h), filtered through a 0.2 μm PTFE membrane filter, diluted 250 times with methanol and analyzed with a Shimadzu GCMS-QP2010 SE GC-MS, equipped with a SHRXI-5MS capillary column. Column temperature was initially 75 °C for 1 minutes, then gradually increased to 300 °C at 10 °C/min. Methyl heptadecanoate was added as internal standard. Calibration curves for oleic acid were obtained using commercially available oleic acid for quantification. Conversions of oleic acid at a given reaction time were calculated by dividing the amount of oleic acid left in the reaction mixture at that given reaction time (calculated using the calibration curve) over the initial amount of oleic acid added.

Recyclability tests were performed on MOF-808-2.5SO_4 to test for catalyst stability. Here, the catalyst after the reaction was quickly washed with 10 mL of anhydrous methanol followed by 6 × 10 mL of anhydrous chloroform, and dried under vacuum at 150 °C between consecutive runs. For control experiments, the reaction was stirred without catalysts or with same amount (200 mg) of activated MOF-808-P, and analyzed in the same manner.

Limonene isomerization: The limonene isomerization reaction was carried out in 4-mL Ace pressure tube (Sigma-Aldrich) loaded with 150 mg of activated catalysts. Each catalyst was first activated under dynamic vacuum at 150 °C for 24 h and stored in an inert atmosphere glovebox. After adding 2.5 mL limonene to the reactor in the glovebox (c.a. limonene:Zr^{4+} mole ratio = 20), the vessels were placed in an aluminum heating block at 60 ^{o}C with stirring. Reaction samples were removed after 1 h, filtered through a 0.2 μm PTFE membrane filter, diluted 1000 times with ethyl acetate and analyzed with a Shimadzu GCMS-QP2010 SE GC-MS, equipped with a SHRXI-5MS capillary column. Column temperature was initially 50 °C for 5 minutes, then gradually increased to 100 °C at 2 °C/min, and finally increased to 200 °C at 5 °C/min. Calibration curves for limonene were obtained using commercially available (R)-(+)-Limonene for quantification. Conversion of limonene was calculated by dividing the amount of limonene left in the reaction mixture (calculated using the calibration curve) over the initial amount of limonene added.

Methylcyclopentane conversion reaction: The mesoporous silica MCF-17 was synthesized by following the literature reported elsewhere.[17] In a typical synthesis, 1,3,5-trimethylbenzene, which was utilized as a pore swelling agent, was added to an aqueous solution of triblockcopolymer Pluoronic P123 and HCl. After stirring of this solution for 2 h at 40 °C, tetraethylorthosilicate was added and the solution was stirred for an additional 20 h. NH_4F was then added, and the solution was allowed to hydrothermally react at 100 °C for 24 h. The precipitated product was collected by filtration and then calcined for 6 h at 550 °C.

Poly(vinylpyrrolidone) (PVP)-capped Pt nanoparticles (NPs) with an average size of 2.5 nm were synthesized by following the literature reported elsewhere.[18] In a typical synthesis, H_2PtCl_6

was used as Pt precursor, which was dissolved in ethylene glycol in the presence of PVP. This solution was reacted at boiling solvent temperatures, and the as-synthesized PVP-capped Pt NPs were washed and re-dispersed in ethanol to give colloidal solution of Pt NPs with the concentration of 1 mg mL^{-1}. For supporting Pt NPs on mesoporous silica MCF-17, this colloidal solution of Pt NPs was added to the supporting materials to give 1wt% of Pt. The colloidal suspension was sonicated for 5 h at room temperature using a commercial ultrasonic cleaner (Branson, 1510R-MT, 70W, 42 kHz). The brown precipitates were separated by centrifugation (4000 rpm, 10 min), washed with ethanol for three times, and dried in an oven at 60 °C overnight.

The Pt NPs supported mesoporous silica was designated as Pt/SiO_2 that was tested for methylcyclopentane conversion reaction as the reference catalyst.

Supporting Pt NPs on MOF-808-P and MOF-808-2.5SO_4 (hereafter Pt/MOF-808-P and Pt/MOF-808-2.5SO_4, respectively) were carried out by following the literature with slight modification.[19] In a typical synthesis, in glovebox, 200 mg of activated MOF powder was suspended in 20 mL of anhydrous pentane, to which an methanol solution of H_2PtCl_6 (0.17 mL) was added dropwise under continuous vigorous stirring. After filtration, the orange powder was dried under dynamic vacuum at room temperature for 24 h and then at 150 °C for 24 h. Partial reduction of Pt was already observed after the heating under vacuum. Further reduction was carried out during the pretreatment of catalysts before reaction. Pt loading on MOF was determined by ICP-OES to be 2 wt%.

The catalytic testing was performed using lab-built plug-flow reactor connected to a Hewlett Packard 5890 gas chromatograph (GC). A 10% SP-2100 on 100/120 Supelco port packed column in line with a FID detector was used to separate and analyze the C1 – C6 hydrocarbons. Mass flow controllers were carefully calibrated using a bubble flow meter and used to introduce the ultra-high purity (99.9999% Praxair) H_2 and He gases. Saturated vapor pressure of methylcyclopentane (MCP) was introduced to the reactor using a bubbler. The reactant flow was carefully calibrated at different temperatures and partial pressures of He carrier. A total flow of 40 mL/min was used. Partial pressure of reactant was calculated by using the known temperature vs. saturated vapor pressure plots and was 50 Torr with 5:1 H_2 excess. 50 – 100 mg charges of the catalysts were diluted by quartz sand loaded in the reactor bed. The actual weight of catalyst used was selected to give similar total conversions in each case. The catalysts were reduced at 150 - 200 °C for 2 h under a flow of 210 Torr H_2 in 550 Torr He prior to catalytic testing. The catalytic activity and selectivity were evaluated for total MCP conversions around 3%.

Results and Discussion

Test reactions for identifying Lewis and Brønsted acidity in sulfated MOF-808. Unlike in the field of acidic zeolites and sulfated metal oxides, where test reactions are often of industrial interest; till now, test reactions in acidic MOFs are merely used for fundamental studies and understanding the nature of the acidic sites (Lewis acidity or Brønsted acidity). For this purpose, each test run typically requires 50-100 mg of MOF often in microcrystalline powder form with particle sizes in the range of a few hundred nanometers to one hundred micrometers. These samples are preferred over large single crystals due to facile diffusion of reactants and products. Careful observation of the condition of MOF crystals before and after catalyst activation and reaction is also necessary to avoid misjudgments.

Scheme 4.1. Cyclization of (±)-citronellal to isopulegol isomers

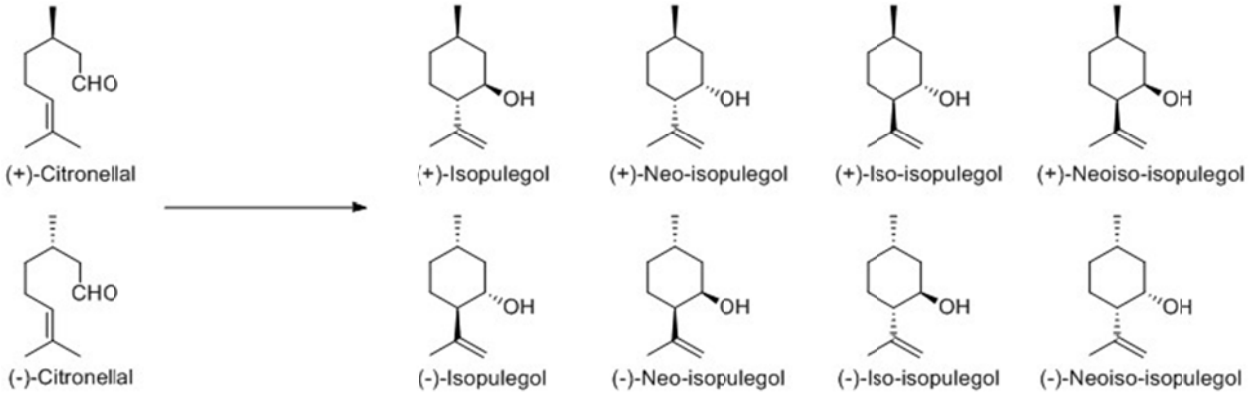

Scheme 4.2. Involved compounds in the alpha-pinene isomerization

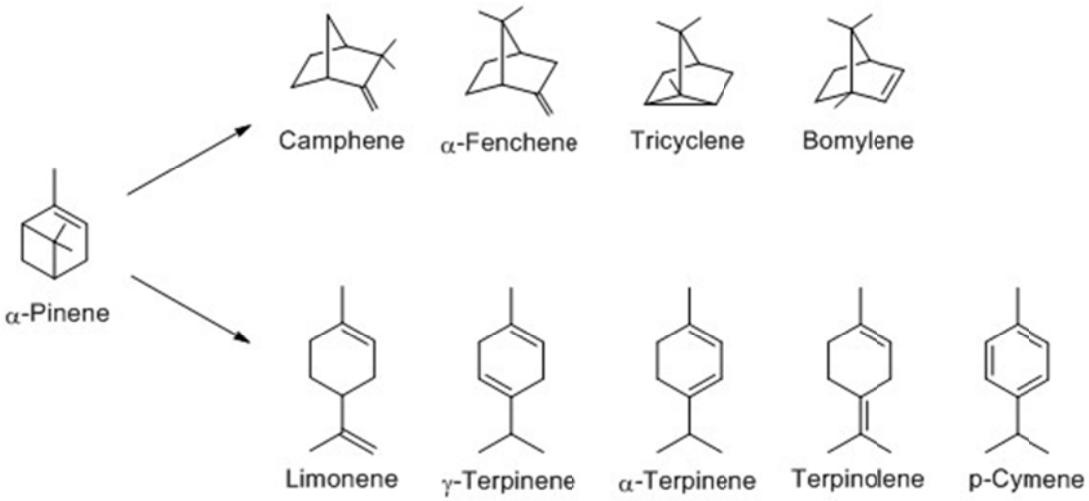

The catalytic activity of MOF-808-xSO_4 was first monitored using the cyclization of citronellal to isopulegol (Scheme 4.1). The product distribution of this reaction is directly affected by the nature of the acidic sites, with Lewis acids only, high selectivity (≥ 70%) towards (±)-isopulegol can be achieved. With Brønsted acids, the selectivity towards (±)-isopulegol is significantly lower.[6c,6d,20] In case of MOF-808- xSO_4, both the conversion and the selectivity depend on the acid treatment (Table 4.1). Acid treatment with low concentration of sulfuric acid significantly increased the activity, as MOF-808-0.65SO_4 converted 45% of citronellal after 6 hours while the conversion with MOF-808 was found to be less than 10%. The maximum activity is obtained by using MOF-808-1.3SO_4 and MOF-808-2.5SO_4, which reach 100% conversion within 2 hours at 60 ^oC, the fastest reported conversion to date among any MOF-based acid catalyst.[6e,21] The selectivity towards (±)-isopulegol decreases from 85% in pristine MOF-808, to 78% in MOF-808-0.65SO_4, 67% in MOF-808-1.3SO_4 and 55% in MOF-808-2.5SO_4, together with 3-5% of further dehydration product. This indicates that the increase in activity from MOF-808 to MOF-808-0.65 is due to the creation of more Lewis acidic sites through substitution of the formate ligands with roughly half equiv. of sulfate ligands. However,

as the concentration of sulfuric acid used in acid treatment is increased, Brønsted acidity begins to appear in MOF-808-xSO_4, leading to distinct product selectivity.

Alpha-pinene isomerization is achieved in presence of strong acid catalysts (Scheme 4.2).[22] Strong Lewis acid sites are beneficial for the formation of bicyclic compounds (e.g. camphene), while strong Brønsted acid sites are responsible for the formation of monocyclic compounds (e.g. limonene). To the best of our knowledge, no catalytic activity of MOF-based solid acids for alpha-pinene isomerization has been reported. Unlike in citronellal cyclization, where MOF-808 showed scarce activity and MOF-808-0.65SO_4 already exhibited moderate activity, no conversion of alpha-pinene over MOF-808 or MOF-808-0.65SO_4 is observed even after 2 days of reaction at 120 ^oC. This is consistent with observed results that if only Lewis acid sites are present (e.g. in calcined zirconia) there is not activity.[22a,b] On the contrary, MOF-808-1.3SO_4 converted 31% of alpha-pinene after 2 days and MOF-808-2.5SO_4 quantitatively completed the reaction after 1.5 days. Selectivity towards camphene and limonene fluctuates between 50-55% and 16-19% (Table 4.1), which is similar to reported value for sulfated zirconia.[22a,b] Beyond the assessment drawn from citronellal cyclization, these results further prove the existence of very strong Brønsted acid sites in MOF-808-1.3SO_4 and MOF-808-2.5SO_4, although the rate is still low compared to sulfated zirconia[22a,b] and H-beta,[22c] typical solid superacids.

Table 4.1. Summary of MOF-808-xSO_4 catalytic performance for citronellal and alpha-pinene isomerization.

Material	Citronellal cyclization[a]		alpha-Pinene isomerization[b]		
	Citronellal conversion, %	(±)-Isopulegol selectivity, %	alpha-Pinene conversion, %	Camphene selectivity,%	Limonene selectivity, %
MOF-808	8.0	85	0	–	–
MOF-808-0.65SO_4	44	78	0	–	–
MOF-808-1.3SO_4	97[c]	67	31	55	18
MOF-808-2.5SO_4	98[c]	55	99[d]	56	16

[a] 50 mg MOF-808-X, 1.5 mL (±)-citronellal, 5mL toluene, 60 ^oC, 8 hours.
[b] 100 mg MOF-808-X, 3 mL alpha-pinene, 120 ^oC, 2 days.
[c] Reaction time: 1.5 hours.
[d] Reaction time: 1.5 days.

From the above results, we were able to trace the generation of both Lewis and Brønsted acid sites in MOF-808 and sulfated MOF-808 materials. MOF-808 is weakly acidic and its acid sites are mainly Lewis acidic. Similar to other Zr MOFs, defects were observed in MOF-808, as proved by the deviation between its determined formula, $Zr_6O_5(OH)_3(BTC)_2(HCOO)_5(H_2O)_2$ and the derived formula of the ideal structure, $Zr_6O_4(OH)_4(BTC)_2(HCOO)_6$. The missing formate linker has resulted in two coordination vacancies on the $Zr_6O_8^{8+}$ SBU and in this case, it was occupied by water molecules. A portion of these water molecules were removed during the activation of the MOF, thus generating Lewis acidic sites in MOF-808.

Table 4.2. Acylation of anisole by different acylation reagents with MOF-808-2.5SO_4 as catalyst.

Acylating Agents	Conversion/%	Selectivity to ketone/%			
		o-	m-	p-	Other Products
Benzoic acid[a]	5.6	-	-	55	45[f]
Benzoic anhydride[b]	98	-	-	98	2[f]
Acetic acid[c]	4.1	-	-	100	-
Acetic anhydride[d]	100	3	-	84	13[g]
2-Chlorobenzoylchloride[e]	100	2.5	-	89	8.5[h]

[a]Anisole, 5mL; benzoic acid, 50 mg; catalyst amount 250 mg; reaction temperature, 453K; reaction time, 12 h.
[b]Anisole, 5mL; benzoic anhydride, 100 mg; catalyst amount 50 mg; reaction temperature, 383K; reaction time, 12 h.
[c]Anisole, 5mL; acetic acid, 25 mg; catalyst amount 50 mg; reaction temperature, 453K; reaction time, 12 h.
[d]Anisole, 5mL; acetic anhydride, 45 mg; catalyst amount 50 mg; reaction temperature, 383K; reaction time, 12 h.
[e]Anisole, 5 mL; 2-chlorobenzoylchloride, 0.25 mL; catalyst amount 100 mg; 383K; 12h.
[f]Phenyl benzoate
[g]Acetal condensation product of acetylanisole.
[h]Phenyl 2-chlorobenzoate (2.6%) and 4-chlorobenzoylphenol (5.9%)

At the beginning stage of sulfation, only part of the monovalent formate groups were substituted by the incoming divalent sulfate groups, as illustrated in MOF-808-0.65SO_4. To balance the charge, either two formate groups must leave per incoming sulfate group, or extra protons must attach to the Zr SBUs. In the former case, more Lewis acid sites will be generated, while in the latter case, we expected to see more Brønsted acid sites. From the determined formula of activated MOF-808-0.65SO_4, $[Zr_6O_{5.7}(OH)_{2.3}(C_9H_3O_6)_2(HCOO)_3(SO_4)_{0.65}](H_2O)$, the system adopts the first route to balance the charge as we observed roughly half the sulfate groups compared to the number of leaving formate groups. This left as many as 3.7 Lewis acidic sites per Zr SBU, which explains why we observed significant activity increase in MOF-808-0.65SO_4, despite insignificant change of acid strength. The appearance of Brønsted acidity in the MOF-808-1.3SO_4 material was evidenced by these catalytic test reactions, which is consistent with other acidity characterization results reported in Chapter III. The source of this Brønsted acidity may be attributed to hydroxyl groups or water molecules that are bound to Zr(IV) in the SBUs, as the adjacent strong electron-withdrawing sulfate groups contribute to stronger acid sites. This assumption that sulfate groups help to generate Brønsted acidity and promote the acid strength is further verified by the fact that MOF-808-2.5SO_4, the completely sulfated version of MOF-808, shows the highest acid strength as the most significant Brønsted acid behavior among all sulfated

MOF-808's. To summarize, sulfation of MOF-808 generates more Lewis acid sites by creating more coordinatively unsaturated sites on Zr SBUs, and when a certain degree of sulfation is acheived, Brønsted acid sites begin to appear and affect the catalytic properties of the materials significantly. The strong electron-withdrawing sulfate groups were believed to play an important role in promoting the Brønsted acid strength in sulfated MOF-808 materials.

Table 4.3. Acylation of toluene by different acylation reagents with MOF-808-2.5SO_4 as catalyst.

Acylating Agents	Conversion/%	Selectivity to ketone/%			
		o-	m-	p-	Other Products
Benzoic acid[a]	-	-	-	-	-
Benzoic anhydride[b]	15	-	-	100	-
Acetic acid[c]	0.5	-	-	100	-
Acetic anhydride[d]	43	10	4	86	-
2-Chlorobenzoylchloride[e]	51	17	4	79	-

[a]Toluene, 5mL; benzoic acid, 50 mg; catalyst amount 250 mg; reaction temperature, 453K; reaction time, 12 h.
[b]Toluene, 5mL; benzoic anhydride, 100 mg; catalyst amount 100 mg; reaction temperature, 383K; reaction time, 12 h.
[c]Toluene, 5mL; acetic acid, 25 mg; catalyst amount 50 mg; reaction temperature, 453K; reaction time, 12 h.
[d]Toluene, 5mL; acetic anhydride, 45 mg; catalyst amount 50 mg; reaction temperature, 383K; reaction time, 12 h.
[e]Toluene, 5mL; 2-chlorobenzoylchloride, 0.25 mL; catalyst amount 100 mg; reaction temperature, 383K; reaction time, 12 h.

Catalytic properties of MOF-808-2.5SO_4 for various acid-catalyzed reactions. We chose MOF-808-2.5SO_4 as the representative material to test our sulfated MOF-808 materials as solid acid catalysts.

Synthesis of fine chemicals and intermediates by Friedel-Craft acylation reactions is an important process in the chemical industry. Typically, these reactions are catalyzed by Lewis acidic aluminum chloride with acid anhydrides and acyl chlorides as the acylation reagents. However, in consonance with green chemistry, heterogeneous catalysts are preferred for their easy separation and less pollution to the environment.

Scheme 4.3. Acylation of anisole and toluene with acid, anhydride and acyl chloride.

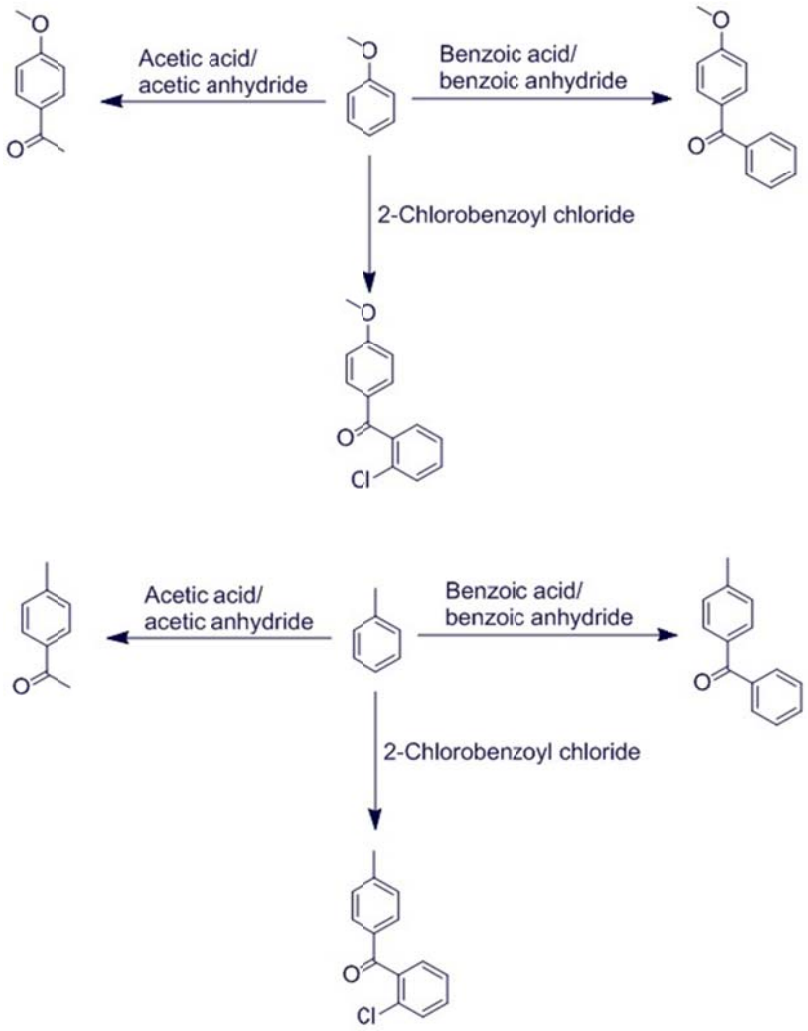

Our study showed that MOF-808-2.5SO_4 is catalytically active in the acylation of anisole with acetic and benzoic acids (aromatics/carboxylic acid/Zr(IV) molar ratio = 120/1/2.5) (Table 4.2). The reactions were carried out at 180 ^oC using a 15 mL Ace pressure tube. The yields of methoxy acetophenone and methoxy benzophenone were 4.1% and 3.3% for 12 h, respectively, with only p-substituted products observed. Acylation of toluene with acetic acid (aromatics/carboxylic acid/Zr(IV) molar ratio = 120/1/2.5) was carried out under same condition and 0.5% of methyl acetophenone is yielded for 12 h (Table 4.3). Further studies were performed to evaluate the efficiency of MOF-808-2.5SO_4 in the acylation of aromatic compounds with different reagents (Tables 4.2 and 4.3). When the acylation was carried out with benzoic/acetic anhydride (aromatics/carboxylic acid/Zr(IV) molar ratio = 120/1/0.5), the reactions took place more readily; full conversion of anhydrides was observed for anisole at 120 ^oC after 12 h with p-substituted products as major products. When toluene is used instead of anisole, 15% and 43% conversion were obtained under the same reaction condition using benzoic and acetic anhydride, respectively. Use of acyl chloride (aromatics/acyl chloride/Zr(IV) molar ratio = 20/1/0.25) also gives similar reactivity at 120 ^oC. MOF-808-2.5SO4 catalyzed the reaction of 2-chlorobenzoyl

chloride with anisole and toluene, affording substituted benzophenone after 12 h in 100% and 51% yield, respectively. In all cases, once the catalyst was removed during the reaction and the mixture was again heated, no further reaction was observed. Therefore, we concluded that the present catalytic reaction is heterogeneous. MOF-808 also gave no catalytic activity towards the formation of ketones.

Limonene, with its d-isomer extracted from rectified orange essential oil, is a terpene hydrocarbon. It is known that limonene will go through disproportionation reaction (Scheme 4.4) in the presence of palladium-barium sulfate catalyst and palladized asbestos under rather vigorous conditions to give mostly p-cymene (compound 6) and menthenes (compound 4 and 5). It can also undergo isomerization reactions at 100 ^{o}C to give a series of compounds listed also in Scheme 4.4.[23]

In our study, limonene was also found readily isomerized over MOF-808-2.5SO_4 at 60 ^{o}C. Full conversion of Limonene (Limonene/Zr(IV) molar ratio = 25/1) was observed after 40 min. The principal products were the isomerization compounds terpinolene (13%), alpha-terpinene (32%), and gamma-terpinene (22%); disproportionation products menthene (12%) and p-cymene (18%) were also found. The ratio of isomerization products to disproportionation products is 2.2. The concentrations of these products remained constant after another 3 h heating at 60 ^{o}C. No reaction (neither isomerization nor disproportionation reactions) was observed if MOF-808 added or MOF-808-2.5SO_4 filtrated out.

Scheme 4.4. Isomerization of limonene.

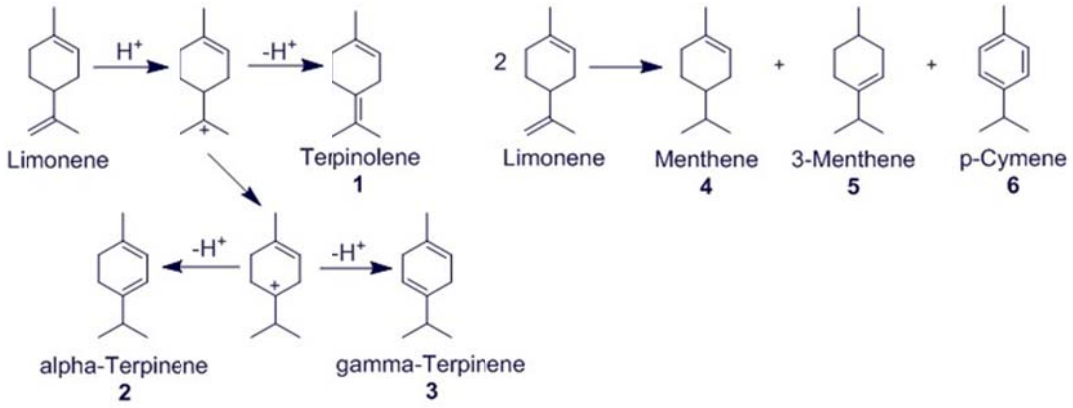

Scheme 4.5. Esterification of methanol with oleic acid.

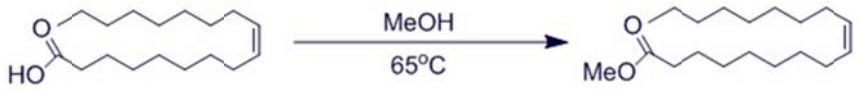

MOF-808-2.5SO_4 was also observed to be catalytically active in the esterification of oleic acid with methanol (methanol/oleic acid/Zr(IV) molar ratio = 55/1/0.15). The reactions were carried out at 65 ^{o}C using a 5 mL Ace pressure tube. The yield of methyl oleate was 80% for 6 h, and below 15% if MOF-808 or no catalysts were applied. It was also shown that MOF-808-

$2.5SO_4$ recovered from the reaction mixture could be reactivated by washing with anhydrous chloroform and heated at 150 °C for 2 h. The reactivated catalysts showed no significant activity loss for the three cycles tested (Figure A4.5).

Various hydrocarbon products can be obtained through gas-phase methylcyclopentane (MCP) conversion via typical reforming pathways such as cracking, dehydrogenation, ring-opening followed with isomerization, and ring-enlargement followed with hydrogenation or dehydrogenation (Scheme 4.6).

The MOF-808-$2.5SO_4$ was applied for gas-phase methylcyclopentane (MCP) conversion, in which MOF-808-$2.5SO_4$ showed catalytic activity at 150 - 200 °C (Figure 4.1). However, loss of crystallinity of MOF-808-$2.5SO_4$ was found after the reaction. Loading Pt nanoparticles to MOF-808-$2.5SO_4$ (i.e., Pt/MOF-808-$2.5SO_4$) can largely increase the catalyst stability. In particular, its catalytic activity based on the number of catalytic sites on the Pt surface is much higher than that of Pt nanoparticles supported on catalytically inactive silica surface (Pt/SiO2) also with distinct product selectivity (Figure 4.1). This can be interpreted with the synergistic catalytic play of Pt nanoparticles and the acidic sites on MOF-808-$2.5SO_4$.

Scheme 4.6. Five reaction pathways of catalytic reforming of MCP, which are indicated by different numbers and colors. As the first pathway, MCP can be converted into the dehydrogenated version of MCP (1, green). Second pathway is ring-opening of MCP followed with isomerization to branched isomers as well as the linear isomer (2, pink). The C5-based cyclic ring of MCP can be further enlarged to C6-cyclic rings through hydrogenation (3, blue) or dehydrogenation (4, red) via cyclohexene intermediate species. The last reaction pathway is cracking (5, gray) to produce C1 ~ C5 based hydrocarbons. Among the five reaction pathways, no cracking was observed in the current study.

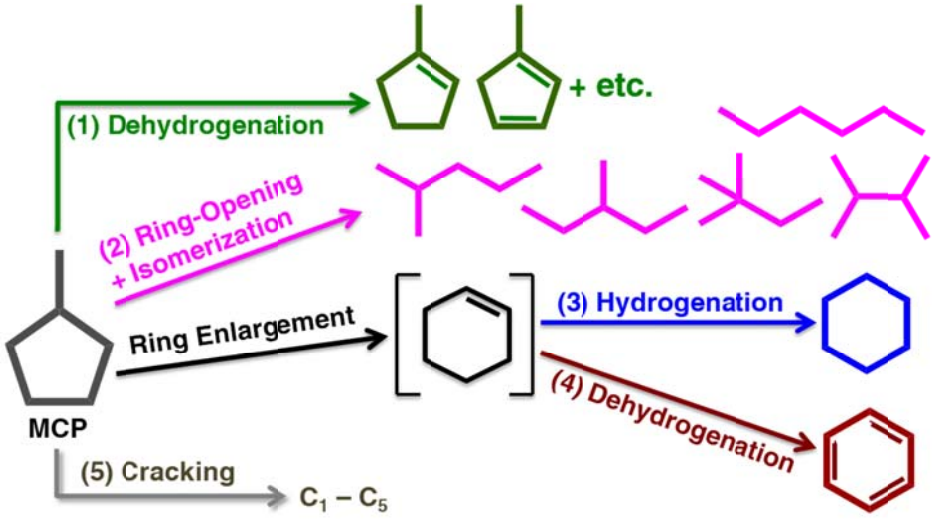

Catalyst	Selectivity (%)			
	Dehydrogenation	Isomerization	Cyclohexane	Benzene
MOF-808-2.5SO_4	61.4	38.6	0	0
Pt/MOF-808-P	13.6	19.0	0	67.4
Pt/MOF-808-2.5$S0_4$	15.8	11.0	24.9	48.3
Pt/SiO2	18.2	81.8	0	0

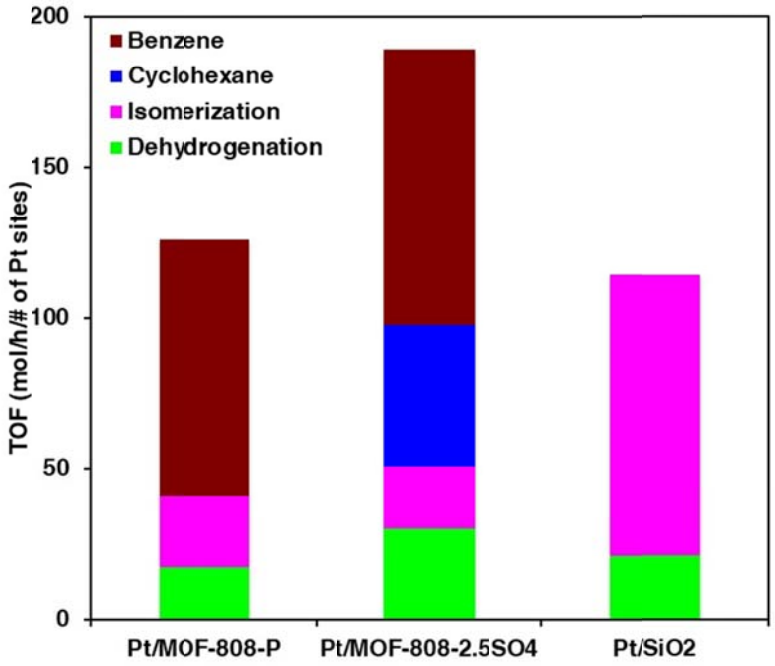

Figure 4.1. Product selectivity data (Table in top) and turnover frequency to various products (Figure in bottom). According to the catalyst, product selectivities and their turnover frequencies (TOFs) can be controlled.

Ammonia adsorption properties of MOF-808-2.5SO_4. The goal of this study was not only to probe the large ammonia uptake capacity for MOF-808-2.5SO_4, but also to examine the reversibility of this adsorption process. Therefore, multiple ammonia adsorption cycles were carried out consecutively, and the surface area of the MOF was retested after the final ammonia run to evaluate the durability of the system. Between each ammonia adsorption cycle, the material was regenerated under vacuum for 2 h at room temperature.

First, MOF-808 was chosen as the control group to test the effectiveness of its pores (18.4 Å in diameter) for the storage of ammonia. The nitrogen adsorption isotherms before and after ammonia adsorption for MOF-808 are shown in Figure A4.8. Fresh MOF-808 exhibits the expected uptake of 580 $cm^3\ g^{-1}$, which is reasonably close to the reported value of MOF-808.[16]

Ammonia isotherms were measured at 298 K for this sample, shown in Figure 4.2, and found to have significant uptake capacities at 760 Torr (250 $cm^3\ g^{-1}$ or 11.2 mmol g^{-1}). The isotherm profile is best described as Type I. The uptake value outperforms the state-of -the-art materials Zeolite 13X (9 mmol g^{-1}) and Amberlyst 15 (11 mmol g^{-1}).[24] The hysteresis observed for MOF-808 is attributed to the strong adsorption behavior of ammonia. In addition, the cycling

experiments for MOF-808 showed a significant decrease in the uptake capacity of the material (20 %, 2.2 mmol g^{-1}) when first cycle is compared to the second. This difference is attributed to the ammonia molecules that are strongly bound to the MOF, and cannot be removed by applying vaccum at room temperature.

After three ammonia adsorption-desorption cycles, the MOF-808 sample shows a decrease of its surface area (N_2 uptake at P/P_0 = 0.9350 cm^3 g^{-1} compared to the as synthetized material = ….). While the adsorption isotherm can still be described as Type IV, both nitrogen uptakes of the steps positions ($P/P_0 < 0.05$ and P/P_0 = 0.05 - 0.1), are diminished. The decrease of the uptake in the first step could be explained by the occupation of adsorption sites with strongly bound ammonia molecules. Nevertheless, the decrease at the second step indicates a partial destruction of the MOF framework upon this ammonia adsorption-desorption process. The same behavior is observed when water is the adsorbate, instead of ammonia.[25] Considering the similarities between water and ammonia, it is reasonable to expect the same degradation behavior in both cases. However, the material still maintains 80 % of its ammonia uptake capacity (9.0 mmol g^{-1}) at 760 Torr.

MOF-808-2.5SO_4 before ammonia adsorption experiments show Type IV N_2 isotherm at 77 K. (Figure A4.9) The fresh MOF-808-2.5SO_4 sample has a BET surface area of 2300 m^2 g^{-1}, comparable to the reported value.[25]

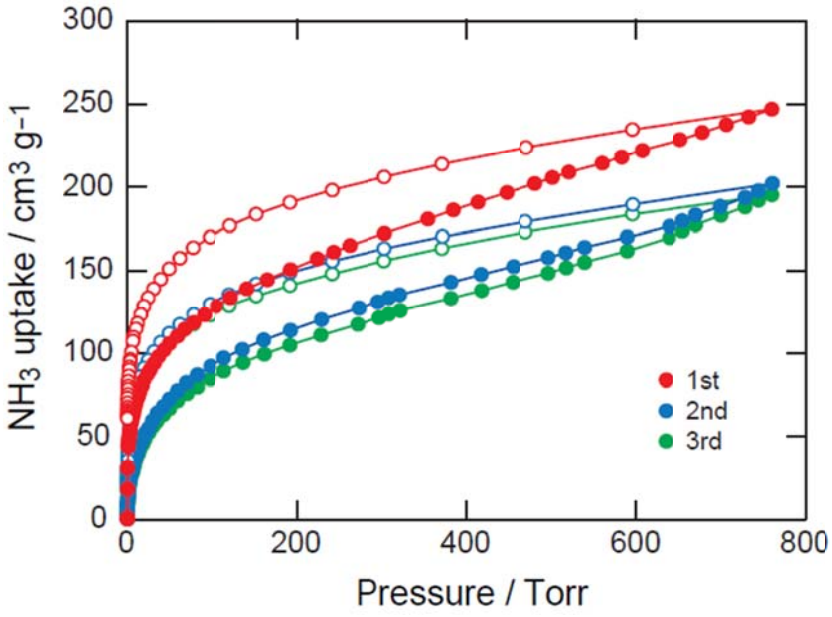

Figure 4.2. Ammonia uptake in MOF-808 at 298 K. Three consecutive cycles are measured. The sample was evacuated for 2 hours at 25 °C between the cycles. Adsorption and desorption points are represented by closed and open symbols, respectively.

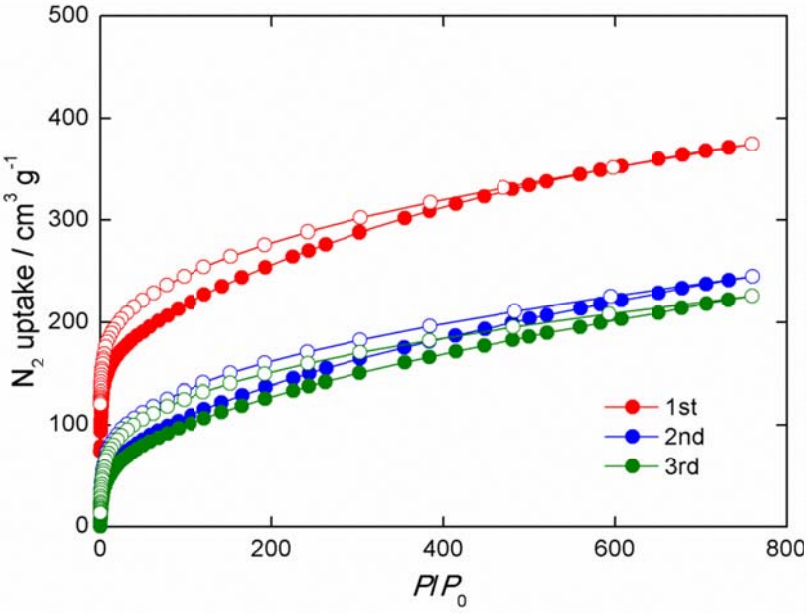

Figure 4.3. Ammonia uptake in MOF-808-2.5SO_4 at 298 K. Three consecutive cycles are measured. The sample was evacuated for 2 hours at 25 °C between the cycles. Adsorption and desorption points are represented by closed and open symbols, respectively.

Ammonia isotherms were measured at 298 K for this sample, shown in Figure 4.3, and found to have significant uptake capacities at 760 Torr (375 cm^3 g^{-1} or 16.7 mmol g^{-1}). This value is 50 % higher than that of MOF-808, despite of similar pore metrics of the two. The value is also the highest among all reported MOF and COF materials, including MIL-101-SO_3H (16.5 mmol g^{-1}),[26] UiO-66-NH_3Cl (11.7 mmol g^{-1}),[26] MOF-205-OH (16.4 mmol g^{-1}),[27] and COF-10 (15.2 mmol g^{-1}).[28] The isotherm profile is best described as Type I. More interestingly, the uptake at low pressure (P < 1.5 Torr) contributes to 32 % of MOF-808-2.5SO_4's total ammonia uptake (5.3 mmol g^{-1}), an ideal compound for removing ammonia at low concentration. This value also stands out in MOF and COF materials.[26] As mentioned above, MOF-808-2.5SO_4 has both Lewis and Brønsted acidic sites, both will contribute to the material's high ammonia uptake capacity, especially in the low pressure range.

The cycle performance results show that for MOF-808-2.5SO_4, a significant decrease (36 %, 6.0 mmol g^{-1}) is found from the first to the second cycle and a constant uptake thereafter. The difference is approximately two times larger than that in MOF-808, which can be explained by the fact that MOF-808-2.5SO_4 has significantly larger amount of both Lewis and Brønsted acidity sites that the latter. Similar to MOF-808, this difference is mainly because of the decrease at low pressure range (P < 5 Torr). This behavior can be explained as some of the ammonia molecules are strongly bound to the MOF framework, especially those acidic sites and cannot be removed by simply evacuating the MOF at room temperature.

After three ammonia adsorption-desorption cycles, the MOF-808-2.5SO_4 sample shows a decreased pore volume with only 400 cm^3 g^{-1} N_2 uptake at P/P_0 = 0.9 (Figure A4.9). The isotherm profile can still be described as Type IV, however, uptakes at both steps (P/P_0 < 0.05 and P/P_0 = 0.05 - 0.1) are decreased. While the first decrease may be explained by the occupation

of adsorption sites by strongly bound ammonia molecules, the uptake decrease at second step indicates a similar partial destruction of the MOF framework upon this ammonia adsorption-desorption process. Despite of this, MOF-808-2.5SO_4 still has significant uptake capacities at 760 Torr (250 cm^3 g^{-1} or 11.2 mmol g^{-1}), a number comparable to fresh MOF-808 and also other materials of the same kind.

Conclusion

In this chapter, we report the catalytic performance, and ammonia adsorption properties for MOF-808 and sulfated MOF-808 materials. While MOF-808 is weakly Lewis acidic and does not exhibit interesting catalytic activity, sulfation of MOF-808 significantly increases the quantity of Lewis acid sites within the MOF and more importantly, generates strong Brønsted acid sites that significantly change the catalytic behavior of the material, as proved by two test reactions. Later, MOF-808-2.5SO4 has found to be catalytically active in various acid-catalyzed reactions including Friedel-Crafts acylation, esterification, and isomerization, as well as in the conversion of methylcyclopentane (MCP) into various hydrocarbons at 150-200 ^oC; the latter being a test reaction for catalytic reforming. MOF-808-2.5SO_4 is also found to be good ammonia capture material that shows high uptake capacity at both low pressure (P < 1.5 Torr) and ambient pressure (P = 760 Torr).

Appendices

Figure A4.1. Conversion of (±)-citronellal over MOF-808-P (blue), MOF-808-0.65SO_4 (wine), MOF-808-1.3SO_4 (orange) and MOF-808-2.5SO_4 (red).

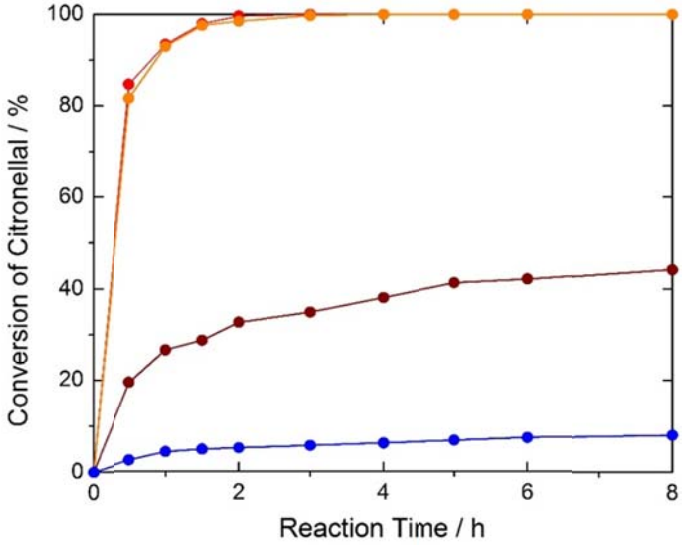

Figure A4.2. Reusability test on MOF-808-2.5SO_4 over (±)-citronellal cyclization: run 1 (red solid), run 2 (olive), run 3 (violet); Filtration test on MOF-808-2.5SO_4 over (±)-citronellal cyclization: after 0.5 h in run 1, the reaction mixture was split in two parts and the catalysts was withdrawn from one sample (red hollow).

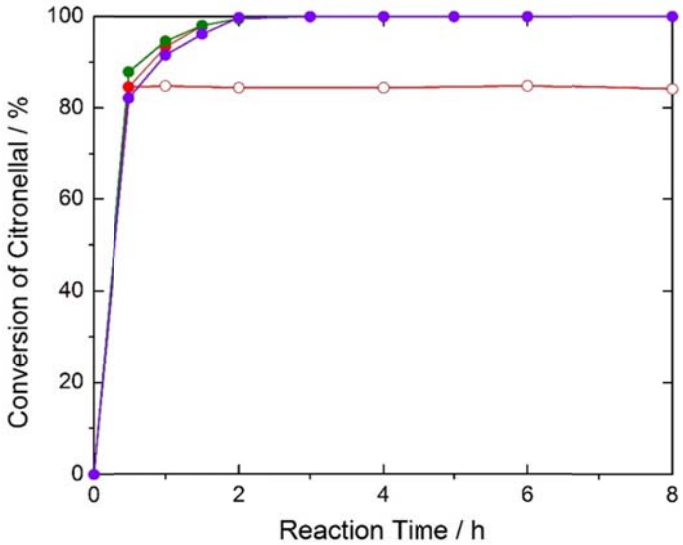

Figure A4.3. Conversion of alpha-pinene over MOF-808-P (blue, hidden under the wine curve), MOF-808-0.65SO_4 (wine), MOF-808-1.3SO_4 (orange) and MOF-808-2.5SO_4 (red).

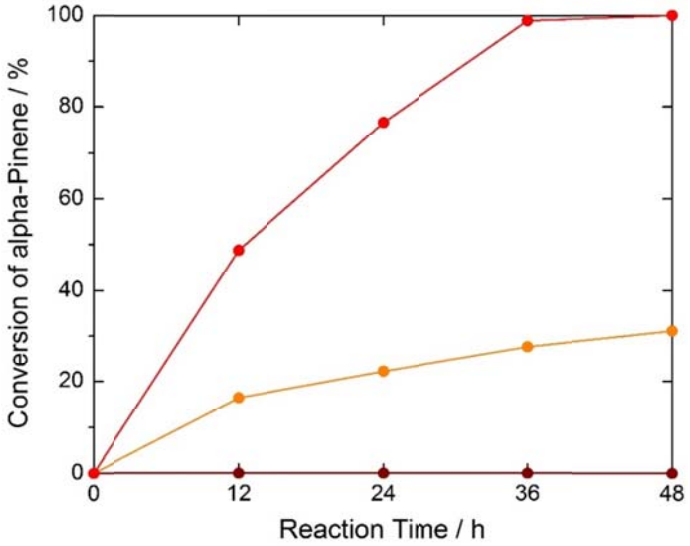

Figure A4.4. Reusability test on MOF-808-2.5SO_4 over alpha-pinene isomerization: run 1 (red), run 2 (olive solid); Filtration test on MOF-808-2.5SO_4 over alpha-pinene isomerization: after 12 h in run 2, the reaction mixture was split in two parts and the catalysts was withdrawn from one sample (olive hollow).

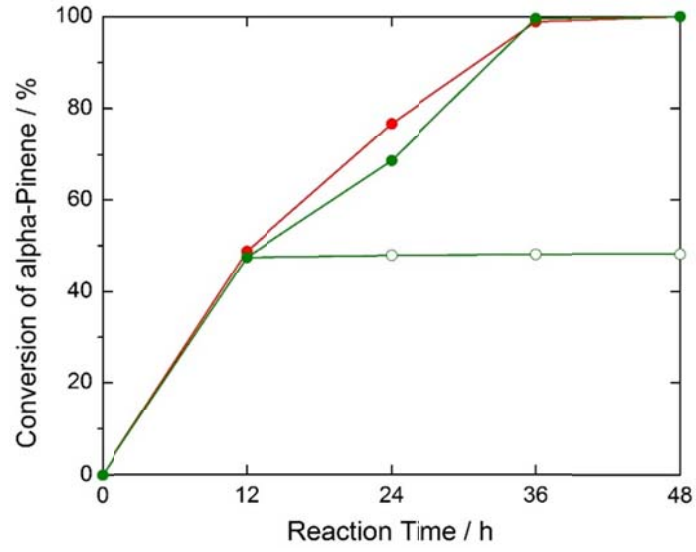

Figure A4.5. Reusability test on MOF-808-2.5SO_4 over esterification reaction of methanol with oleic acid: run 1 (black), run 2 (red), run 3 (blue); Blank tests were performed with no catalyst (pink) and with MOF-808 (green).

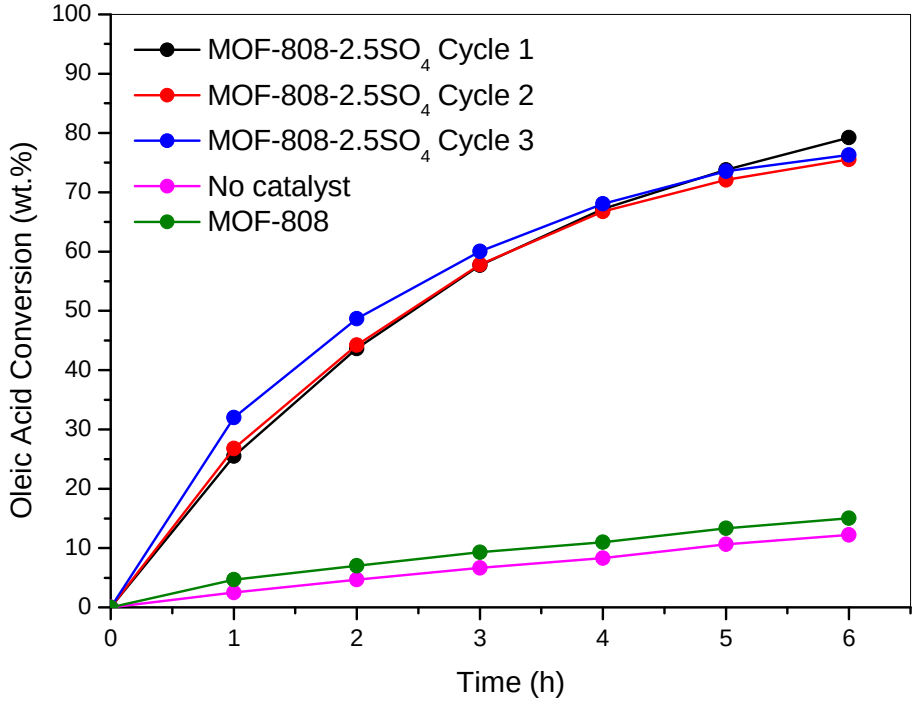

Figure A4.6. Powder X-ray diffraction patterns of MOF-808-2.5SO_4 after anisole acylation reactions with benzoic acid (pink), benzoic anhydride (blue), acetic acid (red), acetic anhydride (black), and 2-chlorobenzoylchloride (green).

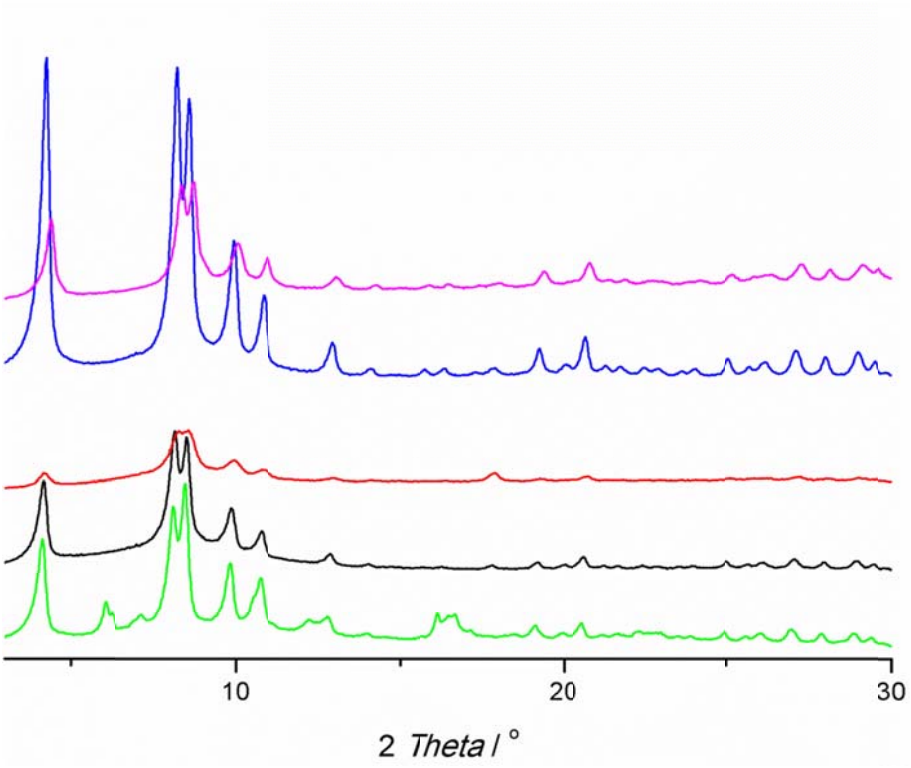

Figure A4.7. Powder X-ray diffraction patterns of MOF-808-2.5SO_4 after toluene acylation reactions with benzoic acid (pink), benzoic anhydride (blue), acetic acid (red), acetic anhydride (black), and 2-chlorobenzoylchloride (green).

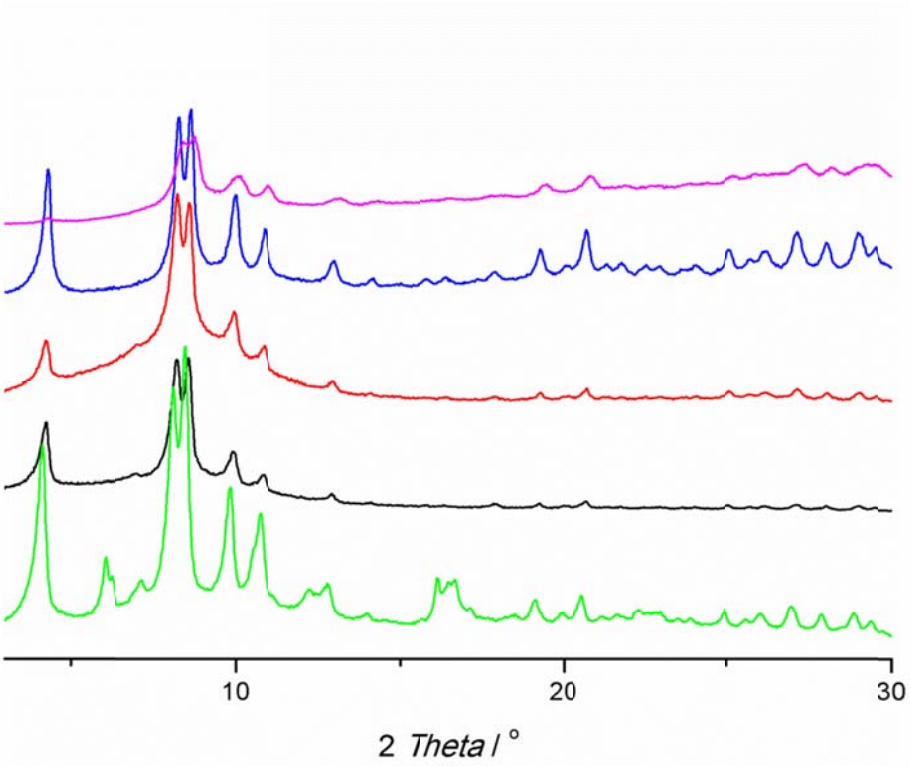

Figure A4.8. Nitrogen adsorption isotherms for MOF-808 before (red) and after ammonia adsorption (blue), measured at 77K with adsorption and desorption branches represented by closed and open circles, respectively. $P/P_{0,}$ relative pressure.

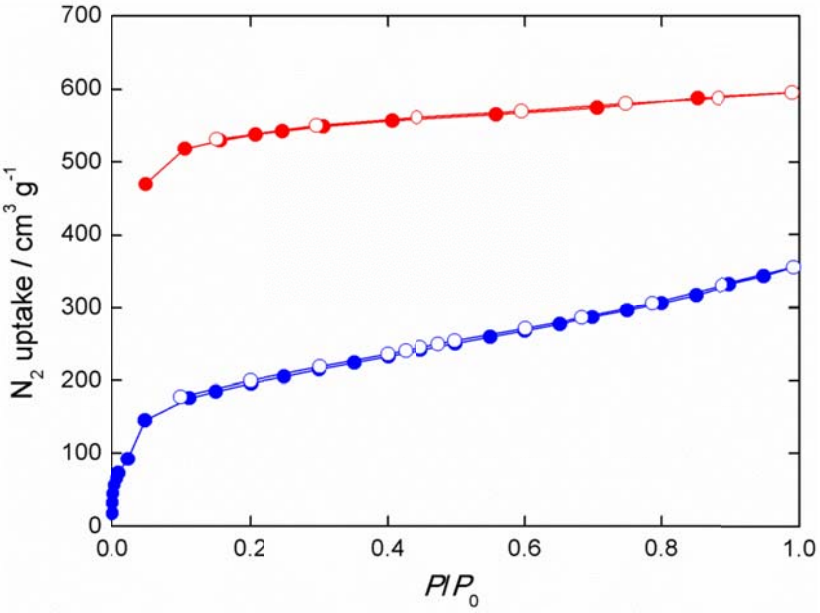

Figure A4.9. Nitrogen adsorption isotherms for MOF-808-2.5SO_4 before (red) and after ammonia adsorption (blue), measured at 77K with adsorption and desorption branches represented by closed and open circles, respectively. $P/P_{0,}$ relative pressure.

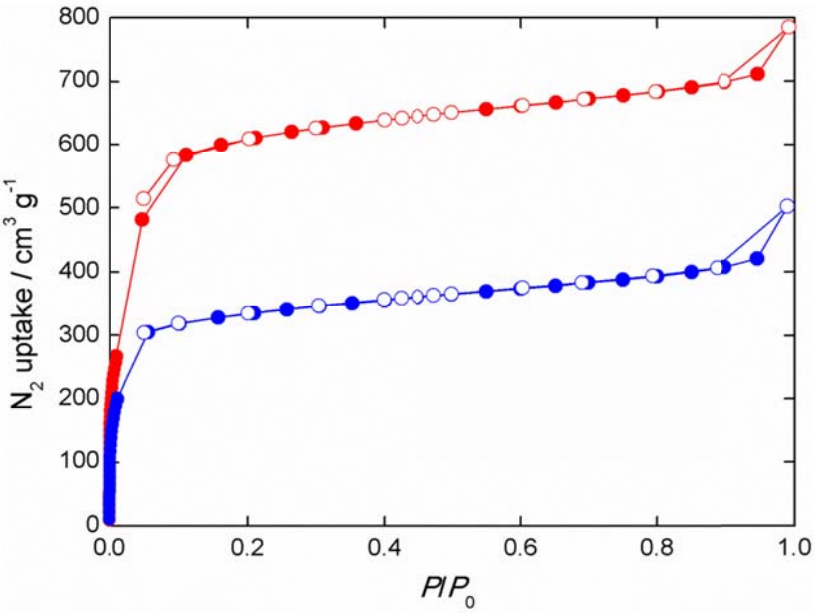

References and Notes

(1) Fujita, M.; Kwon, Y. J.; Washizu, S.; Ogura, K. J. Am. Chem. Soc. **1994**, 116, 1151.

(2) Chen, B.; Eddaoudi, M.; Reineke, T. M.; Kampf, J. W.; O'Keeffe, M.; Yaghi, O. M. J. Am. Chem. Soc. **2000**, 122, 11559.

(3) Chui, S. S. Y.; Lo, S. M. F.; Charmant, J. P. H.; Orpen, A. G.; Williams, I. D. Science **1999**, 283, 1148.

(4) (a) Férey, G.; Mellot-Draznieks, C.; Serre, C.; Millange, F.; Dutour, J.; Surblé, S.; Margiolaki, I. Science **2005**, 309, 2040. (b) Bauer, S.; Serre, C.; Devic, T.; Horcajada, P.; Marrot, J.; Férey, G.; Stock, N. Inorg. Chem. **2008**, 47, 7568. (c) Serra-Crespo, P.; Ramos-Fernandez, E. V.; Gascon, J.; Kapteijn, F. Chem. Mater. **2011**, 23, 2565.

(5) Mondloch, J. E.; Katz, M. J.; Isley III, W. C.; Ghosh, P.; Liao, P.; Bury, W.; Wagner, G. W.; Hall, M. G.; DeCoste, J. B.; Peterson, G. W.; Snurr, R. Q.; Cramer, C. J.; Hupp, J. T.; Farha, O. K. Nat. Mater. **2015**, 14, 512.

(6) (a) Schlichte, K.; Kratzke, T.; Kaskel, S. Microporous Mesoporous Mater. **2004**, 73, 81. (b) Henschel, A.; Gedrich, K.; Kraehnert, R.; Kaskel, S. Chem. Commun. **2008**, 4192. (c) Alaerts, L.; Séguin, E.; Poelman, H.; Thibault-Starzyk, F.; Jacobs, P. A.; De Vos, D. E. Chem.-Eur. J. **2006**, 12, 7353. (d) Vandichel, M.; Vermoortele, F.; Cottenie, S.; De Vos, D. E.; Waroquier, M.; Van Speybroeck, V. J. Catal. **2013**, 305, 118. (e) Cirujano, F. G.; Llabrés i Xamena, F. X.; Corma, A. Dalton Trans. **2012**, 41, 4249. (f) Hwang, Y. K.; Hong, D.-Y.; Chang, J.-S.; Jhung, S. H.; Seo, Y.-K.; Kim, J.; Vimont, A.; Daturi, M.; Serre, C.; Férey, G. Angew. Chem. Int. Ed. **2008**, 47, 4144. (g) Hartmann, M.; Fischer, M. Microporous Mesoporous Mater. **2012**, 164, 38. (h) Kim, J.; Bhattacharjee, S.; Jeong, K.-E.; Jeong, S.-Y.; Ahn, W.-S. Chem. Commun. **2009**, 3904. (i) Maksimchuk, N. V.; Timofeeva, M. N.; Melgunov, M. S.; Shmakov, A. N.; Chesalov, Y. A.; Dybtsev, D. N.; Fedin, V. P.; Kholdeeva, O. A. J. Catal. **2008**, 257, 315. (j) Maksimchuk, N. V.; Kovalenko, K. A.; Fedin, V. P.; Kholdeeva, O. A. Adv. Synth. Catal. **2010**, 352, 2943.

(7) (a) Gascon, J.; Corma, A.; Kapteijn, F.; Llabrés i Xamena, F. X. ACS Catal. **2014**, 4, 361. (b) Liu, J.; Chen, L.; Cui, H.; Zhang, J.; Zhang, L.; Su, C.-Y. Chem. Soc. Rev. **2014**, 43, 6011. (c) Zhang, T.; Lin, W. Chem. Soc. Rev. **2014**, 43, 5982. (d) Yoon, M.; Srirambalaji, R.; Kim, K. Homochiral Chem. Rev. **2012**, 112, 1196. (e) Lee, J. Y.; Farha, O. K.; Roberts, J.; Scheidt, K. A.; Nguyen, S. T.; Hupp, J. T. Chem. Soc. Rev. **2009**, 38, 1450.

(8) Jiang, J.; Yaghi, O. M. Chem. Rev. **2015**, 115, 6966.

(9) (a) Wee, L. H.; Bonino, F.; Lamberti, C.; Bordiga, S.; Martens, J. A Green Chem. **2014**, 16, 1351. (b) Khder, A. E. R. S.; Hassan, H. M. A.; El-Shall, M. S. Appl. Catal. A **2014**, 487, 110. (c) Bromberg, L.; Hatton, T. A. ACS Appl. Mater. Interfaces **2011**, 3, 4756. (d) Zhang, Y.; Degirmenci, V.; Li, C.; Hensen, E. J. M. ChemSusChem **2011**, 4, 59. (e) Janssens, N.; Wee, L. H.; Bajpe, S.; Breynaert, E.; Kirschhock, C. E. A.; Martens, J. A. Chem. Sci. **2012**, 3, 1847. (f) Liang, D.-D.; Liu, S.-X.; Ma, F.-J; Wei, F.; Chen, Y.-G. Adv. Synth. Catal. **2011**, 353, 733.

(10) (a) Bromberg, L.; Su, X.; Hatton, T. A. ACS Appl. Mater. Interfaces **2013**, 5, 5468. (b) Ramos-Fernandez, E. V.; Pieters, C.; van der Linden, B.; Juan-Alcañiz, J.; Serra-Crespo, P.; Verhoeven, M. W. G. M.; Niemantsverdriet, H.; Gascon, J.; Kapteijn, F. J. Catal. **2012**, 289, 42. (c) Chen, J.; Wang, S.; Huang, J.; Chen, L.; Ma, L.; Huang, X. ChemSusChem **2013**, 6, 1545. (d) Wang, S.; Chen, J.; Chen, L. Catal. Lett. **2014**, 144, 1728.

(11) (a) Evans, O. R.; Ngo, H. L.; Lin, W. J. Am. Chem. Soc. **2001**, 123, 10395. (b) Zheng, M.; Liu, Y.; Wang, C.; Liu, S.; Lin, W. Chem. Sci. **2012**, 3, 2623.

(12) (a) Ferm, M.; Hellsten, S. Atmos. Environ. **2012**, 61, 30. (b) Sutton, M. A.; Erisman, J. W.; Dentener, F.; Möller, D. Environ. Pollut. **2008**, 156, 583.

(13) Permissible Exposure Limits for Chemical Contaminants; Cal/OSHA: Oakland, CA; http://www.dir.ca.gov/title8/5155table_ac1.html (accessed on April 12, 2015).

(14) Decoste, J. B.; Peterson G. W. Chem. Rev. **2014**, 114, 5695.

(15) (a) Britt, D.; Tranchemontagne, D.; Yaghi, O. M. Proc. Natl. Acad. Sci. **2008**, 105, 11623. (b) Glover, T. G.; Peterson, G. W.; Schindler, B. J.; Britt, D.; Yaghi, O. M. Chem. Eng. Sci. **2011**, 66, 163. (c) Petit, C.; Huang, L.; Jagiello, J.; Kenvin, J.; Gubbins, K. E.; Bandosz, T. J. Langmuir **2011**, 27, 13043.

(16) Jiang, J.; Gándara, F.; Zhang, Y.-B.; Na, K.; Yaghi, O. M.; Klemperer, W. G. J. Am. Chem. Soc. **2014**, 136, 12844.

(17) Alayoglu,S.; Aliaga, C.; Sprung, C.; Somorjai, G. A. Catal. Lett. **2011**, 141, 914.

(18) An, K.; Alayoglu, S.; Musselwhite, N.; Plamthottam, S.; Melaet, G.; Lindeman, A. E.; Somorjai, G. A. J. Am. Chem. Soc. **2013**, 135, 16689.

(19) Aijaz, A.; Karkamkar, A.; Choi, Y. J.; Tsumori, N.; Rönnebro, E.; Autrey, T.; Shioyama, H.; Xu, Q. J. Am. Chem. Soc. **2012**, 134, 13926.

(20) Smith, M.; March, J. March's Advanced Organic Chemistry: Reactions, Mechanisms, and Structure, 6th ed.; Wiley: Hoboken, **2007**.

(21) (a) Vermoortele, F.; Bueken, B.; Le Bars, G.; Van de Voorde, B.; Vandichel, M.; Houthoofd, K.; Vimont, A.; Daturi, M.; Waroquier, M.; Van Speybroeck, V.; Kirschhock, C; De Vos, D. E. J. Am. Chem. Soc. **2013**, 135, 11465. (b) Vermoortele, F.; Vandichel, M.; Van de Voorde, B.; Ameloot, R.; Waroquier, M.; Van Speybroeck, V.; De Vos, D. E. Angew. Chem.; Int. Ed. **2012**, 51, 4887. (c) Vermoortele, F.; Ameloot, R.; Alaerts, L.; Matthessen, R.; Carlier, B.; Fernandez, E. V. R.; Gascon, J.; Kapteijn, F.; De Vos, D. E. J. Mater. Chem. **2012**, 22, 10313.

(22) (a) Comelli, N. A.; Ponzi, E. N.; Ponzi, M. I. Chem. Eng. J. **2006**, 117, 93. (b) Ecormier, M. A.; Wilson, K.; Lee, A. F. J. Catal. **2003**, 215, 57. (c) van der Waal, J. C.; van Bekkum, H.; Vital, J. M. J. Mol. Catal. A **1996**, 105, 185. (d) Rachwalik, R.; Olejniczak, Z.; Jiao, J.; Huang, J.; Hunger, M.; Sulikowski, B. J. Catal. **2007**, 252, 161.

(23) Hunter, G. L. K.; Brogden Jr., W. B. J. Org. Chem. **1963**, 26, 1679.

(24) Helminen, J.; Helenius, J.; Paatero, E. J. Chem. Eng. Data **2001**, 46, 391.

(25) Furukawa, H.; Gándara, F.; Zhang, Y.-B.; Jiang, J.; Queen, W. L.; Hudson, M. R.; Yaghi, O. M. J. Am. Chem. Soc. **2014**, 136, 4369.

(26) Van Humbeck, J. F.; McDonald, T. M.; Jing, X.; Wiers, B. M.; Zhu, G.; Long, J. R. J. Am. Chem. Soc. **2014**, 136, 2432.

(27) Spanopoulos, I.; Xydia, P.; Malliakas, C. D.; Trikalitis, P. N. Inorg. Chem. **2013**, 52, 855.

(28) Doonan, C. J.; Tranchemontagne, D. J.; Glover, T. G.; Hunt, J. R.; Yaghi, O. M. Nat. Chem. **2010**, 2, 235.

Chapter V

Synthesis of Zinc Metal-Organic Frameworks and their Methane Adsorption Properties

Introduction

Hydrocarbons are the main components of the fuel used to run our automobiles and power our lives. Among them, methane, the lightest of hydrocarbons, draws a lot of attention because it has a higher research octane number (RON = 107), and lower emission of CO_2. It is predicted that the demand of natural gas in unit of energy is to exceeding 200 exajoules per year in 2040, as the second largest energy source.[1] Although natural gas represents over 60 % of the fossil fuels on earth, it remains the least utilized one when compared to oil and coal. Currently, natural gas is utilized mainly as a fuel for electric power plants (31 %), industry (28 %), and houses (19 %).[2]

Growing interest is focused on expanding the use of methane for fueling automobiles. However, one main challenge for this expansion lies in the low energy density of methane in its natural state under ambient conditions (0.04 MJ L^{-1}, compared to 32.4 MJ L^{-1} for gasoline).[3] Three strategies are being developed to overcome this challenge. First is the use of liquefied natural gas (LNG). Here, methane is stored under cryogenic conditions which leads to high reduction in volume to 0.16 vol.% compared to gaseous methane, resulting in the high volumetric energy density of 20-23 MJ L^{-1}. However, the main drawback of this strategy is the high-costly cryogenic system necessary to cool down the whole storage tank to -162 ^{o}C. To date, this technique is mainly used in long distance natural gas transportation.[4] Another strategy is the use of compressed natural gas (CNG). Here, methane is stored under high pressure in fuel tanks attached to the automobile or truck (usually 200 to 250 bar). Under this pressure, the volume of methane is compressed to 1 % of the original value, thus increasing its energy density to approximately 10 MJ L^{-1}. Vehicles using this technology have been designed, and manufactured mainly in Europe, South America, and Asia. Safety concerns have been risen about carrying a highly pressurized methane tank in the automobile, in case of high temperature and/or fire.[5] Lastly is the use of adsorbed natural gas (ANG), in which methane is stored with the help of porous sorbent materials under significantly reduced pressure (35 to 65 bar). The excessive adsorption of methane in porous material is expected to compensate the capacity loss due to operating at lower pressures. Porous carbon and newly developed MOFs are promising candidates as these sorbent materials.[6] ANG is also combined with CNG to give high pressure ANG, where a high pressure CNG tank is filled by sorbent materials. This technique aims to increase the capacity of natural gas storage. The presence of sorbent materials contributes to the increased safety for the high pressure tanks as desorption of methane gas from the sorbent materials takes up significant amount of heat, cools down the whole tank, slows down the methane release and prevents the tank from quick explosion. Vehicle models using this high pressure ANG technique have already been realized by BASF.[7]

The fast pace of development of ANG and high pressure ANG techniques raised higher goals for the sorbent materials. In 2012, U.S. Department of Energy (DOE) has updated the target for methane storage materials for ANG applications, to a gravimetric capacity of 50 wt%

and a volumetric capacity of 250 g L^{-1}.[8] Among these two goals, achieving the desired volumetric capacity is more important when considering the limited size of an automobile fuel tank. Accordingly, new porous adsorbents are required to meet these challenging storage targets. MOFs are known to be useful in the storage of gases, including methane. Among the many MOFs studied for methane storage, HKUST-1, Ni-MOF-74, Co-MOF-74, PCN-14 at 35 bar,[9] plus NOTT-101, NOTT-109, UTSA-20, UTSA-76, Co(BDP) at 65 bar,[10] and MOF-5, MOF-177, MOF-205, MOF-210 at 250 bar[11] as have been outstanding sorbent materials, having some of the highest reported total volumetric storage capacities. Since the automobile industry requires that 5 bar of methane pressure remains unused in the fuel tank, working capacity is the key parameter to evaluating the performance of methane storage materials. At present, the highest working capacities reported for a MOF are 109 g L^{-1} (153 cm^3 cm^{-3}) at 35 bar for HKUST-1 and 164 g L^{-1} (230 cm^3 cm^{-3}) at 80 bar for MOF-519.[11]

Extensive work is ongoing to find materials whose working capacities are larger than those found for the above mentioned materials. Several strategies have been proposed for improved methane storage in MOFs: (a) increase of the number of open metal sites. As shown for HKUST-1, Ni-MOF-74, and PCN-14, these coordinatively unsaturated sites have proved effective in adsorbing methane. However, due to the strong adsorbate-open metal site interactions, MOFs with open metal sites typically exhibit high methane uptake at 5 bar as well, thus limiting their working capacities. Additionally, these open metal sites are sensitive to impurities such as water and hydrogen sulfide, which are often found in natural gas;[12] (b) GCMC simulation results have shown the beneficial effects of MOFs having large volumetric surface area with optimal void fraction of 0.8 and optimal pore size of 4, 8, and 12 Å, suitable for one, two, and three methane molecules to fit in, respectively;[13] (c) small polar functional groups, short alkyl groups and aromatic π-systems are believed to contribute to stronger interaction between framework and methane molecules, thus increase the uptake of methane.[14]

Here, we report the synthesis, crystal structure, porosity, and methane adsorption properties for five zinc based MOFs synthesized using organic linkers containing C=C double bonds [termed MOF-950: $Zr_4O(BTAC)_2$, BTAC = benzene-1,3,5-tri-β-acrylic acid, MOF-905: $Zr_4O(BDC)(BTAC)_{4/3}$, BDC = benzene-1,4-dicarboxylic acid, and functionalized MOF-905: MOF-905-NO_2, MOF-905-Naph, and MOF-905-Me_2], one of which (MOF-905) has working capacities (desorption at 5 bar) of 145 g L^{-1} at 80 bar and 298 K, a value rivaling that of HKUST-1 (143 g L^{-1}), the benchmark compound for methane storage in MOFs.

Experimental Section

Chemicals and supplies. Pyridine (≥ 99%), piperidine (99%), malonic acid (99%), Acetic Acid (≥ 99%), and sulfuric acid (95.0–98.0%) were purchased from Sigma-Aldrich. 1,3,5-Triformylbenzene (98%) was obtained from Acros Organics. Anhydrous N,N-dimethylformamide (DMF) was obtained from EMD Millipore Chemicals; chloroform (HPLC grade with 50 ppm pentene as preservative) was obtained from Fisher Scientific; ethanol (anhydrous, ≥ 99.5%), zinc nitrate hexahydrate [$Zn(NO_3)_2 \cdot 6H_2O$] and Sigmacote® siliconizing reagent were obtained from Sigma-Aldrich. Terephthalic acid (H_2BDC) was obtained from Aldrich. Nitroterephthalic acid (H_2BDC-NO_2) and 2,5-dimethylterephthalic acid (H_2BDC-Me_2) were purchased from TCI. Naphthalene-1,4-dicarboxlic acid (H_2BDC-Nap) was obtained from

Alfa Aesar. All starting materials and solvents, unless otherwise specified, were used without further purification.

Analytical techniques. Single-crystal X-ray diffraction (SXRD) data were collected on a Bruker D8-Venture diffractometer equipped with Mo- (λ = 0.71073 Å) and Cu-target (λ = 1.54184 Å) micro-focus X-ray tubes and a PHOTON 100 CMOS detector. Powder X-ray diffraction patterns (PXRD) were recorder using either a Bruker D8 Advance diffractometer (Göbel-mirror monochromated Cu Kα radiation λ = 1.54056 Å) or a Rigaku Miniflex 600 diffractometer (Bragg-Brentano geometry, Cu Kα radiation λ = 1.54056 Å). Elemental microanalyses (EA) were performed in the Microanalytical Laboratory of the College of Chemistry at UC Berkeley, using a Perkin Elmer 2400 Series II CHNS elemental analyzer. Low-pressure gas (N_2 and CH_4) adsorption isotherms were recorded in-house on a Quantachrome Autosorb-1 volumetric gas adsorption analyzer. High-pressure methane adsorption isotherms were measured using the static volumetric method in an HPA-100 from the VTI Corporation (currently Particulate Systems). Ultra-high-purity grade N_2, CH_4, and He (99.999% purity) gases were used throughout the gas adsorption experiments. A liquid nitrogen bath was used for the measurements at 77 K. A water circulator was used for adsorption measurements at 298, 308, and 318 K.

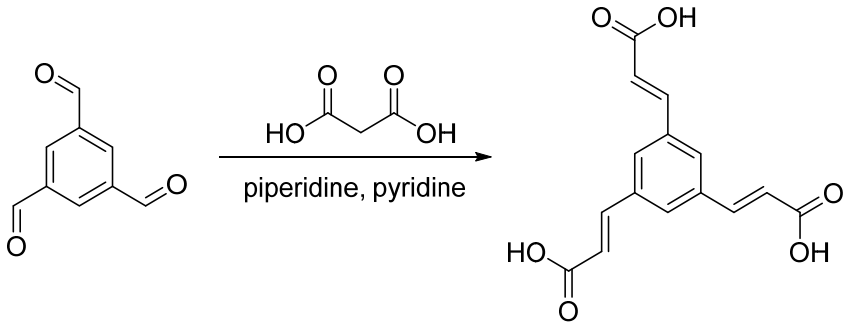

Figure 5.1. Synthesis of benzene-1,3,5-tri-β-acrylic acid (H_3BTAC).

Synthesis of organic linker: Benzene-1,3,5-tri-β-acrylic acid (H_3BTAC) was prepared according to the published procedure with slight modification.[15] Pyridine (80 mL) and a few drops of piperidine was added to a flask containing 1,3,5-triformylbenzene (10.0 g, 61.7 mmol) and malonic acid (24.0 g, 230 mmol). The resulting suspension was heated at 85 °C for 12 hours and refluxed at 120 °C for 1 hour. Pyridine was removed under vacuum before sulfuric acid (1 M, 100 mL) was added to the solution. The precipitate was filtered and washed with water until neutral filtrate. The filter cake was recrystallized in glacial acetic acid and dried under vacuum at 120 °C to give benzene-1,3,5-tri-β-acrylic acid (H_3BTAC) as white solid (14.9 g, 51.7 mmol, 84%). ^{1}H NMR (400 MHz, DMSO), [ppm]: 12.45 (s, 3H), 8.05 (s, 3H), 7.58 (d, J = 16.0 Hz, 3H), 6.75 (d, J = 16.0 Hz, 3H).

Synthesis and Characterization of MOFs:

General procedure for sample preparation. To reduce nucleation in the growth of MOF single-crystals, the inner surface of glass containers were rinsed with Sigmacote® siliconizing reagent, washed three times with acetone, and dried in oven before use. Solvent exchange of the

MOFs is performed by immersing the sample in for three days, during which the solvent was decanted and freshly replenished three times per day.

$Zn_4O(BTAC)_2$, MOF-950. A solvent mixture of H_3BTAC (0.033 g, 0.11 mmol) and $Zn(NO_3)_2 \cdot 6H_2O$ (0.25 g, 0.84 mmol) in 20 mL DMF was placed in a 20-mL screw-capped scintillation vial, which was heated at 85 °C for 3 days. Light yellow crystals were collected and quickly washed three times with 5 mL of fresh DMF. As-synthesized MOF-950 was rinsed 3 times per day with 4 mL of DMF for 3 days and immersed in 4 mL of chloroform for 3 days, during which time the solvent was replaced 3 times per day. The solid was then evacuated under dynamic vacuum first at room temperature for 12 hours and then 80 °C for 4 hours to yield activated sample DMF (Yield: 0.029 g; 62% based on H_3BTAC). ^1H digested solution NMR of activated sample (400 MHz, DMSO-d_6, ppm): 8.05 (s, 3H, 1 × BTAC), 7.60 (d, J = 16.1 Hz, 3H, 1 × BTAC), 6.77 (d, J = 16.1 Hz, 3H, 1 × BTAC). EA of activated sample: Calcd. for $Zn_4C_{30}H_{18}O_{13} = Zn_4O(C_{15}H_9O_6)_2$: C, 42.49; H, 2.14%. Found: C, 41.47; H, 2.09%. ATR-FTIR (4000–400 cm^{-1}): 1647 (m), 1588 (m), 1560 (sh), 1542 (sh), 1527 (m), 1444 (m), 1399 (s), 1299 (w), 1236 (w), 1166 (w), 972 (m), 895 (w), 858 (m), 753 (w), 726 (w), 670 (w), 593 (m), 524 (m), 413 (m).

$Zn_4O(BDC)(BTAC)_{4/3}$, MOF-905. A solvent mixture of H_3BTAC (0.045 g, 0.16 mmol), H_2BDC (0.048 g, 0.29 mmol) and $Zn(NO_3)_2 \cdot 6H_2O$ (0.26 g, 0.87 mmol) in 18 mL DMF and 1.8 mL ethanol was placed in a 20-mL screw-capped scintillation vial, which was heated at 85 °C for 1 day. Light yellow crystals were collected and quickly washed three times with 5 mL of fresh DMF. As-synthesized MOF-905 was rinsed 3 times per day with 4 mL of DMF for 3 days and immersed in 4 mL of chloroform for 3 days, during which time the solvent was replaced 3 times per day. The solid was then evacuated under dynamic vacuum first at room temperature for 12 hours and then 80 °C for 4 hours to yield activated sample (Yield: 0.048 g; 49% based on H_3BTAC). ^1H digested solution NMR of activated sample (400 MHz, DMSO-d_6, ppm): 8.05 (s, 4H, 1.33 × BTAC), 8.03 (s, 4H, 1 × BDC), 7.60 (d, J = 16.1 Hz, 4H, 1.33 × BTAC), 6.77 (d, J = 16.1 Hz, 4H, 1.33 × BTAC). EA of activated sample: Calcd. for $Zn_4C_{28}H_{16}O_{13} = Zn_4O(C_8H_4O_4)(C_{15}H_9O_6)_{4/3}$: C, 40.89; H, 1.96%. Found: C, 39.87; H, 1.82%. ATR-FTIR (4000–400 cm^{-1}): 1644 (m), 1595 (m), 1535 (m), 1397 (s), 1301 (w), 1275 (w), 1236 (w), 1160 (w), 1020 (w), 983 (m), 861 (m), 825 (w), 746 (m), 666 (w), 604 (m), 576 (m), 517 (m).

$Zn_4O(BDC\text{-}Me_2)(BTAC)_{4/3}$, MOF-905-$Me_2$. A solvent mixture of H_3BTAC (0.045 g, 0.16 mmol), $H_2BDC\text{-}Me_2$ (0.067 g, 0.34 mmol) and $Zn(NO_3)_2 \cdot 6H_2O$ (0.26 g, 0.87 mmol) in 18 mL DMF and 1.8 mL ethanol was placed in a 20-mL screw-capped scintillation vial, which was heated at 85 °C for 1 day. Light yellow crystals were collected and quickly washed three times with 5 mL of fresh DMF. As-synthesized MOF-905-Me_2 was rinsed 3 times per day with 4 mL of DMF for 3 days and immersed in 4 mL of chloroform for 3 days, during which time the solvent was replaced 3 times per day. The solid was then evacuated under dynamic vacuum first at room temperature for 12 hours and then 80 °C for 4 hours to yield activated sample (Yield: 0.044 g; 43% based on H_3BTAC). ^1H digested solution NMR of activated sample (400 MHz, DMSO-d_6, ppm): 8.07 (s, 4H, 1.33 × BTAC), 7.67 (s, 2H, 1 × BDC-Me_2), 7.59 (d, J = 16.0 Hz, 4H, 1.33 × BTAC), 6.76 (d, J = 16.0 Hz, 4H, 1.33 × BTAC), 2.46 (s, 6H, 1 × BDC-Me_2). EA of activated sample: Calcd. for $Zn_4C_{30}H_{20}O_{13} = Zn_4O(C_{10}H_8O_4)(C_{15}H_9O_6)_{4/3}$: C, 42.39; H, 2.37%. Found: C, 42.09; H, 2.02%. ATR-FTIR (4000–400 cm^{-1}): 1645 (m), 1594 (m), 1534 (m), 1400 (s), 1360 (m), 1301 (w), 1236 (w), 1194 (w), 1159 (w), 982 (m), 861 (m), 796 (w), 748 (w), 666 (w), 604 (m), 570 (w), 517 (m), 427 (w).

$Zn_4O(BDC\text{-}Nap)(BTAC)_{4/3}$, MOF-905-Nap. A solvent mixture of H_3BTAC (0.045 g, 0.16 mmol), H_2BDC-Nap (0.074 g, 0.34 mmol) and $Zn(NO_3)_2 \cdot 6H_2O$ (0.26 g, 0.87 mmol) in 18 mL DMF and 1.8 mL ethanol was placed in a 20-mL screw-capped scintillation vial, which was heated at 85 °C for 1 day. Light yellow crystals were collected and quickly washed three times with 5 mL of fresh DMF. As-synthesized MOF-907 was rinsed 3 times per day with 4 mL of DMF for 3 days and immersed in 4 mL of chloroform for 3 days, during which time the solvent was replaced 3 times per day. The solid was then evacuated under dynamic vacuum first at room temperature for 12 hours and then 80 °C for 4 hours to yield activated sample (Yield: 0.047 g; 45% based on H_3BTAC). ^1H digested solution NMR of activated sample (400 MHz, DMSO-d_6, ppm): 8.75 (dd, J = 6.7 Hz, 3.4 Hz, 2H, 1 × BDC-Nap), 8.09 (s, 2H, 1 × BDC-Nap), 8.07 (s, 4H, 1.33 × BTAC), 7.69 (dd, J = 6.7 Hz, 3.4 Hz, 2H, 1 × BDC-Nap), 7.60 (d, J = 16.0 Hz, 4H, 1.33 × BTAC), 6.76 (d, J = 16.0 Hz, 4H, 1.33 × BTAC). EA of activated sample: Calcd. for $Zn_4C_{32}H_{18}O_{13} = Zn_4O(C_{12}H_6O_4)(C_{15}H_9O_6)_{4/3}$: C, 44.05; H, 2.08%. Found: C, 43.70; H, 1.98%. ATR-FTIR (4000–400 cm^{-1}): 1644 (m), 1593 (m), 1532 (m), 1400 (s), 1371 (s), 1264 (w), 1237 (w), 1165 (w), 982 (m), 860 (m), 827 (w), 789 (m), 740 (w), 666 (w), 604 (m), 587 (m), 522 (m), 472 (m).

$Zn_4O(BDC\text{-}NO_2)(BTAC)_{4/3}$, MOF-905-$NO_2$. A solvent mixture of H_3BTAC (0.045 g, 0.16 mmol), H_2BDC-NO_2 (0.062 g, 0.29 mmol) and $Zn(NO_3)_2 \cdot 6H_2O$ (0.26 g, 0.87 mmol) in 18 mL DMF and 1.8 mL ethanol was placed in a 20-mL screw-capped scintillation vial, which was heated at 85 °C for 36 hours. Light yellow crystals were collected and quickly washed three times with 5 mL of fresh DMF. As-synthesized MOF-905-NO_2 was rinsed 3 times per day with 4 mL of DMF for 3 days and immersed in 4 mL of chloroform for 3 days, during which time the solvent was replaced 3 times per day. The solid was then evacuated under dynamic vacuum first at room temperature for 12 hours and then 80 °C for 4 hours to yield activated sample (Yield: 0.043 g; 41% based on H_3BTAC). ^1H digested solution NMR of activated sample (400 MHz, DMSO-d_6, ppm): 8.24 (d, J = 1.4 Hz, 1H, 1 × BDC-NO_2), 8.20 (dd, J = 7.9 Hz, 1.4 Hz, 1H, 1 × BDC-NO_2), 8.03 (s, 4H, 1.33 × BTAC), 7.85 (d, J = 7.9 Hz, 1H, 1 × BDC-NO_2), 7.59 (d, J = 16.0 Hz, 4H, 1.33 × BTAC), 6.76 (d, J = 16.0 Hz, 4H, 1.33 × BTAC). EA of activated sample: Calcd. for $Zn_4C_{28}H_{15}NO_{15} = Zn_4O(C_8H_3O_6N)(C_{15}H_9O_6)_{4/3}$: C, 38.76; H, 1.74; N, 1.62%. Found: C, 38.98; H, 1.46; N, 1.65%. ATR-FTIR (4000–400 cm^{-1}): 1643 (m), 1615 (m), 1591 (m), 1532 (m), 1398 (s), 1302 (w), 1276 (w), 1237 (w), 1167 (w), 1133 (w), 1067 (w), 983 (m), 860 (m), 840 (w), 826 (w), 778 (w), 750 (w), 738 (w), 728 (w), 666 (w), 604 (m), 589 (m), 525 (m), 509 (m).

Results and Discussion

As shown in Figure 5.1, the new tricarboxylate organic linker benzene-1,3,5-tri-β-acrylic acid (H_3BTAC) was synthesized by a single-step condensation of 1,3,5-triformylbenzene and malonic acid followed by in situ decarboxylation. All three double bonds generated adopt trans configuration, greatly increasing the symmetry of the H_3BTAC molecule. Reaction of this linker with $Zn(NO_3)_2 \cdot 6H_2O$ in DMF at 85 °C for 3 d afforded block crystals of MOF-950. Single-crystal X-ray diffraction analysis revealed that MOF-950 crystallizes in the cubic $P2_13$ space group with an axis length of 21.2832(4) Å. In this structure, octahedral $Zn_4O(\text{-}COO)_6$ units are linked by tritopic BTAC linkers to afford a three-dimensional framework with a **pyr** topology (Figure 5.2), isoreticular to MOF-150 [$Zn_4O(TCA)_2$; TCA = 4,4′,4″-tricarboxytriphenylamine][16] and MOF-155, [$Zn_4O(BTB\text{-}X)_2$; BTB = benzene-1,3,5-tricarboxylic acid, X = F_2, mNH_2].[17]

However, unlike MOF-150 and MOF-155, which both consist of two-fold interpenetrating frameworks, MOF-950 is noncatenated, which leads to a bicontinuous channel with an internal pore diameter of 8.5 Å, a larger value compared to that in MOF-150 (4.5 Å) and similar to that in MOF-155 (8.5 Å) despite of the usage of a shorter linker.

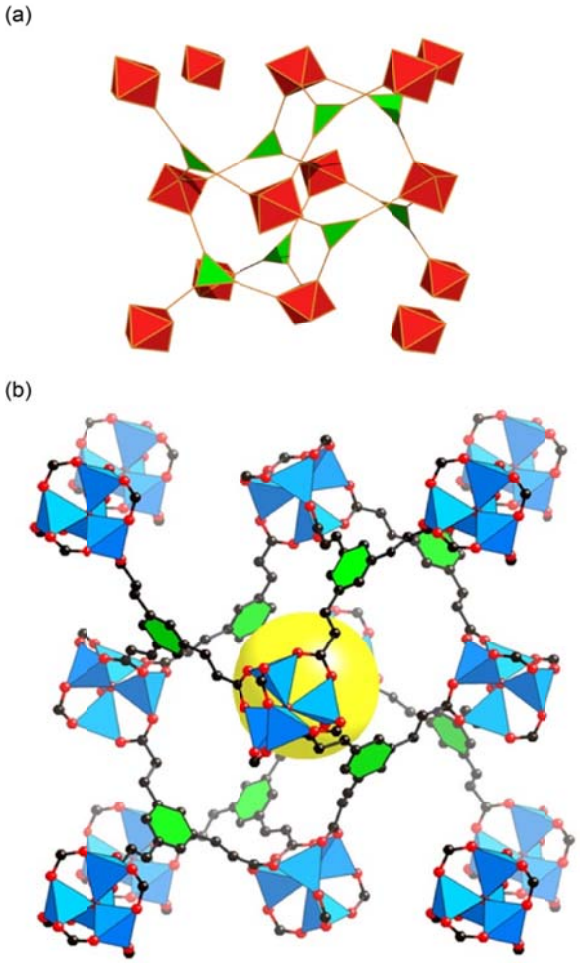

Figure 5.2. The combination of octahedral units with tritopic units produces the **pyr** network (a) exhibited by MOF-950 (b). Atom color scheme: C, black; O, red; Zn, blue polyhedra. H atoms are omitted for clarity. Yellow balls indicate the space in the framework.

The use of ditopic (H_2BDC) and tritopic linkers (H_3BTAC) together with $Zn(NO_3)_2 \cdot 6H_2O$ in DMF/ethanol mixture leads to light yellow crystals of MOF-905 with a truncated octahedral shape. Despite extensive trials to determine the structure of MOF-905 from single crystal X-ray diffraction experiments, this material always grows in polycrystalline form and shows weak diffraction peaks while readily degrading when exposed to ambient air. Its structure was determined by comparison of the experimental PXRD pattern with the one calculated from a structural model based on the **ith-d** net (Figure 5.3), with refined unit cell parameter a = 24.624 Å in the space group $Pm\bar{3}$, isoreticular to MOF-205 (DUT-6).[18] In this structure, each $Zn_4O(-COO)_6$ unit is linked to six carboxylates, four equatorial from BTAC and two axial from BDC.

This results in two types of micropores present in the framework: a dodecahedral pore of 18 Å in diameter, built from four BDC and eight BTAC linkers interconnecting twelve zinc SBUs, and a tetrahedral pore of 6 Å in diameter, build from four zinc SBUs connected by two BDCs and four BTACs. (Figure 5.3) Notably, the ratio between the distances of the carboxylate carbons within the ditopic and tritopic linkers of MOF-905 amounts to 0.602, close to the value in MOF-205 (0.645).[18]

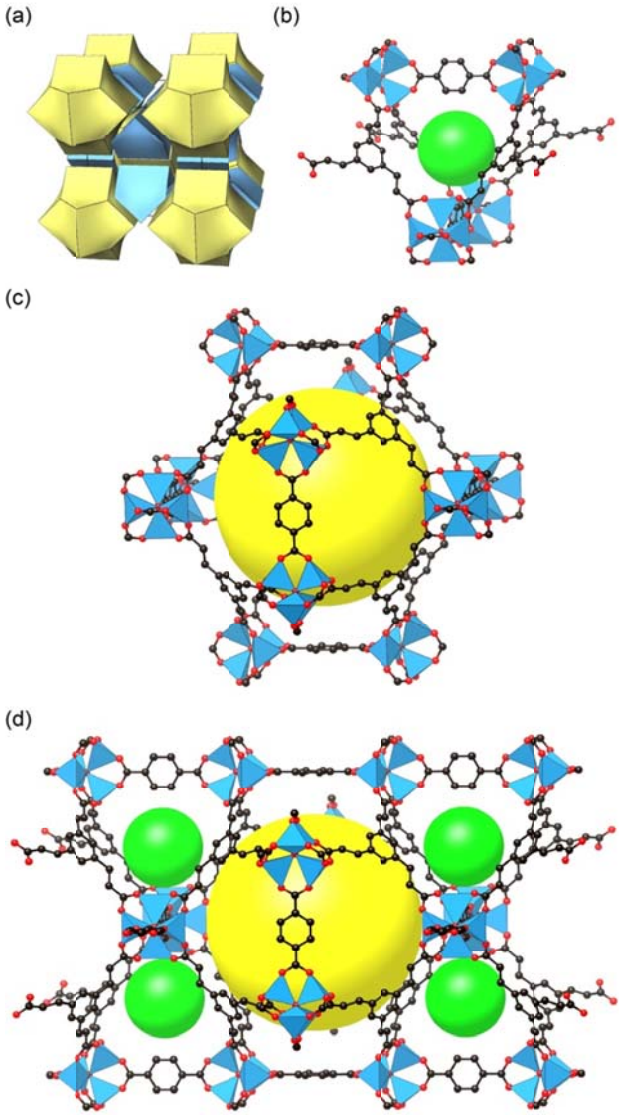

Figure 5.3. Tiling of the **ith-d** network (a) with tetrahedral (b) and octahedral cages (c) exhibited in MOF-905 (d). Atom color scheme: C, black; O, red; Zn, blue polyhedra. H atoms are omitted for clarity. Yellow and green balls indicate the space in the framework.

The appropriate ratio of the distances between BTAC and BDC in forming frameworks with **ith-d** net was further confirmed as dimethyl, naphthalene, and nitro group functionalized MOF-

905 were readily synthesized under the same condition using the linker combination of BTAC and the corresponding BDC linkers (Figure 5.4). Similar to MOF-905, structural determination of these functionalized MOFs by single crystal diffraction techniques was not possible. Instead, their phase purity was confirmed by comparing their PXRD patterns with simulation from model structures (Tables A5.1 to A5.4).

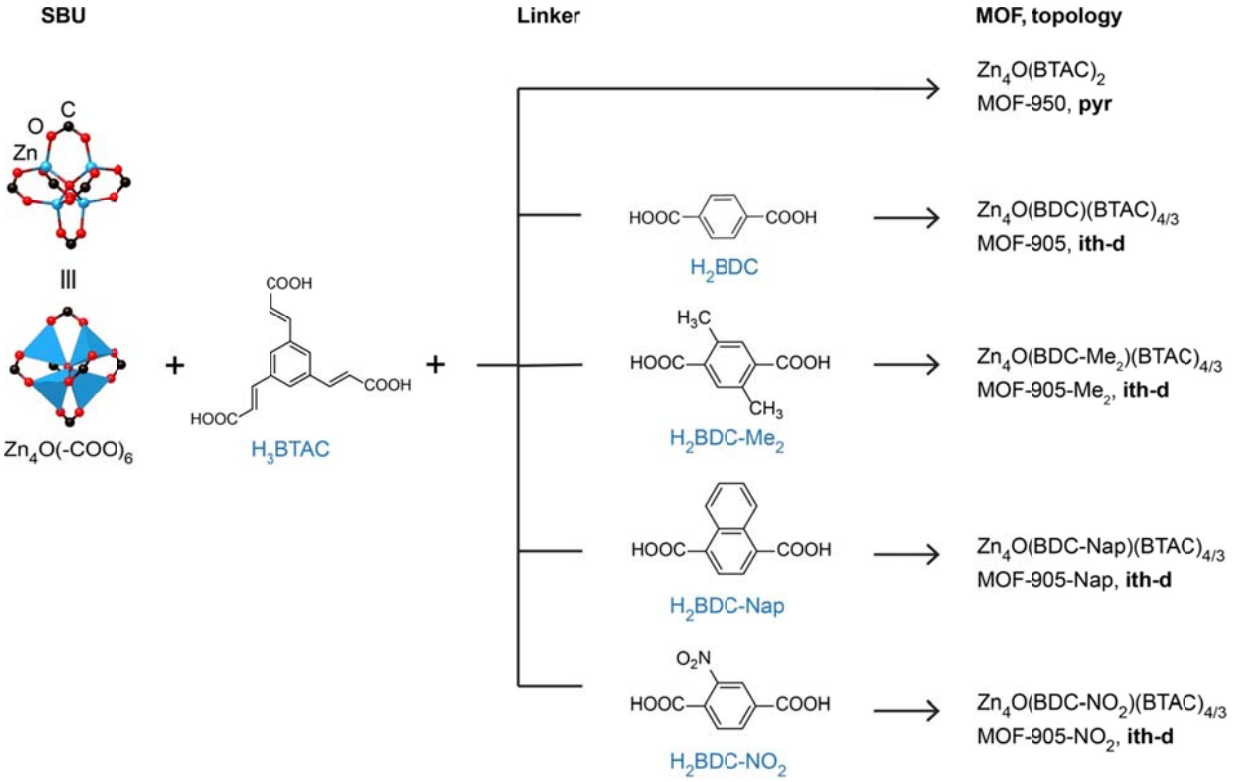

Figure 5.4. $Zn_4O(\text{-}COO)_6$ secondary building units (SBUs) are connected with organic linkers to form MOF-950, MOF-905 and functionalized MOF-905s.

Porosity of MOFs. Prior to the methane adsorption tests, N_2 adsorption isotherms for all MOFs were recorded at 77 K to confirm the presence of the permanent porosity and to calculate their pore volume (Table 5.1 and Figures A5.16-A5.20). The guest-free (activated) materials were obtained by solvent exchange to chloroform followed by the direct evacuation of pores under dynamic vacuum (4×10^{-5} bar). Successful removal of guest molecules from the pore was also confirmed by TGA analysis (Figures A5.6-A5.15). All examined MOFs displayed significant N_2 uptake in the low pressure region ($P/P_0 < 0.05$) and were saturated around $P/P_0 = 0.2$. The profiles of the isotherms are all classified as Type I. Additionally, the adsorption of N_2 was fully reversible, which clearly indicates the presence of permanent microporosity. Compared to MOF-905, functionalized MOF-905 shows smaller N_2 uptake because of the presence of extra functional groups reduces the pore volume. All of these materials exhibit high BET surface areas (> 3000 m^2 g^{-1}) and large pore volumes (ca. 1.3 cm^3 g^{-1}), which are in good agreement with those calculated from their structural models. The BET (Langmuir) surface area, pore volume, crystal

density, pore diameter are summarized along with other bench mark MOFs with $Zn_4O(\text{-}COO)_6$ SBU in Table 5.1.

Table 5.1. Summary of the low pressure sorption, physical and pore-structure properties of the studied zinc MOFs.

Material	Surface area, $m^2\ g^{-1}$		V_p,[a] $cm^3\ g^{-1}$	$d_{crystal}$,[b] $g\ cm^{-3}$	d_{pycno},[c] $g\ cm^{-3}$	Pore diameter,[d] Å	CH_4 uptake,[e] $cm^3\ g^{-1}$	Q_{st}, $kJ\ mol^{-1}$
	BET	Langmuir						
MOF-950	3440	3650	1.30	0.517	0.540	8.5	8.6	11.9
MOF-905	3490	3770	1.34	0.549	0.537	6.0, 18.0	7.7	11.7
MOF-905-Me_2	3920	3640	1.39	0.568	0.515	5.5, 17.6	11.0	10.3
MOF-905-Naph	3540	3310	1.25	0.585	0.553	6.8, 15.3	10.2	11.3
MOF-905-NO_2	3600	3380	1.29	0.580	0.551	5.1, 17.3	8.1	10.7
MOF-205	4080	5700	1.96	0.380	0.40	5.0, 25.0	8.0	10.6
MOF-177	4700	5060	1.83	0.427	0.41	10.8	9.1	9.9
MOF-5	3480	3860	1.39	0.605	0.53	12.8	7.3	10.0

[a]Calculated from uptake at $P/P_0 = 0.9$;
[b]From crystal structure and model structure data;
[c]From pycnometer density data;
[d]Calculated with Platon.[19]
[e]Data at 1.1 bar and 298 K.

Low-Pressure CH_4 Isotherms and Adsorption Enthalpies. Low-pressure CH_4 isotherms for MOF-950, MOF-905, and functionalized MOF-905 were measured up to 1.1 bar at 298, 308, and 318 K (Figures A5.21-A5.25). CH_4 uptakes in these MOFs linearly increase with an increase in the pressure, while no saturation was observed. CH_4 uptake for these new MOFs at 298 K and 1 bar is ranging from 8.1 $cm^3\ g^{-1}$ (MOF-905-NO_2) to 11.0 $cm^3\ g^{-1}$ (MOF-905-Me_2), and these are comparable to the CH_4 uptake in MOF-177 (9.1 $cm^3\ g^{-1}$) under the same conditions (Table 5.1). Such moderate CH_4 uptake capacity below 1 bar should be advantageous to achieving larger working capacity in the practical natural gas storage processes. It is known that low-pressure CH_4 adsorption capacity correlates to the adsorption enthalpy rather than porosity of sorbent materials. Accordingly, the isosteric enthalpy of adsorption (Q_{st}) for CH_4 was calculated based on CH_4 isotherms collected at 273, 283, and 298 K. Figure A5.26 demonstrates the coverage dependencies of Q_{st} calculated from fitting these data. MOF-950 and MOF-905 show similar near-zero coverage Q_{st} values of 11.9 and 11.7 $kJ\ mol^{-1}$. Compared to MOF-905, functionalized MOF-905 shows lower Q_{st} values of 10.3 (Me_2), 11.3 (Naph), and 10.7 (NO_2) $kJ\ mol^{-1}$. These values are comparable to those in MOF-5 (12.3 $kJ\ mol^{-1}$), MOF-177 (9.9 $kJ\ mol^{-1}$), and MOF-205 (10.6 $kJ\ mol^{-1}$),[18b] MOFs with $Zn_4O(\text{-}COO)_6$ SBUs; but less than those of MOFs with open

metal sites: Ni-MOF-74 (21.4 kJ mol^{-1}), PCN-14 (18.7 kJ mol^{-1}), and HKUST-1 (17.0 kJ mol^{-1}).[9b] Considering that the Q_{st} values of MOFs with $Zn_4O(\text{-}COO)_6$ SBUs are not substantially influenced by the surface coverage of CH_4, it is presumed that primary CH_4 adsorption sites are located to near the SBU, while organic linkers show weak affinity with CH_4 molecules in this pressure range (<1 bar).

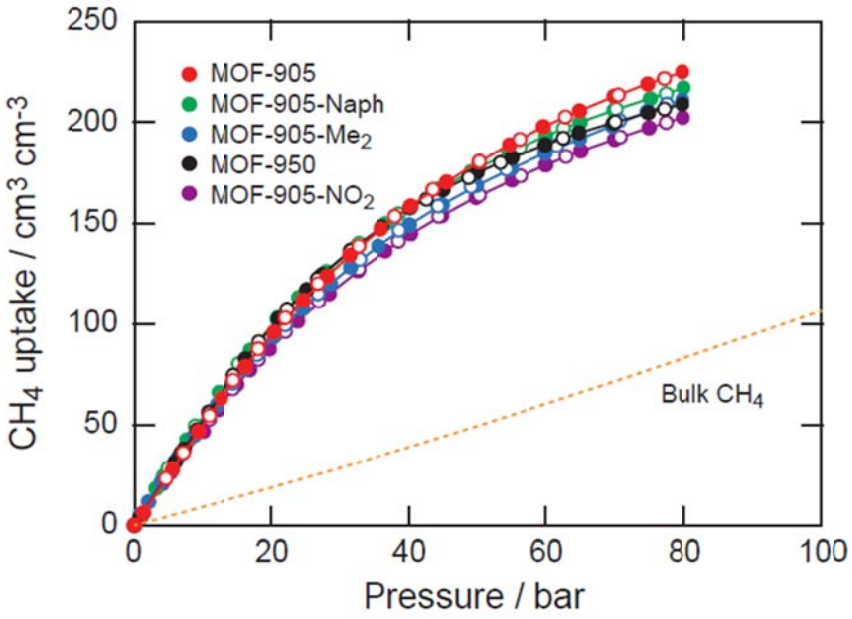

Figure 5.5. Total CH_4 isotherms for MOFs measured at 298 K.

High-Pressure CH_4 Storage. High-pressure excess CH_4 isotherms (up to 80 bar) for MOF-950, MOF-905, and functionalized MOF-905 were recorded at 298 K on a volumetric adsorption analyzer to evaluate the storage performance of CH_4 (Figures A5.27-A5.31). CH_4 uptake in these MOFs gradually increases with increases in pressure, while the CH_4 uptakes are similar to each other below 20 bar. By increasing pressure further, the excess uptakes approach saturation. The excess uptake at 80 bar and 298 K is nearly proportional to the surface area (pore volume) of MOFs. MOF-905 showed the highest CH_4 uptake of 308 cm^3 g^{-1} and this is followed by MOF-950 (297 cm^3 g^{-1}), MOF-905-Me (294 cm^3 g^{-1}), MOF-905-Naph (289 cm^3 g^{-1}), and MOF-905-NO_2 (261 cm^3 g^{-1}). Volumetric excess CH_4 uptake can be calculated by multiplying the bulk density of materials. However, experimental bulk density cannot be the same as theoretical bulk density calculated from the crystal structure when the crystalline MOF sample is not well-activated or contains defect sites in its structure. Therefore, prior to the unit conversion, we sought to estimate the bulk density of these MOFs using a skeletal density of the MOF in question ($d_{skl} = 1/V_{skl}$) and pore volume (V_p), because these are experimentally determined using He pycnometry and N_2 adsorption, respectively:

$$\text{experimental bulk density} = 1/(1/d_{skl} + V_p). \qquad \text{Eq. (5.1)}$$

As demonstrated in Table 5.1, the experimental bulk density for these MOFs was lower by 5-10% compared to theoretical crystal density, which is indicative of the presence of defects in

the MOF crystals. The maximum excess CH_4 uptake for MOF-905 in volumetric units is 165 cm^3 cm^{-3} at 80 bar and 298 K, which outperforms MOF-950 (153 cm^3 cm^{-3}) and functionalized MOF-905 (160, 151, and 144 cm^3 cm^{-3} for Nap, Me_2, and NO_2, respectively).

To explore the potential as sorbent materials in practical applications, the total CH_4 uptake in volumetric units is frequently used. Accordingly, the total uptake was calculated from the excess CH_4 uptake using the following equation:

$$N_{tot} = N_{ex} + \rho_{CH4} \times V_p. \qquad \text{Eq. (5.2)}$$

Table 5.2. Total methane uptake and working capacity (desorption at 5 bar) at 35, 80, and 250 bar and 298 K.

Material	Total uptake at 35 bar, cm^3 cm^{-3}	Total uptake at 80 bar, cm^3 cm^{-3}	Total uptake at 250 bar,[a] cm^3 cm^{-3}	Working capacity at 35 bar, cm^3 cm^{-3}	Working capacity at 80 bar, cm^3 cm^{-3}	Working capacity at 250 bar, cm^3 cm^{-3}
MOF-905	145	225	305	119	200	285
MOF-905-Me_2	138	211	—	111	184	—
MOF-905-Nap	146	217	—	117	188	—
MOF-905-NO_2	132	203	—	107	177	—
MOF-950	145	209	—	109	174	—
MOF-5[b]	126	198	328	104	176	306
MOF-177[b]	122	205	350	102	185	330
MOF-205[b]	120	205	345	101	186	326
MOF-210[b]	82	166	377	70	154	365
Ni-MOF-74[c]	230	267	—	115	152	—
HKUST-1[c]	225	272	—	153	200	—
Al-soc-MOF-1[d]	127	221	—	106	200	—
PCN-14[c]	200	250	—	128	178	—
UTSA-76a[e]	211	257[f]	—	151	197[f]	—
Co(BDP)[g]	161	155[f]	—	203	197[f]	—
AX-21[c]	153	222	—	103	172	—
Bulk CH_4	33	83	263	29	79	260

[a]Calculated with a dual site Langmuir model;
[b]Data from ref. 18b;
[c]Data from ref. 9a;
[d]Data from ref. 18c;
[e]Data from ref. 18d;
[f]Data measured at 298 K and 65 bar;
[g]Data from ref. 18e.

To As shown in Figure 5.5, the total CH_4 uptake calculated, monotonously increases when increasing the pressure without revealing a particular saturation pressure. The volumetric total CH_4 uptakes for MOF-950, MOF-905, and functionalized MOF-905 at 80 bar and 298 K range from 203 (MOF-905-NO_2) to 225 cm^3 cm^{-3} (MOF-905). Remarkably, CH_4 uptake in MOF-905 at 80 bar is 2.7 times larger than bulk CH_4 density at the same temperature and pressure. This value is also greater than MOF-177 (205 cm^3 cm^{-3}) and MOF-205 (205 cm^3 cm^{-3}), and approaching the best performing MOFs, such as MOF-519 (279 cm^3 cm^{-3}), HKUST-1 (272 cm^3 cm^{-3}), and UTSA-76a (257 cm^3 cm^{-3} at 65 bar).

CH_4 storage working capacity. Considering the practical application of methane storage in automobiles, the volumetric working capacity of methane (considering desorption pressure at 5 bar) was also obtained, as shown in Table 5.2. The working capacity of MOF-905 at 35 bar is 119 cm^3 cm^{-3}, while at 80 bar this MOF is able to deliver 200 cm^3 cm^{-3}, which is comparable to the benchmark compound HKUST-1 (200 cm^3 cm^{-3}) at 80 bar, and surpasses all other zinc MOFs. At 80 bar, a tank filled with MOF-905 would deliver 2.5 times more methane than an empty tank.

Conclusion

In this chapter, we report the synthesis, structure, porosity, and methane adsorption properties of five new zinc MOFs with benzene-1,3,5-tri-β-acrylic acid (H_3BTAC) as organic linker. Among them, MOF-905, $Zn_4O(BDC)(BTAC)_{4/3}$, has working capacities (desorption at 5 bar) of 200 cm^3 cm^{-3} at 80 bar and 298 K, a value rivaling that of HKUST-1 (200 cm^3 cm^{-3}), the benchmark compound for methane storage in MOFs. The working capacity of MOF-905 at 80 bar and 298 K also surpasses all reported values for Zn_4O based MOFs including MOF-5, MOF-177, and MOF-205. At 80 bar, a tank filled with MOF-905 would deliver 2.5 times more methane than an empty tank. Comparison between MOF-905 and functionalized MOF-905 of their high pressure methane storage capacity shows that pore size appears to play a more important role than functional groups (methyl, nitro, and naphthalene groups) on the organic linkers.

Appendices

Table A5.1. Crystallographic information and atomic fractional coordinates for the structure model of MOF-905.

Identification Code	MOF-905			
Empirical Formula	$C_{28}H_{16}O_{13}Zn_4$			
Formula Weight	821.97			
Crystal System	Cubic			
Space Group	$Pm\bar{3}$			
a / Å	23.40810			
V/ Å^3	12826.2			
Z	6			
d/g cm^{-3}	0.638			
Atoms	x	y	z	Occupancy
Zn1	1	1.28933	0.56556	0.5
Zn2	0.934	1.21215	0.5	0.5
O1	1	1.25057	0.5	0.25
O2	0.88818	1.2235	0.55917	1
O3	0.94057	1.28227	0.61005	1
O4	1	1.35791	0.54754	0.5
O5	0.95216	1.14275	0.5	0.5
C1	0.89504	1.25506	0.60228	1
C2	0.84909	1.26377	0.64275	1
H2	0.86056	1.27794	0.68533	1
C3	0.79455	1.26225	0.62651	1
H3	0.78266	1.24718	0.58436	1
C4	0.74975	1.27881	0.66672	1
C5	0.70322	1.24257	0.67434	1
H5	0.69819	1.20581	0.6466	1
C6	1	1.38278	0.5	0.25
C7	1	1.44243	0.5	0.25
C8	1	1.47105	0.55228	0.5
H8	1	1.449	0.593	0.5
C9	1	1.11782	0.5	0.25
C10	1	1.05782	0.5	0.25
C11	0.94777	1.02904	0.5	0.5
H11	0.90706	1.05109	0.5	0.5

Table A5.2. Crystallographic information and atomic fractional coordinates for the structure model of MOF-905-Me_2.

Identification Code	MOF-905-Me_2			
Empirical Formula	$C_{30}H_{18}O_{13}Zn_4$			
Formula Weight	848			
Crystal System	Cubic			
Space Group	$Pm\bar{3}$			
a / Å	24.7215			
V/ $Å^3$	15108			
Z	6			
d/g cm^{-3}	0.559			
Atoms	x	y	z	Occupancy
Zn1	0.43944	0	0.70921	0.5
Zn2	0.5	0.06391	0.78812	0.5
O1	0.5	0	0.74952	0.25
O2	0.39683	0.05663	0.71804	1
O3	0.44014	0.10745	0.77705	1
O4	0.45569	0	0.64147	0.5
O5	0.5	0.04493	0.85697	0.5
C1	0.3997	0.09914	0.74614	1
C2	0.35379	0.13741	0.74062	1
H2	0.31894	0.12148	0.7195	1
C3	0.35283	0.18893	0.75768	1
H3	0.38683	0.20428	0.78069	1
C4	0.30573	0.22584	0.74719	1
C5	0.29705	0.2702	0.78177	1
H5	0.32552	0.27699	0.81429	1
C6	0.5	0	0.61641	0.25
C7	0.5	0	0.5569	0.25
C8	0.45036	0	0.52814	0.5
C9	0.39618	0	0.55617	0.25
H9a	0.37627	0.03171	0.54586	0.25
H9b	0.37627	-0.03171	0.54586	0.25
H9c	0.40151	0	0.59464	0.25
C10	0.5	0	0.88212	0.25
C11	0.5	0	0.94245	0.25
C12	0.5	-0.04947	0.97167	0.5
C13	0.5	-0.10357	0.94364	0.25
H13a	0.53171	-0.12348	0.95394	0.25
H13b	0.46829	-0.12348	0.95394	0.25
H13c	0.5	-0.09822	0.90518	0.25

Table A5.3. Crystallographic information and atomic fractional coordinates for the structure model of MOF-905-Naph.

Identification Code	MOF-905-Naph			
Empirical Formula	$C_{32}H_{16}O_{13}Zn_4$			
Formula Weight	870.01			
Crystal System	Cubic			
Space Group	$Pm\bar{3}$			
a / Å	24.74010			
V/ Å^3	15142.7			
Z	6			
d/g cm^{-3}	0.572			
Atoms	x	y	z	Occupancy
Zn1	0.43951	0	0.71012	0.5
Zn2	0.5	0.06385	0.787	0.5
O1	0.5	0	0.74942	0.25
O2	0.39676	0.05657	0.71816	1
O3	0.4402	0.10754	0.77663	1
O4	0.45681	0	0.64366	0.5
O5	0.5	0.04382	0.85458	0.5
C1	0.39968	0.09919	0.74596	1
C2	0.35381	0.13745	0.74037	1
H2	0.31905	0.12156	0.71915	1
C3	0.35275	0.18889	0.75759	1
H3	0.38666	0.20417	0.78071	1
C4	0.30566	0.22579	0.74716	1
C5	0.29702	0.27011	0.78176	1
H5	0.3255	0.27685	0.81424	1
C6	0.5	0	0.61795	0.25
C7	0.5	0	0.55768	0.25
C8	0.44908	0	0.52875	0.5
C9	0.39673	0	0.55497	0.25
H9	0.38718	0	0.59678	0.25
C10	0.34828	0	0.52742	0.25
H10	0.31013	0	0.54903	0.25
C11	0.5	0	0.88042	0.25
C12	0.5	0	0.9416	0.25
C13	0.5	0.0507	0.97107	0.5
C14	0.5	0.10299	0.94495	0.25
H14	0.5	0.11237	0.90316	0.25
C15	0.5	0.15141	0.97257	0.25
H15	0.5	0.18956	0.95096	0.25

Table A5.4. Crystallographic information and atomic fractional coordinates for the structure model of MOF-905-NO_2.

Identification Code	MOF-905-NO_2			
Empirical Formula	$C_{28}H_{12}NO_{15}Zn_4$			
Formula Weight	863.95			
Crystal System	Cubic			
Space Group	$Pm\bar{3}$			
a / Å	23.99180			
V/ $Å^3$	13809.8			
Z	6			
d/g cm^{-3}	0.623			
Atoms	x	y	z	Occupancy
Zn1	0.43694	0	0.70981	0.5
Zn2	0.5	0.06494	0.78691	0.5
O1	0.5	0	0.74889	0.25
O2	0.3933	0.05766	0.71761	1
O3	0.44078	0.10959	0.77619	1
O4	0.45418	0	0.64224	0.5
O5	0.5	0.04629	0.85542	0.5
O6	0.54687	-0.12971	0.93321	0.25
O7	0.37042	0.04689	0.56631	0.25
N1	0.39579	0	0.55641	0.125
N2	0.5	-0.10405	0.94237	0.125
C1	0.39874	0.10173	0.74533	1
C2	0.35524	0.14363	0.73905	1
H2	0.31564	0.12927	0.72275	1
C3	0.36389	0.19789	0.74727	1
H3	0.40277	0.21235	0.76515	1
C4	0.32005	0.23872	0.73382	1
C5	0.31189	0.28422	0.76914	1
H5	0.34012	0.29042	0.80384	1
C6	0.5	0	0.61718	0.25
C7	0.5	0	0.55747	0.25
C8	0.44874	0	0.52856	0.5
C9	0.5	0	0.88053	0.25
C10	0.5	0	0.94076	0.25
C11	0.5	-0.05102	0.96986	0.5

Table A5.5. Crystal data and structure refinement for MOF-950.

Identification code	MOF-950
Empirical formula	$C_{30}H_{18}O_{13}Zn_4$
Formula weight	848.00
Temperature/K	150
Crystal system	cubic
Space group	Pa-3
a/Å	21.2832(4)
α/°	90
Volume/Å^3	9640.8(5)
Z	4
ρ_{calc}/mg mm^{-3}	0.584
m/mm^{-1}	1.320
F(000)	1688
Crystal size/mm^3	0.07 × 0.09 × 0.10
Radiation	CuKα (λ = 1.54178 Å)
θ range	3.6 to 49.7°
Index ranges	$-18 \leq h \leq 16$, $-13 \leq k \leq 21$, $-20 \leq l \leq 21$
Reflections collected	15494
Unique reflections	1633
Restraints/parameters	6/96
R_{int}	0.045
R_1[a], wR_2[b]	0.0824, 0.2495
S(GOF)[c]	1.005
Largest diff. peak/hole / e Å^{-3}	0.36/-0.44

[a] $R_1 = \Sigma||F_o| - |F_c||/\Sigma|F_o|$;

[b] $wR_2 = [\Sigma w(F_o^2 - F_c^2)^2/\Sigma w(F_o^2)^2]^{1/2}$

[c] $S = [\Sigma w(F_o^2 - F_c^2)^2/(N_{ref} - N_{par})]^{1/2}$

Figure A5.1. Comparison of the experimental PXRD patterns of MOF-950: activated (red) and simulated pattern (black) from single-crystal X-ray data.

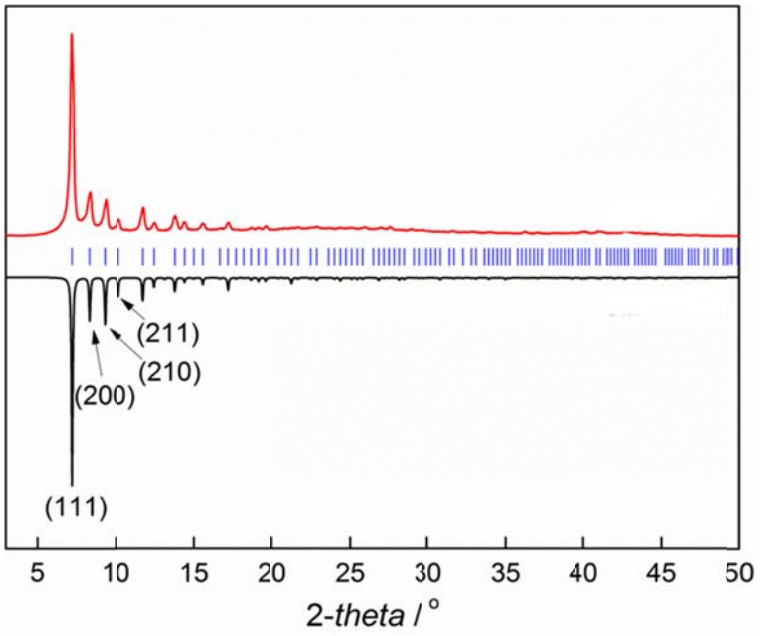

Figure A5.2. Comparison of the experimental PXRD patterns of MOF-905: activated (red) and simulated pattern (black) from model structure.

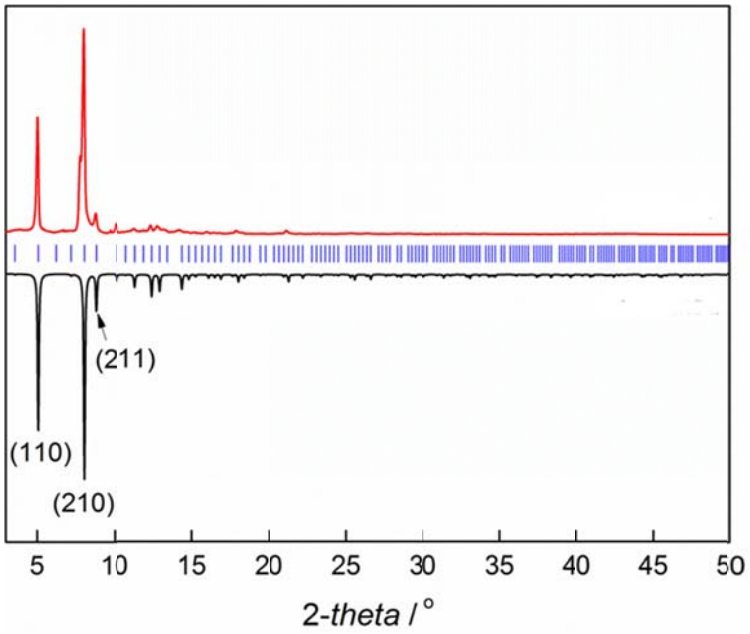

Figure A5.3. Comparison of the experimental PXRD patterns of MOF-905-Me_2: activated (red) and simulated pattern (black) from single-crystal X-ray data.

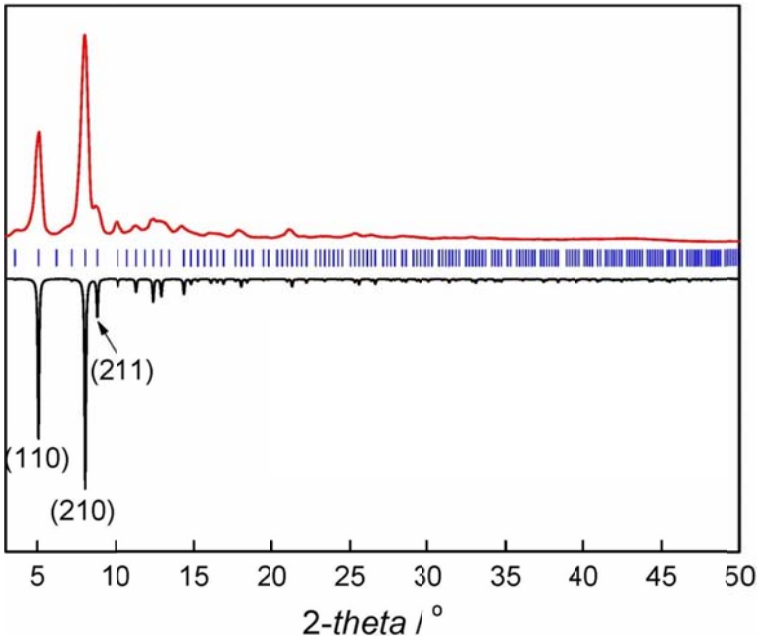

Figure A5.4. Comparison of the experimental PXRD patterns of MOF-905-Nap: activated (red) and simulated pattern (black) from model structure.

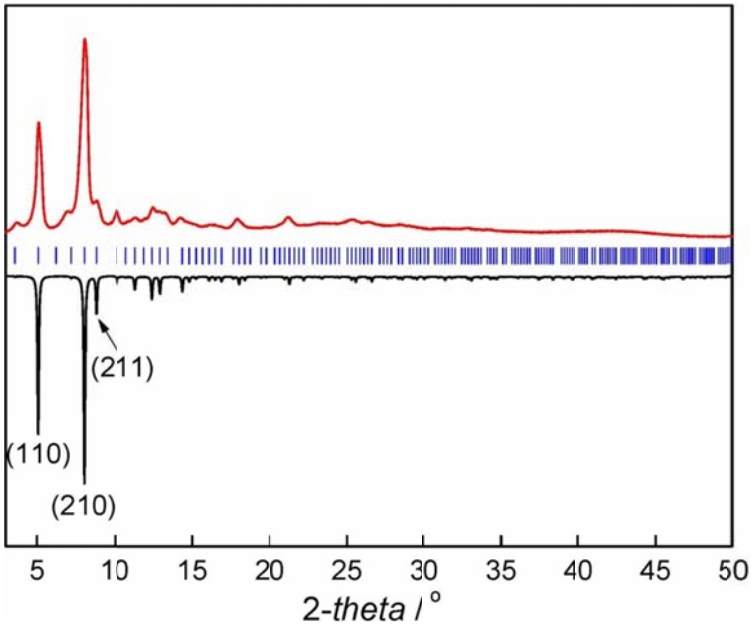

Figure A5.5. Comparison of the experimental PXRD patterns of MOF-905-NO_2: activated (red) and simulated pattern (black) from single-crystal X-ray data.

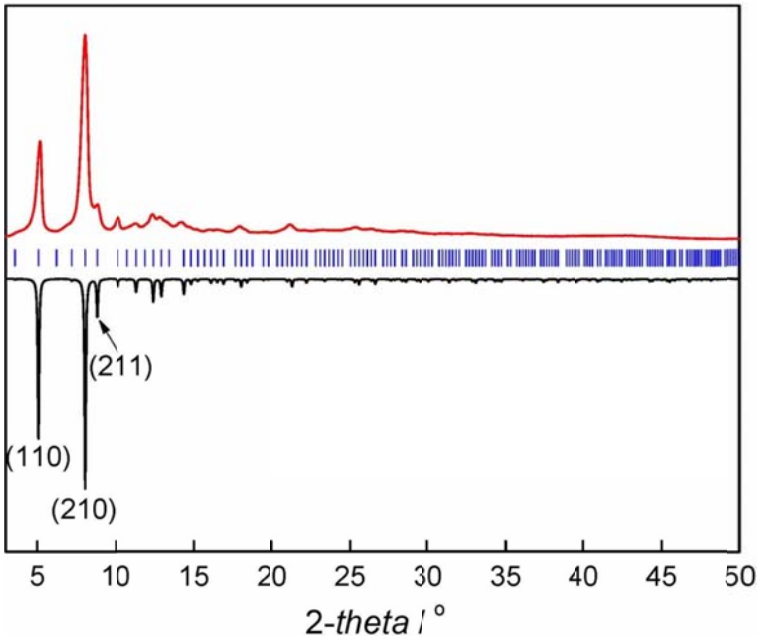

Figure A5.6. TGA trace for activated MOF-950, heating rate: 5 °C min^{-1} in air.

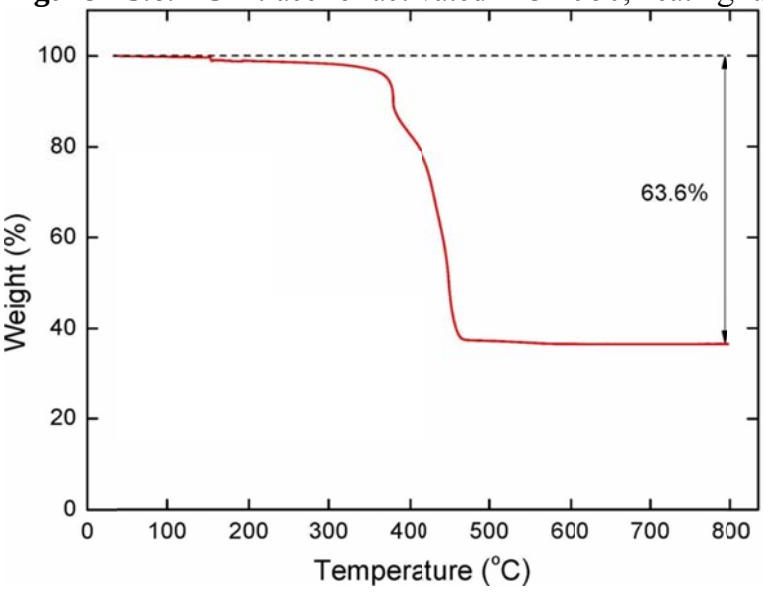

Figure A5.7. TGA trace for activated MOF-950, heating rate: 5 °C min^{-1} in N_2.

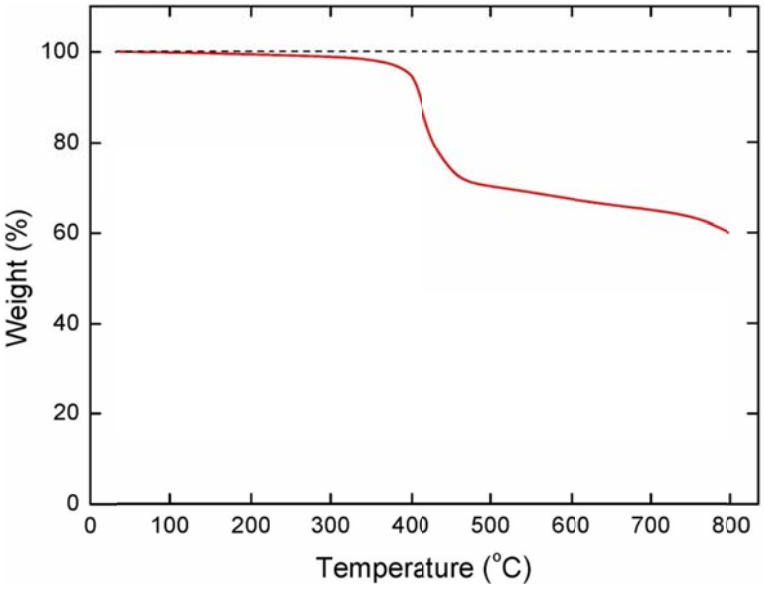

Figure A5.8. TGA trace for activated MOF-905, heating rate: 5 °C min^{-1} in air.

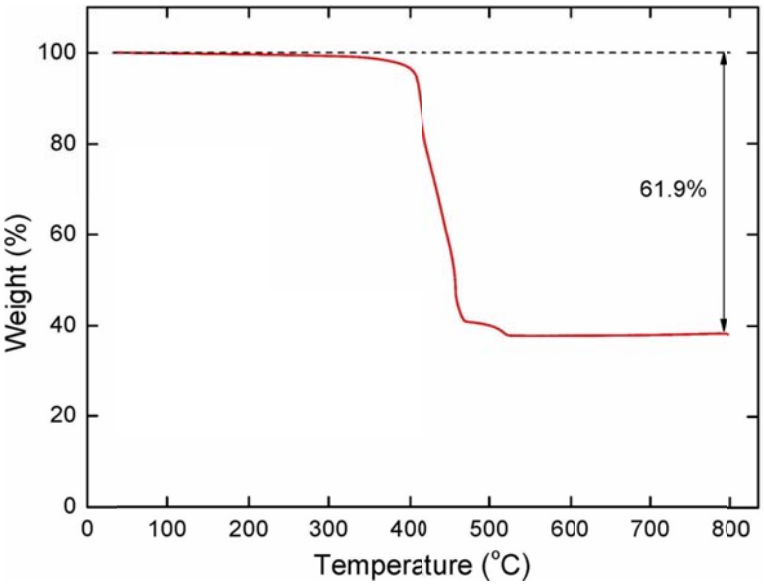

Figure A5.9. TGA trace for activated MOF-905, heating rate: 5 °C min^{-1} in N_2.

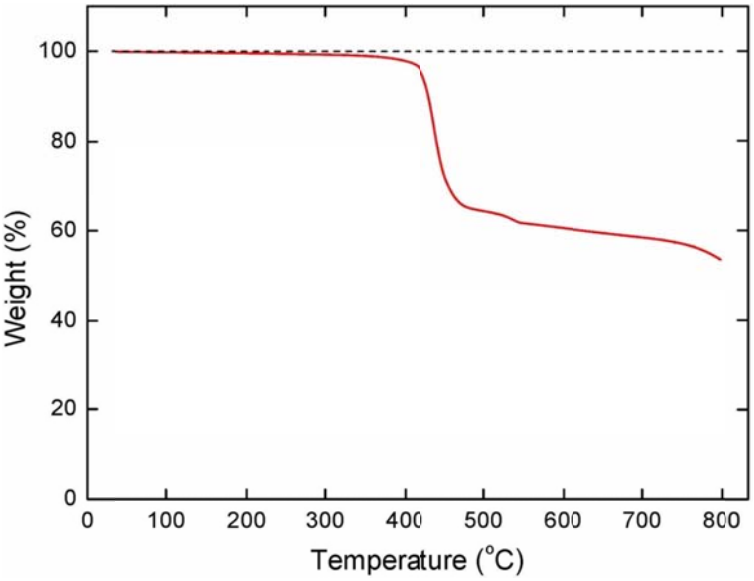

Figure A5.10. TGA trace for activated MOF-905-Me_2, heating rate: 5 °C min^{-1} in air.

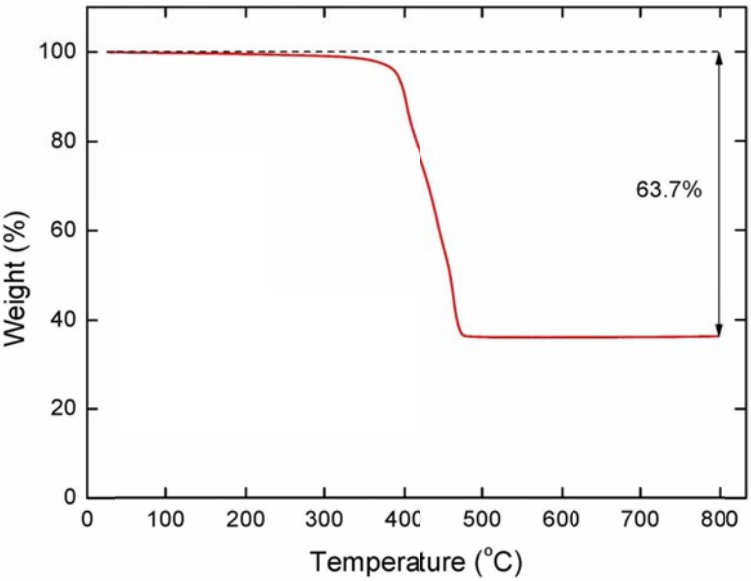

Figure A5.11. TGA trace for activated MOF-905-Me_2, heating rate: 5 °C min^{-1} in N_2.

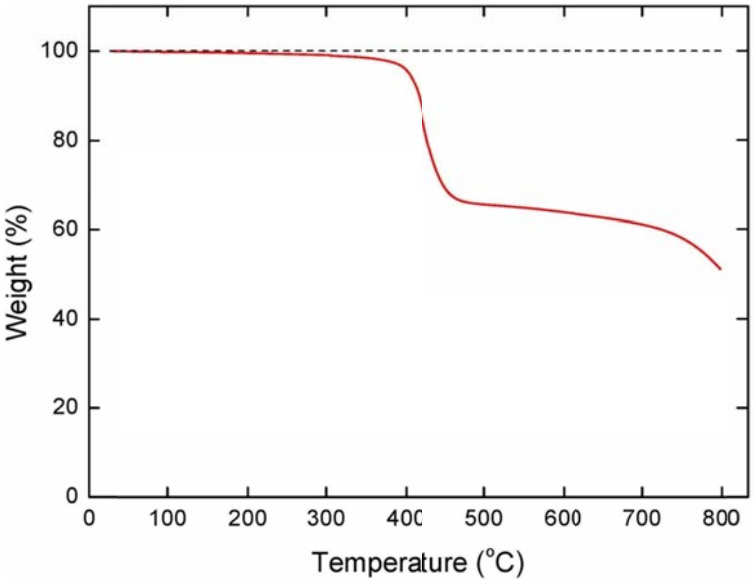

Figure A5.12. TGA trace for activated MOF-905-Nap, heating rate: 5 °C min^{-1} in air.

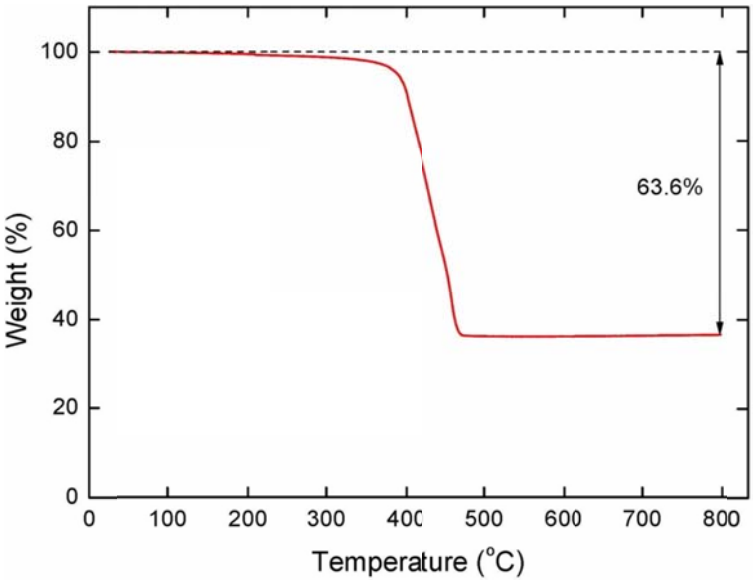

Figure 5.13. TGA trace for activated MOF-905-Nap, heating rate: 5 °C min^{-1} in N_2.

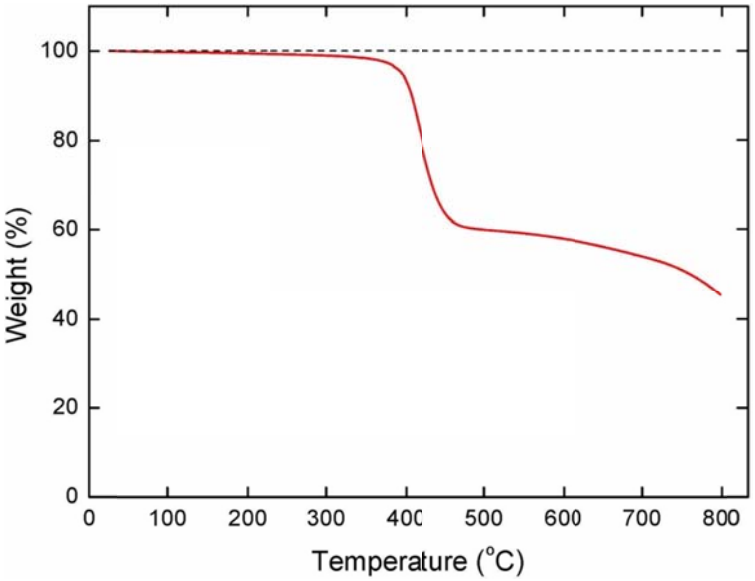

Figure A5.14. TGA trace for activated MOF-905-NO_2, heating rate: 5 °C min^{-1} in air.

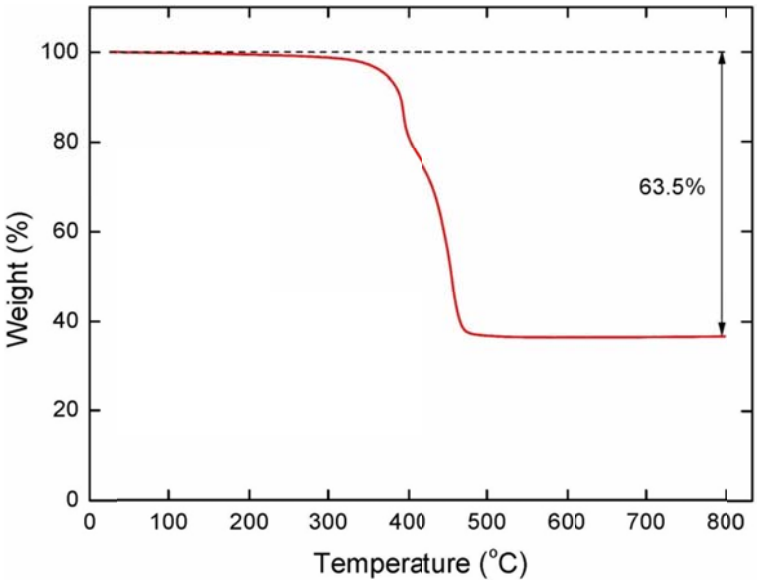

Figure A5.15. TGA trace for activated MOF-905-NO_2, heating rate: 5 °C min^{-1} in N_2.

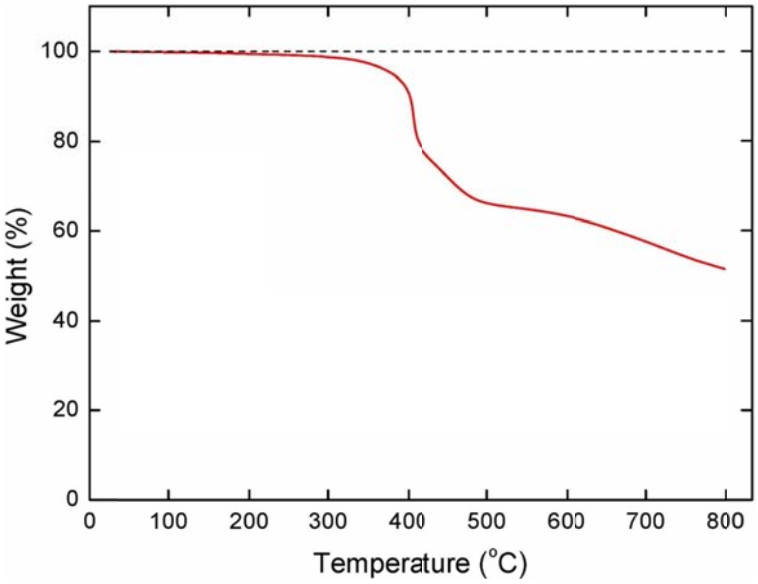

Figure A5.16. N_2 isotherm of MOF-950 at 77 K.

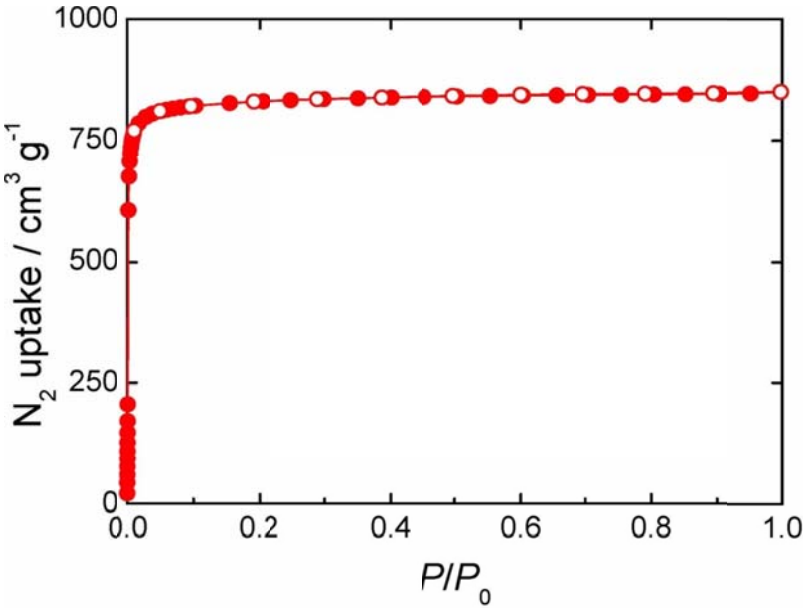

Figure A5.17. N_2 isotherm of MOF-905 at 77 K.

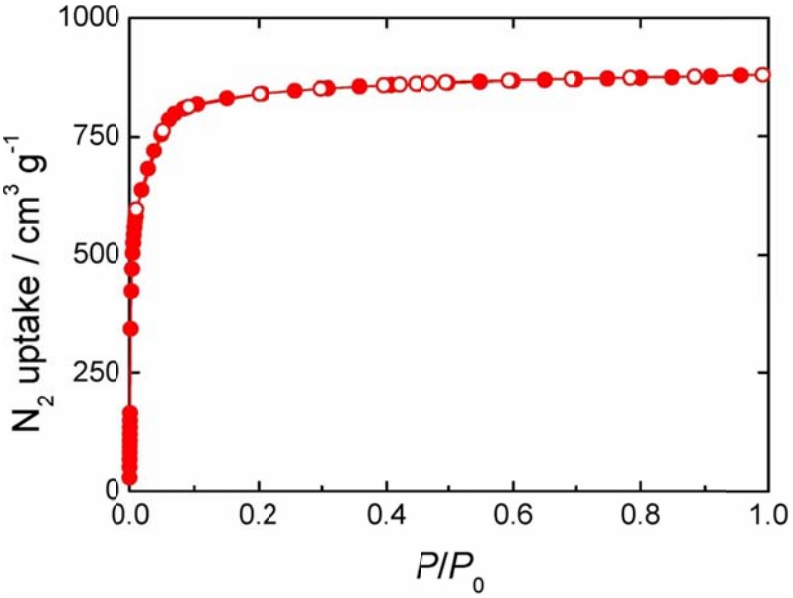

Figure A5.18. N_2 isotherm of MOF-905-Me_2 at 77 K.

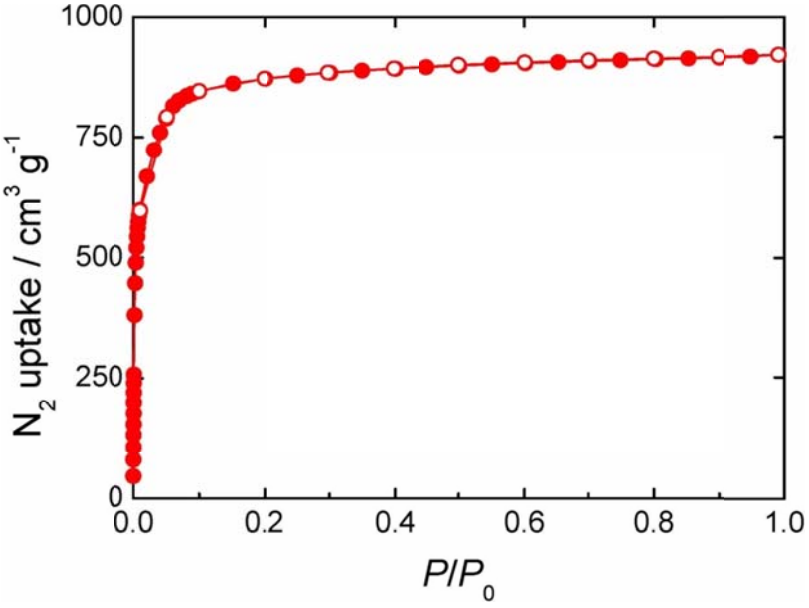

Figure A5.19. N_2 isotherm of MOF-905-Nap at 77 K.

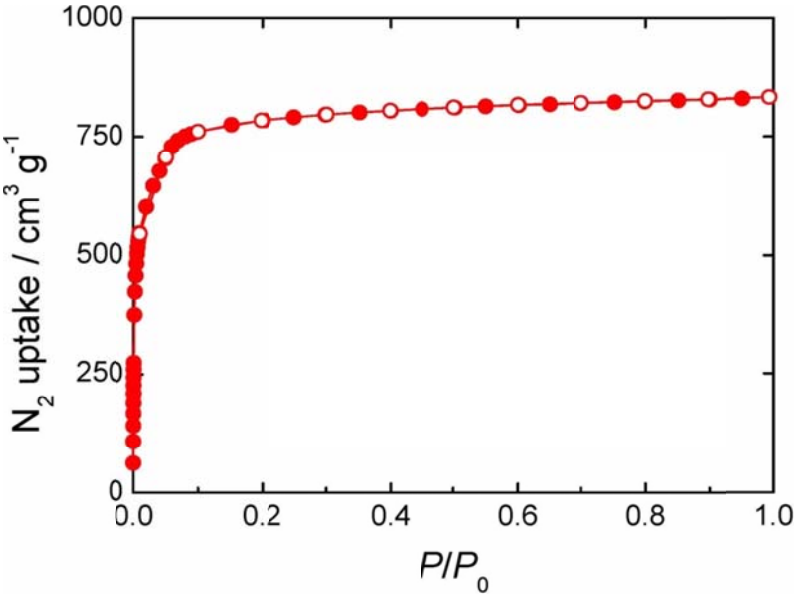

Figure A5.20. N_2 isotherm of MOF-905-NO_2 at 77 K.

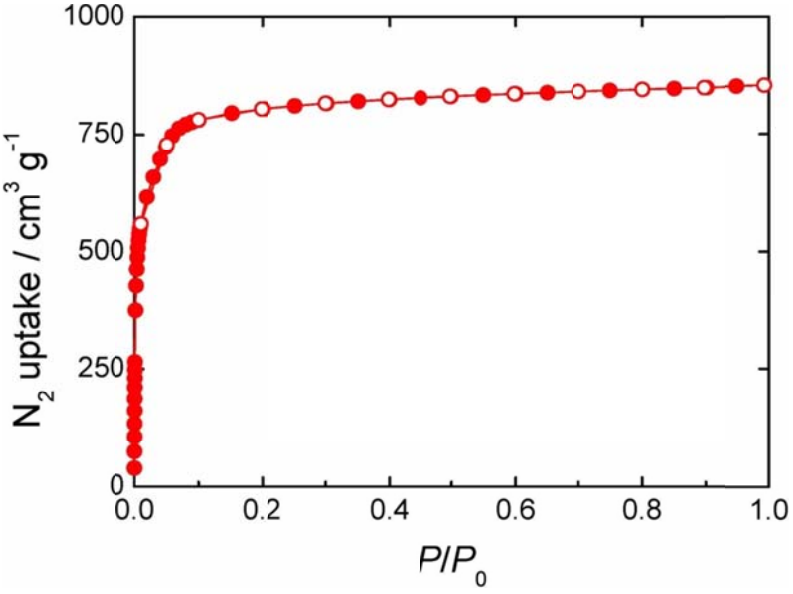

Figure A5.21. Low-pressure CH_4 isotherms for MOF-950 measured at 273, 283, and 298 K.

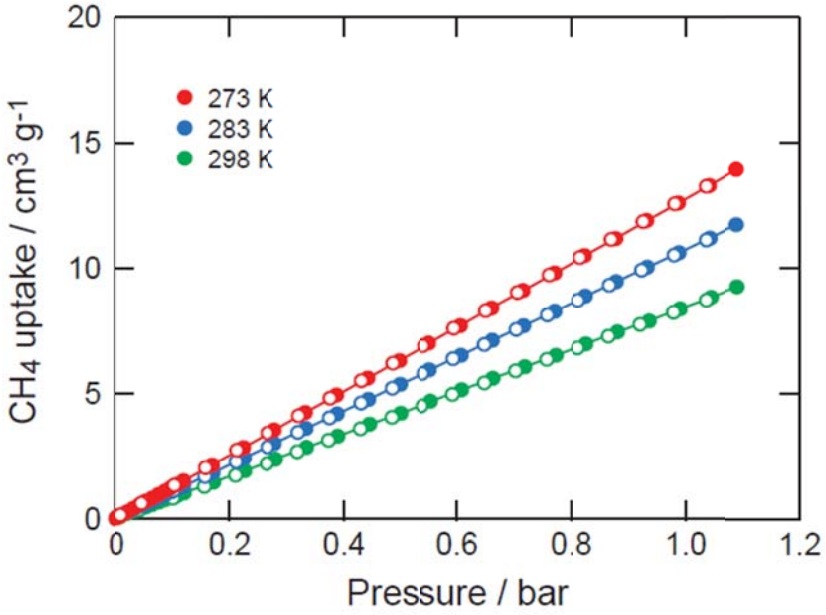

Figure A5.22. Low-pressure CH_4 isotherms for MOF-905 measured at 273, 283, and 298 K.

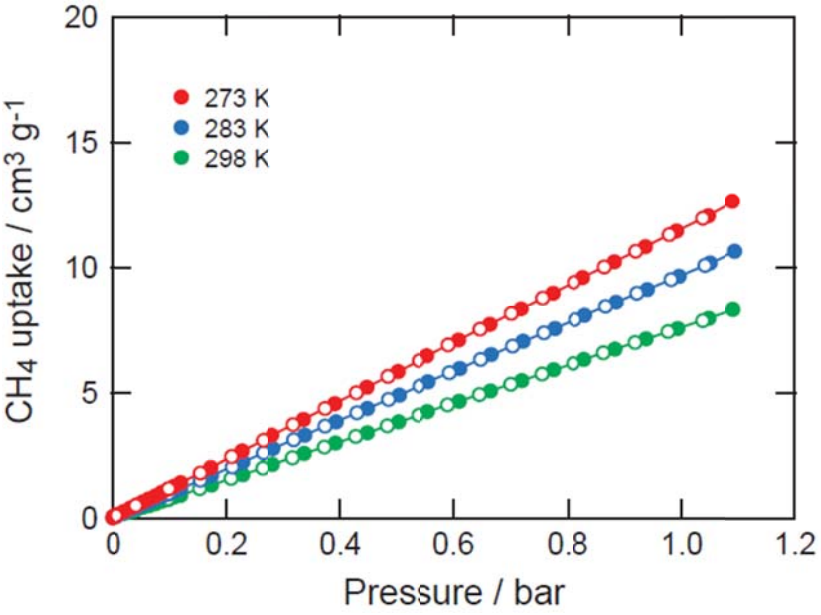

Figure A5.23. Low-pressure CH_4 isotherms for MOF-905-Me_2 measured at 273, 283, and 298 K.

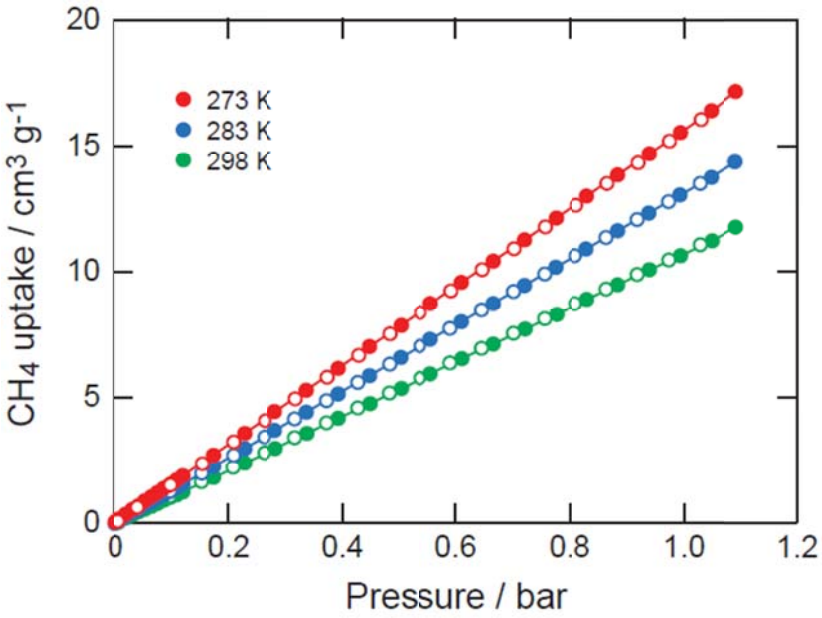

Figure A5.24. Low-pressure CH_4 isotherms for MOF-905-Nap measured at 273, 283, and 298 K.

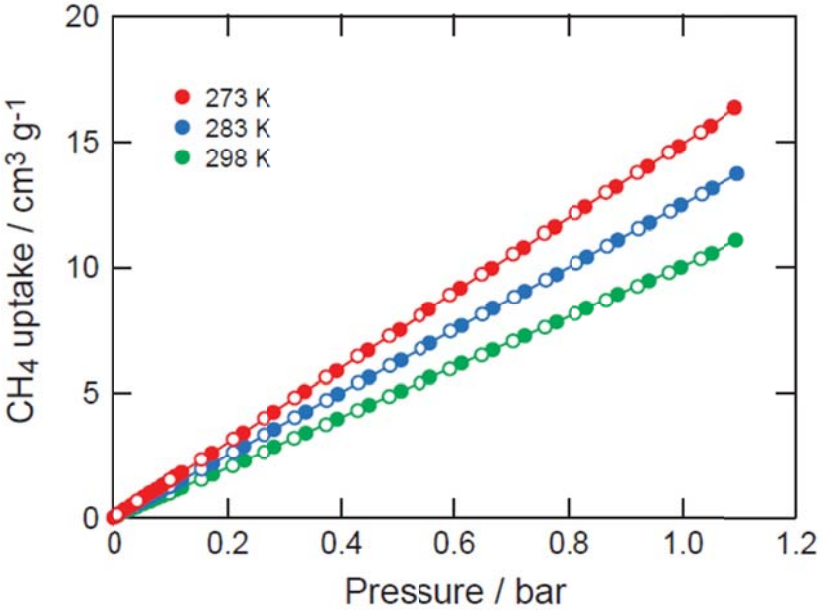

Figure A5.25. Low-pressure CH_4 isotherms for MOF-905-NO_2 measured at 273, 283, and 298 K.

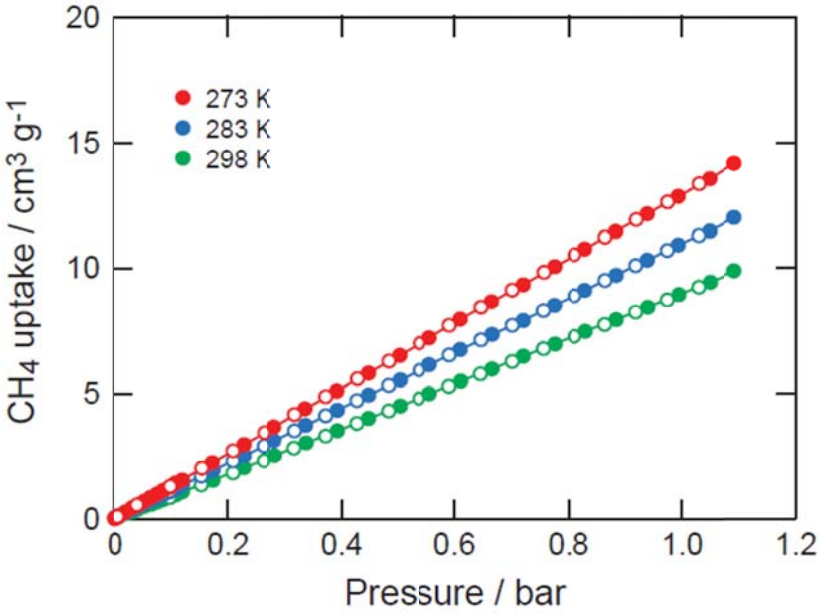

Figure A5.26. Isosteric enthalpies of adsorption for MOFs.

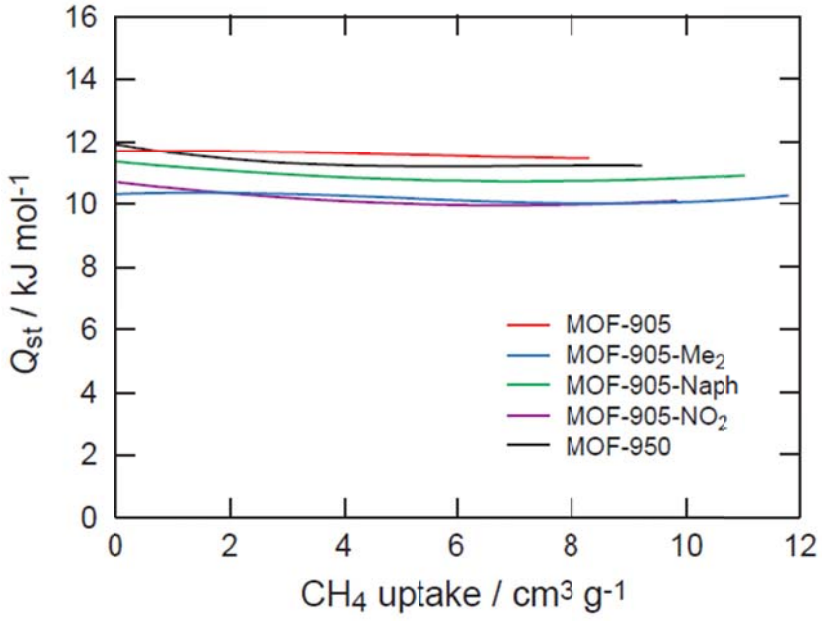

Figure A5.27. Excess and total CH_4 isotherms for MOF-950 measured at 273, 283, and 298 K.

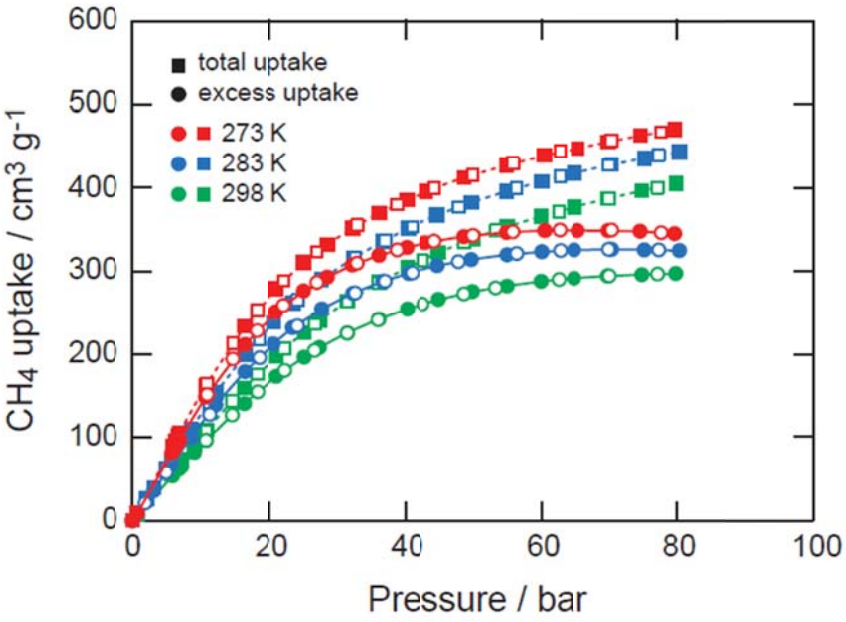

Figure A5.28. Excess and total CH_4 isotherms for MOF-905 measured at 273, 283, and 298 K.

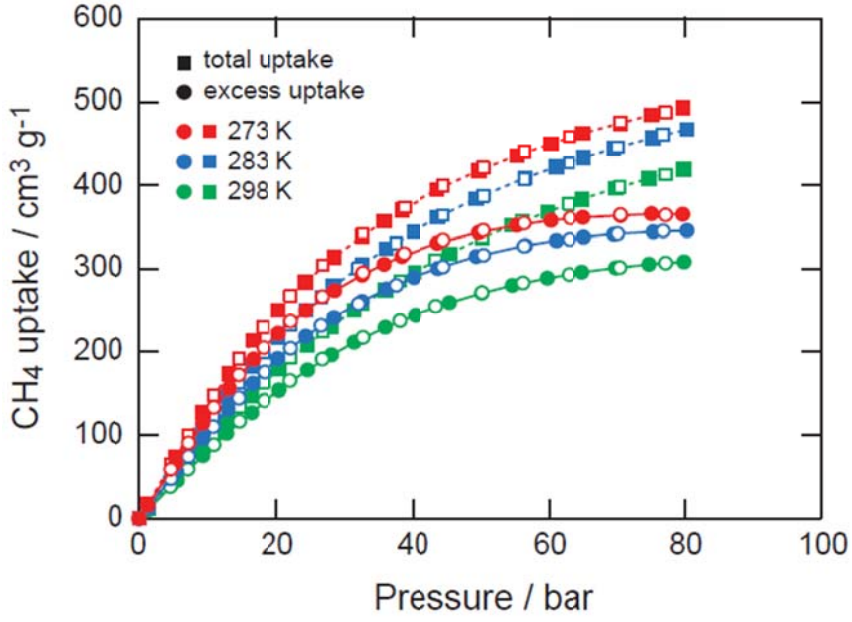

Figure A5.29. Excess and total CH_4 isotherms for MOF-905-Me_2 measured at 273, 283, and 298 K.

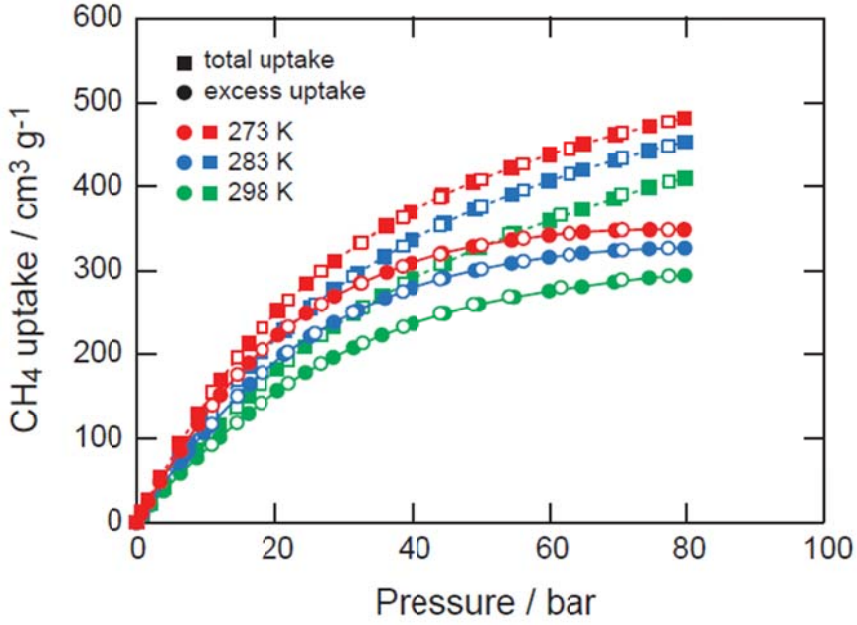

Figure A5.30. Excess and total CH_4 isotherms for MOF-905-Naph measured at 273, 283, and 298 K.

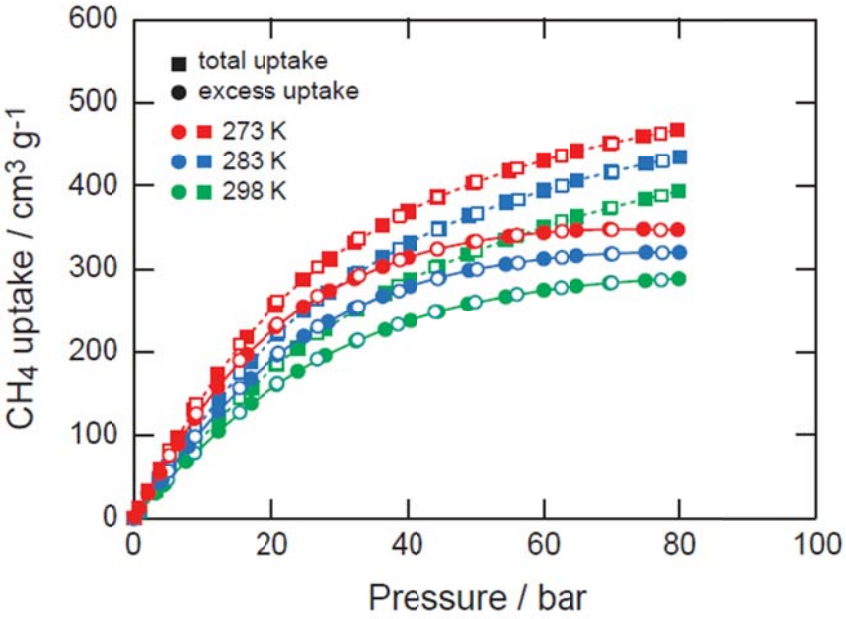

Figure A5.31. Excess and total CH_4 isotherms for MOF-905-NO_2 measured at 273, 283, and 298 K.

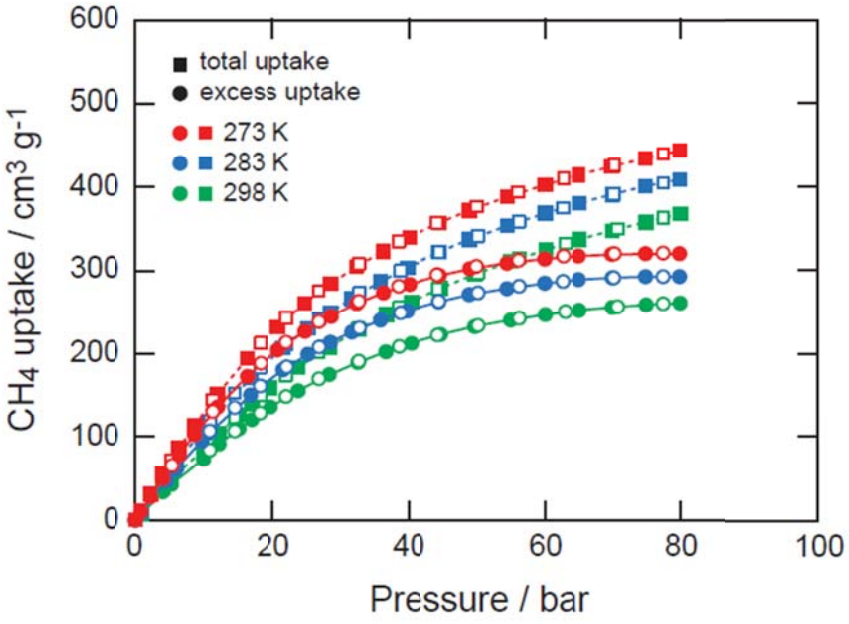

Figure A5.32. Excess CH_4 isotherms for MOFs measured at 298 K.

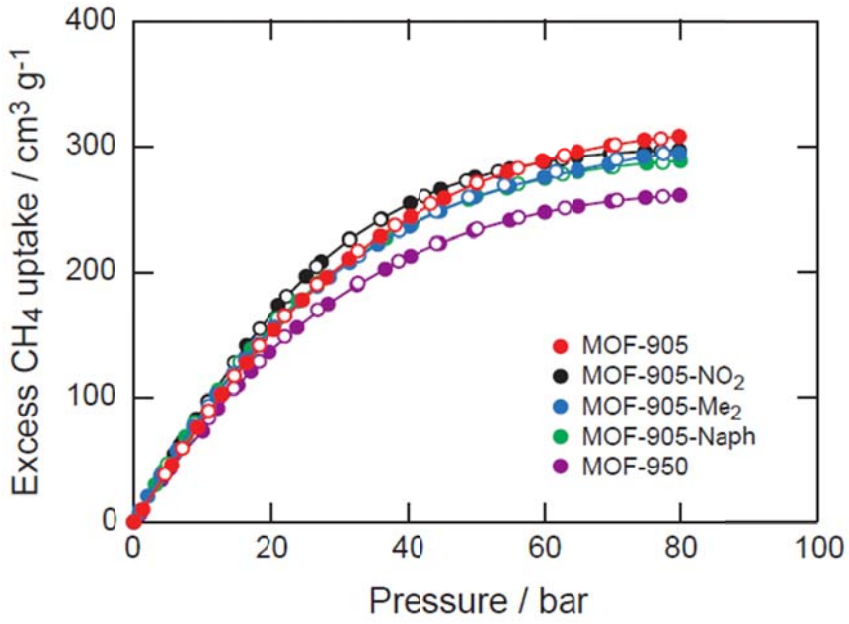

Figure A5.33. Extrapolation of total CH_4 isotherms measured at 298 K. Bulk CH_4 data is overlaid.

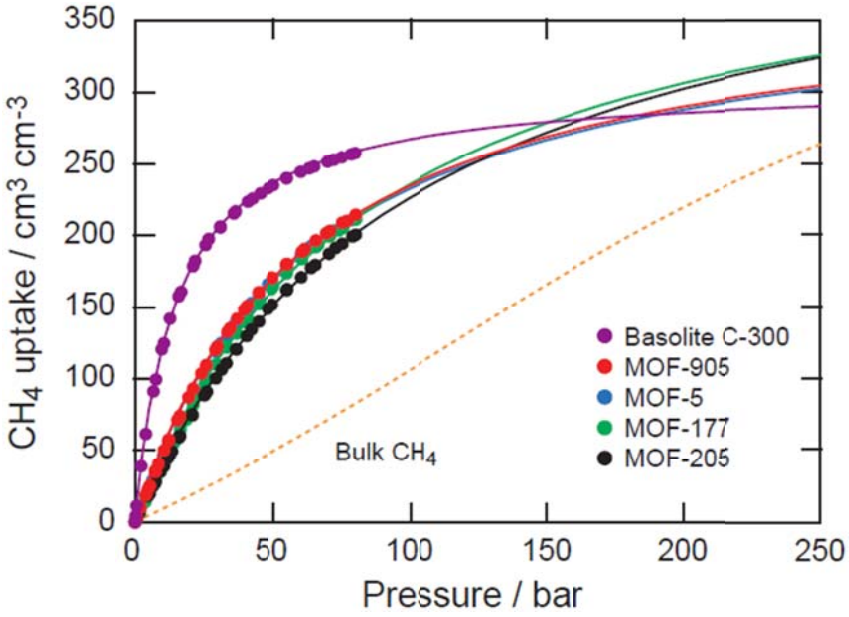

References and Notes

(1) U.S. Energy Information Administration, Annual Energy Outllok 2013 Early Release.

(2) U.S. Energy Information Administration, Natural Gas Annual (October 31, 2014).

(3) Alternative Fuels Data Center – Fuel Properties Comparison, 2013, http://www.afdc.energy.gov/fuels/fuel_comparison_chart.pdf.

(4) Menon, V. C.; Komarneni, S. J. Porous Mater. **1998**, 5, 43.

(5) (a) Talu, O. Proc. IVth Int. Conf. on Fundamentals of Adsorption, Kyoto, **1992**, page 655; (b) Yeh, S. Energy Policy, **2007**, 35, 5865; (c) Whyatt, G. A. Issues Affecting Adoption of Natural Gas in Light- and HeavyDuty Vehicles, **2010**, PNNL-19745.

(6) (a) Wegrzyn, J.; Gurevich, M. Appl. Energy **1996**, 55, 71. (b) Judd, R. W.; Gladding, D. T. M.; Hodrien, R. C.; Bates, D. R.; Ingram, J. P.; Allen, M. Prepr. Pap. Am. Chem. Soc. Div. Fuel Chem. **1998**, 43, 575; (c) Dvorak, K.; Hodrien, R. C. Development of Adsorbed Natural Gas Technology for Large Scale Diurnal Storage Applications, Int. Gas Research Conference, Amsterdam, **2001**; (d) Lau, L. Y.; Judd, R. W. New Approach to Natural Gas Storage – Advances in Adsorbed Natural Gas (ANG) Technology, Int. Gas Research Conference, Paris, **2008**.

(7) Furukawa, H.; Müller, U.; Yaghi, O. M. Angew. Chem. Int. Ed. **2015**, 54, 3417.

(8) Methane Opportunities for Vehicular Energy, Advanced Research Project Agency – Energy, U.S. Dept. of Energy, Funding Opportunity no. DE-FOA-0000672, **2012**.

(9) (a) Mason, J. A.; Veenstra, M.; Long, J. R. Chem. Sci. **2014**, 5, 32. (b) Peng, Y.; Krungleviciute, V.; Eryazici, I.; Hupp, J. T.; Farha, O. K.; Yildirim, T. J. Am. Chem. Soc. **2013**, 135, 11887.

(10) He, Y.; Zhou, W.; Qian, G.; Chen, B. Chem. Soc. Rev. **2014**, 43, 5657.

(11) Gándara, F.; Furukawa, H.; Lee, S.; Yaghi, O. M. J. Am. Chem. Soc. **2014**, 136, 5271.

(12) Wu, H.; Simmons, J. M.; Liu, Y.; Brown, C. M.; Wang, X.-S.; Ma, S.; Peterson, V. K.; Southon, P. D.; Kepert, C. J.; Zhou, H.-C.; Yildirim, T.; Zhou, W. Chem. Eur. J. **2010**, 16, 5205.

(13) Wilmer, C. E.; Leaf, M.; Lee, C. Y.; Farha, O. K.; Hauser, B. G.; Hupp, J. T.; Snurr, R. Q. Nat. Chem. **2012**, 4, 83.

(14) Wang, Y.; Tan, C.; Sun, Z.; Xue, Z.; Zhu, Q.; Shen, C.; Wen, Y.; Hu, S.; Wang, Y.; Sheng, T.; Wu, X. Chem. Eur. J. **2014**, 20, 1341.

(15) Ried, W.; Königstein, F.-J. Chem. Ber. **1959**, 92, 2532.

(16) Chae, H. K.; Kim, J.; Friedrichs, O. D.; O'Keeffe, M.; Yaghi, O. M. Angew. Chem. Int. Ed. **2003**, 42, 3907.

(17) Zhang, Y.-B.; Furukawa, H.; Ko, N.; Nie, W.; Park, H. J.; Okajima, S.; Cordova, K. E.; Deng, H.; Kim, J.; Yaghi, O. M. J. Am. Chem. Soc. **2015**, 137, 2641.

(18) (a) Klein, N.; Senkovska, I.; Gedrich, K.; Stoeck, U.; Henschel, A.; Mueller, U.; Kaskel, S. Angew. Chem. Int. Ed. **2009**, 48, 9954. (b) Furukawa, H.; Ko, N.; Go, Y. B.; Aratani, N.; Choi, S. B.; Choi, E.; Yazaydin, A. O.; Snurr, R. Q.; O'Keeffe, M.; Kim, J.; Yaghi, O. M. Science **2010**, 329, 424. (c) Alezi, D.; Belmabkhout, Y.; Suyetin, M.; Bhatt, P. M.; Weseliński, Ł. J.;

Solovyeva, V.; Adil, K.; Spanopoulos, I.; Trikalitis, P. N.; Emwas, A.-H.; Eddaoudi, M. J. Am. Chem. Soc. **2015**, 137, 13308. (d) Li, B.; Wen, H.-M.; Wang, H.; Wu, H.; Tyagi, M.; Yildirim, T.; Zhou, W.; Chen, B. J. Am. Chem. Soc. **2014**, 136, 6207. (e) Mason, J. A.; Oktawiec, J.; Taylor, M. K.; Hudson, M. R.; Rodriguez, J.; Bachman, J. E.; Gonzalez, M. I.; Cervellino, A.; Guagliardi, A.; Brown, C. M.; Llewellyn, P. L.; Masciocchi, N.; Long, J. R. Nature **2015**, 527, 357.

(19) Spek, A. L. Acta Cryst. **2009**, D65, 148.

Chapter VI

Inclusion of Phosphotungstic Acid (PTA) in Metal-Organic Frameworks and n-Hexane Conversion on Platinum Nanoparticles Supported on PTA-Loaded MOFs

Introduction

Despite the vast interest in greener energy sources and the rapid increase of their use in the global energy market, oil is the leading energy source and will still be for the coming 20 to 40 years.[1] Various products can be produced from a barrel of crude oil, such as gasoline (19 gallons), diesel (10 gallons), and jet fuel (4 gallons).[1] Among them, gasoline, the major fuel of our life, is made from the naphtha (C_6 to C_{12}) feed stock of crude oil.[2] To produce better fuels, catalytic reforming of hydrocarbons is of key importance for the production of high-octane number (ON) gasoline in petroleum chemistry. This catalytic process converts linear hydrocarbons to their corresponding branched isomers. The target, like all catalytic processes, is to optimize both the overall activity and product selectivity simultaneously.[3] In naphtha reforming, cyclizing or cracking the hydrocarbon creates the unwanted byproducts. This chemistry is normally accomplished by the use of a binary catalyst composed of platinum metal loaded on an acidic support, such as a zeolite.[4] Figure 6.1 shows typical pathways for the reforming of n-hexane, a good model reaction for study of the more complex process of naphtha refining. These pathways include: (a) cracking to shorter chain hydrocarbons; (b) isomerization to branched C_6-isomers; (c) cyclization to methylcyclopentane or cyclohexane; (d) dehydrogenation to unsaturated hydrocarbons such as methylcyclopentane and hexene; and (e) aromatization to benzene. Pathway (b) leads to target products which clearly have higher ON than the starting n-hexane molecules.

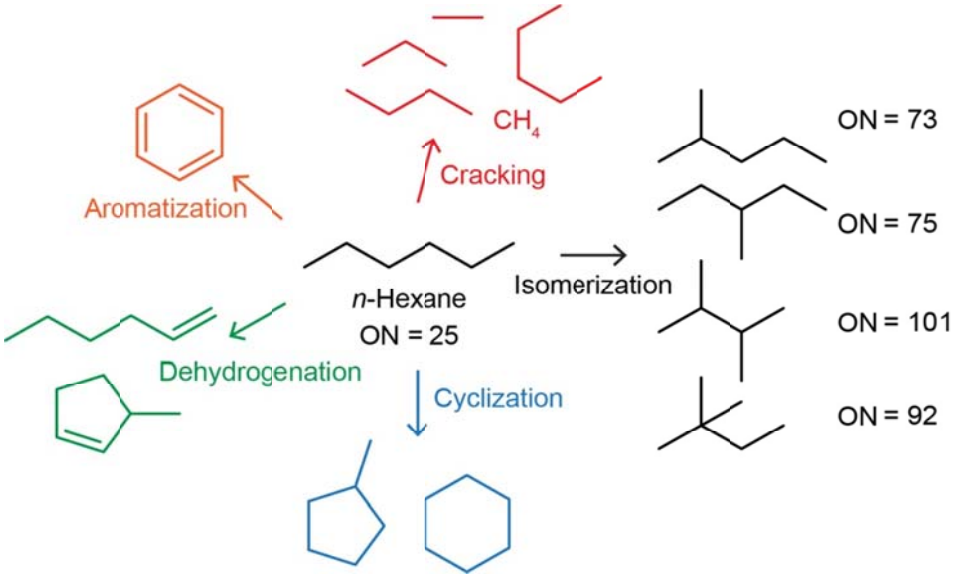

Figure 6.1. Reaction pathways for catalytic n-hexane reforming.

It is demonstrated that the platinum metal catalyzes the dehydrogenation and hydrogenation of the hydrocarbons, while the isomerization occurs on the acidic support via carbocation transition species.[5] Previous studies also reveal that it is possible to change the catalytic activity and selectivity of the system by varying the size and shape of metal nanoparticles, composition of metal nanoparticles, pore matrices of the supporting materials, and chemical composition and acidity of the supporting materials.[6] MOFs are known as versatile materials whose pore matrices and chemical compositions can be changed nearly at will.[7] Recently, MOFs bearing Lewis and Brønsted acidity are also reported as effective solid acid catalysts.[8] Among all MOF-based acid catalysts, one type that has been studied most frequently is the phosphotungstic acid (PTA) encapsulated MOF materials, such as MIL-100, MIL-101, UiO-67, and HKUST-1.[9] They have shown high activity for solution based catalytic reactions, such as production of 5-hydroxymethylfurfural, conversion of cellulose, esterification, and etherification reactions.[9] Despite PTA supported on silica and other metal oxides shows interesting catalytic activity for n-hexane reforming,[10] to-date, no study has been reported using these PTA loaded MOFs on this reaction. Thus, we decide to apply these PTA loaded MOF acids for gas-phase reforming of n-hexane and study their activity as well as the factors that may affect the overall activity and selectivity.

We selected chromium(III) terephthalate (MIL-101), $Cr_3O(OH)(BDC)_3$,[11] as the MOF support because of its high thermal, chemical, and solvent stability, and more importantly its large (~3.5 nm) cavities and (~1.5 nm) apertures that enable PTA (ca. 1.3 nm in diameter and 2.25 nm^3 in volume) encapsulation as well as mass transport. Primitive MIL-101 is known to have mild Lewis acid properties due to the presence of open metal sites on those chromium oxide clusters.[12] With the loading of PTA, the strongest heteropolyacid known with good thermal stability in the solid state, MIL-101 and PTA composites are expected to be formed having both Lewis and Brønsted acid sites. Two methods have been reported to synthesize this composite material which utilize two-step and one-step synthesis approaches. In the first step of the two step synthesis approach, the MOF is prepared. This is followed by the impregnation of PTA molecules into the MOF pores by diffusing the guests into either solvent filled or evacuated pores as the second step. The one-step synthesis approach differs in that PTA molecules are included at the same time as the MOF is being formed.[8e] It was shown that the distribution of included POMs in MIL-101 materials greatly depends on the preparation methods: when the two-step method was used, only a small portion of the large cavities of MIL-101 was occupied by POM molecules, while the medium-sized pores, which represent 60% of the total amount of pores, were not occupied due to a smaller pore opening than the size of the Keggin-type POM. Instead, blockage of the pore openings was observed. This indicates that a considerable number of molecules in these POM-impregnated MIL-101 samples actually reside on the outside surface of the MOF crystals instead of being included within the pores. Alternatively, when the one-step method was used, better-dispersed POM moieties and catalytic activity were obtained in these POM-encapsulated MIL-101 samples. They were measured to have nitrogen sorption isotherms similar to that of pristine MIL-101 with all three steps observed in the profiles. This indicates a more evenly distribution of POMs in both the medium and the large cavities in MIL-101 with no significant blockage of the pore openings.[13]

In the present chapter, we report on the synthesis of Pt/xPTA/MIL-101 (x = 0, 25, and 60, wt % of PTA in PTA/MIL-101 composites) composite catalysts with different PTA loadings, the characterization of their pore matrices and acidity, and the evaluation of the catalyst materials in

the vapor phase hydrogenation of n-hexane. When Pt nanoparticles supported on 60 wt% PTA/MIL-101 (Pt/60PTA/MIL-101) was evaluated, it was found to be highly active (7 times greater than Pt supported on Al modified mesoporous silica MCF-17) and selective (> 90%) toward branched isomer production at 250 ^{o}C. When Pt supported on either the pure MOF or MOF with a smaller PTA loading were tested separately, it was found that both catalysts were relatively inactive. This behavior was attributed to the different acidity of these composite catalysts.

Experimental Section

Chemicals and supplies. Chromium nitrate nonahydrate [$Cr(NO_3)_3 \cdot 9H_2O$, 99%] and terephthalic acid (H_2BDC, ≥ 99.5%) were obtained from Aldrich. Phosphotungstic acid ($H_3PW_{12}O_{40} \cdot xH_2O$) was obtained from Merck & Co Inc. Hydrochloric acid (ACS reagent, 37%) was obtained from EMD Millipore Chemicals. Ethanol (anhydrous, ≥ 99.5%), mesitylene (98%), n-hexane (ReagentPlus, ≥ 99%), ethylene glycol (anhydrous, 99.8%), acetonitrile-d_3 (≥ 99.8 atom% D), tetraethylorthosilicate (99.999%), aluminum chloride ($AlCl_3$, 99.999%), ammonium fluoride (NH_4F, 99.99%), ammonium nitrate (NH_4NO_3, 98%), chloroplatinic acid hexahydrate ($H_2PtCl_6 \cdot 6H_2O$, ≥ 37.50% Pt basis), Poly(vinylpyrrolidone), and Pluronic® P-123 were obtained from Sigma-Aldrich. All starting materials and solvents, unless otherwise specified, were used without further purification.

Analytical techniques. Powder X-ray diffraction patterns (PXRD) were recorder using a Rigaku Miniflex 600 diffractometer (Bragg-Brentano geometry, Cu Kα radiation λ = 1.54056 Å). Carbon, hydrogen, and nitrogen elemental microanalyses (EA) were performed in the Microanalytical Laboratory of the College of Chemistry at UC Berkeley, using a Perkin Elmer 2400 Series II CHNS elemental analyzer. Inductively coupled plasma-optical emission spectroscopy (ICP-OES) was performed on a PerkinElmer Optical Emission Spectrometer Optima 7000DV instrument. Scanning electron microscope (SEM) images were obtained using a Zeiss Gemini Ultra-55 analytical scanning electron microscope with a working distance of 8.4 mm and a low acceleration voltages (5 keV) to avoid damage to the samples during observation. All MOF SEM samples were prepared by direct deposition of MOF/acetone dispersion (1 mg mL^{-1}) on the silicon substrate heated on a hot plate (60 °C). Attenuated total reflectance (ATR) FTIR spectra of neat samples were performed in-house on a Bruker ALPHA Platinum ATR-FTIR Spectrometer equipped with a single reflection diamond ATR module. Thermal gravimetric analysis (TGA) curves were recorded in-house on a TA Q500 thermal analysis system under gas flow. One-pulse ^{31}P solid-state nuclear magnetic resonance (SSNMR) spectra were acquired on a Tecmag Discovery spectrometer at 7.05 T using a 4 mm Doty triple resonance magic-angle spinning (MAS) probe. The Larmor frequency of ^{31}P is 141.49 MHz. Continuous-wave ^{1}H heteronuclear decoupling (~ 50 kHz decoupling field) was applied for ^{31}P NMR data acquisition. The 90° pulse of ^{31}P pulse (2.8 μs) was measured on $NH_4H_2PO_4$. The pulse delay was 60 s, and the sample spinning rates were between 7 and 10 kHz. The ^{31}P chemical shifts were externally referenced to $NH_4H_2PO_4$, which is 0.81 ppm relative to 85% H_3PO_4 (primary reference). Low-pressure gas (N_2) adsorption isotherms were recorded in-house on a Quantachrome Autosorb-1 volumetric gas adsorption analyzer. A liquid nitrogen bath was used for the measurements at 77 K. Acetonitrile isotherms were measured in-house on a BEL Japan BELSORP-aqua3. Prior to the acetonitrile adsorption measurements, acetonitrile-d_3 (analyte) was flash frozen under liquid

nitrogen and then evacuated under dynamic vacuum at least five times to remove any gases in the liquid reservoir. The measurement temperature was controlled with a water circulator. Helium was used for the estimation of dead space for gas and water adsorption measurements. Ultra-high-purity grade N_2 and He gases (Praxair, 99.999% purity) were used throughout the experiments.

Synthesis and Characterization of Pt nanoparticles supported on PTA/MOF. In this work, MIL-101 and PTA/MIL-101 composites were synthesized in water using an HF-free procedure reported in literature.[14]

MIL-101. A mixture of H_2BDC (2.08 g, 12.5 mmol) and $Cr(NO_3)_3 \cdot 9H_2O$ (5.00 g, 12.5 mmol) in 50 mL deionized water was stirred at room temperature for 20 minutes before placed in a 100-mL Teflon-lined autoclave bomb, which was heated at 220 °C for 18 hours. The vessel was slowly cooled to room temperature and green solids were quickly separated using a centrifuge (5,000 rpm, 8 min). As-synthesized MIL-101 was washed 4 times per day with 50 mL of deionized water for 3 days and immersed in 50 mL of ethanol for 3 days, during which time the solvent was replaced 4 times per day. The solid was then evacuated under dynamic vacuum first at room temperature for 24 hours and then 150 °C for 24 hours to yield activated MIL-101 (Yield: 1.85 g, 61.9% based on Cr). EA of activated sample: Calcd. for $Cr_3C_{24}H_{17}O_{16}$ = $Cr_3O(OH)(H_2O)_2(C_8H_4O_4)_3$: Cr, 21.74; C, 40.18; H, 2.39%. Found: Cr, 20.18; C, 42.47; H, 2.99%. ATR-FTIR (4000–400 cm^{-1}): 1618 (m), 1543 (w), 1509 (m), 1397 (s), 1162 (w), 1019 (w), 880 (w), 831 (w), 811 (w), 746 (m), 714 (w), 648 (sh), 580 (m), 439 (m).

25 wt% PTA/MIL-101 Composite Material, 25PTA/MIL-101. A mixture of H_2BDC (2.08 g, 12.5 mmol), $Cr(NO_3)_3 \cdot 9H_2O$ (5.00 g, 12.5 mmol), and PTA (1.25 g, 0.434 mmol, anhydrous basis) in 50 mL deionized water was stirred at room temperature for 20 minutes before placed in a 100-mL Teflon-lined autoclave bomb, which was heated at 220 °C for 18 hours. The vessel was slowly cooled to room temperature and green solids were quickly separated using a centrifuge (5,000 rpm, 8 min). As-synthesized 25PTA/MIL-101 was washed 4 times per day with 50 mL of deionized water for 3 days and immersed in 50 mL of ethanol for 3 days, during which time the solvent was replaced 4 times per day. The solid was then evacuated under dynamic vacuum first at room temperature for 24 hours and then 150 °C for 24 hours to yield activated 25PTA/MIL-101 (Yield: 2.32 g, 58.2 % based on Cr). EA of activated sample: Calcd. for $Cr_3P_{0.083}WC_{24}H_{17.25}O_{19.33}$ = $(H_3PW_{12}O_{40})_{0.083}[Cr_3O(OH)(H_2O)_2(C_8H_4O_4)_3]$: Cr, 16.29; P, 0.27; W, 19.20; C, 30.11; H, 1.82%. Found: Cr, 16.76; P, 0.28; W, 19.82; C, 29.69; H, 2.24%. ATR-FTIR (4000–400 cm^{-1}): 1712 (vw), 1619 (m), 1543 (w), 1509 (m), 1397 (s), 1162 (w), 1079 (w), 1019 (w), 981 (w), 881 (w), 825 (m), 745 (m), 715 (w), 582 (m), 464 (m).

60 wt% PTA/MIL-101 Composite Material, 60PTA/MIL-101. A mixture of H_2BDC (2.08 g, 12.5 mmol), $Cr(NO_3)_3 \cdot 9H_2O$ (5.00 g, 12.5 mmol), and PTA (5.00 g, 1.74 mmol, anhydrous basis) in 50 mL deionized water was stirred at room temperature for 20 minutes before placed in a 100-mL Teflon-lined autoclave bomb, which was heated at 220 °C for 18 hours. The vessel was slowly cooled to room temperature and green solids were quickly separated using a centrifuge (5,000 rpm, 8 min). As-synthesized 60PTA/MIL-101 was washed 4 times per day with 50 mL of deionized water for 3 days and immersed in 50 mL of ethanol for 3 days, during which time the solvent was replaced 4 times per day. The solid was then evacuated under dynamic vacuum first at room temperature for 24 hours and then 150 °C for 24 hours to yield activated 60PTA/MIL-101 (Yield: 4.03 g, 55.1 % based on Cr). EA of activated sample: Calcd. for $Cr_3P_{0.36}W_{4.32}C_{24}H_{18.08}O_{30.40}$ = $(H_3PW_{12}O_{40})_{0.36}[Cr_3O(OH)(H_2O)_2(C_8H_4O_4)_3]$: Cr, 8.89; P, 0.64; W,

45.27; C, 16.43; H, 1.04%. Found: Cr, 9.11; P, 0.65; W, 45.30; C, 16.85; H, 1.84%. ATR-FTIR (4000–400 cm^{-1}): 1710 (vw), 1620 (m), 1546 (w), 1509 (w), 1395 (s), 1164 (w), 1080 (w), 1018 (w), 972 (m), 899 (m), 819 (s), 743 (m), 667 (w), 585 (m), 514 (w), 458 (m).

Synthesis of MCF-17 and Al-modified MCF-17. MCF-17 type mesoporous silica was synthesized and aluminated according to reported literature methods.[4b,6b,15] In a typical experiment, mesitylene, acting as a pore swelling agent, was added to an aqueous solution containing triblockcopolymer Pluoronic® P123 and hydrochloric acid. After stirring of this solution for 2 hours at 40 °C, tetraethylorthosilicate (TEOS) was added and the solution was stirred for additional 20 hours. Ammonium fluoride was then added and the solution was allowed to hydrothermally react at 100 °C for 1 day. The MCF-17 product was then calcined for 6 hours at 550 °C. The pore size of the material is 30 to 50 nm and the Langmuir surface area is approximately 1000 $m^2 g^{-1}$.

The calcined MCF-17 sample was grafted with aluminum by slurring with anhydrous aluminum chloride in absolute ethanol, in order to give a Si/Al ratio of 10:1. The slurring solution was stirred overnight at room temperature, followed by removal of ethanol under vacuum. The precipitate was dried at 130 °C for 1 hour, and subsequently calcined at 550 °C for 4 hours in air. To introduce acidic sites in Al-modified MCF-17, Al-MCF-17, the sample was slurred in 1M aqueous solution of ammonium nitrate for 4 hours at room temperature. The sample was then filtered, washed with distilled water, and dried at 130 °C for 1 h. This process was repeated three times and the final product was calcined at 550 °C for 4 hours in air to give acidic Al-MCF-17.

Synthesis of Pt Nanoparticles. Poly(vinylpyrrolidone) (PVP)-capped Pt nanoparticles (NPs) with an average size of 3 nm were synthesized by following the literature reported elsewhere.[6f,6g] In a typical synthesis, PVP and $H_2PtCl_6 \cdot 6H_2O$ were dissolved in 10 mL of ethylene glycol separately, mixed in 50 mL round bottom flask at room temperature under constant stirring, and aged in the pre-heated oil bath at 180 ºC for 30 minutes. The final suspension was naturally cooled to room temperature, mixed with excess amount of hexane to help nanoparticles separate by centrifugation, and washed with a solution composed of ethanol and acetone (volume ratio is about 1:3) for 3 times. Finally, Pt nanoparticles were re-dispersed and kept in ethanol to give colloidal solution of Pt nanoparticles with the concentration of 1 mg/mL.

Synthesis of Pt Nanoparticles supported on MCF-17, Al-MCF-17, and PTA/MOF composites. For supporting Pt nanoparticles on mesoporous silica MCF-17, Al-MCF-17, and PTA/MOF composites, 10 mL of this colloidal solution of Pt nanoparticles was added to the 500 mg of supporting materials to give ca. 0.1 wt% of Pt. The colloidal suspension was sonicated for 5 h at room temperature using a commercial ultrasonic cleaner (Branson, 1510R-MT, 70W, 42 kHz). The precipitates were separated by centrifugation (4000 rpm, 10 min), washed with ethanol for three times, and dried in an oven at 60 °C overnight.

The Pt nanoparticles supported materials were designated as Pt/MCF-17, Pt/Al-MCF-17, and Pt/xPTA/MIL-101 (x = 0, 25, and 60, wt% of PTA in PTA/MIL-101 composites), respectively.

Catalytic Reaction Studies. Gas phase n-hexane hydroisomerization reaction was carried out on the catalysts described above. A tubular fixed-bed flow reactor was used for all catalytic measurements at 1 bar and 200 – 260 ºC. A stainless steel reactor tube with ¼ inch diameter was

loaded with 200 – 300 mg of catalyst, whose ends were capped with a purified thermal silica paper. The remaining space in the reactor tube was filled with purified fused alumina granulate and the ends of the tube were capped with glass wool.

Before the actual reaction measurements, the catalysts were pretreated at 250 ºC for 2 hours under a gas mixture of H_2 (Praxair, 5.0 UHP, 10 sccm) and N_2(Praxair, 5.0 UHP, 10 sccm) with a heating rate of 2 K/min. After the pretreatment, the gas flow was changed to 16 sccm H_2 and n-hexane was introduced using a liquid flow pump (Teledyne ISCO 500D) at a rate of 1.4 mL/hour. In the reactor head, n-hexane was evaporated and mixed with H_2 gas to give a two-component gas flow with n-hexane:H_2 mole ratio of 1:5. A Baratron type manometer (890B, MKS Instruments) was used to monitor the reactor head pressure. At the reactor outlet, the flow lines were maintained at 423 K to enable vapor phase sampling of the reaction products. An in-line gas chromatography-mass spectrometry (GC-MS, HP 6890 Series) equipped with an Aldrich HP-1 capillary column, a flame ionization detector (FID), and a mass selective detector (MSD) was used to analyze the product composition. A GC-MSChemstation software (HP) was used for automatic sampling, data collection, and post-run processing.

Results and Discussion

Inclusion of PTA in MIL-101. One-step synthesis of MIL-101 and PTA/MIL-101 materials was carried out hydrothermally form a mixture of Cr^{3+}, H_2BDC, and PTA at 218 °C (no PTA when synthesizing MIL-101). This HF-free approach is reported to give MIL-101 materials with very similar thermal and chemical stability and properties to those synthesized using HF, despite subtle but considerable differences in the crystal structure (no F within the crystalline structure). More importantly, using this HF-free approach, we not only avoid the use of harmful and corrosive HF, but also eliminate the side reactions between HF and PTA to allow potential one-step encapsulation of PTA molecules.

MIL-101 synthesized accordingly, was obtained as powders of 200-600 nm-sized, octahedral microcrystals (Figure 6.2a). Phase purity and porosity were established using powder X-ray diffraction (PXRD) (Figure 6.2d) and nitrogen sorption measurements (Figure 6.2e), respectively, and its chemical composition was found to be in agreement with the calculated value of $Cr_3O_9(OH)(H_2O)_2(C_8H_4O_4)_3$, despite a slight excess of the carbon and hydrogen content due to the presence of residual free acid and water molecules.

Inclusion of PTA into MIL-101 was achieved by adding different amount of PTA into the starting mixture without changing any other parameters. We observed that the presence of PTA in the reaction mixture significantly changed the morphology of the obtained solids. Resultant particles were up to 5 μm in size, with a morphology comprising octahedral and truncated-octahedral crystals on the surface (Figures 6.2b and 6.2c). This particle appearance is markedly different from that of MIL-101 as significant number of aggregation and inter-growth of nanocrystals are evidenced. Elemental analysis of these materials shows presence of phosphorous and tungsten and the molar ratio of W/P is very close to 12. Assuming all PTA molecules are incorporated in their dehydrated acid form, this one-step approach incorporates 45 to 50% of input PTA into the solids, a value that doesn't change much with different PTA input amounts. Hereafter, the different materials were designated xPTA/MIL-101, x = 25 and 60, where x = wt% of PTA in composite materials.

The quantity of N_2 gas adsorbed by xPTA/MIL-101 samples was significantly smaller than that of the original MIL-101, which indicates smaller pore volumes in these materials (Figure 6.2e). This is expected because of the loading of the MIL-101 pores with PTA in the composite materials. The larger the PTA loading is, the smaller the pores become. This is further proved by smaller pore sizes in xPTA/MIL-101 samples compared to that in the pristine MIL-101 as illustrated by the plot of their pore size distribution (Figure A6.1b).

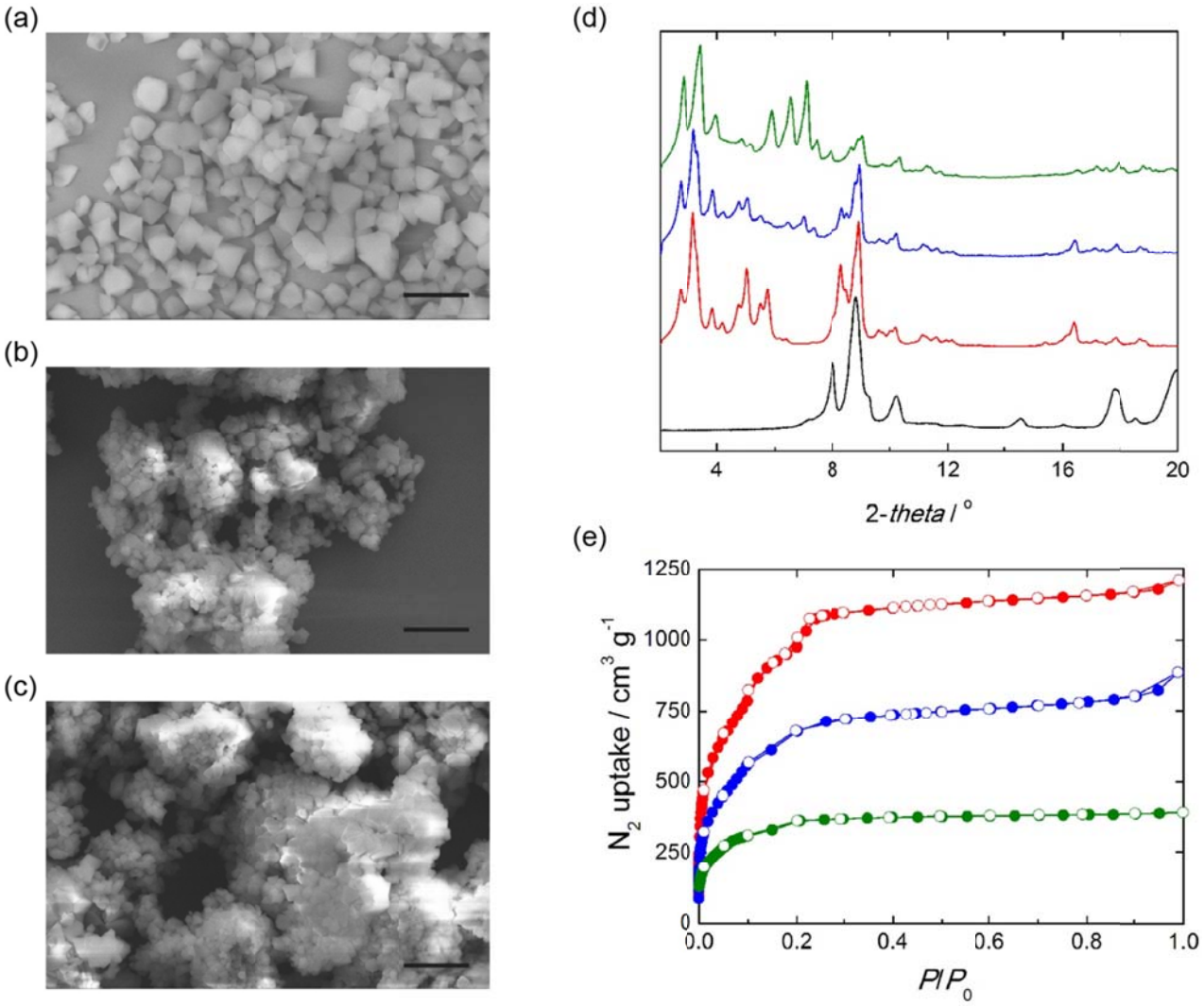

Figure 6.2. (a) to (c) Scanning electron microscopy (SEM) images for (a) MIL-101, (b) 25PTA/MIL-101, and (c) 60PTA/MIL-101 (scale bar: 2 μm). (d) Comparison of experimental powder X-ray diffraction patterns of PTA (black), MIL-101 (red), 25PTA/MIL-101 (blue), and 60PTA/MIL-101 (green). (c) Nitrogen adsorption isotherms for MIL-101 (red), 25PTA/MIL-101 (blue), and 60PTA/MIL-101 (green) at 77K with adsorption and desorption branches represented by closed and open circles, respectively. P/P_0, relative pressure.

The crystal structures of the xPTA/MIL-101 samples were probed via PXRD, with resulting data shown in Figure 6.2d. Significant changes in the diffraction patterns were observed after incorporation of PTA in MIL-101, compared with that of pristine MIL-101. In particular, several new peaks emerged between 6^o and 8^o (2θ value). They become more visible in the higher PTA loading sample (60PTA/MIL-101). None of these newly appeared peaks overlaps with those of pure PTA. In fact, they all lie in the Bragg peak positions of the unit cell of MIL-101, which shows null intensity at these positions (Figure A6.2). According to literature, this PXRD pattern indicates that there are ordered PTA assemblies residing in both the large cages and small pores of MIL-101, and the PTA assemblies in the small pores or cages may possess higher degrees of freedom than those in the large cages. These ordered PTA assemblies prevail when larger amount of PTA molecules are encapsulated into the framework, as demonstrated by the more intense peaks in 60PTA/MIL-101 than those in 25PTA/MIL-101.

Thermal gravimetry (TG) traces of activated MIL-101, 25PTA/MIL-101, and 60PTA/MIL-101 under a flow of air are displayed in Figures A6.6-A6.8. As expected, PTA/MIL-101 samples exhibit lower weight loss than MIL-101. Assuming all organic compounds will be burned out, Cr(III) will become Cr_2O_3, and PTA molecules are not affected since P(V) and W(VI) are at their highest oxidation state. We expected MIL-101 and PTA/MIL-101 samples to lose 69%, 52%, and 28% of their weight, respectively. These numbers are in good agreement with the observed experimental data, which proves our proposed material compositions are correct. To further study the proper activation conditions for theses samples, TG traces of as-synthesized samples (samples were quickly washed with deionized water and ethanol before air-dried) were taken under a flow of N_2 and displayed in Figures A6.9-A6.11. A first weight loss up to 80 ^oC corresponds to the removal of free water and ethanol molecules. The second major weight loss was found between 300 and 500 ^oC in all samples, this step corresponds to the collapse of the framework and the degradation of the organic compounds. However, we did not observe a third weight loss step that is only found in the PTA/MIL-101 composite materials between 230 and 250 ^oC. The weight loss increases as the loading of PTA in the composite material. Considering the fact that we use hydrated PTA as the starting material and the solids are precipitated out from aqueous media, we attribute this step to the dehydration of PTA, a necessary step to expose its strong Brønsted acidity.

Infrared (IR) spectroscopy characterization reveals additional absorption bands in both PTA containing materials, corresponding to phosphotungstate structure at 1080, 972, 889, and 819 cm^{-1}. These absorption bands are attributed to vibrational modes of $\upsilon_{as}(P\text{-}O_a)$, $\upsilon_{as}(W{=}O_d)$, $\upsilon_{as}(W\text{-}O_b)$, and $\upsilon_{as}(W\text{-}O_c)$, respectively.[16] The $\upsilon_{as}(P\text{-}O_a)$, $\upsilon_{as}(W\text{-}O_b)$, and $\upsilon_{as}(W\text{-}O_c)$ vibrational bands are remarkably shifted in comparison to PTA hydrate (1072, 902, and 773 cm^{-1}, respectively). This shift may be attributed to the confinement effect of PTA inside the porous solid.[16] Additionally, a very weak absorption band appears at 1710 cm^{-1} [$\upsilon_{as}(C{=}O)$] in both PTA/MIL-101 samples, which is assigned to the presence of free carboxylic acid.

In order to conclude about the PTA structure after its incorporation into MIL-101 pores, one-pulse ^{31}P solid-state nuclear magnetic resonance (SSNMR) spectra were acquired for both PTA/MIL-101 samples along with PTA hydrate and $CrPW_{12}O_{40}$ hydrate, a byproduct that has strong interaction between Cr(III) and PTA. As shown in Figure A6.15, both 25PTA/MIL-101 and 60PTA/MIL-101 exhibit single resonance at -16 ppm, which is very similar to that of PTA hydrate (resonance at -15.5 ppm). All three spectra are distinct from that of Cr(III) salt of PTA,

which has broader resonance bands at lower field due to its paramagnetic nature. The unchanged chemical shift indicates that the integrity of the PTA unit is maintained inside MIL-101.

Characterization of acidity in PTA/MIL-101 composite materials by acetonitrile adsorption measurements. The successful inclusion of PTA molecules into MIL-101's pores has raised the need to further evaluate their acidity. As stated in Chapter III, adsorption of volatile bases such as NH_3, pyridine, n-butylamine can be used to determine the number of acid sites on solid acid materials. However, due to their strong basicity and the high desorption temperature needed to desorb, these basic molecules are not applied to the characterization of MOF-based solid acids. Instead, acetonitrile, a small molecule with low basicity ($pK_b = 24$), has been successfully applied to characterize acidic properties of sulfated zirconium MOF-808.

Here, we report characterization of acidity in PTA/MIL-101 materials using acetonitrile adsorption measurements, and in addition, we also study the desorption behavior of adsorbed acetonitrile using TG analysis. We anticipate that these results would show the possibility of using acetonitrile based TPD technique and if possible, other combined in situ techniques to study MOF-based solid acid materials.

Prior to the acetonitrile sorption measurements, samples were activated at 150 and 250 ^oC. We chose two different activation temperatures because we wanted to study the acidity changes after PTA dehydration, which occurs between 230 to 260 ^oC, as indicated by TG traces (Figures A6.10 and A6.11). To carry out this experiment, samples synthesized from the same batch were separately activated and measured. The strength of acidic sites is characterized by the ease of dissociation of acetonitrile. To evaluate this factor, the samples were evacuated at 25 °C for 2 hours after isotherm measurements. Typical pressure in the sample cell after the regeneration process was 5 Pa. We then collected the acetonitrile-d_3 isotherms up to three cycles for the materials studied here.

The acetonitrile-d_3 isotherm of MIL-101 (activated at 150^oC) measured at 25 °C is shown in Figure 6.3a. The adsorbed amount of acetonitrile gradually increases with increasing pressure up to $P/P_0 = 0.13$, followed by two abrupt acetonitrile uptake steps in the pressure ranges of $P/P_0 =$ 0.13 to 0.20 and $P/P_0 = 0.21$ to 0.27, and the maximum uptake reaches 770 $cm^3\ g^{-1}$ at $P/P_0 = 0.9$. A significant decrease from the first to the second cycle and a constant uptake thereafter was found for MIL-101. This difference is mainly due to the decreased uptake at lower pressure range ($P/P_0 = 0 – 0.05$). This behavior can be explained if some of the acetonitrile molecules are strongly bound to the framework, not being desorbed under the aforementioned regeneration conditions. If this is the case, the acetonitrile release requires further energy input (higher temperature and/or better vacuum). This indicates the presence of acidic sites in pristine MIL-101 activated at 150 ^oC. MIL-101 activated at higher temperature (250 ^oC) exhibited very similar acetonitrile-adsorption behavior to those of MIL-101 activated at lower temperature (150 ^oC). Apparently, activating MIL-101 at higher temperature does not generate more acidic sites. This is in agreement with the fact that no extra weight loss step occurred in the TG trace of MIL-101 between 150 and 250 ^oC.

The acetonitrile-d_3 isotherm of 25PTA/MIL-101 (activated at 150^oC) measured at 25 °C is shown in Figure 6.3b. Similar to pristine MIL-101, the adsorbed amount of acetonitrile gradually increases with increasing pressure up to $P/P_0 = 0.2$, followed by an abrupt acetonitrile uptake step in the pressure range of $P/P_0 = 0.21$ to 0.27, and the maximum uptake reaches 520 $cm^3\ g^{-1}$ at $P/P_0 = 0.9$. The maximum uptake is lower than MIL-101 because the pore volume of

25PTA/MIL is smaller. The adsorption step found in the pressure range of P/P_0 = 0.13 to 0.20 in MIL-101 is not observed in 25PTA/MIL-101, which could be assigned to the blocked small pores by PTA molecules in the material. Similar to pristine MIL-101, a significant decrease from the first to the second cycle and a constant uptake thereafter was found for 25PTA/MIL-101 as well. This indicates the presence of acidic sites in 25PTA/MIL-101 activated at 150 ^oC, which absorb acetonitrile molecules strongly in an irreversible process at room temperature. 25PTA/MIL-101 activated at higher temperature (250 ^oC) exhibited a slightly higher (30 $cm^3\ g^{-1}$) uptake of acetonitrile in the first cycle, while the uptake of acetonitrile in the second circle is quite similar to those of samples activated at 150 ^oC. These findings indicate a slight increase of the number of the acidic sites in 25PTA/MIL-101, which is in good agreement with the fact that a tiny weight loss step was found on TG trace of 25PTA/MIL-101 between 230 and 250 ^oC.

The adsorption behavior becomes very different in 60PTA/MIL-101 samples. As shown in Figure 6.3c, the adsorbed amount of acetonitrile-d_3 in 60PTA/MIL-101 (activated at 150 ^oC) gradually increases with increasing pressure up to P/P_0 = 0.05, followed by two abrupt acetonitrile uptake step in the pressure ranges of P/P_0 = 0.05 to 0.12 and P/P_0 = 0.21 to 0.27, and the maximum uptake reaches 230 $cm^3\ g^{-1}$ at P/P_0 = 0.9. Despite the fact that 60PTA/MIL-101 has the largest loading of PTA in all samples, interestingly, only a very slight decrease in acetonitrile uptake (8 $cm^3\ g^{-1}$) from first cycle to second cycle was observed. This clearly shows that the major type of acidic sites in both MIL-101 and 25PTA/MIL-101 are not present in 60PTA/MIL-101 material. On the contrary, 60PTA/MIL-101 activated at 250 ^oC exhibited higher acetonitrile uptake in the first cycle and a significant decrease in uptake (95 $cm^3\ g^{-1}$) from first cycle to second cycle compared to other samples. These findings indicate: (a) strong acidic sites are present in 60PTA/MIL-101 activated at 250 ^oC; and (b) these acidic sites are not generated or activated at 150 ^oC. This is also consistent with the finding that 60PTA/MIL-101 has a significant weight loss step between 230 and 260 ^oC, which is assigned to the dehydration of PTA molecules.

To further study the acid strength of PTA/MIL-101 materials, samples loaded with acetonitrile-d_3 were quickly transferred and subjected to TG measurements under a flow of nitrogen. TG traces were plotted in Figures A6.12 to A6.14. Two major weight loss steps were observed in pristine MIL-101 and 25PTA/MIL-101 samples in the ranges of below 50 ^oC and 325 to 500 ^oC. While the second weight loss corresponds to the collapse of the framework and degradation of the organic struts, the first weight loss step might be assigned to desorption of the physisorbed and chemisorbed acetonitrile molecules. The TG trace of acetonitrile loaded 60PTA/MIL-101 sample shows an extra step in the range of 200 to 300 ^oC. This weight loss may be attributed to desorption of the chemisorbed acetonitrile molecules. The different temperatures required to desorb chemisorbed acetonitrile molecules in 25PTA/MIL-101 and 60PTA/MIL-101 samples undoubtedly support the presence of two different types of acidic sites. The elevated temperatures required to desorb acetonitrile in 60PTA/MIL-101 supports the presence of stronger acidic sites. These results obtained are preliminary; however, they clearly support the notion that it is possible to conduct TPD experiments on MOF-based acid materials using carefully chosen base probes, such as acetonitrile and carbon monoxide. We hope that this work can inspire individuals to explore this field, which will lead to a better understanding to the acid properties of MOF-based acid materials.

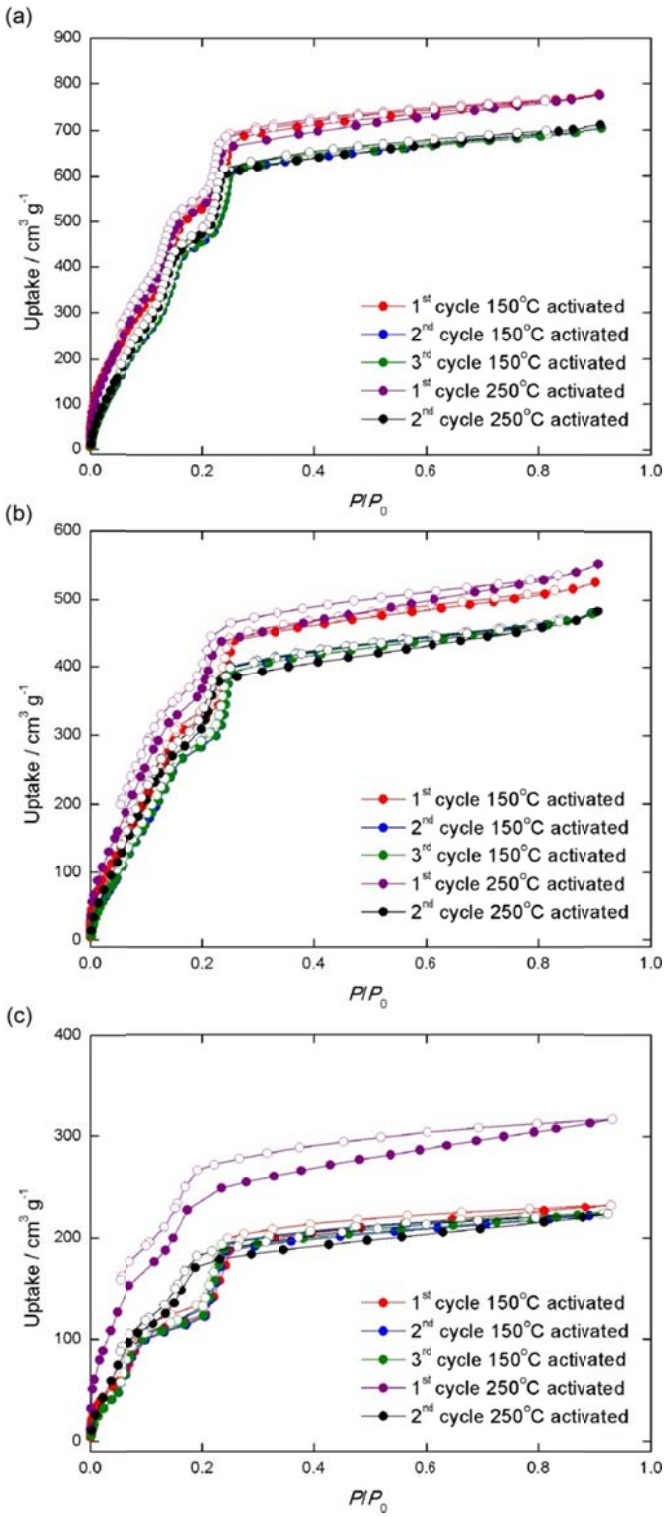

Figure 6.3. Acetonitrile-d_3 isotherms of MIL-101 (a), 25PTA/MIL-101 (b), and 60PTA/MIL-101 (c) measured at 25 ^{o}C with adsorption and desorption branches represented by closed and open circles, respectively. P/P_0, relative pressure. Three consecutive cycles were taken for samples activated at 150 ^{o}C, two consecutive cycles were taken for samples activated at 250 ^{o}C. The samples were evacuated for 2 hours at 25 ^{o}C between the cycles.

n-Hexane conversion. Hydroisomerization of n-hexane was carried out on Pt/MIL-101 and Pt/xPTA/MIL-101 samples (x = 25, 60). The overall activity of all tested catalysts is shown in Figure 6.4. The activity is displayed as a mass activity, which is based on the total mass of the catalyst. The specific product selectivity of the reaction is also shown in Figure 6.4; this data is obtained at approximately 5% total hexane conversion. Pt/MIL-101 without PTA loading showed no activity toward n-hexane hydroisomerization at 250 ^{o}C. On the other hand, Pt/60PTA/MIL-101 shows good activity (1.25×10^{-7} mol s^{-1} g^{-1}) and high selectivity (> 90%) towards isomerization of n-hexane under the same conditions. Interestingly, although we expected the material to exhibit activity in between Pt/MIL-101 and Pt/PTA/MIL-101, the Pt/25PTA/MIL-101 sample showed almost no activity and little selectivity towards isomerization (the same level as Pt/MIL-101). This inconsistency in the catalytic activity indicates that the activity and also selectivity of the PTA loaded MOF catalysts are not merely a linear function of the acid loading in the MOFs. Indeed, a similar effect has been observed for polyoxometalate-containing mesoporous silica catalysts.[17] As reported in literature, strong polyoxometalate acids can react with the surface oxide/hydroxide groups of silica and metal oxide supports and lose some of their acidity.[17] Similarly, PTA may interact with the MOF frameworks and, depending on the loading of the PTA, some fractions of its protons might get transferred to less acidic sites.

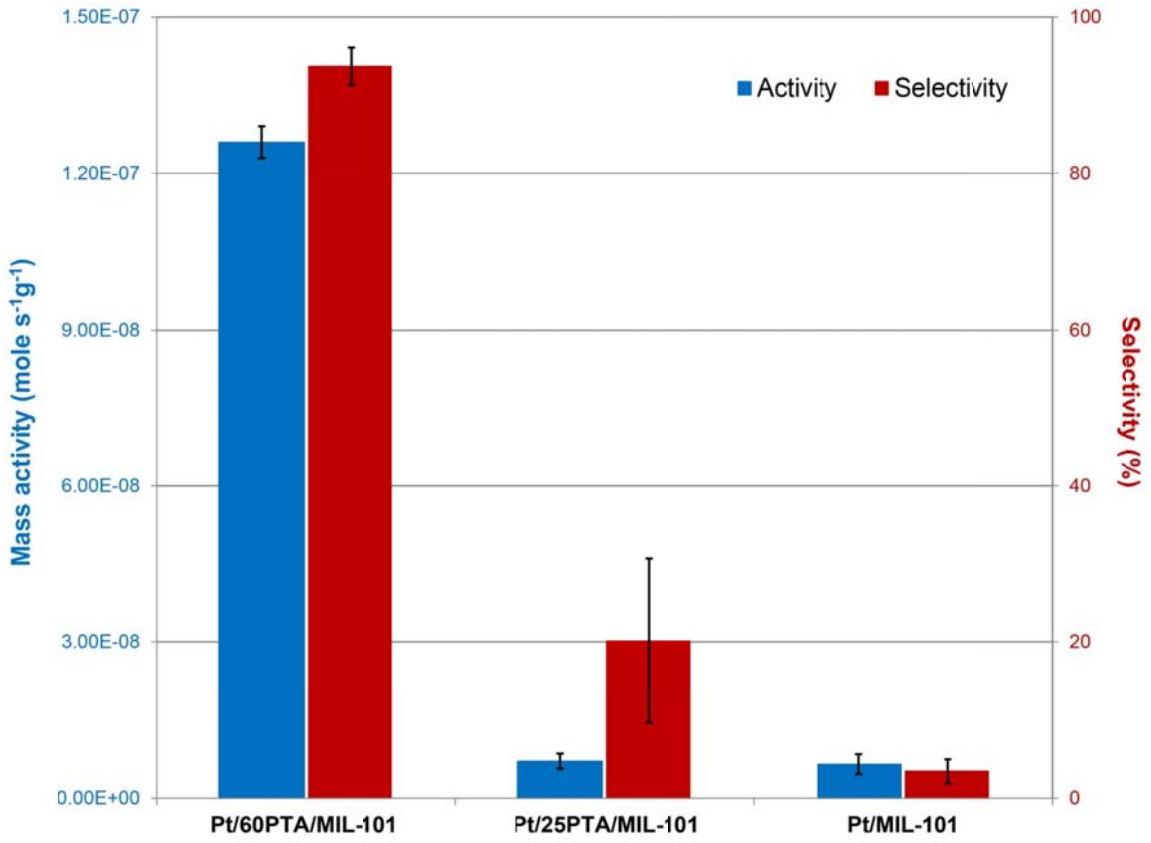

Figure 6.4. The overall mass activity (blue bar) and the isomer selectivity (red bar) of n-hexane hydroisomerization at 250 ^{o}C using various Pt supported on MOF-based catalysts.

Previous characterization has confirmed the integrity of PTA structures when loaded by one pot synthesis into MIL-101's cages; however, their protonation state is uncertain. Acidity characterization of samples with different PTA loading using adsorption of acetonitrile has given hints of two types of acidic sites present in these PTA loaded MIL-101 samples. One type is present in Pt/MIL-101 and Pt/25PTA/MIL-101, the other type is present in Pt/60PTA/MIL-101. This is in good agreement with the catalytic behavior of these composite catalysts. To further prove our hypothesis, we carried out qualitative characterization of acidic sites by adsorbing acetonitrile-d_3 and taking IR spectra for all three catalysts. As shown in Figure A6.16, two peaks were observed in the IR spectra in the region corresponding to absorption by triple bonds: one at 2312 – 2320 cm^{-1} and the other at 2260 – 2271 cm^{-1}. According to literature data, the bands at higher and lower wavenumbers can be tentatively attributed to the adsorption on acidic sites and the physisorbed CD_3CN, respectively. The peak at 2320 cm^{-1} for MIL-101 is attributed to Lewis acid sites of the pure MOF, whereas the more intense peak at 2312 cm^{-1} for 60PTA/MIL-101 might be due to Brønsted acid sites. The absence of this peak for 25PTA/MIL-101 might indicate the absence of Brønsted sites, and therefore, negligible activity towards n-hexane isomerization.

Reaction activity and isomer selectivity of the acid-encapsulated MOF catalyst was compared to aluminum modified mesoporous silica catalyst (Figure 6.5) The aluminosilicate catalyst was previously shown to have high selectivity towards isomerization due to its mild acidic character and have comparable activity to zeolite catalysts.[6f] Figure 6.5a presents reaction activity in terms of turnover frequency (TOF) and isomer selectivity for Pt/60PTA/MIL-101, Pt/Al-MCF-17, and Pt/MCF-17. The TOF is based on the total surface area of Pt, which is calculated based on geometrical methods and TEM analysis of average nanoparticle size (3 nm). The MOF based catalyst Pt/60PTA/MIL-101 was highly selective and almost 7 times more active than the Pt/Al-MCF-17 catalyst at 240 ºC and 1 bar. At these reaction conditions, the pure Pt/MCF-17 was not active at all. Both MOF and aluminosilicate based catalysts maintained excellent selectivity and showed increased activity as a function of temperature as presented in Figure 6.5b. The apparent activation energy (76.5 kJ/mole) for n-hexane hydroisomerization on MOF based catalyst was two times lower than the activation energy (153.2 kJ/mole) on silica based catalyst (Figure A6.17).

Finally, the stability of MOF based catalyst was tested as it is one of the key parameters of hydroisomerization catalysts. The reaction was carried out for about 10 hours at 250 ºC and 1 bar. We observed a slight catalyst deactivation during the first three hours of operation, after which the deactivation was minimal (Figure 6.6). A similar deactivation trend was observed when the same catalyst was cycled 3 times as presented in the inset of Figure 6.6. In between cycles, the catalyst was flowed with H_2 and N_2 gas mixture at 250 ºC. High temperature aerobic treatment was avoided as MOF catalysts were more susceptible to decomposition in air than in H_2 and N_2 gas mixture as demonstrated by TG analyses (Figures A6.8 and A6.18).

We performed N_2 adsorption-desorption (Figure A6.1), powder XRD (Figures 6.2 and A6.5), and SEM studies (Figures 6.2 and A6.19) before and after 10 hours of reaction to characterize the structural integrity of the Pt/PTA/MIL-101 catalyst under reaction conditions. As shown, slightly decrease in XRD peak intensity, N_2 uptake and change in the pore distribution was observed after the reaction. However, no evidence of structural decomposition was observed in SEM images of the MOF crystals (Figure A6.19).

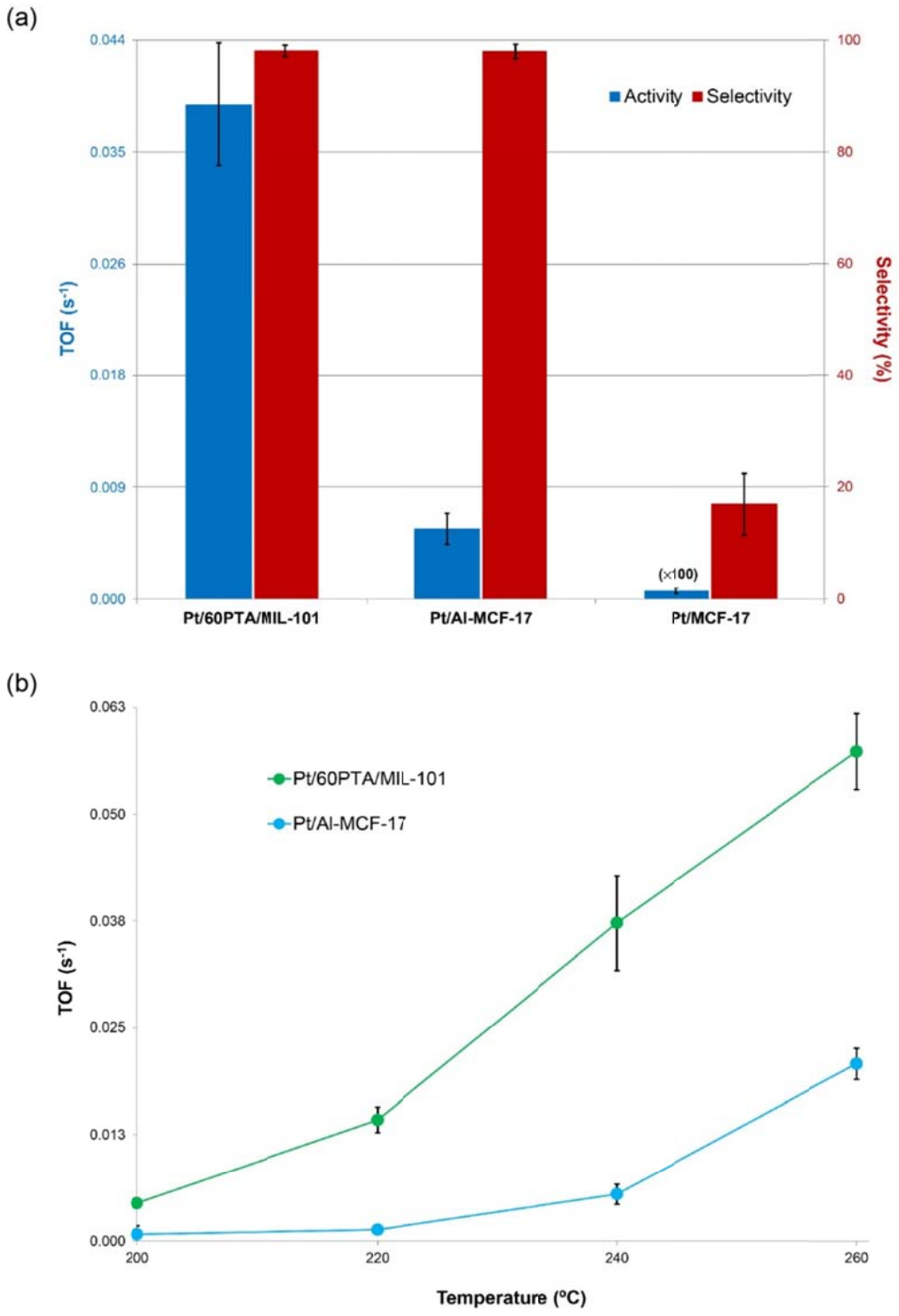

Figure 6.5. (a) The overall turnover frequency (blue bar) and the isomer selectivity (red bar) of n-hexane hydroisomerization at 250 ^{o}C using various catalysts; and (b) overall turnover frequency (moles hexane converted per mole Pt site per second) plotted against temperature for evaluated catalysts. Pt/MCF-17 is not shown due to its very low activity.

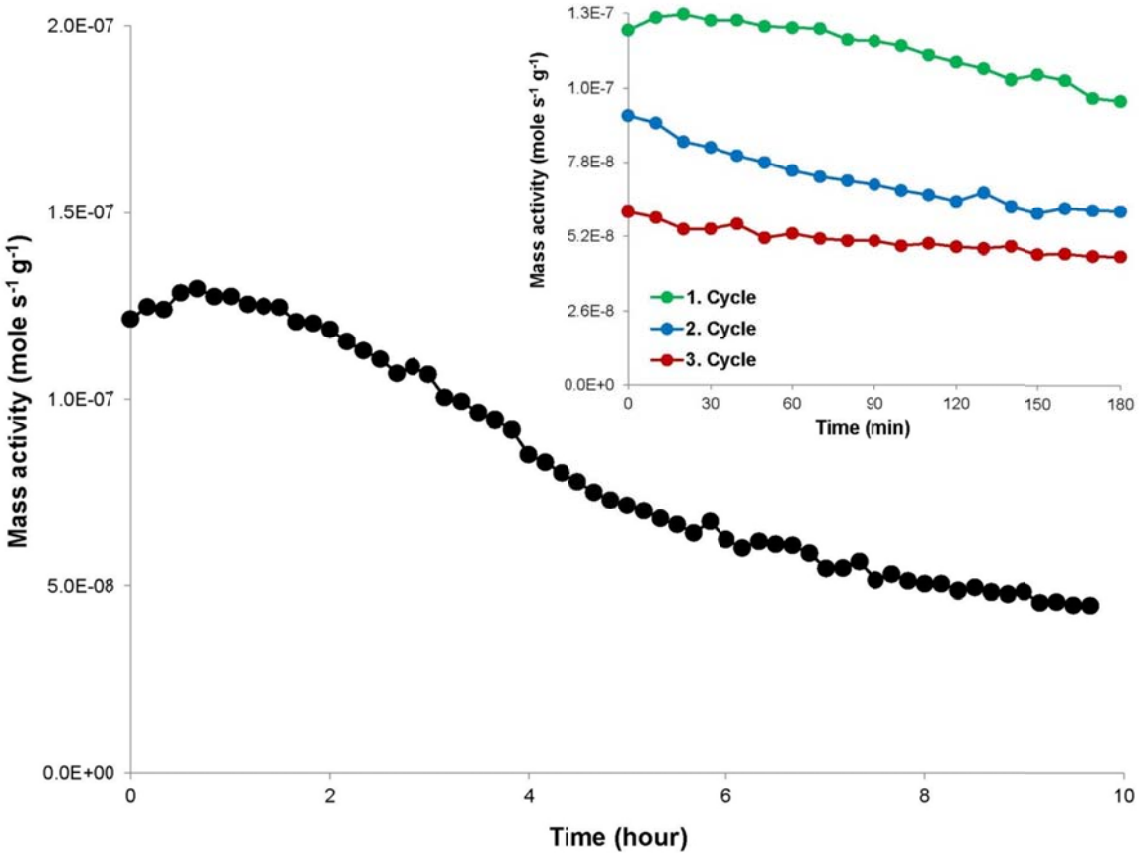

Figure 6.6. Cycle performance of Pt/60PTA/MIL-101 at 250 ^{o}C.

The decrease in the intensity of the XRD peaks might indicate partial degradation of the MOF structure. This is consistent with the changes observed from the N_2 sorption studies: decrease in the surface area and the smaller pores in the MOF catalyst. However, SEM images demonstrate that the structural decomposition is not severe under these reaction conditions, and also show amorphous stuff on the surface of MOF crystals. These observations imply that the deactivation of the catalyst are predominantly due to amorphous species deposited in the pores of the MOF. Indeed, numerous studies have shown that this type of deactivation is typical for various polyoxometalate containing aluminosilicate catalysts.[17c] And it is widely accepted that the main reason for the deactivation of polyoxometalate based catalysts is the formation of carbonaceous or oligomeric unreactive species that bind irreversibly to acid sites.[17c] Nevertheless, more studies are needed to thoroughly and precisely characterize the structural change of the MOF based catalysts under reaction conditions to design more stable and more efficient MOF based hybrid catalysts.

Conclusion

In this chapter, we report the synthesis, structure, porosity, and acidity of phosphotungstic acid (PTA) loaded in MIL-101, a chromium terephthalate MOF with 3.5 nm large pores. Among them, 60PTA/MIL-101 (with a 60 wt% loading of PTA in the composite material) exhibits

strong Brønsted acidity as characterized by acetonitrile-d_3 sorption studies, while MIL-101 and 25PTA/MIL-101 materials exhibit only weak Lewis acidity. We believe the major reason for this non-linear corelation between acid strength and the loading of PTA is the different protonation states of the PTA included. These acid properties have direct impct on the catalytic performance of these materials toward hydroisomerization of n-hexane. Although Pt/MIL-101 and Pt/25PTA/MIL-101 were found to be inactive in the catalytic conversion of n-hexane to isomers, when Pt/60PTA/MIL-101 is used as catalysts the isomerization became the dominant pathway with high activity and selectivity (> 90%) at 250 ^{o}C. Coking was found as the main reason for the slow deactivation of the Pt/60PTA/MIL-101 catalyst.

Appendices

Figure A6.1. (a) N_2 isotherms and (b) pore size distribution of PTA/MOF samples before vapor phase n-hexane reforming reaction: MIL-101 (red), 25PTA/MIL-101 (blue), and 60PTA/MIL-101 (green); and after vapor phase n-hexane reforming reaction: MIL-101 (pink), 25PTA/MIL-101 (light blue), and 60PTA/MIL-101 (light green). Isotherms were measured at 77 K with adsorption and desorption branches represented by closed and open circles, respectively. P/P_0, relative pressure.

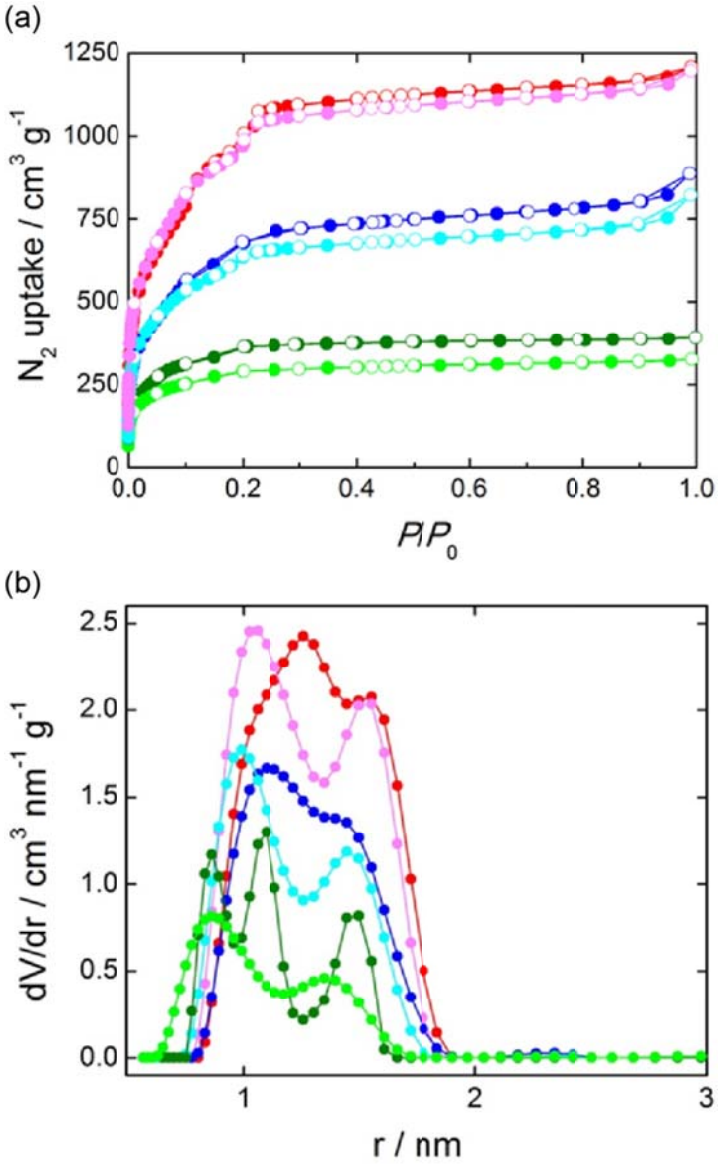

Figure A6.2. Comparison of the experimental PXRD patterns of PTA (black), MIL-101 (red), 25PTA/MIL-101 (blue), and 60PTA/MIL-101 (green) and simulated Bragg peak positions (magenta) from reported MIL-101 structure.[11]

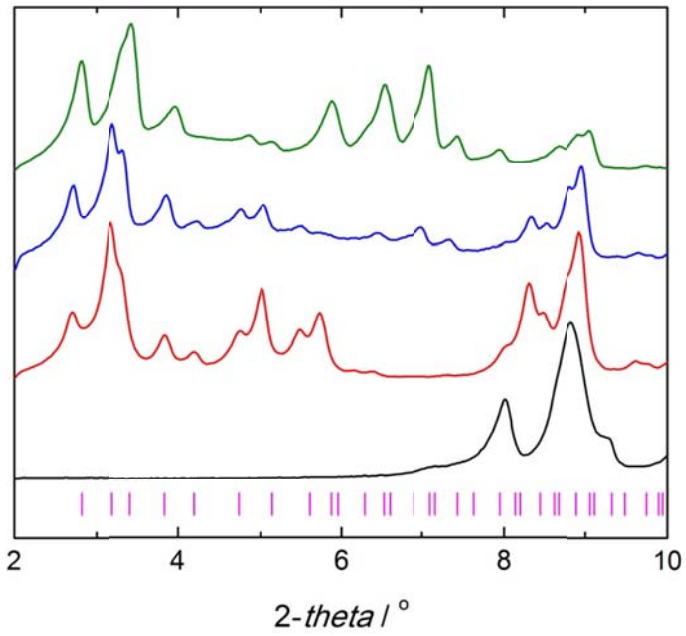

Figure A6.3. Comparison of the experimental PXRD patterns of MIL-101: before vapor phase n-hexane reforming reaction (black) and after the reaction (red).

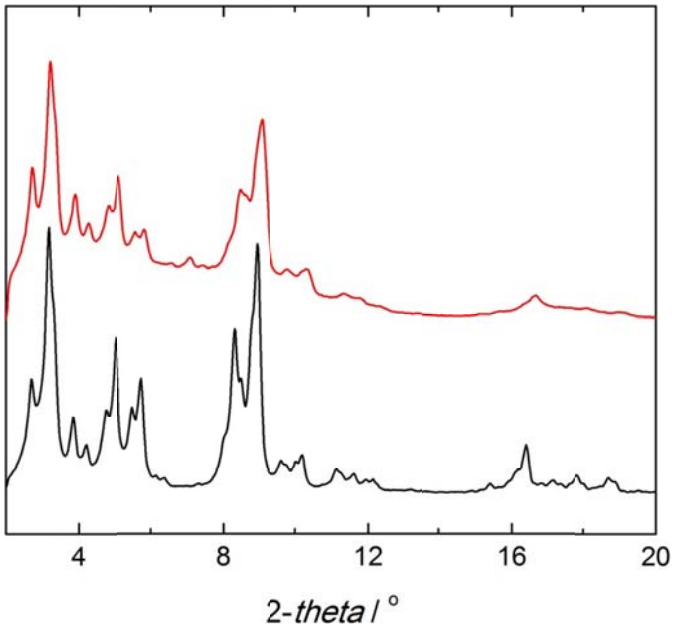

Figure A6.4. Comparison of the experimental PXRD patterns of 25PTA/MIL-101: before vapor phase n-hexane reforming reaction (black) and after the reaction (red).

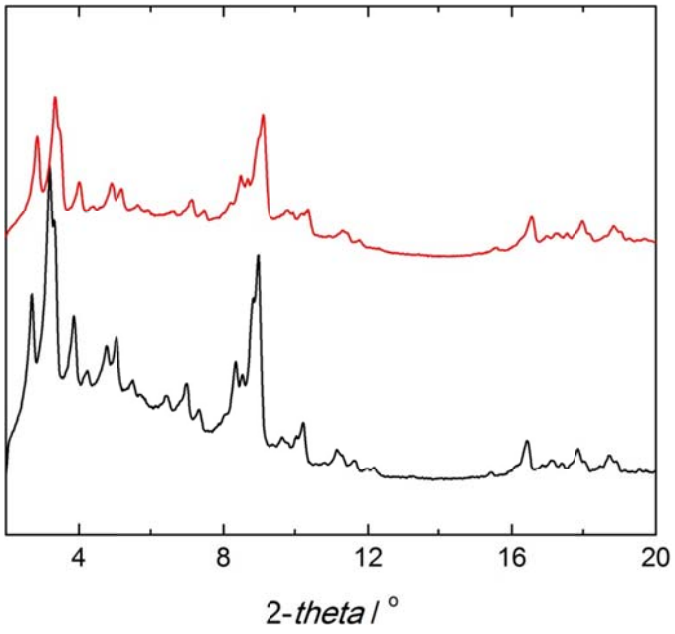

Figure A6.5. Comparison of the experimental PXRD patterns of 60PTA/MIL-101: before vapor phase n-hexane reforming reaction (black) and after the reaction (red).

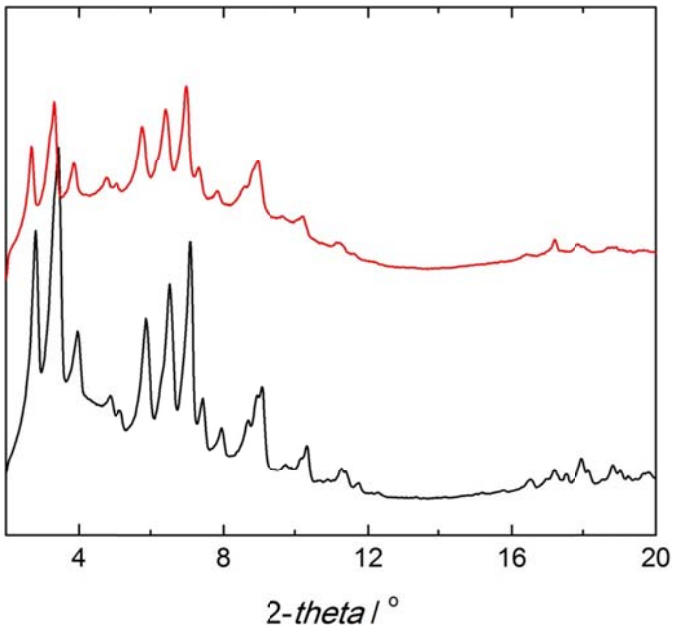

Figure A6.6. TGA trace for activated MIL-101, heating rate: 5 °C min^{-1} in air.

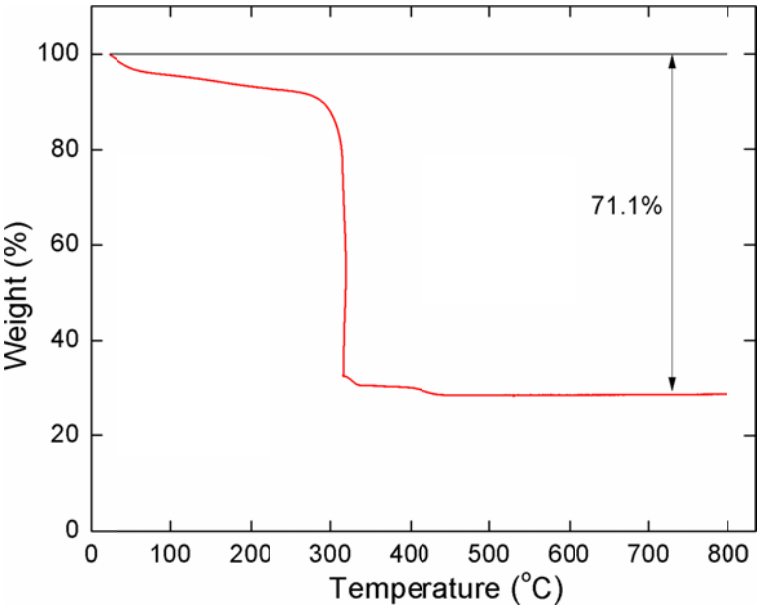

Figure A6.7. TGA trace for activated 25PTA/MIL-101, heating rate: 5 °C min^{-1} in air.

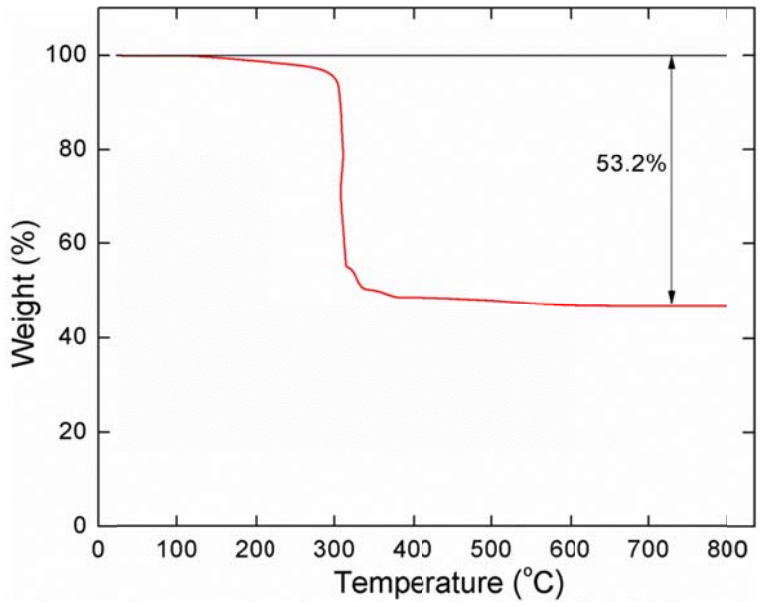

Figure A6.8. TGA trace for activated 60PTA/MIL-101, heating rate: 5 °C min^{-1} in air.

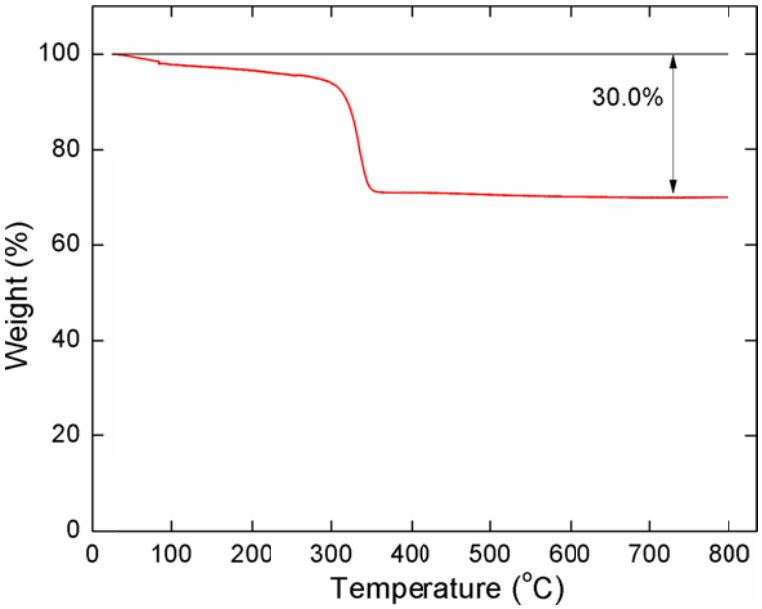

Figure A6.9. TGA trace for as-synthesized MIL-101, heating rate: 5 °C min^{-1} in N_2.

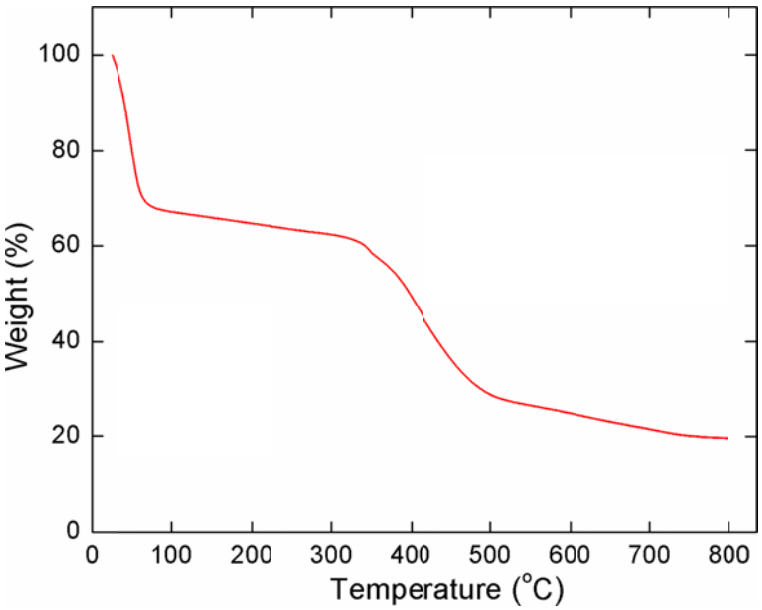

Figure A6.10. TGA trace for as-synthesized 25PTA/MIL-101, heating rate: 5 °C min^{-1} in N_2.

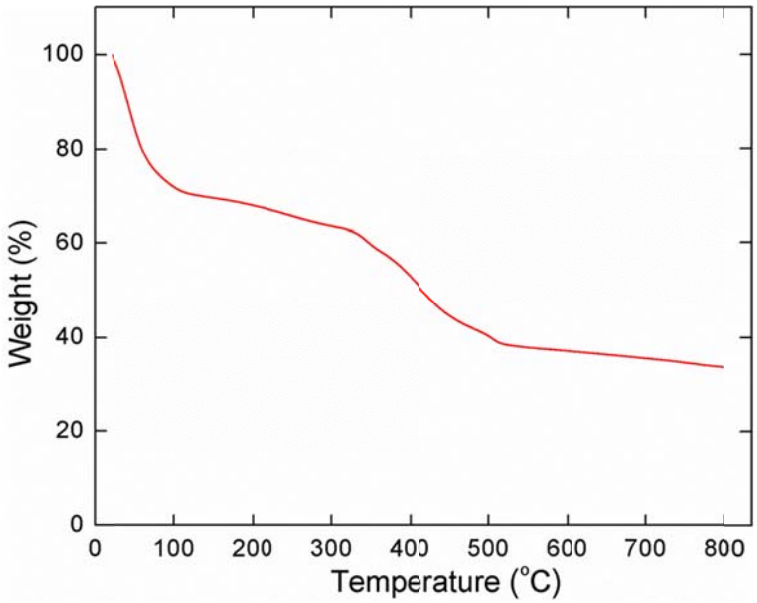

Figure A6.11. TGA trace for as-synthesized 60PTA/MIL-101, heating rate: 5 °C min^{-1} in N_2.

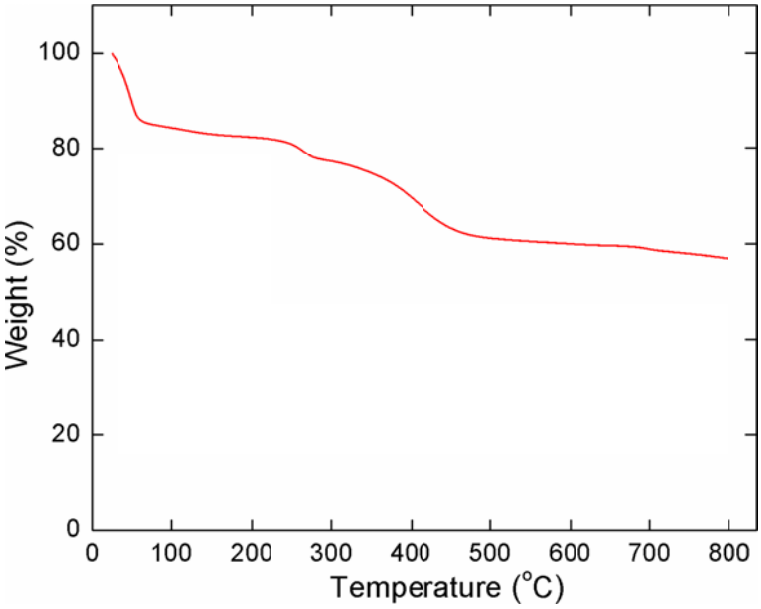

Figure A6.12. TGA trace (red) and derivative weight **(**blue) for acetonitrile-d_3 loaded in MIL-101, heating rate: 5 °C min^{-1} in N_2.

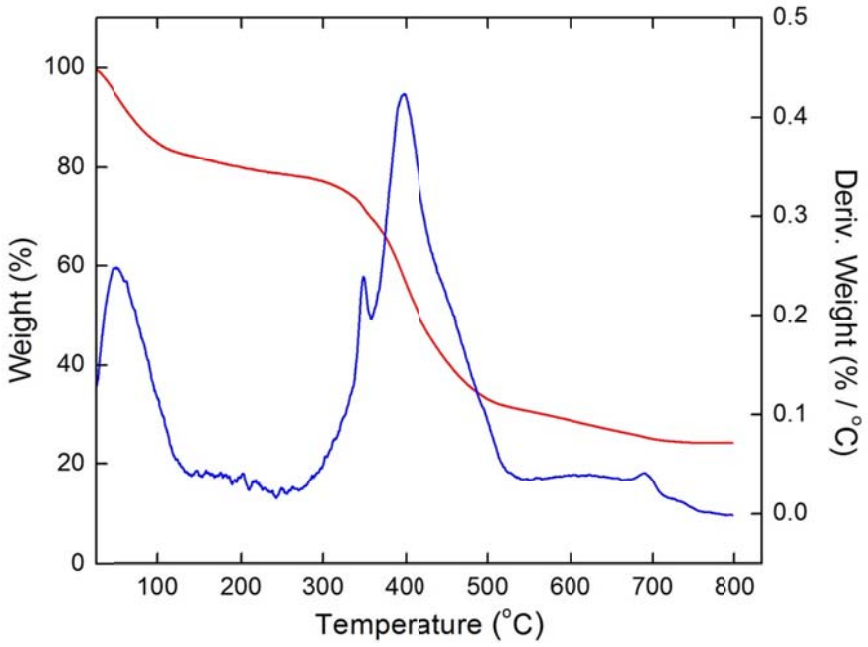

Figure A6.13. TGA trace (red) and derivative weight (blue) for acetonitrile-d_3 loaded in 25PTA/MIL-101, heating rate: 5 °C min^{-1} in N_2.

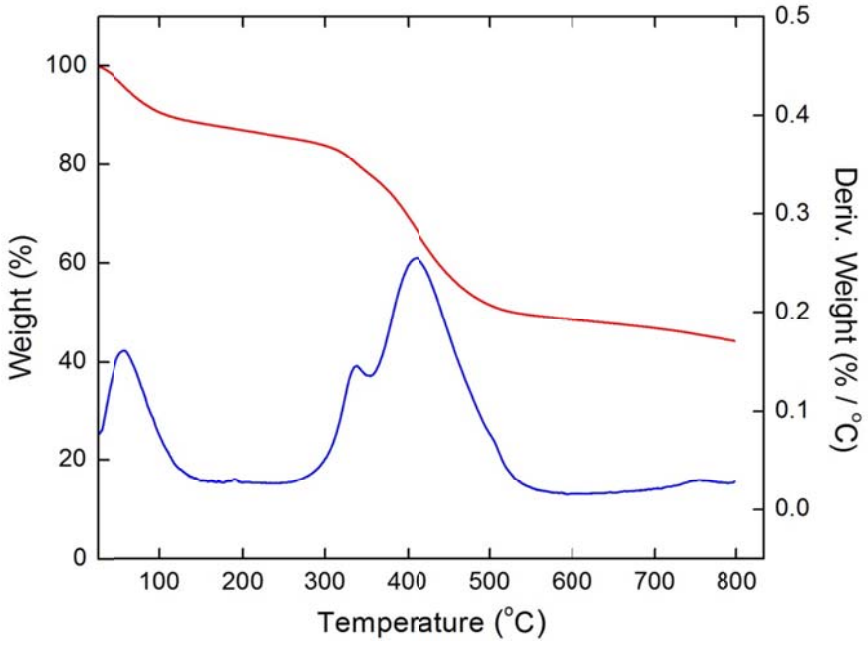

Figure A6.14. TGA trace (red) and derivative weight (blue) for acetonitrile-d_3 loaded in 60PTA/MIL-101, heating rate: 5 °C min^{-1} in N_2.

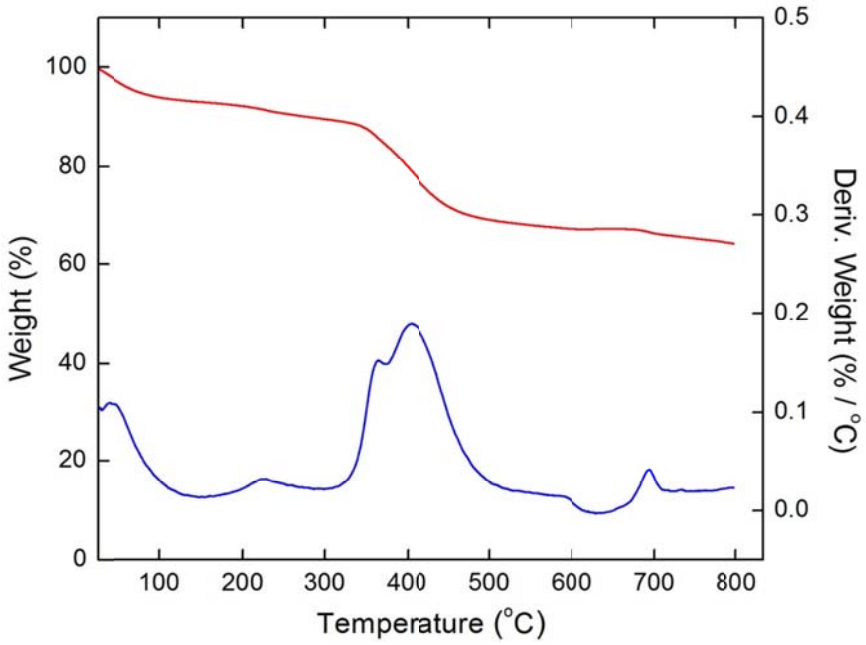

Figure A6.15. ^{31}P MAS NMR spectra of $CrPW_{12}O_{40}$ hydrate (a), PTA hydrate (b), 25PTA/MIL-101(c), and 60PTA/MIL-101(d). The asterisks denote spinning sidebands.

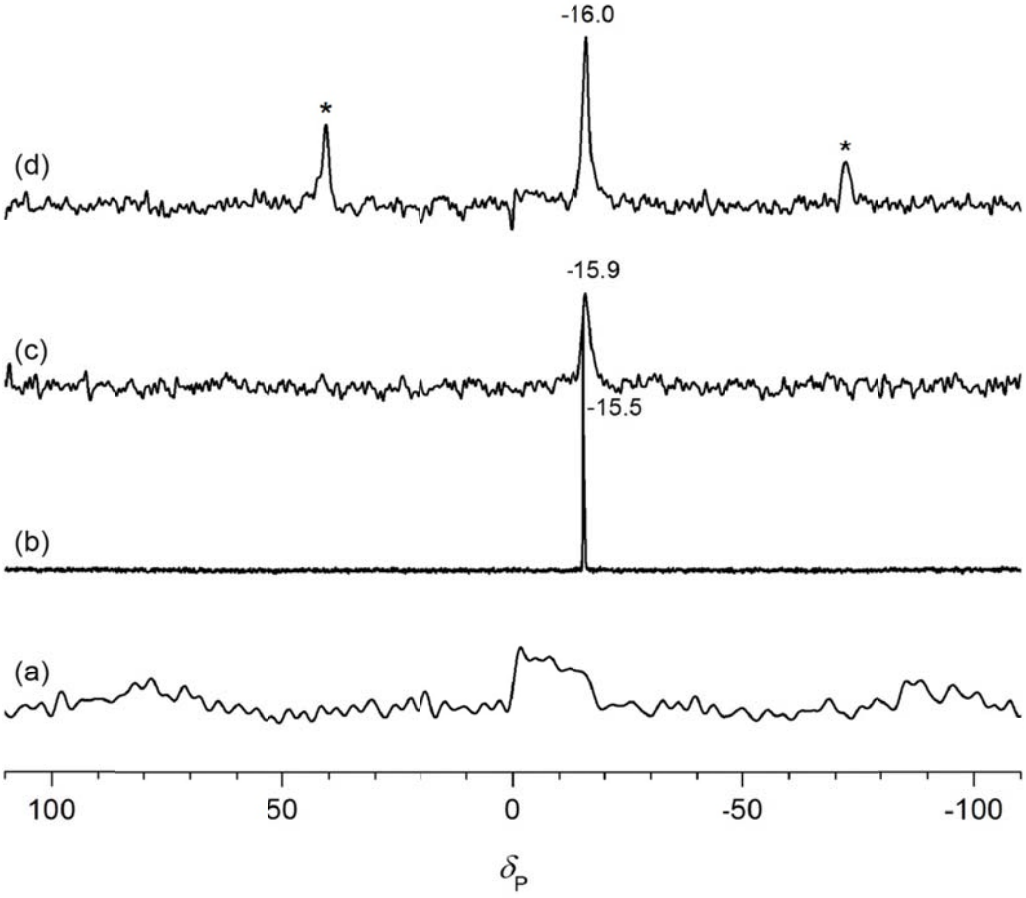

Figure A6.16. IR spectra of acetonitrile-d_3 adsorbed in MIL-101 (black), 25PTA/MIL-101 (blue), and 60PTA/MIL-101 (red). Spectra were zoomed in for the region corresponding to adsorption by triple bonds.

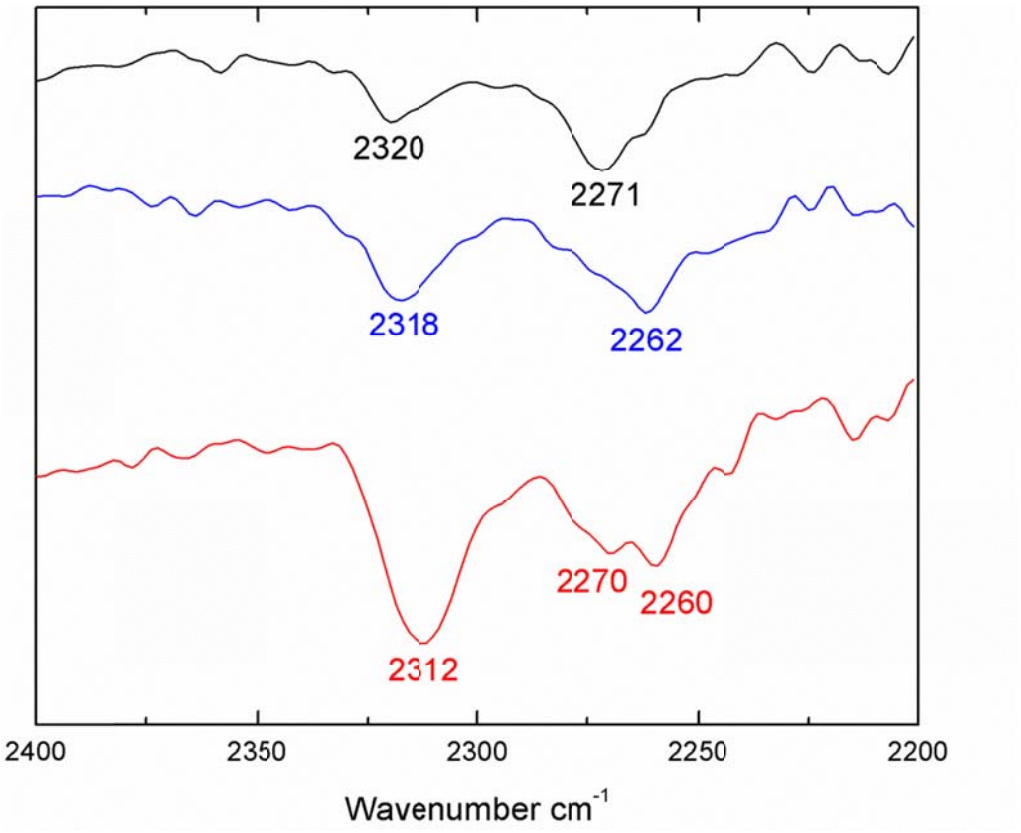

Figure A6.17. Arrhenius plots of n-hexane hydroisomerization on Pt/60PTA/MIL-101 and Pt/Al-MCF-17.

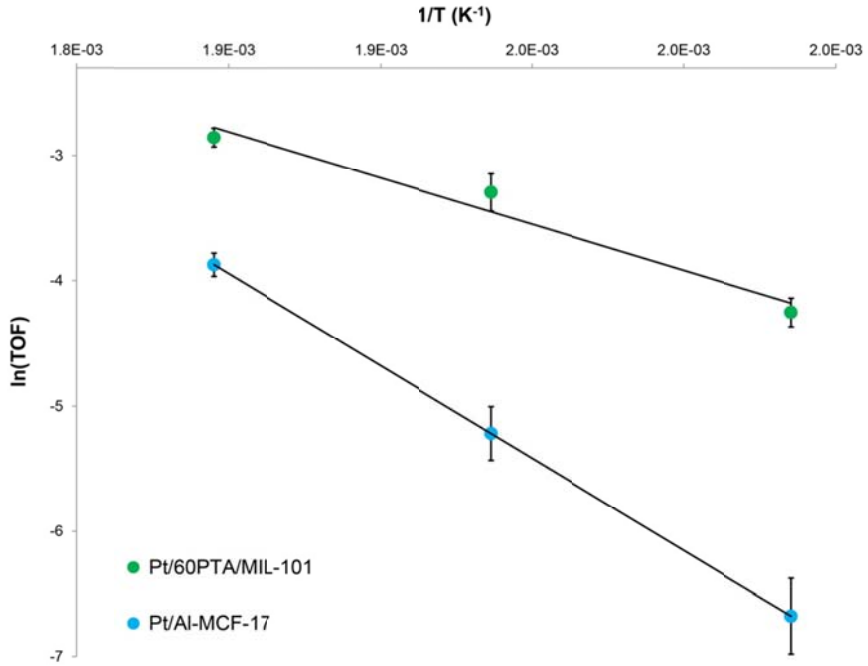

Figure A6.18. TGA trace for activated 60PTA/MIL-101, heating rate: 5 °C min^{-1} in 5% hydrogen and 95% nitrogen.

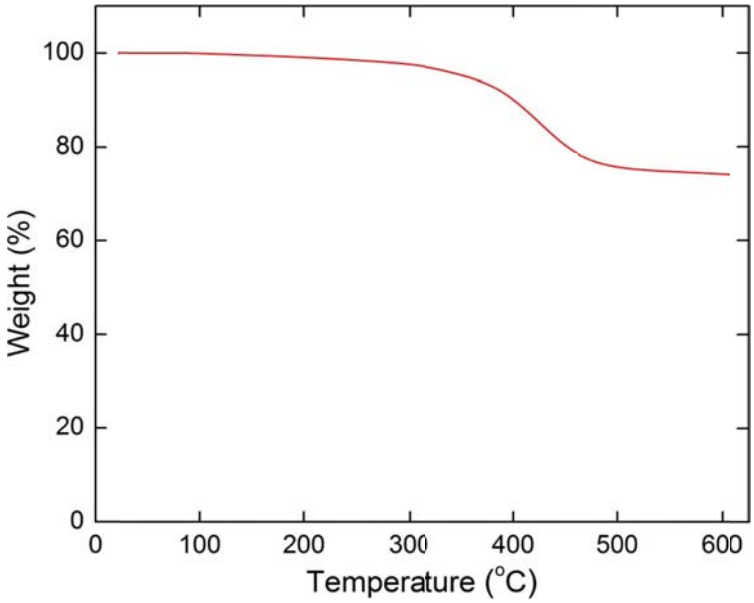

Figure A6.19. Scanning electron microscopy (SEM) images for Pt/60PTA/MIL-101 after 10 hours' reaction at 250 ^{o}C (scale bar: 1 μm).

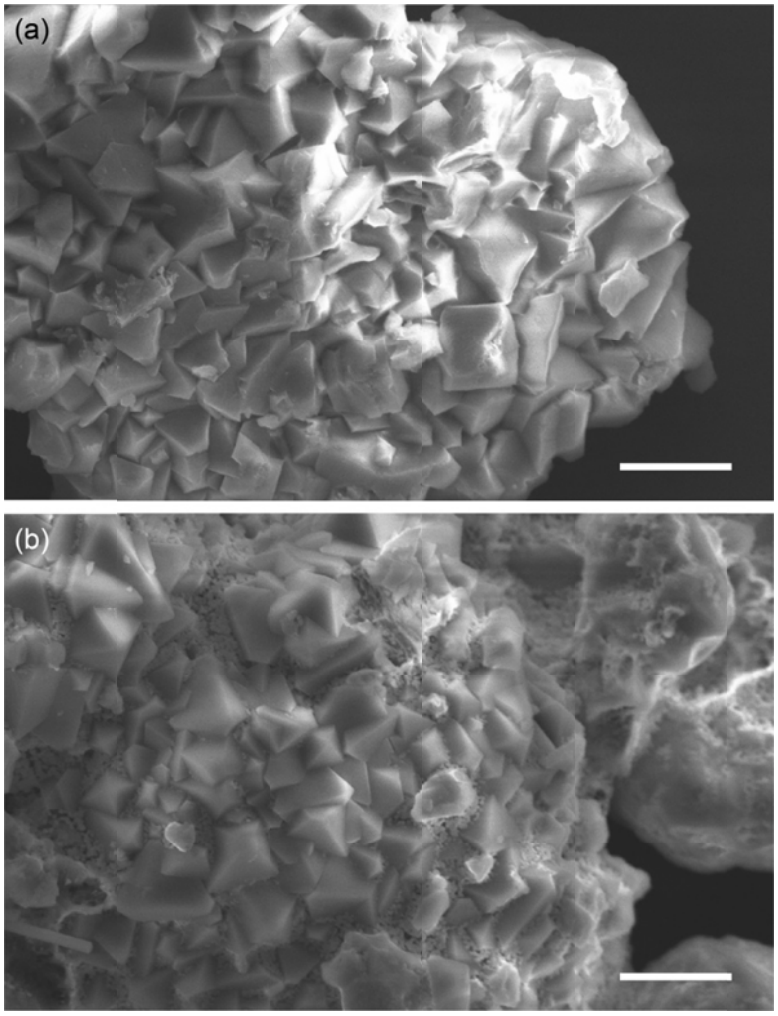

References and Notes

(1) U.S. Energy Information Administration, Annual Energy Outllok 2013 Early Release.

(2) Somorjai, G. A.; Li, Y. Introduction to Surface Chemistry and Catalysis; Wiley: Hoboken, NJ, **2010**, chapter 7.

(3) (a) Somorjai, G. A.; Park, J. Y. Angew. Chem. Int. Ed. **2008**, 47, 9212. (b) Clark, J. H. Green Chem. **1999**, 1, 1.

(4) (a) Sinfelt, J. H. Catal. Lett. **1991**, 9, 159. (b) Han, Y.; Lee, S. S.; Ying, J. Y. Chem. Mater. **2007**, 19, 22922. (c) Yang, M.; Somorjai, G. A. J. Am. Chem. Soc. **2004**, 126, 7698.

(5) (a) Iglesia, E.; Soled, D. G.; Kramer, G. M. J. Catal. **1993**, 144, 238. (b) Antos, G. J.; Aitani, A. M. Catalytic Naphtha Reforming; Marcel Dekker: New York, **2004**.

(6) (a) Davis, S. M.; Zaera, F.; Somorjai, G. A. J. Am. Chem. Soc. **1982**, 104, 7453. (b) Na, K.; Jo, C.; Kim, J.; Cho, K.; Jung, J.; Seo, Y.; Messinger, R. J.; Chmelka, B. F.; Ryoo, R. Science **2011**, 333, 328. (c) Alayoglu, S.; Aliaga, C.; Sprung, C.; Somorjai, G. A. Catal. Lett. **2011**, 141, 914. (d) Pushkarev, V. V.; An, K.; Alayoglu, S.; Beaumont, S. K.; Somorjai, G. A. J. Catal. **2012**, 292, 64. (e) Pushkarev, V. V.; Musselwhite, N.; An, K.; Alayoglu, S.; Somorjai, G. A. Nano Lett. **2012**, 12, 5196. (f) Musselwhite, N.; Na, K.; Alayoglu, S.; Somorjai, G. A. J. Am. Chem. Soc. **2014**, 136, 16661. (g) Musselwhite, N.; Na, K.; Sabyrov, K.; Alayoglu, S.; Somorjai, G. A. J. Am. Chem. Soc. **2015**, 137, 10231.

(7) Furukawa, H.; Cordova, K. E.; O'Keeffe, M.; Yaghi, O. M. Science **2013**, 341, 1230444.

(8) (a) Gascon, J.; Corma, A.; Kapteijn, F.; Llabrés i Xamena, F. X. ACS Catal. **2014**, 4, 361. (b) Liu, J.; Chen, L.; Cui, H.; Zhang, J.; Zhang, L.; Su, C.-Y. Chem. Soc. Rev. **2014**, 43, 6011. (c) Zhang, T.; Lin, W. Chem. Soc. Rev. **2014**, 43, 5982. (d) Yoon, M.; Srirambalaji, R.; Kim, K. Homochiral Chem. Rev. **2012**, 112, 1196. (e) Jiang, J.; Yaghi, O. M. Chem. Rev. **2015**, 115, 6966.

(9) (a) Wee, L. H.; Bonino, F.; Lamberti, C.; Bordiga, S.; Martens, J. A. Green Chem. **2014**, 16, 1351. (b) Khder, A. E. R. S.; Hassan, H. M. A.; El-Shall, M. S. Appl. Catal. A **2014**, 487, 110. (c) Bromberg, L.; Hatton, T. A. ACS Appl. Mater. Interfaces **2011**, 3, 4756. (d) Zhang, Y.; Degirmenci, V.; Li, C.; Hensen, E. J. M. ChemSusChem **2011**, 4, 59. (e) Janssens, N.; Wee, L. H.; Bajpe, S.; Breynaert, E.; Kirschhock, C. E. A.; Martens, J. A. Chem. Sci. **2012**, 3, 1847. (f) Bromberg, L.; Su, X.; Hatton, T. A. ACS Appl. Mater. Interfaces **2013**, 5, 5468. (g) Ramos-Fernandez, E. V.; Pieters, C.; van der Linden, B.; Juan-Alcañiz, J.; Serra-Crespo, P.; Verhoeven, M. W. G. M.; Niemantsverdriet, H.; Gascon, J.; Kapteijn, F. J. Catal. **2012**, 289, 42. (h) Chen, J.; Wang, S.; Huang, J.; Chen, L.; Ma, L.; Huang, X. ChemSusChem **2013**, 6, 1545. (i) Wang, S.; Chen, J.; Chen, L. Catal. Lett. **2014**, 144, 1728.

(10) (a) Ono, Y. In Perspectives in Catalysis; Thomas, J.M.; Zamaraev, K. I., Eds.; Blackwell: London, **1992**; p 341. (b) Misono, M. Catal. Rev. Sci. Eng. **1988**, 29, 269.

(11) Férey, G.; Mellot-Draznieks, C.; Serre, C.; Millange, F.; Dutour, J.; Surblé, S.; Margiolaki, I. Science **2005**, 309, 2040.

(12) (a) Hwang, Y. K.; Hong, D.-Y.; Chang, J.-S.; Jhung, S. H.; Seo, Y.- K.; Kim, J.; Vimont, A.; Daturi, M.; Serre, C.; Ferey, G. Angew. Chem., Int. Ed. **2008**, 47, 4144. (b) Hong, D.-Y.;

Hwang, Y. K.; Serre, C.; Ferey, G.; Chang, J.-S. Adv. Funct. Mater. **2009**, 19, 1537. (c) Herbst, A.; Khutia, A.; Janiak, C. Inorg. Chem. **2014**, 53, 7319.

(13) Juan-Alcañiz, J.; Ramos-Fernandez, E. V.; Lafont, U.; Gascon, J.; Kapteijn, F. J. Catal. **2010**, 269, 229.

(14) Bromberg, L.; Diao, Y.; Wu, H.; Speakman, S. A.; Hatton, T. A. Chem. Mater. **2012**, 24, 1664.

(15) Jun, S.; Ryoo, R. J. Catal. **2000**, 195, 237.

(16) Canioni, R.; Roch-Marchal, C.; Sécheresse, F.; Horcajada, P.; Serre, C.; Hardi-Dan, M.; Férey, G.; Grenèche, J.-M.; Lefebvre, F.; Chang, J.-S.; Hwang, Y.-K.; Lebedev, O.; Turner, S.; Van Tendeloo, G. J. Mater. Chem. **2011**, 21, 1226.

(17) (a) Mastikhin, V. M.; Kulikov, S. M.; Nosov, A. V.; Kozhevnikov, I. V.; Mudrakovsky, I. L.; Timofeeva, M. N. J. Mol. Catal. **1990**, 60, 65. (b) Kozhevnikov, I. V.; Kloetstra, K. R.; Sinnema, A.; Zandbergen, H. W.; van Bekkum, H. J. Mol. Catal. A **1996**, 114, 287. (c) Kozhevnikov, I. V. Chem. Rev. **1998**, 98, 171.

Chapter VII

Concluding Remarks and Future Outlook

This work demonstrates the viability of assembling metal-organic framework (MOF) materials based on Zn(II), Zr(IV), and Cr(III) metal ions with carboxylate-type organic secondary building units for various applications concerning gas storage and solid acid design. As discussed throughout the body of this dissertation, the synthesis of crystalline extended structures connected by strong bonds has opened up a new area of chemistry, where the molecular units become part of a new environment: the enclosed pores. The well-defined spatial arrangement around these pores has allowed us to determine that the properties of the molecular units are influenced by the intricacies of the pores. Moreover, design and control of the obtained structures has been exhibited, allowing the tuning of materials toward the target application.

There has been a rapid advancement in this field from the progression of discovering new materials to designing useful materials. The challenging transition was studied here as I am trying to identify the crucial criteria for each application and discuss the factors from materials' perspective to satisfy those. In Chapter II, the need to capture water vapor at low humidity requires MOFs to exhibit pore filling or condensation of water into the pores at $P/P_0 < 0.1$. Thus we have designed small pore zirconium MOF, MOF-801, $Zr_6O_4(OH)_4(fumarate)_6$, for this purpose. MOF-801 is shown to have high uptake, recyclability, and water stability. In Chapter III and IV, the need to capture harmful ammonia gas also required MOFs to have strong binding sites for capturing the basic ammonia gas at low concentration. Thus we have designed strongly acidic zirconium MOF, sulfated MOF-808, $Zr_6O_5(OH)_3(BTC)_2(SO_4)_{2.5}$, for this purpose. This sulfated MOF-808 is shown to take up 5.3 mmol ammonia at $P < 1.5$ Torr, and 16.7 mmol ammonia at $P = 760$ Torr per gram material, one of the highest values for MOF-based ammonia capture material. In Chapter V, the need to store methane gas at 80 bar and increase the working capacity (between 5 and 80 bar) requires MOFs to have both high surface area and suitable pore sizes. For this purpose, we designed zinc MOFs using organic linkers having delocalized π-electrons and with suitable pore matrices. The star compound, MOF-905, $Zn_4O(BDC)(BTAC)_{4/3}$, shows 200 $cm^3\ cm^{-3}$ working capacity between 5 and 80 bars, the highest of all zinc MOFs and is equivalent to the benchmark HKUST-1 compound.

It is clear that MOFs are promising materials for gas sorption related applications. However, for the above mentioned three gases (water, ammonia, and methane), challenges still remain. For water storage, extensive studies are still needed in this field: (a) to discover more water stable MOFs as potential candidates; (b) to develop systems that can adsorb water at low P/P_0 (< 0.05), while can be easily regenerated (room temperature under vacuum or heating to 80 ^oC); (c) to realize large-scale production and fabrication of the material; and (d) to design prototypic devices using these materials with the attempts to lower costs. For ammonia capture, future study should focus on evaluation of the under humid conditions. For methane storage, there are several potential research directions: (a) the synthesis of new MOFs with 10 Å (diameter) pores as these small cages are proved to be extremely important for high volumetric methane storage; (b) the clarification of the effect of functional groups on MOFs' methane storage capacities and identification of powerful organic functional groups; (c) the modification the pore interiors of extended MOFs to intensify the interaction between methane molecules and the MOF backbone.

This includes introduction of metal ions, nanoparticles, and complexes; and (d) a close collaboration with industry to facilitate the measurement at higher pressure (up to 250 bar), enlarging the scale of synthesis, and optimizing the fabrication of materials.

When it comes to the design and synthesis of MOF-based solid acids, three approaches have been proposed: (1) acidic functional groups bound to the organic linker; (2) acidic ligands bound to the inorganic cluster; and (3) acidic molecules encapsulated in MOF pores. While in the first approach, the acidity of the MOF is mostly decided by the acidity of the free acidic functional group, the latter two strategies will see more interaction between the framework and the acidic groups, which is of great importance to understand the chemistry within the pores. A new type of MOF-based solid acid is demonstrated by the controllable sulfation of zirconium MOF, MOF-808, on the inorganic cluster. The substitution of terminal formate groups in MOF-808 with sulfate groups has given the sulfated MOF-808 strong acidity that has not been previously observed. The material has shown activity for acid catalyzed Friedel-Crafts acylation, esterification, isomerization, as well as the conversion of methylcyclopentane (MCP) into various hydrocarbons at 150-200 ^{o}C. Another MOF-based acid was synthesized by including phosphotungstic acid (PTA) into the large cages of MIL-101. Interestingly, we observed that the Brønsted acidity (comes from PTA) of the composite material is not directly proportional to the loading of PTA, but instead, is not exhibited until a certain degree of PTA loading is reached. This is explained by the different protonation status of the PTA in the material and the highest loaded composite material, Pt/60PTA/MIL-101 is shown to effectively catalyze hydroisomerization of n-hexane at 250 ^{o}C.

For the field of MOF-based solid acid materials, there is still a limited number of MOFs available, raising the urgent demand for further development of acid stable MOFs. Regarding the term “stability”, two aspects are involved. First, stability towards acidic protons: Brønsted acid catalyzed reactions involve the transfer of protons from the catalyst acidic sites to substrates for the activation of the reactant, which, however, could lead to the slow destruction of the framework if those protons migrate to the carboxylates in the framework instead of returning to their origin. Second, stability towards reactivation: the MOF has to be stable towards conditions to regenerate the acidic sites or to dredge the tunnels, which nowadays are typically done through high temperature calcination or use of strong chemicals. The need exists for developing MOFs in which the metal-link binding units are not carboxylates but other, more acid-resistant, linkages.

However, at the same time, we should clearly state that we are not aiming at making MOF-based solid acid materials the same as those inorganic solid acids in terms of stability, reactivity, and target reactions. The versatile and flexible nature of MOFs guides their applications toward those requiring fine design at the active sites, such as the enzyme-type catalysis and the multicomponent catalysis. For example, enclosing a typical metal catalyst with acidic MOFs is expected to alter the catalyst activity and selectivity. In a way, the MOF in this case acts as a complex ‘ligand’ enclosure for metal nanoparticles where it is possible to impart the MOF designable attributes onto the metal catalyst. This includes variation of organic linker’s length and functional groups as well as incorporation of multiple metal ions into the MOF enclosures. It is clear that acidity, both of Lewis and Brønsted type, should be another likely avenue of modifying the enclosures and accessing completely different kind of reactivity for these traditional catalyst systems. Indeed, the interfacing of acidic MOFs with metal nanoparticles in the way we envision here provides even a more powerful means of making mesoscopic systems when coupled with multivariate MOFs. Here, nanometer regions replete with acidic sites can be

intermingled with regions of moderate acidity or even basic sites. Thus one can potentially design the interior of the MOF to have compartments of different scales of acidity that are linked but which potentially can operate differently; aspects very common in biology while remaining uncommon in synthetic systems.